ON THE PROGRESSION OF LEACHING FROM LARGE PARTICLES IN HEAPS

YOUSEF GHORBANI

SOUTH AFRICA-CAPE TOWN, 2012

UNIVERSITY OF CAPE TOWN
IYUNIVESITHI YASEKAPA • UNIVERSITEIT VAN KAAPSTAD

minerals to metals
DEPARTMENT OF CHEMICAL ENGINEERING

CeBER
CENTRE FOR BIOPROCESS ENGINEERING RESEARCH

On the progression of leaching from large particles in heaps

by

Yousef Ghorbani

B.Sc. (Eng), M.Sc. Eng (Minerals Processing), Iran

A thesis submitted at the University of Cape Town in fulfilment of the requirements for the degree of

Doctor of Philosophy

Department of Chemical Engineering

University of Cape Town

December 2012

SYNOPSIS

Although heap leaching is by now a well-established technology choice in the mining industry, the process remains limited by low recoveries and long extraction times. It is becoming increasingly clear that the successful application of heap leaching technology will ultimately depend on having a comprehensive understanding of the underlying fundamental processes for optimisation to take place. Ores are placed in heaps in a relatively coarse particle size distribution, reaching up to 25 mm top size for crushed and agglomerated ores and as much as 500 mm for ROM ores in dump leaching. Leaching from such large particles is poorly understood and commonly assumed to follow shrinking core type behaviour. However, a comprehensive literature review has returned virtually no evidence to support this assumption, nor is there much of an understanding how exactly minerals leach from any solid matrix.

The subject of this research was, therefore, to understand more clearly the diffusion reaction phenomena of reagents through large particles and to provide true and reliable physical parameters to formulate the relevant modelling approaches to large particle leaching. A combination of standard optical microscopy, SEM, QEMSCAN and X-ray CT techniques has been used for the characterization of crack networks and mineral dissemination in the ore particles, which are important characteristics that determine the diffusion of reagents into and out of particles and the reactions within.

In this study, three large particle size classes (+23/-25, +14/-16, +5.25/-6.75 mm) were prepared from a sphalerite ore from the Northern Cape, South Africa, by two different methods of comminution (HPGR and cone crusher). A high-resolution industrial X-ray CT system was adapted for characterising the spatial distribution of cracks and the mineral dissemination in the samples. The samples were then leached in continuous flooded packed bed leach reactors in the presence of a microbial culture, predominately *L. ferriphilum.* The pH, redox potential, Fe^{+3} and Fe^{+2} concentration as well as total Fe, Zn, Mg, Al and planktonic cell concentration in the effluent solution were measured regularly. The reactors were stopped five times over the course of the 11 months of experiments to investigate the progress of leaching by analysing individual tagged particles using X-ray CT scanning. These results were validated with traditional techniques such as SEM/EDS and

QEMSCAN on other particles sampled from the same reactor. Planktonic and sessile microbial populations were also monitored by quantitative real time polymerase chain reaction (qRT PCR).

Characterisation of the feed particles consistently identified the prevalence of cracks and higher porosity for particles prepared by compression breakage (HPGR) as compared to those prepared by conventional crushing by impact breakage (cone crusher). Comparison of the zinc extraction over 11 months of leaching from ore crushed by HPGR was consistently better than that prepared by cone crusher and showed 10 to 15% additional zinc leach extraction. The implications of this is that the large sphalerite-bearing particles prepared by the HPGR are likely to be more suitable to leaching, since the presence of cracks provides an additional surface-front of target mineral grains for attack by the leaching solution, and a higher prevalence of attachment sites for microorganisms for regeneration of ferrous to ferric iron as leach reagent. It was furthermore noted that access to a mineral grain is necessary for it to leach but that mineral association, sphalerite composition and precipitation are the rate-limiting factors.

Investigation of mineral conversion within single ore particles through X-ray CT indicated that leaching from large particles leads to approach complete conversion near the surface, but only partial conversion in the grains that are closer to the centre of particles. After all minerals near the surface are depleted, leaching regime changes from the readily accessible grains on the particle surface to the more inaccessible grains within particles. In the HPGR product, the reaction zone covers both the particle surface and a relatively deep subsurface zone, which is connected to the surface through cracks. In some particles, even grains close to the centre of the particles can dissolve early if they are connected to particularly deep cracks. In the case of the cone crusher product, the outer surface of the particle is the main reaction surface with only limited reaction occurring in the subsurface zones and not nearly as deep as the particles crushed by HPGR. This implies the existence of micro-cracks in these particles, which are not detectable by the techniques used here. The results indicated that the penetration depth (P_d) is as function of both the comminution mode and the particle size/radius (R). It is clear that prevalence of cracks and particle porosity play key roles in increasing the penetration depth, and as these characteristics are more pronounced in HPGR-crushed particles.

Application of the shrinking core and shrinking sphere models showed that leaching from large particles does not follow either of the two. In fact, three different stages during the leaching process were identified. The first stage refers to leaching of grains at the surface of the ore particles, followed by a second stage, which is leaching of the grains located in the subsurface within the thickness of the penetration depth. A third stage relates to very slow, linear leaching from uncracked zones within the particle, primarily the inner core. Application of a simplified reaction-diffusion model in spherical coordinates showed that there is a good agreement between the trends predicted by a first order particle diffusion-reaction model and the average conversion X (Zn) over time from different position within the ore particle evaluated by direct observation using X-ray CT. This analysis also suggests that the progression of leaching is governed by a combination of reaction and diffusion and not solely by one or the other, as implied in the simplified shrinking core/sphere models.The following alternative model analysis was considered in extension of the intrinsic kinetics equation of the leaching. It is assumed that there is a readily leachable fraction (α) of Zn in the ore, which is accessible through the pore network and a poorly leachable fraction (1-α), which is locked within zones that are not cracked:

$$X(t) = \begin{cases} \alpha\left[1 - \left(1 + (\varphi - 1)\frac{Kt}{\alpha}\right)^{\frac{1}{1-\varphi}}\right] + \beta t \\ \alpha + \beta t \qquad\qquad t > \frac{\alpha}{K(1-\varphi)} \end{cases} \quad if \;\; \varphi < 1$$

A simple linear term (βt) is added to the equation to cover the very slow rate at which the reaction proceeds after depletion of the leachable fraction (α). The core model parameters can be directly related to just two principal variables, particles size (R) and crushing mode, thus providing a simple, but effective modelling tool which adequately describes leaching from large particles, based on actual, rather than assumed phenomena. By directly observing the leaching of individual ore particles, and the effects of networks and mineralogy of the ore sample on it, this research has provided a sound understanding of the underlying mechanisms of metal extraction. This work has set out a systematic approach to assess a particular ore in this regard and should set the route forward for systematic assessment of an ore towards the design of an efficient heap leach operation to leach it.

DECLARATION

I declare that this thesis is my own work. It is being submitted for the degree of Doctor of Philosophy (PhD) in the University of Cape Town. This thesis has not been submitted before for any degree or examination in any other university.

…….

Yousef Ghorbani

… day of …….. 2012

DEDICATION

This thesis is dedicated to my parents, who taught me the value of education. I am deeply indebted to them for their endless support and encouragement and unwavering faith in me.

ACKNOWLEDGEMENTS

It would not have been possible to write this doctoral thesis without the help and support of the kind people around me, to only some of whom it is possible to give particular mention here.

I wish to sincerely thank my supervisors. Dr. Jochen Petersen, for allowing me to explore this field of research. I am grateful for his constructive criticism and guidance throughout this work, and his words of encouragement. Dr. Megan Becker for her constructive criticism mostly in the mineral characterization part of this research. Dr. Aubray Mainza for his contribution in the comminution part of this thesis. Prof. Jean Paul Franzidis for his friendly advice, enthusiasm and for criticising this research in a constructive manner. I am grateful to Dr Kirsten Corin for the QXRD analysis; Prof. Dave Reid (Department of Geological Science, UCT), Paul Keanly (X-Sight X-ray Services), and the Centre for Advanced Scanning Technologies (Department of Physics, UCT) for their advice and support. Financial support from the South Africa Research Chair Initiative (SARChI) in Mineral Beneficiation, and a Research Niche Area (RNA) grant from the National Research Foundation (NRF) are also acknowledged.

I would like to thank Prof. Sue Harrison, Dr. Rob van Hille for questions, comments and remarks during our usual seminars and annual PhD progress report. They contributed tremendously to the success of this research. I wish to thank the entire staff of Chemical Engineering Department for the smiling faces and the ready-to-help attitude.

It was a pleasure to share doctoral studies and life with wonderful people like Charlotte Matdat, Danny Stevenson, Fahimeh Foudzi, Hamied Amoohadi, Mario Baatjies, Meraj Moayer, Naadia van der Bergh, Reza Foudazi, Shirin Taherzadeh, Sima Raoufi, Trisha Daya, Umut Kadir Erol.

Last but not least, a big thank you to my parents, brothers and sisters have given me their unequivocal support throughout, as always, for which my mere expression of thanks likewise does not suffice.

I bless the name of the God Almighty, for making it possible for me to attain this height. I thank God for making this a reality, for it is not by my power nor by my strength, but by the spirit of the highest God.

I finish with a final silence of gratitude for my life.

STATEMENT OF ORIGINALITY

I declare that the work presented in this thesis is to the best of my knowledge, original, except as acknowledged in the text, and that the material has not been submitted, either in whole or in part, for another degree at this or any other university.
The subject matters that comprise original contributions to this field of knowledge are:

- Volumetric distribution maps of the grain and crack networks within the ore particles and trends of their changes during the leaching process.

- A better understanding of the effective role of the grinding methodology on microbial attachment and micro-crack growth during the leaching process.

- A test of the hypothesis that leaching from large particles occurs only at the surface and in subsurface regions which are accessible from the surface by cracks and pores. Results provided sufficient evidence to prove the hypothesis.

- A clear image of the rate-limiting factors such as mineral association and the physical properties of the particles, and their effects on the metal extraction

- Proposed a mathematical approach to large particle leaching in this study based on a sound understanding of the underlying mechanisms; this in return can help to optimise heap leach operation.

LIST OF PUBLICATIONS AND PRESENTATIONS

1. Ghorbani, Y., Becker, M., Petersen, J., Mora, S. H., Mainza, A., Franzidis, J-P., 2010, Estimation method of spatial distribution of surface and bulk porosity in large single ore particles by X-ray computed tomography, Mineral Processing Conference, 6-7 August, Southern African Institute of Mining & Metallurgy Western Cape Branch.

2. Ghorbani, Y., Petersen, J., Becker, M., Mainza, M., Franzidis, J-P., 2010, Large particle effects in chemical/biochemical heap leach processes-A review, Biohydrometalorgy Conference, 8-9 November, Cape Town, South Africa.

3. Ghorbani, Y., Becker, M., Petersen, J., Mora, S. H., Mainza, A., Franzidis, J-P., 2010, Use of X-ray computed tomography to investigate crack distribution and mineral dissemination in sphalerite ore particle, Process Mineralogy Conference, 10-12 November, Cape Town, South Africa.

4. Ghorbani, Y., Becker, M., Mainza, M., Franzidis, J-P., Petersen, J., 2011, Large particle effects in chemical/biochemical heap leach processes-A review, Minerals Engineering 24, 1172-1184 (Rated as one of the top 25 hottest articles, Minerals Engineering, 2011).

5. Ghorbani, Y., Becker, M., Petersen, J., Morar, S. H., Mainza, A., Franzidis, J-P., 2011, Use of X-ray computed tomography to investigate crack distribution and mineral dissemination in sphalerite ore particles, Minerals Engineering 24, 1249-1257.

6. Ghorbani, Y., Petersen, J., Becker, M., Mainza, A., Franzidis, J-P., 2011, Investigation of heap leaching of individual large particles using 3D characterization by X-ray computed tomography, 22. World Mining Congress & Expo, 2011, September 11-16, 2011, İstanbul, Turkey, Volume III, 287-295.

7. Ghorbani, Y., Petersen, Tupikina, O.V., Harrison, S.T.L., Becker, M., Mainza, A.N., Franzidis, J-P., 2011, Investigation of the bioleaching of coarse sphalerite ore particles by a mixed culture of mesophilic chemolithotrophs in saturated leach reactors, the 19th International Biohydrometallurgy Symposium (IBS2011), September 18-22, 2011, Changsha-China, Volume I, 249-257 (Awarded as the first class of the fellowship).

8. Ghorbani, Y., Mainza, A.N., Petersen, J., Kalala, J.T., Becker, M., Franzidis, J-P., 2011, Use of X-ray computed tomography to quantify the differences in cracks and pores in sphalerite ore particles when crushed using an HPGR and cone crusher for heap leach feed preparation, Fifth international conference on: Autogenous and semiautogenous grinding technology, September 25-29, 2011, Vancouver, B.C., Canada.

9. Ghorbani, Y., Petersen, J., Becker, M., Mainza, A., Franzidis, J-P., 2011, Investigation of heap leaching at the particle scale using X-ray computed tomography, International Conference on Percolation leaching: The status globally and in southern Africa, 8-9 November 2011, Misty Hills, Muldersdrift, South Africa, 221-236.

10. Ghorbani, Y., Mainza, A.N., Petersen, Becker, M., Franzidis, J-P., J., Kalala, J.T., 2012, Investigation of particles with high crack density produced by HPGR and its effect on percolation in the course of heap leaching, Comminution '12, 8th International Comminution Symposium, April 17-20, 2012, Cape Town, South Africa.

11. Ghorbani, Y., Petersen, J., Harrison, S.T.L., Tupikina, O.V., Becker, M., Mainza, A.N., Franzidis, J-P., 2012, An experimental study of the long-term bioleaching of large sphalerite ore particles in a circulating fluid fixed-bed reactor, Hydrometallurgy, (129-130), 161-171.

12. Ghorbani, Y., Mainza, A.N., Petersen, J., Becker, M., Franzidis, J-P., Kalala, J.T., 2012, Investigation of particles with high crack density produced by HPGR and its effect on the redistribution of the particle size fraction, Minerals Engineering- DOI:10.1016/j.mineng. 2012.08.010.

13. Ghorbani, Y., Becker, M., Petersen, J., Mainza, A., Franzidis, J-P., 2012, Investigation of the mineral composition and association as rate-limiting factors in large particle leaching, process Mineralogy Conference, 9-11 November, cape Town, South Africa.

14. Ghorbani, Y., Petersen, J., Becker, M., Mainza, A.N., Franzidis, J-P., 2013, Investigation and Modelling of the Progression of Zinc Leaching from Large Sphalerite Ore Particles, Hydrometallurgy, (131-132), 8-23.

TABLE OF CONTENTS

LIST OF TABLES

LIST OF FIGURES

NOMENCLATURE

Abbreviations

2-D	Two-dimensional space
3-D	Three-dimensional space
BET	Brunauer-Emmett-Teller
BMA	Bulk modal analysis
BSE	Back-scattered electron
DNA	Deoxyribonucleic acid
EMPA	Electron Microprobe Analysis
EPS	Exopolysaccharide
FEG	Field emission gun
gDNA	Genomic deoxyribonucleic acid
HPGR	High Pressure Grinding Rolls
ICP	Inductively Coupled Plasma
MeS	A type sulfide mineral
MLA	Mineral Liberation Analyser
MSE	Mean squared error
OES	Optical Emission Spectrometer
PCR	Polymerase chain reaction
PLS	Pregnant leach solution
PSD	Particle size distribution
QEMSCAN	Quantitative Evaluation of Minerals by Scanning Electron Microscopy
qRT PCR	Planktonic and sessile microbial populations were monitored by quantitative real time polymerase chain reaction
QXRD	Quantitative X-Ray Diffraction
RLE	Roast-Leach-Electrowinning
ROI	Region of Interest
ROM	Run-of-mine ore
SDD	Silicon drift detector
SEM/EDS	Scanning Electron Microscope and Energy Dispersive Spectrometry
WDXRF	Wavelength dispersive X-ray Fluorescence
X-ray CT	X-ray Computed Tomography
XRF	X-ray Fluorescence

Chemical formulas

$CaCO_3$	Calcium carbonate
$CH_2(CH_2CHO)_2$	Glutaraldehyde
Cl^-	Chloride ion
Cu	Copper
Fe	Iron
Fe^{2+}	Ferrous iron
Fe^{3+}	Ferric iron
H^+	Hydrogen ions
H_2	Molecular hydrogen
H_2S	Hydrogen sufide
H_2SO_4	Sulfuric acid
K^+	Potassium ion
Mg	Magnesium
Mn	Manganese
Na^+	Sodium ion
$NaHCO_3$	Sodium bicarbonate or sodium hydrogen carbonate
Pb	Lead
S	Sulfur
S^{2-}	Sulfide ion
SO_2	Sulfur dioxide
SO_4^{2-}	Sulfate ion
Zn	Zinc

Greek notations

ε	Fraction of ore porosity
Λ	Wavelength (Å)
P	Density (g/cm^3)

Notation

C_{Ab}	Concentration of reagent A external to particle	mol A/cm^3
C_B^{ini}	Initial extractable grade of solid reactant B	mol B/g ore
Da	Damköhler numbers	
D_{Ae}	Effective pore diffusivity of reagent A	m/s
F(sp)	Specific grinding Force	N/mm^2
fi	Fraction of the total number of electrons contributed by element i	
h	Thickness of the object	cm
I	Intensity of attenuated X-rays	
I_0	Intensity of the incident X-rays	
LLD	Lower limit of detection	
M	Coefficient	
nd	Not detected	
R	Average of the particle size class	mm
v v m	Gas volume flow per unit of liquid volume per minute (volume per volume per minute)	
W(sp)	Specific Energy	kWh/t
X	Mineral conversion from the ore sample	%
Ze	Effective atomic number	
μ	Linear attenuation coefficient	cm^{-1}

Minerals

$CuFeS_2$	Chalcopyrite
$Fe_{16}O_{28}(SO_4)4H_{16}$	Schwertmannite
Fe_7S_8	Pyrrhotite
FeS_2	Pyrite
$KFe_3(SO_4)_2(OH)_6$	Jarosite
MnS	Alabandite
MoS_2	Molybdenite
PbS	Galena
SiO_2	Quartz
ZnS	Sphalerite

1 INTRODUCTION

1.1 Background

Heap leaching from low-grade ores has become a major contributor to the total global extraction of economically important metals, notably copper, gold, silver and uranium (Padilla *et al*., 2008). Despite the widespread use of heap leaching in industry, the process remains limited by low recoveries, long extraction times, and high operating costs, especially in terms of acid consumption. However, as the technology becomes more and more adopted, it becomes increasingly apparent that the successful application of heap leaching technology will ultimately depend on having a comprehensive understanding of the fundamental processes underlying it.

In general, heap leaching is most applicable to the leaching of low grade ores. Ore is typically crushed to a size range suitable for controlled irrigation and percolation and deposited in heaps. The heaps are irrigated with lixiviant from the top and, for heap bioleaching, aerated from the bottom. Metal values are leached from the ore particles and recovered from the leach solution percolating through the bed. However, the process of heap leaching is not efficient, in that it is characterised by low recoveries and long extraction times. This inefficiency is a result of poor permeability through and into the ore, which results in an uneven distribution of the leaching solution, which has been identified as a key limitation of heap leaching technology (Dixon and Petersen, 2003).

In heap leach applications, the major technical challenge is to expose the mineral grains within the ore to the lixiviant, be it acid, ferric ions or bacteria and oxygen to facilitate rapid reaction and removal into the flowing PLS.

One possible approach to improving recovery in the heap is to introduce fractures into large ore particles, so increasing the surface area available for lixiviant attack. Extensive cracking can be induced in a number of ways; for example by applying sufficient

pressure to crack the rock matrix such as High Pressure Grinding Rolls (HPGR) or by inducing extensive thermal stresses that induce differential expansion of the mineral phase within the rock. The comminution principle utilized in the HPGR, which is compression as a breakage mechanism, is different from that in conventional crushers or tumbling mills where impact and abrasion breakage mechanism are dominant. The HPGR breaks particles predominantly in an autogenous way, unlike other comminution devices (Unlanda and Szczelina, 2004; Daniel, 2007). As a result, the product from a HPGR is different, and may be expected to have a different behaviour in downstream processes (Aydoğan *et al*., 2006; Apling and Bwalya, 1997). Differences in particle porosity and crack network distribution will almost certainly have an influence on the efficiency of the leaching process.

The relatively coarse particle size distribution is one of the unique features of heaps, typically 25 mm top size for crushed and agglomerated ores and larger for run-of-mine dump leaching operations. Leaching from such large particles is poorly understood and commonly assumed to follow shrinking core type behaviour. In fact, there are virtually no literature sources, which offer any evidence for the validity of this assumption in the given context. A conventional shrinking core approach would work only for gangue particles, which are homogeneously porous and have mineral grains well distributed throughout (Liddell, 2005; Velardo *et al*., 2002; Vegliò *et al*., 2001).

Recent experimental evidence suggests that in fact leaching from large particles occurs only at the surface and in subsurface regions, which are accessible from the surface by cracks and pores (Liddell, 2005; Malmström *et al.*, 2008; Sracek *et al*., 2006; Strömberg and Banwart, 1999). This indirectly relates leaching behaviour to the method by which the ore has been crushed prior to leaching.

Ores are present in heaps with relatively coarse particle size distributions and the actual progression of leaching from large particles has never been systematically explored, primarily because one cannot look inside them. In order to understand more clearly the diffusion of reagents through large particles and to provide true and reliable physical

parameters to formulate the relevant modelling approaches to large particle leaching, it is necessary to begin by studying the process in 3-D. The use of traditional experimental methods cannot realize this, as they are usually destructive. However, an improved understanding of leaching from large particle systems can be achieved with high resolution 3-D X-ray Computed Tomography (CT) as it is non-destructive. This can be used to measure the distribution of cracks and the dissemination of minerals in ore particles, which are important characteristics that determine the diffusion of reagents into and out of particles and the reactions within. Observations using this technique can be coupled with the results from other modern automated mineralogy measurement techniques, more traditional column leach experiments and solution chemistry, in order to identify the progress of heap leaching at the particle scale. With such insight, it would be possible to describe leaching from within large particles with a suitable model.

1.2 Research aims and objectives

In order to effectively understand and formulate models for bioleaching from large particles, fundamental study of the rate controlling factor(s) is important. Hence, the objective of this work was the systematic investigation of leaching behaviour at the surface and the interior of large particles in the context of chemical leaching and bioleaching of a typical sulfide ore. In more specific terms, this work investigated leaching behaviour of typical sufide ore with the following objectives:

- To determine the effect of particle size on the kinetics of (bio) leaching processes;
- To investigate intra-particle diffusion-reaction phenomena and their relationship with the network of cracks and pores, particle size distribution and mineralogy;
- To give a clear image of the rate-limiting factors such as mineral association, and the physical properties of the particles, and their effects on the metal extraction.

These objectives will provide a sound understanding of the underlying mechanisms and will help to formulate appropriate modelling approaches to large particle leaching, which in turn can help to optimise heap leach operation with more appropriate process models.

1.3 Scope and limitation of the thesis

Since the chemical/biochemical leaching of the ore samples and investigation of the effective parameters are extremely diverse, the scope and boundaries of this study are illustrated by Figure 1.1. This research involves a systematic investigation of leaching behaviour at the surface and in the interior of large particles (from 5 to 25 mm). Chemical leaching and bioleaching are investigated for a typical sulfide ore at ambient temperature. Only mixed culture of mesophilic microorganisms is considered in the bioleaching.

This project investigates the effects of ore mineralogy, topology (surface properties), 3-D characteristics of the crack and micro-crack network, and grain distribution on the leaching behaviour of large particles. The particle shape and the surface chemistry will not be focussed upon. This study investigates the effect of the comminution devices (HPGR vs. cone crusher) on leaching behaviour of the ore particles. Quantitative and qualitative analysis of samples was carried out before, during and after leaching. A deeper analysis of the mechanics of crack formation and propagation within the different comminution devices was not considered in this study.

The focus was on the fundamental and systematic investigation of leaching behaviour and identification of factors, which influence the rate of chemical/biochemical processes within coarse sulfide mineral particles.

Physical and chemical characterization		
Key characteristic mapped in 3D	**Ore Type**	**Mineralogy and surface properties**
Tomography of cracks, voids and micro-structure	Sulfide ores	Mineral composition and dissemination
Grain distribution	Oxide ores	Particle Size distribution (5 to 25 mm)
Free surface		Acid consumption
Liberation		Formation of precipitates
Mineralogical association	Carbonate	Galvanic interactions
Mechanical imperfections on particle surface		
Particle shape		
Evolvement of permeability of ore granular media		Hydrophobicity

Comminution
Principal breakage mechanisms
Impact
Compression
Abrasion
Attrition

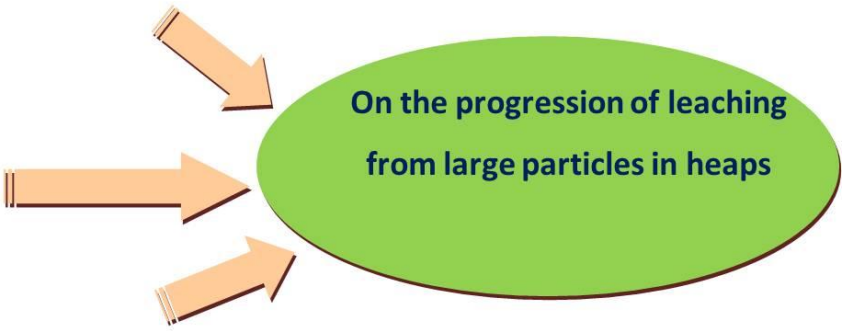

Chemical/biochemical leaching			
Microorganisms	**pH**	**Temperature**	**Chemical Reagent**
Mesophiles	Acidic	Ambient temperatures (below 40°C)	Sulphuric acid
Moderate thermopiles	Alkali	Between 45 - 60 °C	
Thermopiles		60- 80°C	
Extreme thermopiles		greater than 80 °C	
Abiotic			

Figure 1.1: Area shaded in orange colour highlights the key components and the scope of the thesis.

1.4 Hypotheses

The following hypotheses have been formulated:

- Leaching from large particles occurs only at the surface and in subsurface regions, which are accessible from the surface by cracks and pores.

- The cracks produced by comminution with compression breakage (HPGRs) rather than conventional impact crushers significantly promote subsurface leaching.

1.5 Key questions

In this research, the objectives were met by addressing the following key questions:

- Is there a difference between HPGR cracked products and conventionally crushed products?
- What is the minimum size of large particle in heap leaching for which intra-particle diffusion becomes the dominant leach mechanism?
- What is the relative importance of various factors influencing the leaching from large particles, such as topology, crack network, particle size distribution and mineralogy?
- How can the crack network, grain distribution and mineral dissemination in large particles be described or mapped in terms of reasonably simple model parameters?
- What are the limitations in commonly assumed models for leaching from large particles?
- What is the most appropriate modelling approach to large particle leaching?

1.6 Research approach and organisation of thesis

The experimental approach to this project has been divided into three parts (Figure 1.2). Firstly, large particle size classes (+23/-25, +14/-16, +5.25/-6.75 mm) were prepared from a sphalerite ore bulk sample from the Northern Cape, South Africa, by two different methods of comminution (High Pressure Grinding Rolls (HPGR) and cone crusher). Secondly, physical and chemical characterization of selected ore particles was done. Thirdly, the ore samples were then leached in continuous flooded packed bed leach reactors. The reactors were stopped from time to time to investigate the progress of leaching by analysing individual tagged particles using X-ray CT scanning. These results were validated using traditional techniques such as Scanning Electron Microscope and Energy Dispersive Spectrometry (SEM/EDS), Electron Microprobe (EMPA) and Quantitative Evaluation of Minerals by Scanning Electron Microscopy (QEMSCAN). Planktonic and sessile microbial populations were also monitored by quantitative real time polymerase chain reaction (qRT PCR).

The body of this thesis is divided into seven chapters starting with the introduction where the background, scope of the thesis and key questions are presented in Chapter 1. This is followed by a critical review of the literature in Chapter 2 on the mechanism of bioleaching, the application of bioleaching techniques, heap leaching, leaching rate during the heap processes, effective parameters in heap leaching related to single ore particles and particle models within heap leach modelling. Chapter 3 describes sampling and analytical methods.

The results and discussions are then divided into three chapters; Chapter 4 describes and discusses the mineralogical characterisation of the sphalerite ore samples, Chapter 5 describes and discusses the effect of the comminution devices on the ore particle size distribution and crack density and Chapter 6 describes and discusses the leaching process in the leach reactors and selected ore particles.

Some final conclusions as well as several recommendations for further research are given in Chapter 7. The complete set of results from the various experiments is given in the Appendices.

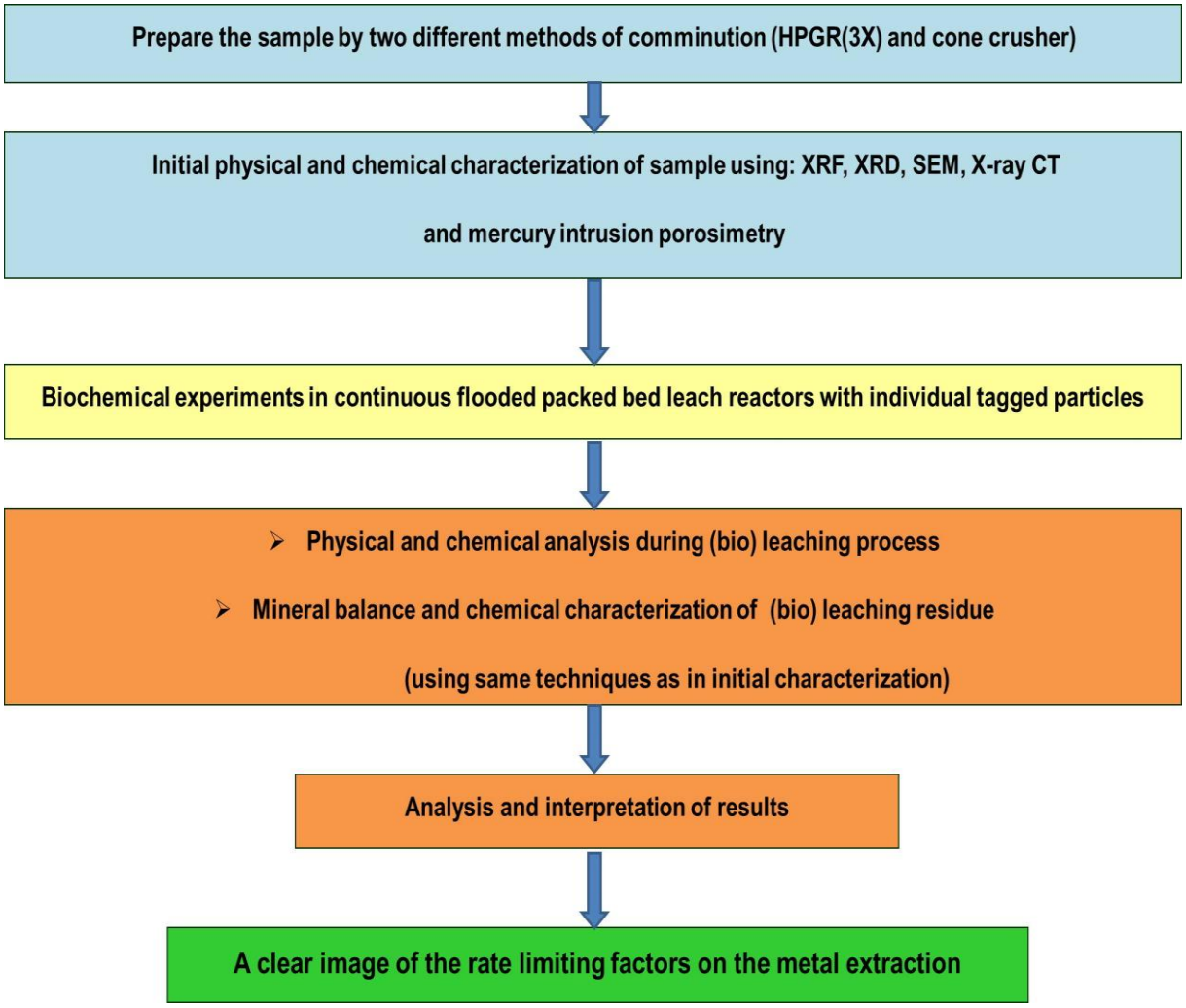

Figure 1.2: Experimental approach flow diagram.

2 LITERATURE REVIEW

2.1 Introduction

With the typical ore grades declining and the economic and environmental cost of energy increasing, less energy intensive metal extraction techniques are becoming more attractive. One of these methods is heap leaching, which from its first implementation for the recovery of gold from low-grade ores by cyanidation in the early 1970s, has, in conjunction with solvent extraction and electrowinning, developed into a key hydrometallurgical technology for the recovery of base metals, primarily copper from both oxides and secondary sulfides.

Heap and dump leaching offer a number of advantages embracing simple equipment, low investment and operation cost, and reasonable yields over a period of recirculation. In the immediate future, heap leaching is likely to be a major area of expansion. In the United States, approximately one-third of gold and nearly 30% of total new copper production come from heap leaching. Nearly all new copper and gold mines involve some ore processing by heap leaching. Although heap leaching for zinc and uranium has been considered before, it is gaining renewed attention. Despite the current widespread use of heap leaching in industry, the process is still limited by low recoveries, long extraction times, and high operation costs, especially in terms of acid consumption and at its core, this relates to a limited fundamental understanding of the process. This knowledge is derived from the investigation of the interactions between the physical, chemical and biological processes that drive a heap (Acevedo, 2002; Dreisinger, 2006; Mellado *et al*., 2009).

2.2 The mechanism of bioleaching

The mechanism of bioleaching of sulfide minerals was first proposed by Silverman and Ehrlich (1964) and this has been a subject of much debate in the last decade (Boon, 2001; Hansford, 1997; Pogliani and Donati, 1999; Sand *et al.*, 1999; Tributsch, 2001). It is now generally accepted that mineral bioleaching is a combined chemical/microbial process in which ferric-iron and protons form part of the reactant of the leaching reaction. The key role of the microorganisms is to generate/regenerate the leaching agents and to facilitate the reaction by creating a reaction space in which the leaching takes place. It has been reported that microorganisms form an exopolysaccharide (EPS) layer when they attach to the mineral (Gehrke *et al.*, 1998; Sand *et al.*, 2006) but not when growing as planktonic (free) cells (Devasia *et al.*, 1993). Bioleaching reactions take place most rapidly and efficiently within this EPS layer and therefore the EPS serves as the reaction space (Sand *et al.*, 2001; Tributsch, 2001).

Mechanistically, bioleaching of sulfide mineral proceeds via three main sub-processes (Boon, 2001; Clark and Norris, 1996; Hansford and Vargas, 2001) as shown in Figure 2.1: (1) chemical attack of the sulfide mineral by ferric-iron and/or protons, releasing the metal into solution (as in the case of copper) or exposing metal of interest for cyanidation (the case of occluded gold), ferric-iron is reduced to ferrous-iron in the process and sulphur species are formed. Here, the ferric-iron is the oxidizing agent; it oxidizes the metal sulfide via two pathways depending on the mineral type: the thiosulfate and polysufide mechanisms (Sand *et al.*, 1999). (2) Microbial oxidation of reduced ferrous-iron to ferric-iron, (3) Microbial oxidation of sulphur moiety to elemental sulphr and/or sulfate ion respectively.

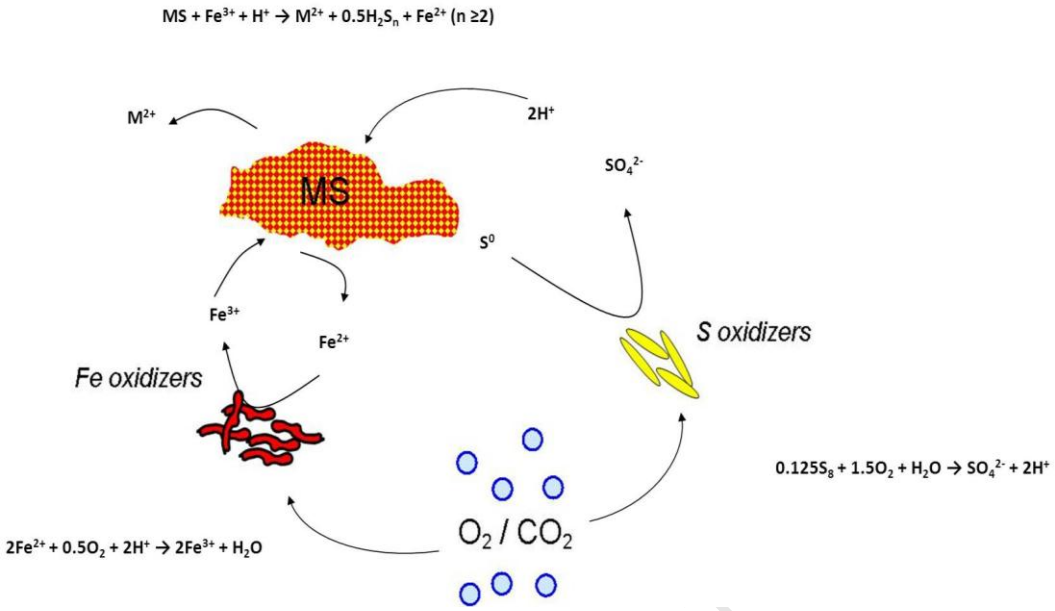

Figure 2.1: The schematic representation of bioleaching mechanism (Source: Hansford and Vargas, 2001).

A thiosulfate mechanism was proposed for the oxidation of acid insoluble metal sulfides such as pyrite (FeS_2) and molybdenite (MoS_2), and a polysulfide mechanism for acid soluble metal sulfides such as sphalerite (ZnS), chalcopyrite ($CuFeS_2$) or galena (PbS). In the thiosulfate pathway (Figure 2.2a), solubilisation is through ferric iron attack on the acid-insoluble metal sulfides with thiosulfate being the main intermediate and sulfat the end product. Significant amounts of elemental sulfur (10-20%) may be produced in the absence of sulfur-oxidizing bacteria (Sand *et al*. 1999). In the polysulfide pathway (Figure 2.2b), solubilisation of the acid-soluble metal sulfide is through a combined attack by ferric iron and protons with elemental sulphur as the main intermediate. This elemental sulphur is relatively stable but may be oxidized to sulfate by sulphuroxidizing microbes such as *Acidithiobacillus thiooxidans* or *Acidithiobacillus caldus* (Rawlings, 2005). The important reactions in bioleaching of sulfide minerals as shown in Figure 2.2 are represented in Eq. (2.1 to 2.3).

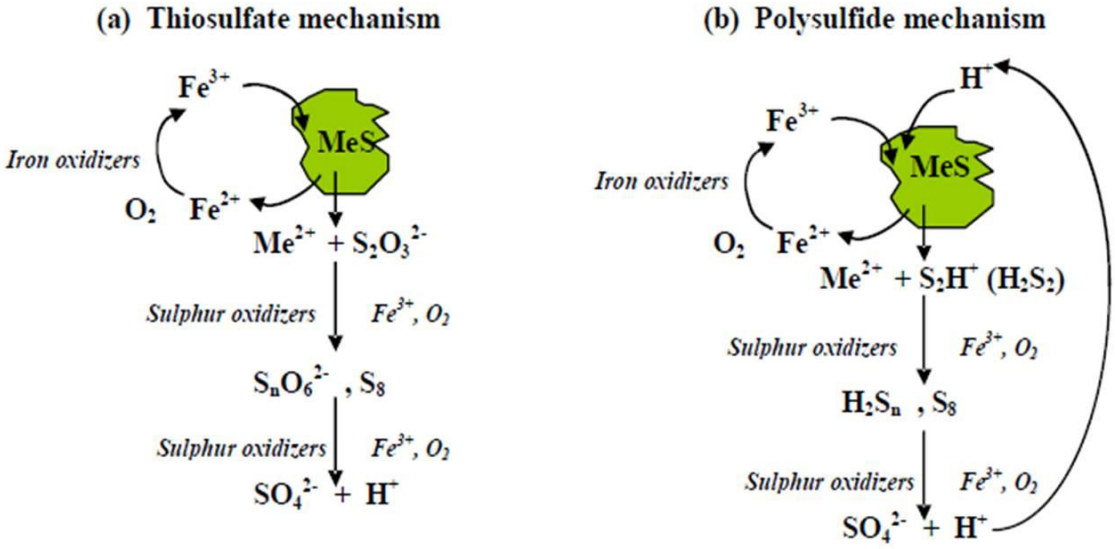

Figure 2.2: Schematic representation of bioleaching mechanism showing the sulphur pathways (a) the thiosulfate pathway, and (b) the polysulfide pathways as proposed by Sand *et al.*, (1999) for bioleaching of sulfide mineral of the type MeS. Source: Adapted from Rohwerder *et al.*, (2003).

$$MeS + 2Fe^{3+} \rightarrow Me^{2+} + 2Fe^{2+} + S^{o} \qquad \text{Eq. (2.1)}$$

$$4Fe^{2+} + O_2 + 4H^{+} \rightarrow Fe^{3+} + 2H_2O \qquad \text{Eq. (2.2)}$$

$$2S + 3O_2 + 2H_2O \rightarrow 2H_2SO_4 \qquad \text{Eq. (2.3)}$$

The ferrous iron produced in Eq. (2.1) is re-oxidized back to ferric iron as shown in Eq. (2.2) by iron-oxidizing microorganisms so that the leaching reaction in Eq. (2.1) can continue in a cyclic manner. The sulphur species are oxidized to sulphuric acid by sulphur oxidizing microbes. The role of the microorganisms in the solubilisation of metal sulfides is not only to provide sulphuric acid for a proton attack, but also to keep the iron in the oxidized ferric state for an oxidative attack on the mineral. From the latter, it can be seen that the microbial ferrous-iron oxidation to ferric-iron is a critical sub-process in the bioleaching of sulfide minerals.

2.3 The application of bioleaching techniques

At the industrial scale, bioleaching is applied in two main types of processes: stirred tank type and irrigated dump and heap processes. Stirred tank bioleaching allows for good control of pertinent operating parameters. It is can be operated under conditions necessary for optimum microbial activity, resulting in a better performance and high productivity. Tank bioleaching requires relatively long residence times. The mineral feed needs to be in the form of a finely milled concentrate, similar to smelting and roasting. This precludes the technique from use with low-grade ores and thus is mostly used in biooxidation of ore concentrates. Tank bioleaching has high operating costs, primarily due to the high solution inventories needed because of limitations on slurry densities; hence, it is used for leaching of high value ore/concentrate. The setup is such that the bioreactors are arranged in series and/or parallel. The tanks are well aerated and operated in a continuous stirred mode. The feed is added to the first tank and the overflow stream is connected from tank to tank until biooxidation of the mineral concentrate is sufficiently complete (Brandl *et al.*, 2001; Sand *et al.*, 1999). The relatively homogeneous nature of the slurry in tank bioleaching allows for good control of process parameters over other techniques. However, limitations in reactor volume restrict its application to the treatment of mineral concentrates or when moderate volumes of ore are to be processed (Acevedo, 2002; Brierley, 2008).

Heap and dump bioleaching are examples of the percolation type. Heap bioleaching has become widely practised for copper extraction from low-grade deposits. Unlike dump leaching, heap bioleaching involves the use of size reduction prior to stacking. In-situ bioleaching involves leaching of the ore in place, using drill hole solution systems without actual removal from the ore body due to inaccessibility of the site. It is used for low-grade ore and in cases where it is not economical to pre-treat the ore by the conventional mining methods (Brandl *et al.*, 2001; Brierley, 2008). Commercial application of in-situ, dump and heap leaching to bioleaching and recovery of copper are widely reported (Brierley, 2008; Padilla *et al*., 2008).

2.4 Heap leaching

Heap leaching from low-grade ores has become a major contributor to the total global extraction of economically important metals, notably copper, gold, silver, and uranium (Padilla *et al*., 2008).

Crushed or run-of-mine ore (ROM) is piled on an impermeable pad and leaching reagents are introduced by irrigation (continuously or intermittently) from the top, and the solution is left to seep through the ore bed where it can react with the target minerals. The desired element from the related mineral is extracted and the solution becomes increasingly loaded as it percolates through the pile. Leaching may be facilitated by microorganisms resident within the ore bed. The pregnant leach solution (PLS) is collected by a drainage system at the base of the pile and channelled to the PLS pond. The PLS is then pumped to the processing facility where the value metal is recovered through a suitable technology (by solvent extraction, cementation or adsorption). The ‘‘barren’’ leach solution is pumped to the barren solution pond from where, after solution make-up, it is reapplied to the surface of the heap (Figure 2.3).

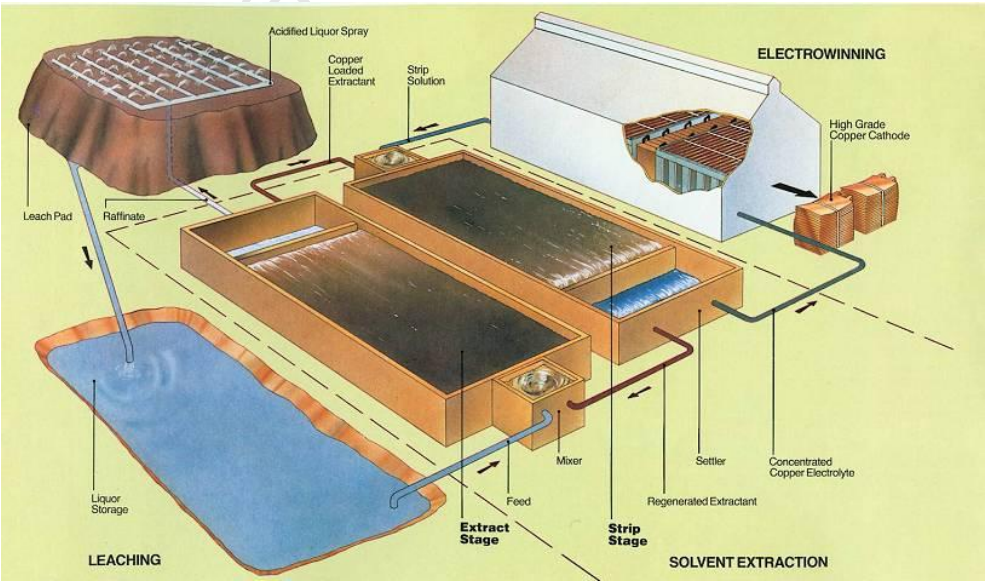

Figure 2.3: A schematic of the heap leach operation, Web reference at http://electrochem.cwru.edu/encycl/art-m02-metals.htm

This technique is mostly applied to bioleaching of copper and refractory gold-bearing ores (Rawlings, 1999; Rawlings *et al.*, 2003; Watling, 2006).

2.4.1 Heap leaching and conventional methods

In the immediate future, heap leaching is likely to be a major area of expansion, through new-patented processes (Pradhan *et al*., 2008; Thiel and Smith, 2004). In the United States, approximately one-third of gold and nearly 30% of total new copper production come from heap leaching. Nearly all new copper and gold mines involve some ore processing by heap leaching (Acevedo, 2002). Heap leaching has been considered for zinc leaching (Petersen and Dixon, 2007a) and uranium is gaining renewed attention (Carlsson and Buchel, 2005; Shakir *et al*., 1992). Operated correctly, heap leaching offers economic recovery of resources that would be too marginal for other process routes, such as concentration followed by smelting or autoclaving (Petersen and Dixon, 2007b). This method may therefore be particularly attractive for remote and marginal mines.

Heap bioleaching has become a reasonably well established technology for the extraction of low-grade secondary copper sulfides and the oxidation of refractory gold ores. At present, the technology is being developed also for the recovery of primary copper sulfides using thermophilic microbes (Pradhan *et al*., 2008; Petersen and Dixon, 2007a; Nicol *et al*., 2011).

Heaps and dumps present a number of advantages and disadvantages (Table 2.1) compared to conventional milling and flotation of sulfide ores (Acevedo, 2002; Brierley, 2008).

Table 2.1: Advantages/disadvantages of heap leaching.

Advantages	Disadvantages
Low capital and operating costs	Lower recoveries than mill/float or mill/leach
Absence of milling step, may require crushing and agglomeration	Long leach cycles and hold-up
Simplicity of atmospheric leach processes	Lengthy pilot test programme
Can be used to treat low-grade ores, wastes and small deposits	Large footprint
Absence of liquid-solid separation step allows counter current operation	
Metal tenor may be built up by recycling solution over heaps	
Simplicity in equipment and operation	Environmental release of PLS
Shorter start-up times	
Less intensive environmental regulatory concerns	

2.4.2 Kinetic aspects in heap (bio) leaching

Although the concept of heap bioleaching appears to be very simple, the sub-processes taking place within the heap are rather complex, and their interactions are not yet fully understood. Dixon and Petersen (2003) distinguish between different processes ranging from the macro- to the grain-scale, as is illustrated in Figure 2.4. At the macro scale, kinetics are governed primarily by transport of mass and energy into, through, and out of the heap structure.

At the aggregate scale, gas uptake into the liquid phase, intra-and inter-particle diffusion within the stagnant zones, and bacterial growth and oxidation are all contributing to the leaching kinetics. Aggregate scale processes at the 'meso'-scale occur at the level of a cluster of ore particles. The important processes at this level are oxygen uptake into solution from the air space, diffusion of dissolved chemical species through the inter-particle pores, and microbial processes.

Scale	Sub-processes	Illustration
Mineral grain	Ferric reduction Mineral oxidation Sulfur oxidation Surface processes	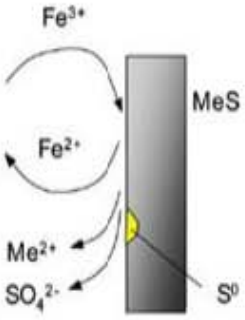
Ore particle	Topological effects Intra-particle diffusion Particle size distribution	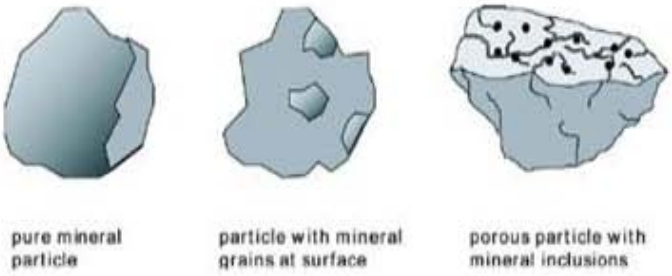
Stagnant cluster	Gas adsorption Inter- and intra-particle diffusion Microbial growth Microbial attachment Microbial oxidation	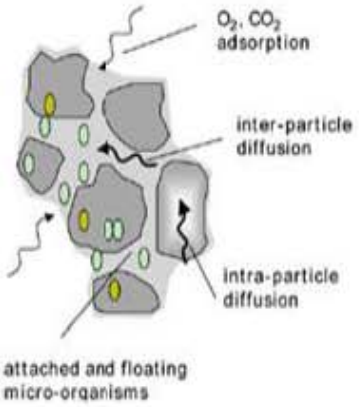
Heap	Unsaturated solution flow Gas advection Water vapour transport Heat balance	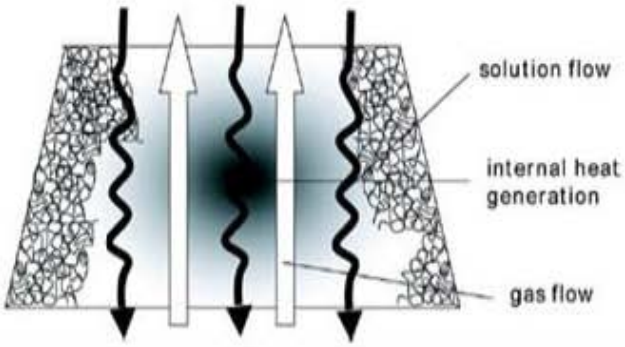

Figure 2.4: Schematic representation of sub-processes in heap bioleaching (Source: Dixon and Petersen, 2003).

Oxygen is a key reactant in heap bioleaching, as the microbes oxidize ferrous iron and reduced sulphur species only to the extent to which oxygen is available in the system. Oxygen uptake into solution across the gas-liquid interface is a temperature dependent mass transfer step. The mass transfer coefficient is subject to measurement, and has been highlighted as an important parameter in heap leach modelling (Bouffard, 2003; Petersen, 2010).

The dissolved chemical species (reactants and reaction products) must diffuse through the stagnant solution occupying the bed voidage in order to be recovered in the PLS, or to be delivered to the site of chemical reactions within the ore particles. The extent of this inter-particle pore diffusion effect on extraction rate and mineral leaching depends on the length of the diffusion pathway, which may be significant for systems with poor solution distribution (Dixon and Petersen, 2003).

At the particle scale, leaching is governed by the way in which mineral grains are distributed within a single particle - this is referred to as the topological effect. Mineral grains may be present as anything from free grains to encapsulated local spots inside a particle. Their distribution and accessibility within particles directly determine the leachability of the target mineral. Furthermore, in low-grade ores the mineralogy of the gangue matrix is also of some significance, as it can interfere with mineral leaching and biological phenomena (Park and Levenspiel, 1977). Another important process at the particle level is the transport of reactants to, and reaction products from, reaction sites within the particle. This process is diffusion governed and limited by the size and porosity of the ore particle, the concentration gradient, and the diffusivity of the species.

Finally, at the grain scale, the chemical and electrochemical interactions at the grain surface determine the leaching kinetics (Harneit, *et al*., 2006). The chemical reactions are primarily a function of temperature (characterized by the activation energy), and concentration of reactants. The reaction may be further complicated due to interaction between different minerals (galvanic interaction), as is the case with pyrite being

present in many base metal sulfide ores. In addition, the direct microbial interaction with exposed mineral surfaces (contact leaching mechanism) as reported by Sand *et al.* (2001) might also be significant at this level. Recent studies have shown that this may be important in heap bioleaching as bacterial attachment is a function of available substrate surfaces (Chiume *et al*., 2010; Africa *et al*. 2010*;* 2007).

2.4.3 Sphalerite ore

2.4.3.1 Sphalerite mineralogy

Sphalerite (Zn, Fe) S), is the major ore of zinc in all sulfide-rich base metal deposits. It is widely distributed in nature and is present in a variety of sulfide deposits. The simple formula, ZnS, belies the minerals' ability to incorporate a broad range of trace elements, often at levels that are economic to exploit or pose an environmental hazard. The broad range of trace element incorporation in sphalerite correlates with the colour shown by natural specimens, which ranges from white, yellow, brown, red, pink, green, grey-black and black. Pure sphalerite (ZnS) is a clear honey colour crystal. As its iron content increases, it assumes a dark metallic appearance. A dark black colour ('marmatite') normally indicates high Fe content (_> 6 wt. %), but other elements (e.g., Mn, Co) are also highly influential on colour (McClung and Viljoen, 2011). It is commonly associated with other metal sulfide minerals such as pyrite (FeS_2), galena (PbS) and/or pyrrhotite ($Fe_{1-x}S$) and may be accompanied by one or more of the copper and/or copper-iron sulfides, including covellite (CuS), idaite (Cu_5Fe< 1S6), bornite (Cu_5FeS_4), chalcopyrite ($CuFeS_2$), and cubanite ($CuFe_2S_3$) or intermediate solid solution ((Cu, Fe) $_{1+x}$S)) (Harmer *et al*., 2007).

2.4.3.2 Sphalerite Bioleaching

In recent years, great interest has emerged in the use of biological mineral processing technologies. In particular, the bioleaching of sulfide minerals has been frequently

studied, due to its widespread application in the processing of copper, uranium, refractory gold and other precious and semi-precious metals, utilising both heap and tank leaching processes (Rawlings *et al*., 2003). Currently, the majority of sphalerite ores are treated through flotation, followed by smelting. However, smelting is becoming increasingly cost intensive due to tightening environmental restrictions. In addition, due to the need to process complex ores of increasingly low grades, concentration of ores by flotation is becoming more and more difficult. These difficulties have left producers searching for more cost effective and environmentally acceptable processing options. The hydrometallurgical processing of sphalerite presents a possible alternative to pyrometallurgical techniques. Over the last few years, several innovative leaching processes have been developed for zinc extraction, such as copper catalysed ammonia leaching, pressure leaching, persulfate leaching, simultaneous leaching, heap bioleaching and tank bioleaching (Raghavan *et al*., 1999; Herrero *et al*., 2010; Santos *et al*., 2010). Of these, the bioleaching processes present some of the most promising technology, due to their inherent low costs and environmental advantages. Further interest has been generated in the bioleaching of sphalerite due to its possible environmental implications; bioleaching has been suggested as a possible means of removing trace amounts of metals such as zinc and iron from contaminated sediments and soils, and may also be involved in the production of heavy metal contaminated mine run-off (Silva, 2004)

2.5 Leaching rate during the heap processes

Metal extraction rates in copper sulfide heap leaching typically show an initially fast leaching rate, reaching up to 50-60 percent extraction over the first few months, followed by a slower constant rate period, reaching up to 80-90 percent copper extraction over the following 12-24 months (Figure 2.5). For copper oxide minerals, whether alone or in mixed sulfide/oxide ores, more than 90 percent extraction can be common in the first 30 days (Watling, 2006 and Dreisinger, 2006). This is considered to

represent the change in leaching from the readily accessible grains on the particle surface to the more inaccessible grains within particles (Watling, 2006). Typical recovery in base metal sulfide heap leaching is about 60-70 percent (Brierley, 2008; Dreisinger, 2006, Thiel and Smith, 2004) over a 1-2 year period, after which the operation is usually discontinued due to the slow rates. Rapid leaching occurs in all size classes only initially, leading to near complete conversion in the smaller sizes, but only partial conversion in the larger sizes. After this initially rapid phase, leaching slows down dramatically. This was explained by the fact that after depletion of the easy-to-leach surface minerals, ferric iron or acid have to migrate deeper into particles via a pore network, and the reduced ferrous form has to return to the surface to be re-oxidised. Hence, it is likely that the grains near the surface will be depleted much more rapidly, and a slower-leaching mineral at the surface might dissolve preferentially over a fast-leaching mineral deep inside a particle (Ogbonna *et al*., 2006).

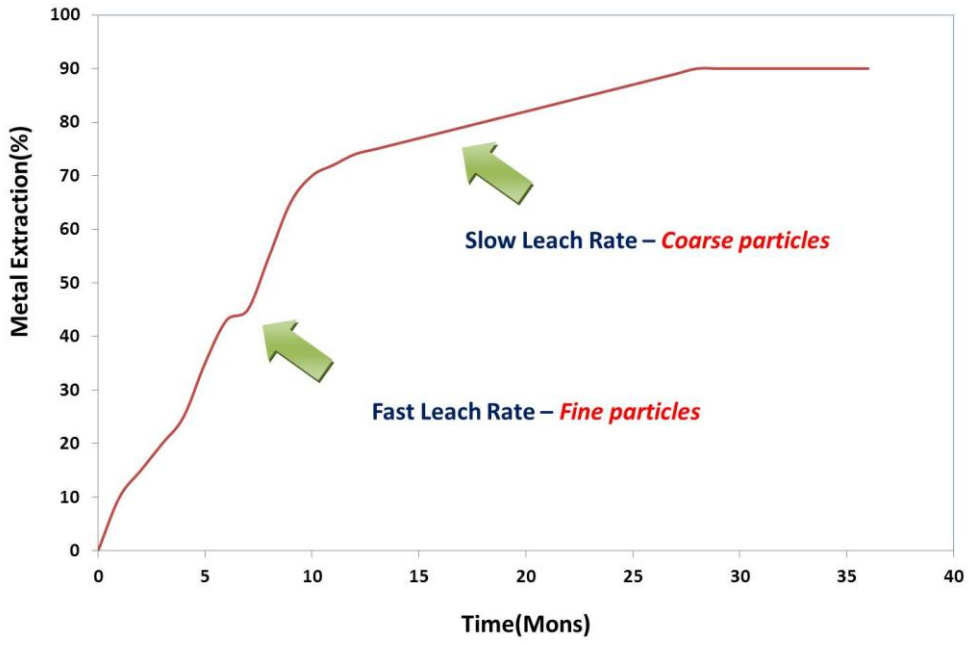

Figure 2.5: Metal extraction rate in heap leach process (adapted from: Dreisinger, (2006)).

2.5.1 Mechanism of leaching from large particles

In the current climate, where energy costs are a major consideration during ore processing, the relatively coarse particle size used in heap leaching is a key factor contributing to the economic exploitation of ores through heaps by avoiding energy intensive comminution. Typically, the feed size is < 25 mm for crushed and agglomerated ores and as large as 500 mm for run of mine ore types found in dump leaching (Watling, 2006).

Due to larger ore particle sizes encountered in heap leaching, chemical diffusion within the solution filled rock pores always affects the extraction rates. However, mixed leaching kinetics occur when slowly reacting mineral grains (e.g., chalcopyrite) or very large mineral grains are present within the ore. In these cases, the mineral dissolution rate must be considered along with diffusion (Barstlett, 1992).

Leaching of minerals from whole ore particles, where the key reagent has to migrate from the particle surface, will result in a rim-leaching effect in larger particles (Ogbonna, 2006). All fast-leaching minerals near the surface are depleted first, before the leach front can migrate further into the particle. Hence, if competition exists for reagents between different mineral phases, then this is likely to be skewed in favour of the slower-leaching mineral near the surface, rather than the faster-leaching closer to the centre. Once, the fast-leaching mineral has been depleted from the surface, rather than leaching more of the fast-leaching mineral deeper inside the particle. The effect is exaggerated with increasing particle size.

2.5.2 Chemical weathering

Oxidation of sulfides in a rock by chemical and biochemical leaching is a natural phenomenon, similar to the processes that occur in heap leaching. Investigating mechanisms of weathering could provide useful understanding of heap kinetics,

especially for leaching from large particles. The intrinsic properties of the sulfides (chemical composition, crystal structure, defect density and distribution, etc.) largely control their rate of oxidation, but also vary with the ambient physio-chemical settings (López *et al*., 2007; Gerke *et al*., 1998; Strömberg and Banwart, 1999; Evans and Banwart, 2006). For example, marcasite and framboidal pyrite will oxidize quickly while crystalline pyrite will oxidize slowly (Malmström *et al*., 2008).

Of particular importance is the presence of a fluid phase (e.g. oxygenated water) that facilitates the oxidation process by providing for a variety of reactions to occur at the fluid-mineral interface as well as serving to remove oxidation products from the interface that may otherwise impede further reactions. The nature and extent of reactions occurring at the sulfide-solution interface are very much dependent on the composition of the solution. This in turn is influenced by the enclosing mineral assemblage (except at very high flow rates). Therefore, rock-forming minerals that occur together with a sulfide or an assemblage of sulfides also indirectly affect the rate of oxidation of the latter. Oxygen is an important chemical weathering agent, and there are many metals present in the rocks. When these metals react with the water and oxygen, they form oxides. To elucidate the oxidation of sulfide minerals in a rock, both the chemical and physical aspects of mineral-solution interaction have to be considered (López *et al*., 2007; Malmström *et al*., 2008):

2.5.2.1 Chemical aspects

Since all sulfide minerals were formed in the presence of an oxygen-depleted fluid under conditions far removed from the oxygen-rich atmosphere of the earth surface (Lefebvre *et al*., 2001), they are unstable when exposed to an oxygenated environment. In the presence of a contacting fluid phase, the relative stability of sulfide minerals can generally be assessed with the aid of pH-Eh diagrams, provided the persistence of metastable mineral phases, either primary or formed during oxidation, is taken into consideration (Sracek *et al*., 2006; Evans and Banwart, 2006). Under acidic conditions,

most metals tend to remain in solution, as dissolved ions, and a variety of processes (including microbial mediation and electrochemical reactions) readily occur to accelerate the oxidation of various sulphides. Thus, the ability of the associated non-sulfide minerals to control the solution pH is perhaps the most important factor influencing the rate of oxidation of sulfides in a rock. In-situ neutralization of the acid generated during sulfide oxidation by reactions with the associated non-sulfide minerals usually leads to the formation of secondary mineral coatings on the reacting sulfides. Depending on the nature and thickness of the coatings thus formed, oxidation of the relevant sulfide(s) occurs at a reduced rate or is totally arrested (Sracek *et al*., 2006; Evans and Banwart, 2006).

Mineral-solution interaction involving rock-forming minerals, especially non-silicates, in a sulfide containing rock, also affect the oxidation rate of the associated sulfides by modifying the composition and ionic strength of the solution concerned of Cl^- and SO_4^{2-} inhibited pyrite oxidation. Thus, dissolution of halite and gypsum in a sedimentary rock containing pyrite would impede the oxidation of pyrite while the dissolution of carbonate would enhance the process (Lefebvre *et al*., 2001; Sracek *et al*., 2006). While other iron sulfides are likely to be have similarly as pyrite, the influence of different salt types and ionic strength on the rate of oxidation is not clear. For example, upon investigating the mechanism of pyrite oxidation in aqueous mixtures, pyrite oxidation rates increased linearly with substrate concentrations of $CaCO_3$ and $NaHCO_3$, whereas effect of the solutions of other metallic sulfides is difficult to investigate (López *et al*., 2007; Lefebvre *et al*., 2001; Malmström *et al*., 2008).

2.5.2.2 Physical aspects

The extent that a mineral assemblage can affect the chemistry of an associated liquid phase (solution) is largely determined by the duration of contact between the reacting minerals and the solution. The longer the contact time, the more closely the solution chemistry will be governed by the relevant mineral-solution equilibria. Since the rate of

heterogeneous reactions involving a gas-solid or solid-solid couple at ambient temperatures without the intervention of a liquid phase is extremely slow, the most intensive sulfide weathering occurs under conditions transitional from unsaturated to saturated moisture. This is reflected in the field by the supergene mineralization process occurring in response to a fluctuating water table in sulfide-rich terrains. Above the saturated zone, rapid sulfide oxidation depends on the trapping of sufficient moisture to facilitate and maintain the oxidation process. Temporary depletion of moisture will lead to the formation of efflorescent minerals and arrest the sulfide oxidation (Gerke *et al*., 1998; Lefebvre *et al*., 2001; Evans and Banwart, 2006).

2.6 Effective parameters in heap leaching related to single ore particles

During the leaching process, physical, chemical and biological reactions take place in the ore bed under irrigation, and natural subsidence, dissolution, deposition and solute transfer occur as a result. Hence, the pore structure of the bed continues to evolve and has temporal and spatial variability (Kirjavainen and Heiskanen, 2007). Bacterial and chemical leaching are influenced by environmental, biological and physico-chemical factors, which affect the yield of metal extraction (Table 2.2) (Ahonen and Tuovinen 1995; Dwivedy, 1995; Malik *et al*., 2004; Prosser and Box, 1983; Pradhan *et al*., 2008; Sandström and Petersson, 1997). Correct chemical and physical conditions must exist for the percolation leaching system to function: a suitable ore particle size, access of oxygen and humidity to the mineral surfaces, reduced acid consumption, the presence of sulfides susceptible to bacterial oxidation, and minimal precipitated basic ferric salts, which might block the percolation channels (Deveci, 2004; Olubambi *et al*., 2007).

Table 2.2: Factors and parameters influencing bacterial mineral oxidation and metal mobilization (Source: Pradhan *et al*., 2008; Kirjavainen and Heiskanen 2007).

Physical and chemical parameters	Biological parameters	Properties of the minerals to be leached	Processing
• Temperature • pH • Redox potential • Water potential • Oxygen content and availability • Carbon dioxide content • Mass transfer • Nutrient availability • Iron(III) concentration • Light • Pressure • Surface tension • Presence of inhibitors and etc.	• Microbial diversity • Population density • Microbial activities • Spatial distribution of microorganisms • Metal tolerance • Attachment to ore particles • Adaptation abilities of microorganisms, and inoculums	• Mineral type • Acid consumption, • Mineral composition • Mineral dissemination • Grain size • Free surface area • Porosity • Hydrophobicity • Galvanic interactions • Formation of secondary	• Leaching mode (in situ, heap, dump, or tank leaching) • Pulp density • Stirring rate (in case of tank leaching operations) • Heap geometry (in case of heap leaching)

Acid consumption by gangue minerals is a very important parameter for heap leaching performance because the major rate-limiting step is the lateral diffusion of acid, and a faster rate of acid gangue dissolution effectively lengthens the distance over which the acid must diffuse, and makes it more difficult for acid to penetrate to the back of the pores. Sulphuric acid is usually a major processing cost, although the sulfide heap leach reactions should be acid neutral or even acid generating. Maintenance of the pH in the preferred range between 1.0 and 2.0 for microbial iron and sulphur oxidation is also important for ferric ion and acid regeneration by the microbial population (Helle *et al*., 2005). In addition, the geometry of the heap (size, especially height) may also affect the bioleaching process and rate of recovery. For these leaching systems to function, the leach environment must be kept in such conditions that the requirements of the bacteria are adequately met (Helle and Kelm, 2005; Kirjavainen and Heiskanen, 2007; Suzuki, 2001).

2.6.1 Properties of heap leach ores

Geotechnical properties (heap stability, ore compression, settlement, ore durability); hydraulic properties (percolation, flow versus ore load, drain-down moisture content), metallurgical testing and impact of mineralogy, are the major ore properties that could have an effect on biochemical heap leach operation. The factors that are influenced by the mineralogy of an ore are (Baláž *et al*., 1994; Dai and Jeffrey, 2006; Senanayake, 2007) are listed as follows:

(1) The degree of comminution required for effective liberation of the desired mineral;

(2) Applicability of physical beneficiation techniques for upgrading the ore;

(3) The nature and quantity of lixiviant to be used;

(4) Leach liquor characteristics;

(5) Residue mineralogy.

The mineralogy of ores is a key factor in predicting their expected behaviour during subsequent processing (Pownceby *et al*., 2007). To obtain optimum results during base metal recovery from a complex sulfide ore, process design must start from a complete and detailed mineralogy study (Olubambi *et al*., 2007).
Some of the parameters, which are related to mineral and structural properties of ore particles, are described in the next sections.

2.6.1.1 Crystal surface defects

It is well recognised that the surfaces of crystals are not atomically smooth, even under ideal equilibrium conditions. They contain numerous microtopographical features. Some of the more important of these are presented schematically in Figure 2.6, which shows crystalline terraces (atomically flat regions), steps and kink sites. Arrows indicate the

relative number of orthogonal directions in which atoms (ions) may move from the different surface sites in order to become solvated. The height of the steps may vary from atomic to polyatomic size, and mineral surfaces cleaved under carefully controlled conditions exhibit numerous steps varying in height from < 5 nm to > 100 nm. Consequently, milled minerals should exhibit a variety of micro-topographical patterns, composed of steps of different heights separated by terraces of varying size and shape that are generated during fracture and abrasion of the mineral particles (Tromans and Meech, 1999; 2002).

Tromans and Meech (2002) have discussed surface-controlled mechanisms of mineral dissolution. They recognised the presence of more reactive and less reactive surface sites and the enhanced reactivity of edge (step) sites. Attention is confined to differences between terrace and step sites only, because these are far more numerous than kink sites and are likely to be more important in determining overall mineral dissolution rates.

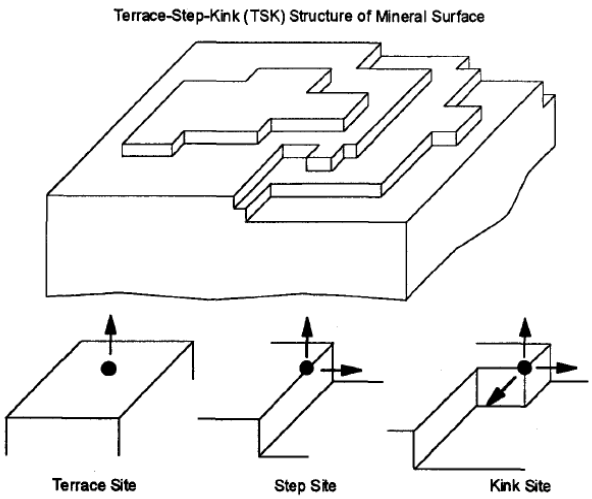

Figure 2.6: Schematic diagram showing a Terrace-Step-Kink structure of mineral surfaces and the general location of terrace, step and kink sites for dissolution (Source: Tromans and Meech 2002).

The initial bacterial activity on the surfaces of the sulfide minerals occurs mostly along former cracks, fractures, lineation, grain boundaries, and zone contacts, contacts between different generations or compositions, etc. Mechanical imperfections are deviations in the sulfide crystal structures. Such defects usually contain high amounts of strain energy, and can thus be of use by the bacterial during the oxidation process. The rate of oxidation will therefore be higher at sites of defects, containing strain energy (Chandraprabha *et al*., 2003; Dai and Jeffrey, 2006; Tromans and Meech, 2002; Ubaldini *et al*., 1997).

2.6.1.2 Particle size

In nonporous materials, particle size and shape are the factors which determine the surface area of the particles. With a few exceptions, the reactions involved in mineral treatment are heterogeneous (i.e. the reaction takes place at the boundary between phases) and hence the rate is expected to be proportional to the interfacial area. The most significant point to be made about these two factors is that there are a number of instances where the rate is not dependent on the particle size (Deveci, 2004; Mazuelos *et al*., 2001; Strömberg and Banwart, 1999). Leaching kinetics is affected by the particle size of the material that is leached, and generally, a smaller particle size gives faster leaching kinetics, since finer particles have a larger specific surface area.

2.6.1.3 Grain distribution and free surface

The mineral grains can be classified, according to their accessibility to leach solutions, into five classes as described in Table 2.3. Types (d) and (e) do not contribute to the rate, at least in the early stages of leaching, but can become involved in the leaching process later if through prolonged contact with the leach solution; new cracks and fissures are generated in the gangue, thus making them accessible.

Table 2.3: The mineral grains classification, according to their accessibility to leach solutions.

Classes	Illustration
a) Grains exposed to the leach solutions at the surface of particles	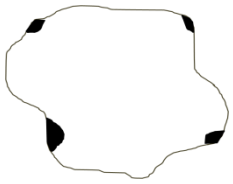
b) Grains exposed to the leach solutions via pores or cracks	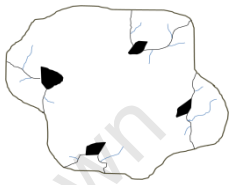
c) Grains which become exposed to the leach solutions only after other grains have reacted	
d) Grains from which pores or fissures that do not extend to the particle surface depart	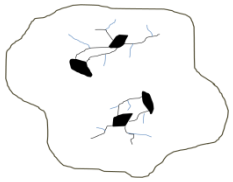
e) Grains located inside the particles and not connected to a pore	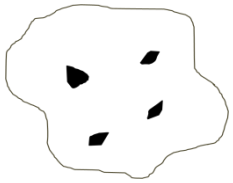

For the particles of the type shown in Table 2.3, four rate regimes can be identified according to their size (Rossi, 1990):

- The particle size is comparable with the size of the mineral grains; this is the case of very high-grade ROM ores or of concentrates. In this case, the reaction rate is close to that of the fully liberated grains and the inert matrix plays a minor role. Leaching is surface-chemical reaction-controlled and/or film diffusion rate controlled.

- The particle size is larger than that of the mineral grains, although the latter are all accessible to the leach solutions from the start of the reaction. Most of the surface of the mineral grains is surrounded by impervious inert gangue and leach solution can only access thereto through the pores and/or cracks. Leaching is therefore still surface-chemical reaction-controlled, but the gangue reduces the rate by blocking access of the leach solutions to most of the surface. Thus, diffusion control comes into play. In this case, particle size does not significantly affect reaction rate.
- The ratio between particle radius and embedded mineral grain radius is even larger than in the two preceding cases. The characteristic feature of this situation is that not all the grains are accessible at the start of leaching, although the overall rate is still controlled by the surface chemical reaction. The outer mineral grains and the inert gangue hinder accessibility to the inner grains. The rate exhibits a further reduction.
- In the largest particles sizes the kinetics is diffusion-controlled or mixed (diffusion and surface-chemical reaction-controlled). The effect of the gangue is to increase the diffusion path length-thereby reducing the overall rate still further.

2.6.1.4 Porosity

The rate of reaction of a particle with a reagent in a fluid phase, in which it is immersed, is usually controlled either by molecular diffusion through a boundary layer extending into the fluid or by the reaction at the surface. If the particle contains cracks or holes, which are open to the fluid, the reagent diffuses into the interior of the particle and reacts there. Under steady state conditions, the rates of diffusion and reaction are the same, and this state is maintained by a concentration gradient of the reagent within the holes. If the chemical reaction is slow, the concentration gradient is shallower than that in the bulk fluid. Under these circumstances, the reaction proceeds on the walls of holes at virtually the same rate as on the external surfaces. In other words, the area over which reaction takes place is not the external area but the total area, including that of all open pores (Cariaga *et al*., 2005). As it is not unusual for the internal area to be far

greater than the external area, the porosity becomes a dominant factor (Bachu and Cuthiell, 1990; Deschamps *et al*., 2008).

If the chemical reaction at the surface is fast, the concentration gradient is steep and reagent is consumed before it penetrates into the particle. Under these circumstances, the internal surfaces play no part, and particle size is the important factor as with non-porous particles (Cariaga *et al*., 2005; Muñoz *et al.*, 1997).

The solid/liquid contact area, which in low-porosity rocks is mainly a function of particle size of the material, is a major factor in determining the kinetics of the leaching reactions. Typical to leaching processes is their selectivity with respect to certain minerals or groups of minerals. The leaching effect is also able to penetrate into microfissures and micropores of the rock mass, thus reducing the need for energy consuming crushing and grinding operations. The optimization of a leaching process thus requires quantitative information on the effect of grain size, as well as on the propagation of the leaching effect inside the mineral grains (Muñoz *et al*., 1997; 2006).

2.6.2 The connection between comminution and leaching behaviour

While the response of particles to breakage is influenced by their mineralogical properties, comminution in turn affects mineral and elemental distribution within particle size ranges. Mineralogical differences within varying particle sizes therefore affect their responses to leaching in different conventional and bioleaching media. Owing to the differences in the mineralogical compositions at different particle sizes, there exist some variations in the microbe-mineral interaction in bioleaching (Liu and Zhou, 2008; Mehta and Murr, 1983; Urbano *et al*., 2007).

Since most minerals have some unknown grain size distribution, texture, exposure, and spatial distribution within the ore particles, they must be initially "unlocked" or "liberated" before separation can be undertaken (Miller *et al*., 2003). The concept of exposure and liberation of a particular mineral in an ore feed may be graphically

expressed as shown in Figure 2.7. In a typical mineral dressing process, the ore feed must be reduced by fracture into particles with sizes smaller than the valuable mineral grains. These liberated mineral grains can then be separated from each other and concentrated, based on their distinct physical and chemical properties. Considering hydrometallurgical extraction of metallic values, the mineral grains need not necessarily be liberated as free grains; since partial exposure of mineral grains may provide sufficient surface front for chemical attack by leaching solution (Hsih *et al*., 1995).

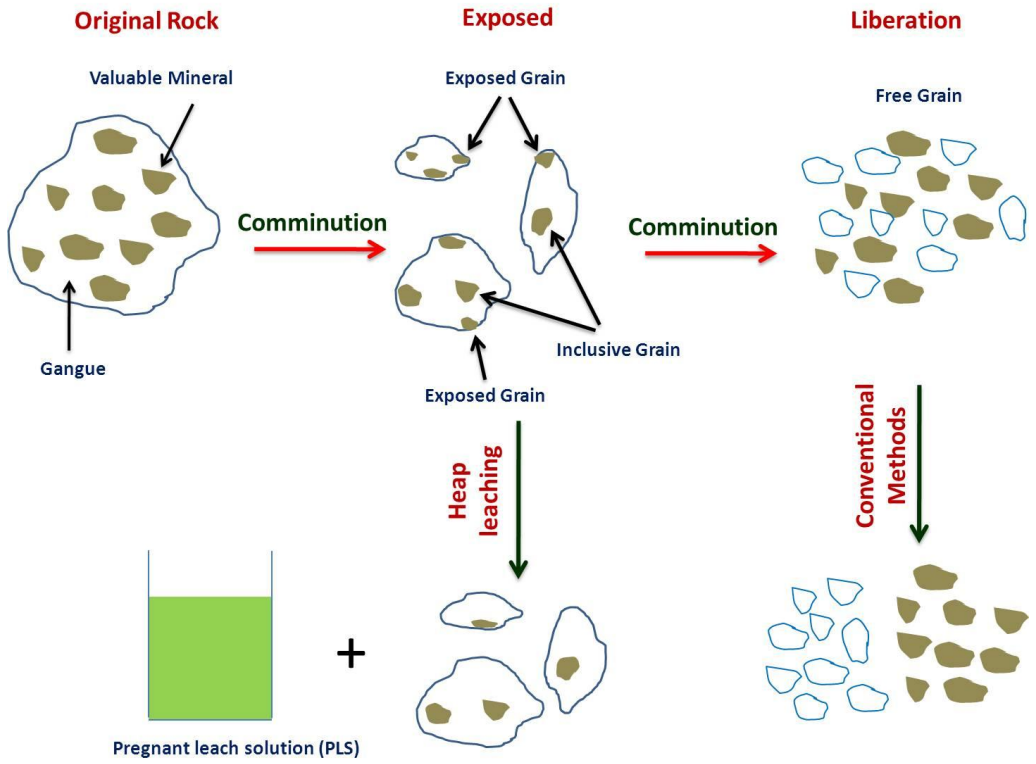

Figure 2.7: The concept of exposure and liberation of mineral by hydrometallurgy and that by physical separation process (adapted from: Hsih *et al*. (1995)).

As mentioned above, crack distribution plays a key role in this partial exposure of mineral grains. This relates leaching behaviour to the method by which the ore has been crushed prior to leaching (Unlanda and Szczelina, 2004).

2.6.2.1 High-pressure grinding rolls (HPGR)

High-pressure grinding rolls (HPGR) have been available as a comminution technology for over 20 years. It is between 20 and 50 percent more energy-efficient than conventional crushers and mills (Daniel, 2007). The comminution principle, which is compression as a breakage mechanism utilized in the HPGR, is different from that in conventional crushers or tumbling mills where impact and abrasion breakage mechanism are dominant. The HPGR breaks particles predominantly in an autogenous way, unlike other comminution devices (Unlanda and Szczelina, 2004; Daniel, 2007).

As a result, the product from a HPGR is different, and may be expected to have a different behaviour in downstream processes (Aydoğan *et al*., 2006; Apling and Bwalya, 1997). Differences in particle porosity and crack network distribution will almost certainly have an influence on the efficiency of the leaching process. Results of studies using the HPGR on semi-refractory gold ores from Nevada and South Africa showed that the leachability of the ores was better after high pressure grinding particularly in the coarser size fractions (Klymowsky *et al*., 2002). Similarly, the results of several studies on dump and heap leach copper ores from Chile and the US showed that HPGR comminution resulted in an increase in copper extraction when compared to the conventionally comminuted ore (Apling and Bwalya, 1997; Daniel, 2007; Klymowsky *et al*., 2002).

In addition to the HPGR, since the late 1980s, microwave heating of ores has been proposed as a means of, firstly, reducing the net comminution energy, and secondly, enhancing the liberation of value mineral phases (Kingman and Rowson, 1998). Selective heating of distributed mineral phases has the potential to induce controlled fracture within the rock (Haque, 1999). If the fracturing takes place along the grain boundaries of value mineral phases, these phases could be effectively liberated, allowing increased accessibility of lixiviant solutions into the ore particle (Jones *et al*., 2005; Kingman *et al*., 2004).

2.6.2.2 HPGR breakage mechanism

The basic machine concept and operation is relatively simple. The material is force-fed into the unit by creating a head of material over the machine, as seen in Figure 2.8. Two counter-rotating rolls allow the compression breakage to be used in a continuous rather than batch operation.

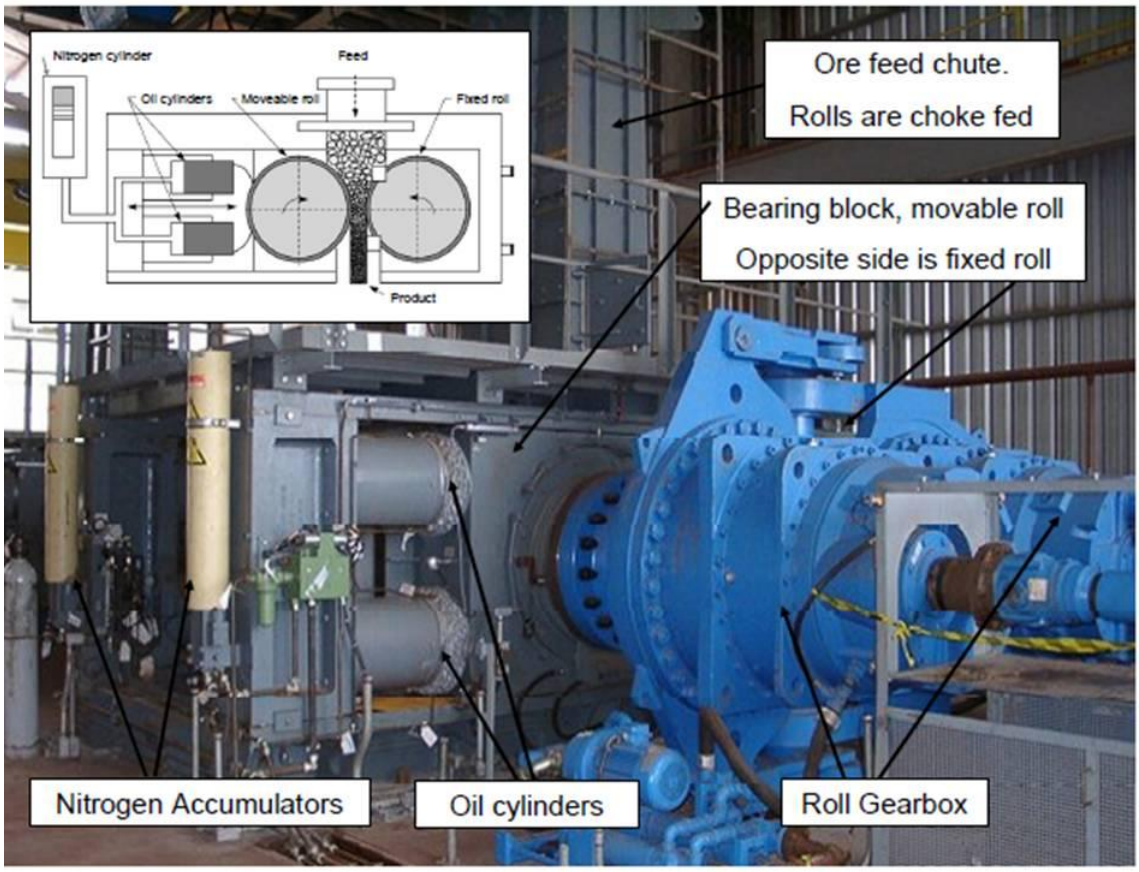

Figure 2.8: The main components of a 650 tph Polysius HPGR unit that is being used in an iron ore peletising plant in Brazil. Web reference at http://www.goldenqueen.com/gall07.htm.

One of the rollers in the HPGR rotates on a fixed axis while the other is allowed to move linearly with a pressing force applied to the moving roll. The moveable roller is forced up against the material in the gap between the rollers by a hydraulic oil pressure system. This oil pressure acts through four or two cylinders (depending on the manufacturer) and transmits the grinding force over the cross-section of the diameter of the rolls

where the bed has formed. The amount of material in the gap, or compression zone, may be manipulated to a limited degree to result in optimum operating conditions, but generally, it is a characteristic of the process ore, roll diameter and surface characteristics. During processing, the particle bed is compressed to a density of greater than 70% solids by volume. The material is usually agglomerated into a cake (flake) that may have to be de-agglomerated before passing on to subsequent processes. This is achieved by either immersing the product in water in a sump under the discharge end of the rolls or by using a hammer, impact or ball mill (Schönert, 1988). The philosophy of the roll design has many factors and is constantly changing due to new advances being developed. The length / diameter ratio of the roll varies between 0.4 and 0.7 depending on the application and the specific throughput requirements. Special applications bring the ratio closer to 1.0 when a high throughput is required. The roll bearings are of a self-aligning roller type that is mounted in large, heavy duty bearing housings. The bearing blocks are installed in a rigid frame that forms the structure of the HPGR. Hydraulic cylinders are mounted in the frame to apply the grinding force to the movable roll (Otte, 1988).

In the HPGR, the grinding force is transferred from one particle to the next, with a small proportion of the particles coming into direct contact with the rolls. Schönert's (1988) remarks in his fundamental study of comminution processes was that in any comminution process the particles are broken by contact forces, which deform the particle and cause a stress field. As the stress, level meets the criteria of either yielding or fracturing then the particle will be deformed in-elastically or broken, respectively. The number of contact forces depends on the mode of stressing being in either single particle mode or multiple particles (Schönert, 1988). Schönert stated that comminution devices such as crushers, mills and HPGR all stress the material by compression and shear. Both single particle and bed particle stressing experiments were conducted as part of his fundamental research and Schönert concluded that inter-particle bed breakage has a lower efficiency than single particle stressing. The efficiency may drop by as much as a factor of two to three depending on the conditions relating to the number

of contact forces (Schönert, 1996). Schönert and Lui (1996) claimed that even though the inter particle process is less efficient than single particle stressing; they found that when a bed of particles is compressed and crushed, the result is that the material is crushed more efficiently than in a ball mill.

2.6.3 Visualization techniques for ore characterisation

In recent years, automated mineralogy has become established as an essential technology for the reliable acquisition of statistically sound comprehensive mineralogical and metallurgical data. This has had a revolutionary effect on the industrial use of such data in the study of geology, mining and mineral processing (Gottlieb, 2008). Usually such studies are conducted in order to evaluate and improve process efficiency. This quantitative data is derived from images of the mineralogically classified ores or plant products in question. The ability of image-based techniques to quantify liberation and association parameters of ore minerals makes them highly preferable to assay-type approaches. A large range of techniques is available for the acquisition of image data, and the ability of each of these systems to discriminate between mineral species varies widely (Fandrich *et al*., 2007; Pownceby *et al*., 2007). The demand for accurate composition and phase distribution analyses in complex ore assemblages is increasing rapidly as mineral processing studies become more sophisticated.

Significant grain boundary fracture will enhance the exposure/liberation of minerals during comminution. However, there is no convincing experimental evidence to describe the extent to which this actually occurs in practice or to indicate what processes can be employed to enhance intergranular fracture (Fandrich *et al*., 2007). However, an improved understanding of the leaching from large particle systems can be achieved with the use of an advanced diagnostic and non-destructive technique, such as high-resolution X-ray CT system (Garcia *et al*., 2009; Lin and Miller, 2005; Miller *et al*., 2003; Solymar and Fabricius, 1999; Yang *et al*., 2008).

In order to understand more clearly the reagent diffusion through the large particles and to provide true and reliable physical parameters to formulate the relevant modelling approaches to large particle leaching, it is necessary to study the 3-D progression of diffusion and reaction first. However, the use of traditional experimental methods cannot realize this, as they are all destructive. An improved understanding of the leaching from large particle systems could be achieved with a high-resolution X-ray CT system adapted to the mineral context.

2.6.3.1 X-ray computed tomography

X-ray CT is a state-of-the-art, non-invasive technology which has been used effectively for several years to describe and visualise characteristics of the interior of solid objects (Lin and Miller, 2005; Geet *et al*., 2000). The principle behind the use of X-ray CT is the use of an X-ray beam signal that is a function of the incident X-ray energy and the linear attenuation coefficient, which is proportional to the local mean density of the particle. With the advances in X-ray CT resolution down to the micro and even nanometer scale, in computing power, and in software development for quantitative data analysis, applications of this technology in mineralogical analysis are becoming more common. Some of the most recent applications have been in different disciplines, such as quantification of porous media (Rattanasak and Kendall 2005), geological application, steel degradation within concrete-civil engineering application, quality control-embedded contamination in wool, mechanical engineering, palaeontology (Remeysen and Swennen, 2008; De Beer *et al*., 2004; Tsakiroglou and Payatakes, 2000). Process mineralogy is also widely used within the petroleum industry to identify and characterize internal structural characteristics within drill core material and fluid saturations and distributions within core material systems (Remeysen and Swennen, 2008; Coles *et al*., 1998).

Observations using this technique can be coupled with the results from other modern automated mineralogy measurements in 2D such as QEMSCAN or MLA, more traditional

column leach experiments and solution chemistry considerations, in order to identify the progression of heap leaching at the particle scale. The distribution of cracks and mineral dissemination in ore particles is an important characteristic that determines the diffusion of reagents in and out of particles and reactions within. Recent developments in X-ray CT systems, as an advanced diagnostic and non-destructive technique, have established the technology as a tool for the acquisition of 3-D mineralogical and structural data.

For monochromatic X-ray sources the relationship between the intensity of the incident and attenuated X-rays (respectively, I_0 and I) and h, the thickness of the object, may be expressed by Beer's law, Eq. (2.4) (Van Geet *et al*., 2000):

$$\frac{I}{I_0} = \exp(-\mu h) \qquad \text{Eq. (2.4)}$$

The linear attenuation coefficient, μ, is known to depend predominantly on two processes, namely photoelectric absorption and Compton scatter at energy levels below 200 kV. This may be expressed as Eq. (2.5) (Demir and Sahin, 2009):

$$\mu = \rho\left(a + b\frac{Z^{3.8}}{E^{3.2}}\right) \qquad \text{Eq. (2.5)}$$

where ρ is the bulk density of the material, Z is the bulk atomic number of the material, E is the X-ray energy and a and b the energy-dependent coefficients. The first and second terms of Eq. (2.5) correspond to Compton scatter and photoelectric absorption, respectively (Van Geet *et al*., 2001). A third process that occurs is Coherent scattering (Thomson/Rayleigh type); however, this is negligible and therefore not incorporated in the equation (Van Geet *et al*., 2005).

For mixtures of atoms, the effective atomic number Z_e is used:

$$Ze = (\sum f_i Z_i^{3.8})^{\frac{1}{3.8}} \qquad \text{Eq. (2.6)}$$

where f_i is the fraction of the total number of electrons contributed by element i, and Z_i is the atomic number of element i. As described by Eq. (2.5), the linear attenuation

coefficient (μ) will become increasingly dominated by photoelectric absorption due to the presence of the factor $Z^{3.8}$ in Eq. (2.6) (Boespflug *et al*., 1995).

In classical X-ray radiography, the internal features of an object are superimposed on the plane of the final image. This means that the detected value of one ray is the sum of the attenuation coefficients of every point lying along the X-ray path (Van Geet *et al*., 2000). By taking X-ray radiographs of the object from many different angles, a 3-D reconstruction of the object can be obtained. Several algorithms are used to reconstruct virtual 2-D slices through the object, which enables visualisation of the distribution of features of varying linear attenuation coefficient. The final visualisation of the CT data remains a 2-D image, where every pixel actually represents information of a 3-D voxel. In what follows, the term pixel and voxel will be used interchangeably for CT data, but it should be kept in mind that it physically always represents voxels.

2.7 Particle models within heap leach modelling

Most of the early heap bioleaching models dealt with leaching at the particle scale (Braun *et al*., 1974; Barstlett, 1992; Davis and Ritchie, 1987; Roman, 1974; Shafer *et al*., 1979). More recent bioleaching models emphasize the effects of bulk scale phenomena, such as liquid flow, gas flow, and temperature distribution, on heap performance (Dixon, 2000; Dixon and Petersen, 2003; Leahy *et al*., 2007; Moreno *et al*., 1999; Ogbonna *et al*., 2006; Petersen and Dixon, 2002; Pantelis *et al*., 2002; Sidborn *et al*., 2003). Although both, particle scale and bulk scale, effects are important in heap bioleaching, little has been done to systematically integrate particle scale models into bulk scale models. Most existing bulk scale models account for the effect of particle topology using simplified models such as the shrinking core model, applied to an average particle size. Implicit in this is an assumption regarding the relative significance of particle scale phenomena, and which process (diffusion or reaction kinetics) is limiting at the particle scale. A conventional shrinking core approach would work only for gangue particles that are

homogeneously porous and have mineral grains well distributed throughout (Liddell, 2005; Velardo *et al*., 2002; Vegliò *et al*., 2001). The shrinking core model has been shown to be a poor predictor of leach kinetics based on the crushed ore size distribution. However, the model itself is a very useful tool to analyse commercial heap data (Miller, 2003). Shrinking core models have proved to be extremely useful in describing the leaching behaviour of many ores and flotation concentrates, although they tend to be used as empirical tools rather than in any predictive way: data is obtained from batch leaching, which is then fitted according to the topological model equations, and then the set of parameters that gives the best fit is chosen as best representative of the system. There are no reliable criteria to predict *a priori* the rate-controlling regime in which a given system will operate. Clearly, obtaining these criteria will require a greater understanding of the controlling processes on a microscopic level (Liddell, 2005; Velardo *et al*., 2002).

Part of this difficulty in understanding leaching reactions lies in their heterogeneous nature and the variability from one ore or concentrates to another. However, another part stems from the fact that the conventional shrinking-core equations have been narrowly focused on the dissolved reactant and the particles being leached (Liddell, 2005). Models usually assume spherical geometry of the particles, although ore or concentrate particles are never spherically symmetric. Deviation from the spherical shape leads to an increase in the surface-to-volume ratio (Rossi, 1990). Furthermore, particle scale effects in heap bioleaching are influenced by other factors, including the particle size distribution, the ore mineralogy, surface properties, pore size distribution and microbial interactions.

2.8 Summary and aspects towards formulating a hypothesis

Heap leaching is a well-established mining technology that involves stacking crushed ore into piles constructed on an impermeable layer fitted with a solution drainage system,

or arranged on a slope to facilitate drainage. In many cases, the ore is agglomerated through tumbling with acid and/or irrigation solution prior to stacking.

There are, however, a significant number of aspects of the technology that are not well-correlated. Most significant amongst these are the inter-relationship between the geo-technical and geo-mechanical properties of the ore and their effect on the leach kinetics and economic recovery of the valuable constituent. As the technology becomes more and more adopted, it is increasingly clear that the successful application of heap leaching technology will ultimately depend on having a comprehensive understanding of the underlying fundamental processes for optimisation to take place.

Ores are placed in heaps in a relatively coarse particle size distribution, reaching up to 25 mm top size for crushed and agglomerated ores and as much as 500 mm for ROM ores in dump leaching. Leaching from such large particles is poorly understood. Most models of the overall process account for leaching at the particle scale with the shrinking core model applied to a single 'average' particle size. However, a comprehensive literature review has returned virtually no evidence to support the assumption that large particle leaching follows shrinking core type behaviour. On the contrary, recent experimental evidence suggests that leaching from large particles occurs only at the surface and in subsurface regions, which are accessible from the surface by cracks and pores. This would suggest that leaching behaviour might be closely related to the method by which the ore has been crushed prior to leaching.

Given that unique to heap leaching is the relatively coarse particle size distribution, the major technical challenge is to expose the mineral grains within the ore to the lixiviant, be it acid, ferric ions or bacteria and oxygen. One possible approach to improving recovery in the heap is to introduce fractures into large ore particles, so increasing the surface area available for lixiviant attack. Extensive cracking can be induced in a number of ways; for example using HPGR, which applies sufficient pressure to crack the rock matrix.

The actual progression of leaching from large particles has never been systematically explored and no model used to describe leaching from large particles is based on actual physical observation. Base on this problem statement through literature review the following hypotheses have been formulated:

- Leaching from large particles occurs only at the surface and in subsurface regions, which are accessible from the surface by cracks and pores.
- The cracks produced by comminution with HPGRs rather than conventional impact crushers significantly promote subsurface leaching.

Using X-ray CT offers a non-destructive technique for visualizing features in the interior of large ore particles to obtain digital information on their 3-D geometry and topology. This can be used to measure the distribution of cracks and the dissemination of minerals in ore particles, which are important characteristics that determine the diffusion of reagents into and out of particles and the reactions within.

3 MATERIALS AND METHODS

In this chapter, details of the ore sample and the different instruments and operating conditions that were used for ore characterization or leaching studies are described.

A detailed description of the methods such as calibration of X-ray CT, analysis of X-ray CT images, the leach experiments microbial cultures preparation and investigation of the microbial populations during leaching are given.

3.1 Materials

3.1.1 Sample preparation

A bulk sample (12 tonnes) of sphalerite ore was obtained from the Gamsberg Zinc mine in the Northern Cape Province, South Africa. The bulk sample was initially crushed by a jaw crusher from 300 mm top size down to -40 mm. The jaw crusher product was representatively split into 250 kg bags for further crushing by either HPGR or cone crusher at Mintek in Randburg, South Africa. HPGR test work was conducted using a Köppern unit equipped with 1 m diameter rolls and 0.25 m width that was fully instrumented to control and record hydraulic and nitrogen pressures and throughput. The unit was fitted with profiled Hexadur rolls (Figure 3.1). The top feed size to the unit was 40 mm. It was operated at three different pressures (45, 95 and 120 bars). The same top size was also fed to the cone crusher and crushed down to -25 mm. Products from the cone crusher and HPGR were then screened into five size fractions (+23/-25, +16/-23, +14/-16, +6.75/-14, +5.25/-6.75 mm). In this study, subsamples from the large size fraction (+23/-25 mm), medium size fraction (+14/-16 mm) and small size fraction (+5.25/-6.75 mm) were analysed. The overview of the sample preparation used for this study is summarised in Figure 3.2.

a

b

Figure 3.1: a. Köppern HPGR b. Hexadur rolls.

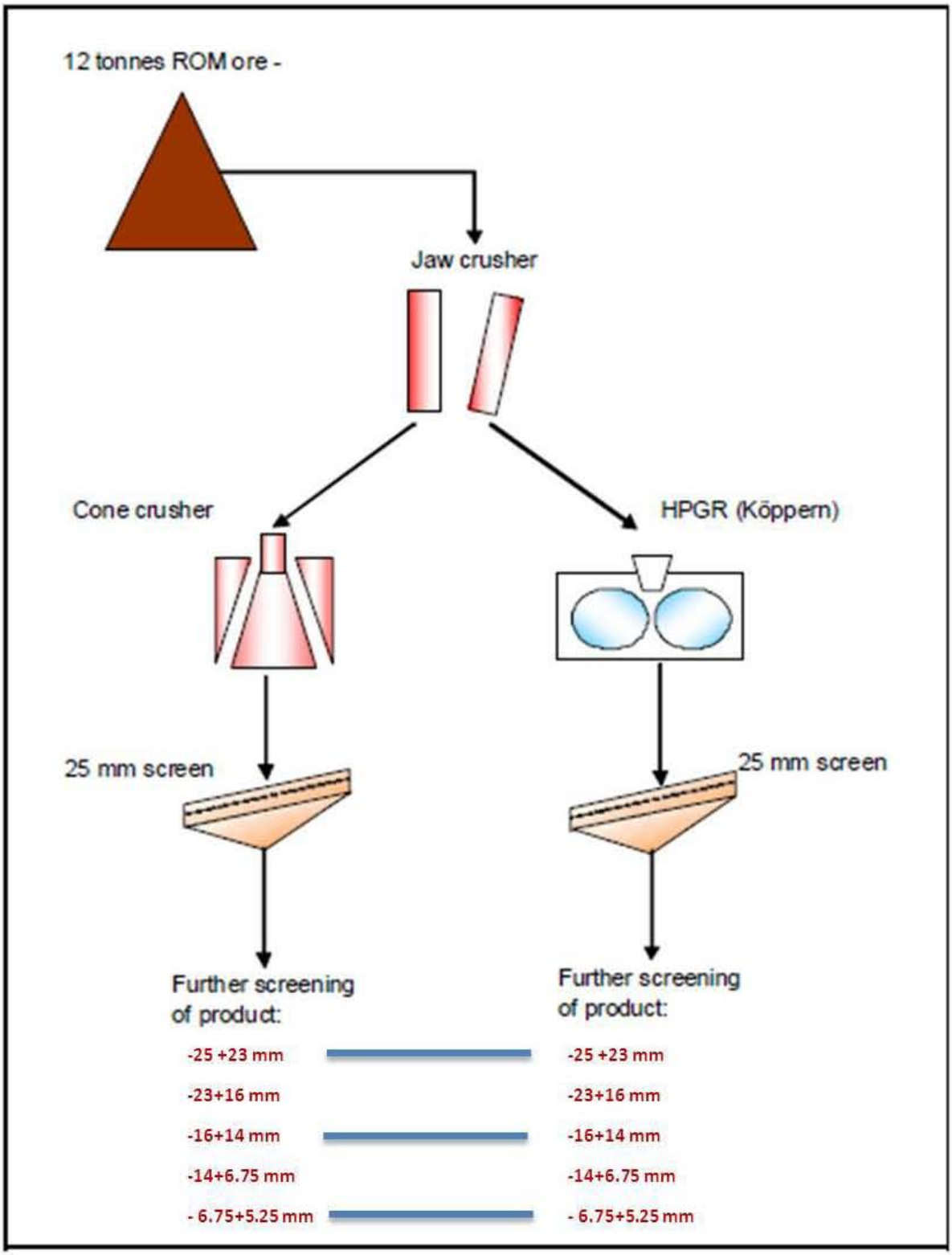

Figure 3.2: Procedure used for sample preparation.

3.1.2 Sample analysis

3.1.2.1 Quantitative Evaluation of Minerals by Scanning Electron Microscopy (QEMSCAN)

QEMSCAN was used to determine bulk mineralogy and crack characterization in the ore sample (prior to and post leaching) as well as monitor the changes in mineralogy over the 11 month experiment. The QEMSCAN unit used in this study was located at the University of Cape Town, and is based on a LEO SEM platform equipped with two Bruker 4010 SDD detectors. Operating conditions were set at 25 kV and 5 nÅ beam current.

Measurements of the bulk mineralogy were obtained using the bulk mineralogical analysis (BMA) routine on a series of sized samples (+120; +90; +63; +38; -38) µm (Figure 3.3a). Samples were dry sized to avoid the dissolution of any soluble precipitates that may have formed during the course of the leach experiments. Individual ore particles (5 to 25 mm) that were sampled at each of the reactor stoppages were analysed using the Field Image analysis routine (Figure 3.3b). Ore samples were mounted in epoxy resin and prepared into polished 30 mm diameter mounts. A pixel spacing between 3 and 5 µm was used for BMA analysis (depending on the size fraction) and a pixel spacing of 20 µm was used for the field image analysis. QEMSCAN results were processed to determine modal mineralogy, texture, mineral associations and 2D porosity.

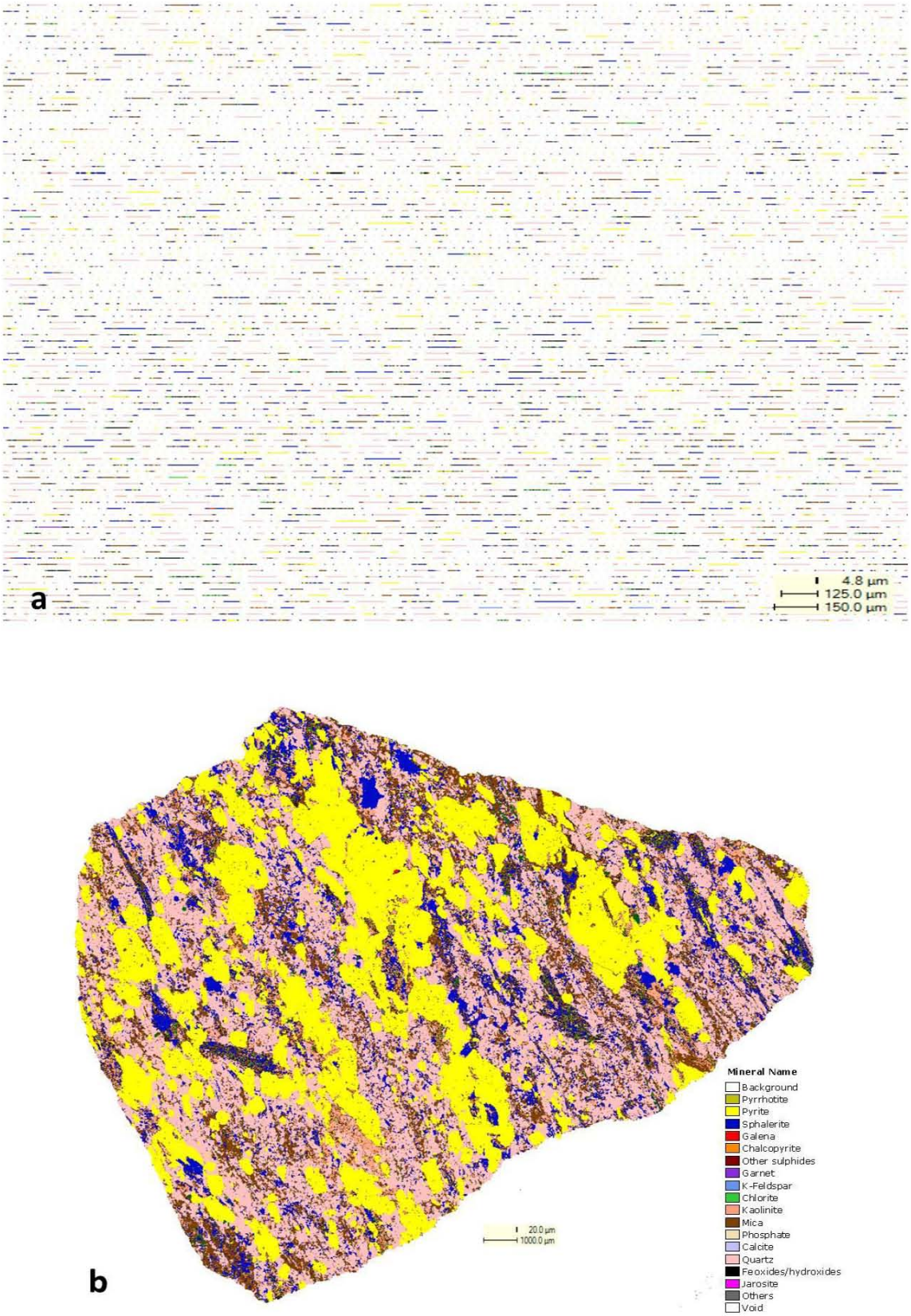

Figure 3.3: QEMSCAN Image the bulk modal analysis (a) and field image analysis (b).

3.1.2.2 Quantitative X-ray Diffraction (QXRD)

Quantitative X-ray diffraction was used to determine the amount of the different major mineral phases. Samples were analysed using a Bruker D8 advance laboratory X-Ray Diffractometer equipped with a $C\check{o}K_{\alpha}$ as a radiation source (λ= 1.78897 Å) and a position sensitive detector (Bruker Vantec), operating at 35 kV and 40 mA with Bragg Brentano geometry. Samples were prepared for analysis using a McCrone micronizing mill. Phase quantification was performed using the Bruker Topas Rietveld refinement software.

3.1.2.3 X-ray Fluorescence (XRF)

The chemical assays were determined using wavelength dispersive X-ray Fluorescence spectrometry. Selected samples were prepared into fusion discs for major element analysis on a Philips PW1480 wavelength dispersive XRF spectrometer with a dual target Mo/Sc x-ray tube. All measurements are made with the tube at 50 kV, 50 mA. Intensity data are collected using the Philips X40 software. All peaks are corrected for background. Matrix corrections are made on all elements using the de Jongh model in the X40 software. Theoretical alpha coefficients calculated using the Philips on-line ALPHAS programme, are used in the de Jongh model.

The results from QEMSCAN were validated by comparison with XRF data and QXRD data. Figure 3.4 shows evaluation of chemical assay determined by QEMSCAN compared to chemical assay identified by XRF.

Zn correlation is considered to be relatively good. Weaker Fe and Si correlations are most likely due to minor compositional variations that were not accounted for. Only S is not well correlated by the two methods due to the different method of analyses (LECO). Raw analyses data of QEMSCAN and XRF are given Appendix I.

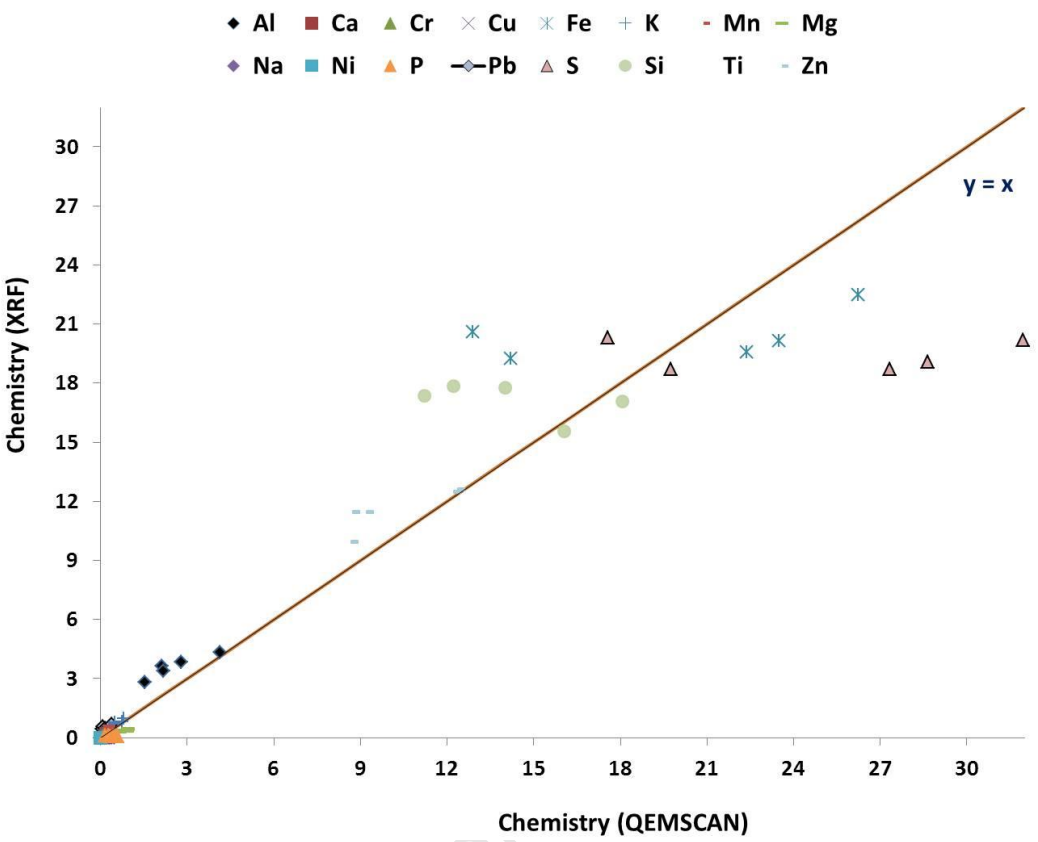

Figure 3.4: Evaluation of chemical assay (QEMSCAN) vs. chemical assay (XRF).

3.1.2.4 Electron Microprobe Analysis (EMPA)

Selected samples of the feed and residue of the reactors were analysed by EMPA to determine sphalerite composition (mineral chemistry) and the amount of impurities. Elemental mapping was also used for 2D characterization of unreacted sphalerite within the residue of the reactors. Microprobe analysis of the samples was performed at the University of Cape Town using a Jeol JXA 8100 electron microprobe, equipped with four wavelength-dispersive spectrometers. Operating conditions for quantitative analysis were set at 25 kV and 20 nÅ with counting times set on 10s for peak and 5s for background (both upper and lower). Pyrite was used as a standard for Fe and S and the related metal standards were used for Zn, Mn and Cu for calibration. A pixel spacing of

1 µm was used for analysis elemental mapping. Preliminary investigations showed negligible Cd, and so this element was not included in the quantitative analysis. EPMA analyses were performed on the same blocks that were used for QEMSCAN analysis.

3.1.2.5 X-ray CT

X-ray CT was used for 3-D characterization of the cracks distribution and the minerals dissemination in ore particles prior to leaching, during the course of the leach experiments and after leaching. The non-destructive nature of this technique allowed a virtual "in-situ" characterisation of the ore particles during leaching. An HMXST CT scanner at X-Sight X-ray Services in Stellenbosch, South Africa, with 225 kV X-ray source, 3 µm resolution reflection target, and interchangeable Nano-tech 1 µm transmission target was used. Further details of the X-ray CT conditions are given in Table 3.1.

Table 3.1: Experimental conditions used for X-ray CT measurements.

X-ray energy	130 kV and 200 kV micro-focus source with 3 µm focal spot size
X-ray intensity	120 µA beam current
Integration frames	Each projection image was exposed for 1 second per frame - no integration of frames
Random movements	No random movements and continuous rotation of sample
Beam hardening filters	A software correction was used which modifies the Beer-Lambert Law (attenuation curve) to match the sample. A pre-set correction was chosen including both linear and quadratic curve fitting
Second radiation filters	1mm Cu

3.1.2.6 Scanning Electron Microscope and Energy Dispersive Spectrometry (SEM/EDS)

SEM/EDS images of selected samples were taken to investigate the surface morphology of the particles, specifically to characterise microbial attachment and any soluble minerals that may have precipitated during the course of the leach experiments. Images were obtained on a Nova Nano field emission gun (FEG) SEM at the University of Cape Town. The EDS spectra were collected with an Oxford Instruments X-MAX 20 mm2 silicon drift detector (SDD) at beam energy of 20 keV.

Describing of the crack within the ore sample and precipitation using SEM/EDS required no delicate sample preparation step (such as coating with gold or carbon). Samples used to investigate microbial attachment were prepared by sinking each particle in 1% glutaraldehyde solution for a day, followed by dehydrolysis of the sample with different ethanol volumes starting; 30%, 50%, 70%, 80%, 90% and 100%. For each ethanol volume, incubation time was 15 minutes. It should be note that glutaraldehyde is frequently used as a disinfectant and sterilizing agent against bacteria and viruses (1-2% solution), an embalming fluid and tissue fixative.

3.1.2.7 Mercury Porosimetry and BET Physical Gas Adsorption

Mercury Porosimetry and BET Physical Gas Adsorption are two of only a few analytical techniques applicable over a wide range of pore sizes, and the data they produce can be used to analyse various characteristics of the pore space and of physical properties of the solid material itself. An Autopore II 9220, 60000 psia (414 MPa) mercury porosimeter was used, covering the pore diameter range-lower limit of detection (LLD) from ~360 to 0.003 µm. The surface area and pore size of individual ore particles was also analysed with a TriStar 3000 physical gas (with N_2) adsorption. The detection limit of surface area was > 0.01 m^2/g, and for pore diameter: 0.5 -100 nm. Representative

samples from medium size fraction (-16+14 mm) and small size fraction (-6.75+5.25 mm) were analysed by mercury Porosimetry and BET Physical Gas Adsorption.

3.2 Methods

3.2.1 Calibration of X-ray CT

Prior to the use of the X-ray CT for investigating the 3-D features of the sphalerite particles, a calibration was needed in order to be able to identify the optimal measurement settings to differentiate between the various minerals present in the ore particles, given that there is some overlap in the grey level brightness. In practice, density measurement from X-ray tomography data can be obtained either by calibrating the CT machine with objects of known density and obtaining a correlation that relates density with the attenuation coefficient, or by using a dual energy scanning to determine directly the density of the material. In this study, a dual energy scanning method was used for calibration, as it allows one to determine both the density and the effective atomic number of the object of interest separately. Thus, the sensitivity of the analysis is significantly increased. High purity samples of five different sulfide minerals (Table 3.2), common in typical Pb-Zn-sulfide ore deposits were selected for calibration.

Table 3.2: Physical characteristics of minerals used for X-ray CT calibration.

Calibration minerals	Chemical formula	Density (g/cm^3)	Effective atomic number (Ze)
Galena	PbS	7.4	78.3
Pyrite	FeS_2	5.01	22.1
Chalcopyrite	$CuFeS_2$	4.19	25.0
Sphalerite	ZnS	4.05	27.2
Pyrrhotite	Fe_7S_8	4.61	23.2
Quartz*	SiO_2	2.62	14.4

*Quartz was not used for the calibration

The QEMSCAN and QXRD results confirmed the presence of all five of these minerals in the ore sample (see Table 4.1).

X-ray CT calibration was performed at high (200 kV) and low (130 kV) energy settings. Figure 3.5(a) presents a comparison of the linear attenuation coefficient as a function of density (ρ) and Figure 3.5(b) as a function of the effective atomic number ($Ze^{3.8}$). By plotting the mass absorption coefficient of these reference materials versus $Ze^{3.8}$, it is possible to obtain the coefficients *a* and *b* in Eq. (2.5) in chapter 2, using a linear regression for a standard sample size (Van Geet *et al*., 2000).

From these equations, density and (effective) atomic number can be calculated as follows (Van Geet *et al*., 2000; Van Geet *et al*., 2001):

$$\mu_h = \rho\left(a_h + b_h\frac{Z^{3.8}}{E^{3.2}}\right) \text{ and } \mu_l = \rho\left(a_l + b_l\frac{Z^{3.8}}{E^{3.2}}\right) \qquad \text{Eq. (3.1)}$$

$$\rho = \frac{a_l\mu_h - a_h\mu_l}{a_l b_h - a_h b_l}, \qquad Z = \sqrt[3.8]{\frac{b_h\mu_l - b_l\mu_h}{a_l\mu_h - a_h\mu_l}} \qquad \text{Eq. (3.2)}$$

Subscripts h and l refer to the high and low energy scans, respectively. Once these coefficients *a* and *b* were obtained, a comparison of the mean measured density and effective atomic number against the real density and real effective atomic number was performed for the different minerals used for calibration (Figure 3.6 a, b). This comparison was considered to represent a suitable calibration of the system.

Given the calibration, Eq. (3.1) and (3.2) can be used to extract density and atomic number from any component (Van Geet *et al*., 2000; Coles *et al*., 1998). This procedure is, however, sensitive to noise (Van Geet *et al*., 2005; Han and Demir, 2009), which were minimized with the use of both physical (1 mm Cu filter) and software corrections (Table 3.1).

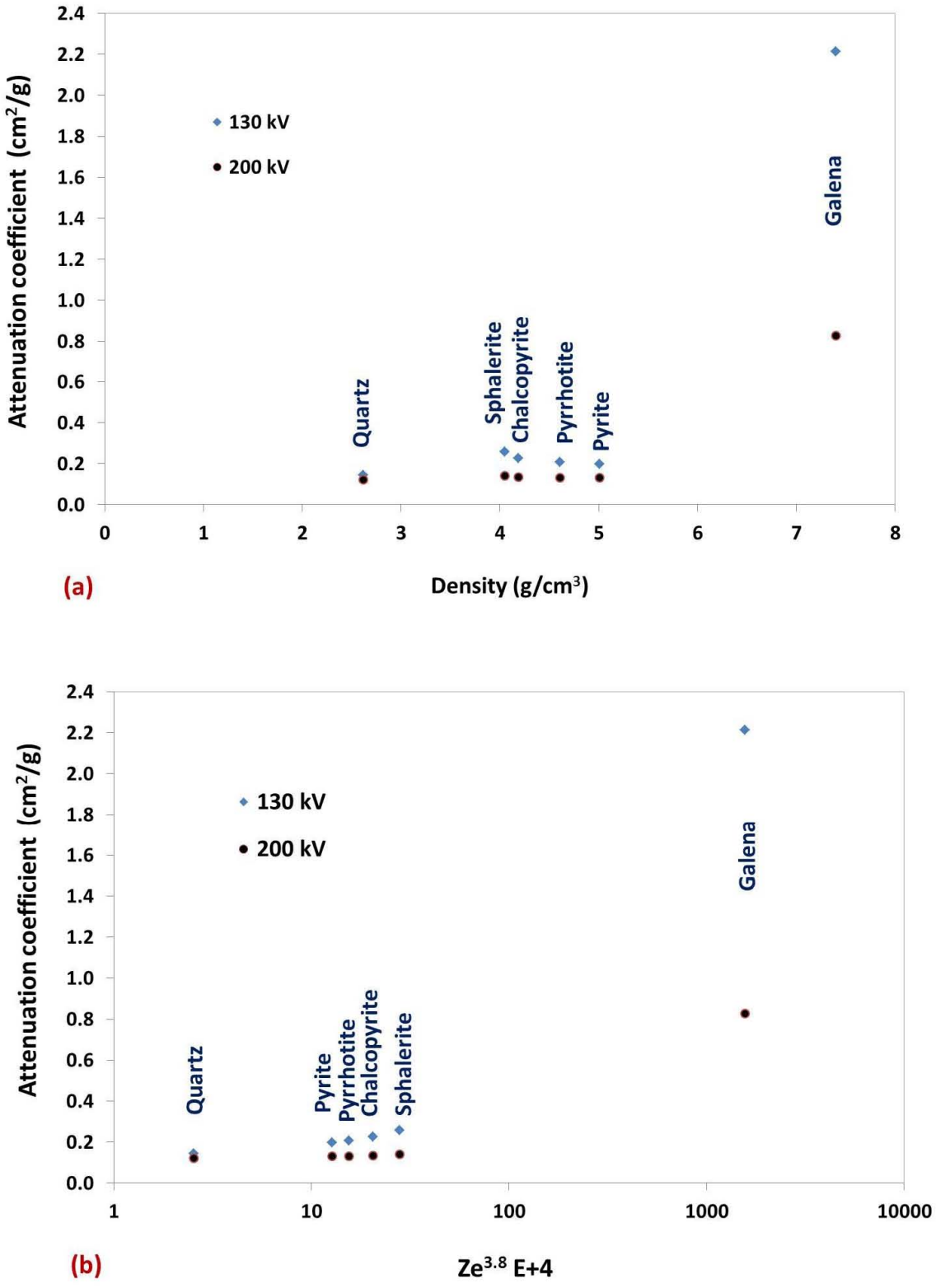

Figure 3.5: Plots of (a) X-ray attenuation coefficient versus density; and (b) effective atomic number ($Ze^{3.8}$) for calibration of different minerals.

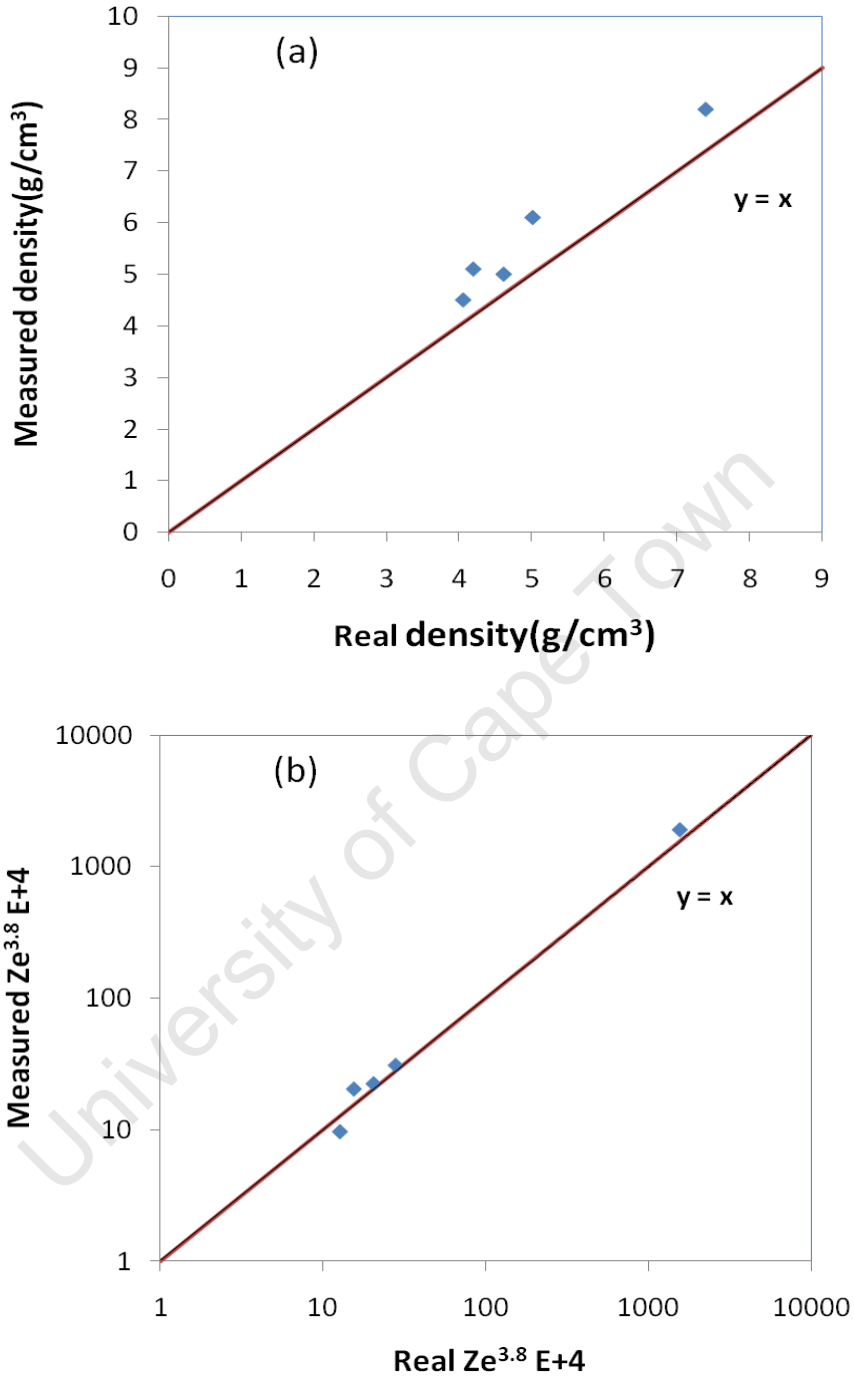

Figure 3.6: Comparison of (a) The measured density versus real density; and (b) the real effective atomic number versus the measured effective atomic number obtained for the different minerals used for calibration by means of the dual energy method.

3.2.2 Analysis of X-ray CT images of individual tagged particles

Following the reconstruction of the acquired X-ray CT data, the images of the ore particles were analysed using the VGStudio Max 2.1 image analysis software (Volume Graphics GmbH located at Heidelberg, Germany). Figure 3.7 gives an example of a reconstructed sphalerite ore particle along with an illustration of three 2-D slices of the particle in different x, y, and z directions.

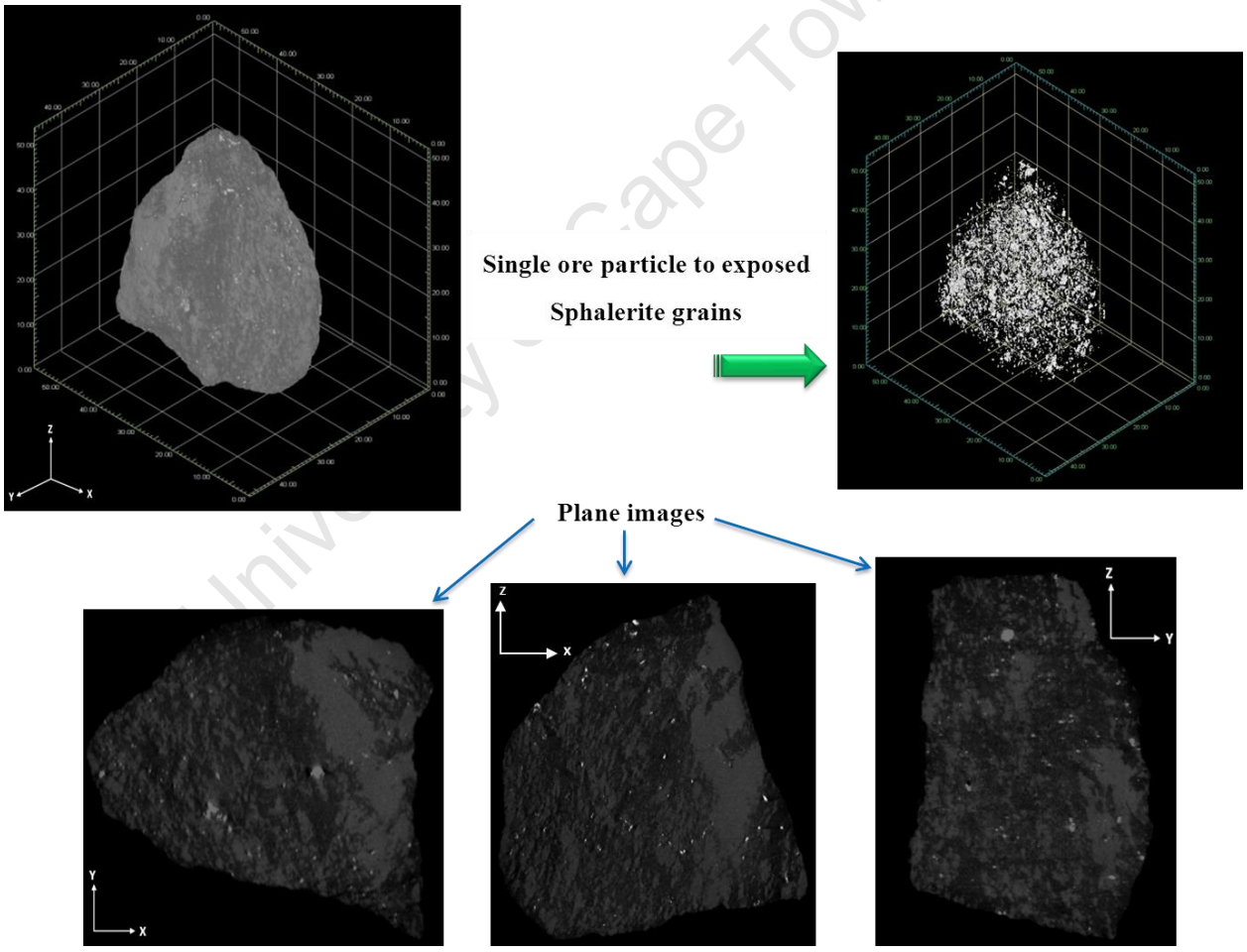

Figure 3.7: 3-D image of a single ore particle (40 mm) where the different grey levels represent the different minerals (top left) which is then processed to virtually processed to extract all minerals other than sphalerite (top right). Plane images of the ore particle are also shown in the x, y, and z-directions to reveal textual details of the ore particles.

Three phases can be distinguished: the bright white grains with a high attenuation value correspond to sphalerite and galena (Ze > 27), light grey represents the iron and copper sulfides (pyrite, pyrrhotite and chalcopyrite, Ze: 22-25) and dark grey with low attenuation values represents the various silicate gangue minerals, primarily quartz (Ze < 15). In order to derive quantitative mineralogical results from the tomographic images, a robust methodology was needed to assign a mineral phase composition to each voxel. A thresholding technique that assigns cut-off attenuation coefficient values between the peaks of the various phases was used in conjunction with some knowledge of the various minerals that are present in the ore. The thresholding technique was able to differentiate between the silicate gangue minerals (quartz), sphalerite and galena. Due to the similarity in effective atomic number of the iron and copper sulfides (Ze: 22-25), differentiation between these phases was not possible, but due to the very low abundance of chalcopyrite and pyrrhotite in the ore, it was assumed that the major phase in this grey level region was pyrite (see Table 3.2).

Figure 3.8 shows a reconstruction of the same particle from Figure 3.7, showing the phase segmentation. Each of the different minerals has been assigned a false colour to facilitate their distinction. The comparison in terms of the types of minerals present and the textures between QEMSCAN and X-ray CT was relatively good. Appendix II shows analysis of X-ray CT images of individual tagged particles using VGStudio Max 2.1 image analysis software.

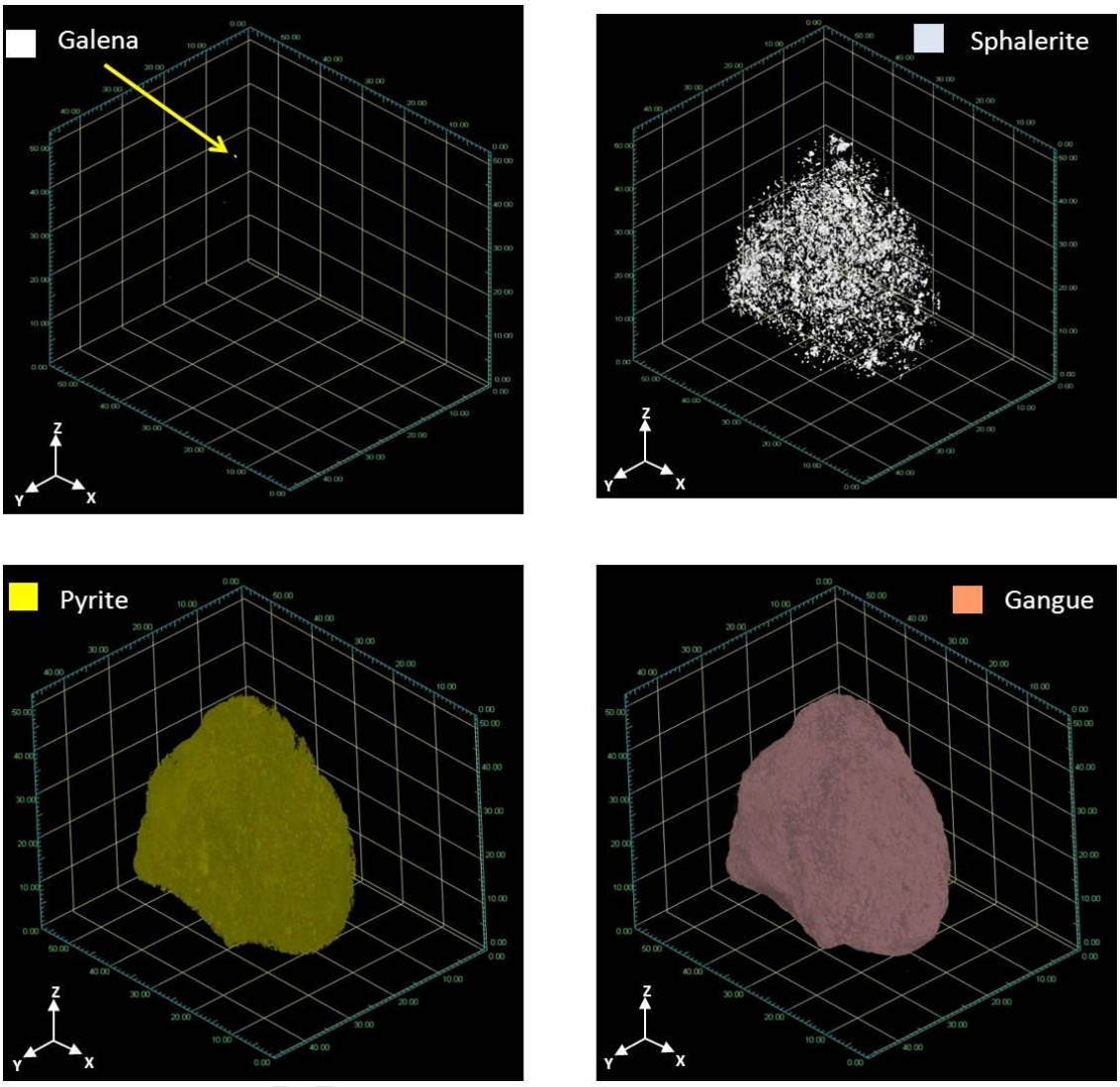

Figure 3.8: 3-D image of the ore particle (40 mm) from Figure 3, with false colour representation of galena (a), sphalerite (b), pyrite (c) and gangue (predominantly quartz) (d).

3.2.3 Leach experiments

The ore samples investigated were prepared by different crushing conditions and screened into different size fractions as detailed in Table 3.3. After initial characterization of the ore samples, they were packed into leach reactors (Figure 3.9a), in which the leach solution was continuously circulated around stacked baskets (Figure 3.9b) containing ore particles. Figure 3.9c shows a schematic drawing of the leach

reactor. The particles were fully immersed in leach solution and the reactor was operated in continuous mode. Internal circulation of the leach solution was achieved through a central draft tube into which air was bubbled at 1500 mL/min (0.2 vvm).

Table 3.3: Summary of the leach reactors.

Reactor	Crusher conditions	Size fraction (mm)	Total mass (g)
A	HPGR-95 bars	Small size fraction (-6.75+5.25)	3300
B	HPGR-95 bars	Medium size fraction (-16+14)	3400
C	HPGR-95 bars	Large size fraction (-25+23)	3600
D	HPGR-120 bars	Large size fraction (-25+23)	3600
E	Cone Crusher	Small size fraction (-6.75+5.25)	3300
F	Cone Crusher	Medium size fraction (-16+14)	3400
J	Cone Crusher	Large size fraction (-25+23)	3600
K	HPGR-45bars	Large size fraction (-25+23)	3600

After initial chemical leaching with H_2SO_4 at pH 1.0 for 30 days, fresh leach solution, containing 1 g/L ferrous iron and pH adjusted to 1.50 with concentrated H_2SO_4 was pumped into the reactor at 50 mL/hr, and the equivalent amount of leach solution overflow was withdrawn, by means of a peristaltic pump. The pH, redox potential, Fe^{3+} and Fe^{2+} concentration as well as total Fe, Zn, Mg, Al and planktonic cell concentration in the effluent solution were measured regularly. All pH measurements were performed using a Metrohm 704 pH meter and probe, which was calibrated at pH 1.0 and 4.0, each time before use. Redox potentials were determined using a Metrohm 704 voltmeter with a Ag/AgCl reference electrode. The precision of the measurements was tested using a Crison standard redox solution having a potential of 468 mV at 25°C. Concentrations of ferrous iron were determined spectrophotometrically (Helios spectrophotometer) using the 1, 10-phenanthroline method. Metal concentration (total Fe, Zn, Mg, Al) in solution were assessed using Inductively Coupled Plasma (ICP) Varian 730-ES, Optical Emission Spectrometer (OES).

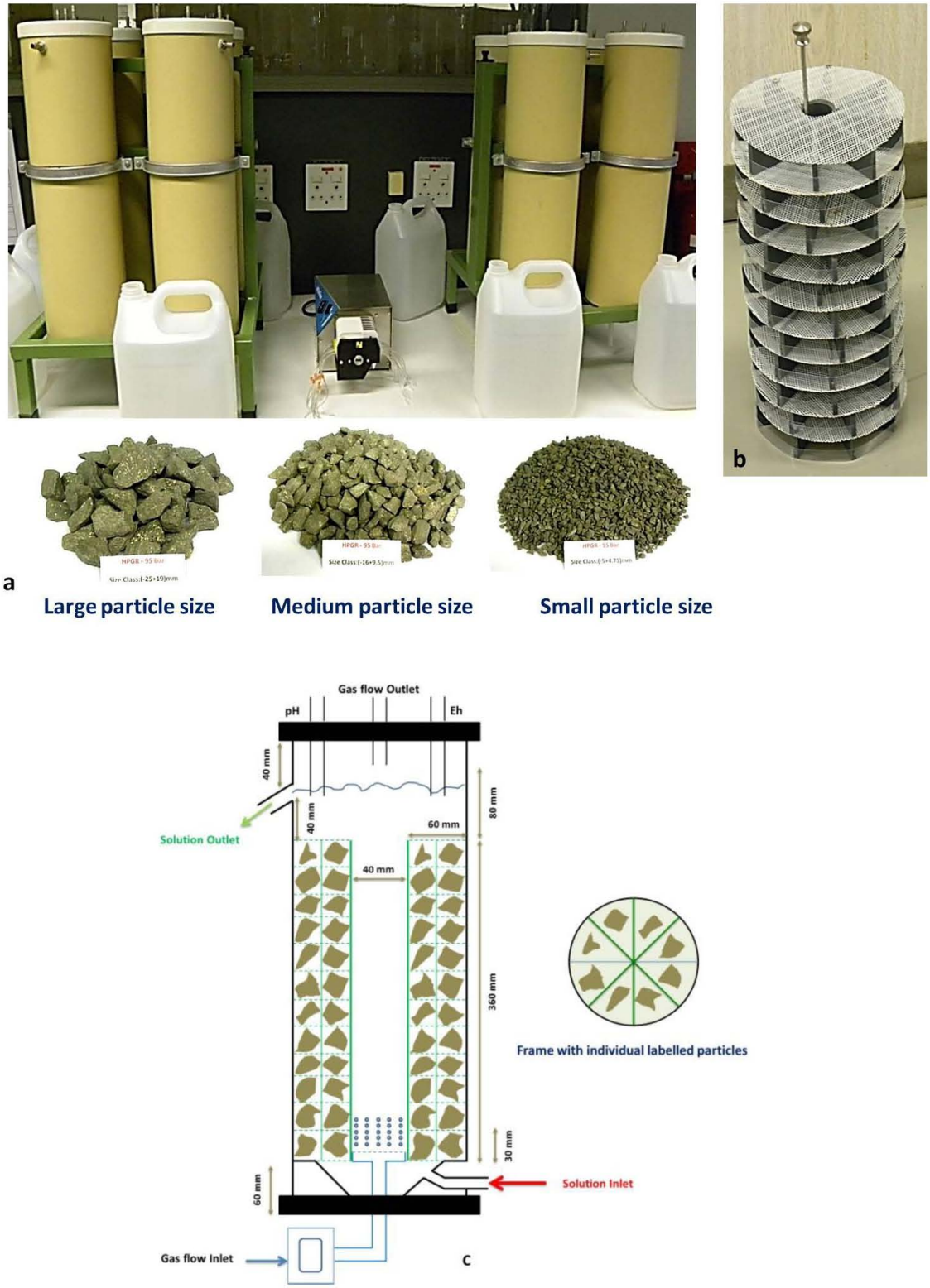

Figure 3.9: Leach columns, set up of leach reactors with stand and 8-channel pump-head (a), designed frame inside the leach reactor loosely holding individual labelled particles (b), a schematic drawing of leach reactor (c).

The concentration of the cells in the PLS, as well as cells detached from the ore surface (cells/mL), was determined microscopically using a Thoma counting chamber and an Olympus epifluorescent microscope using 1500x magnification (under oil immersion). During the reactor stoppages, the colonisation of the surface of the ore particles by sessile cells was investigated. The reactors were stopped from time to time to investigate the progress of leaching by analysing X-ray CT images of individual tagged particles each time (Figure 3.10).

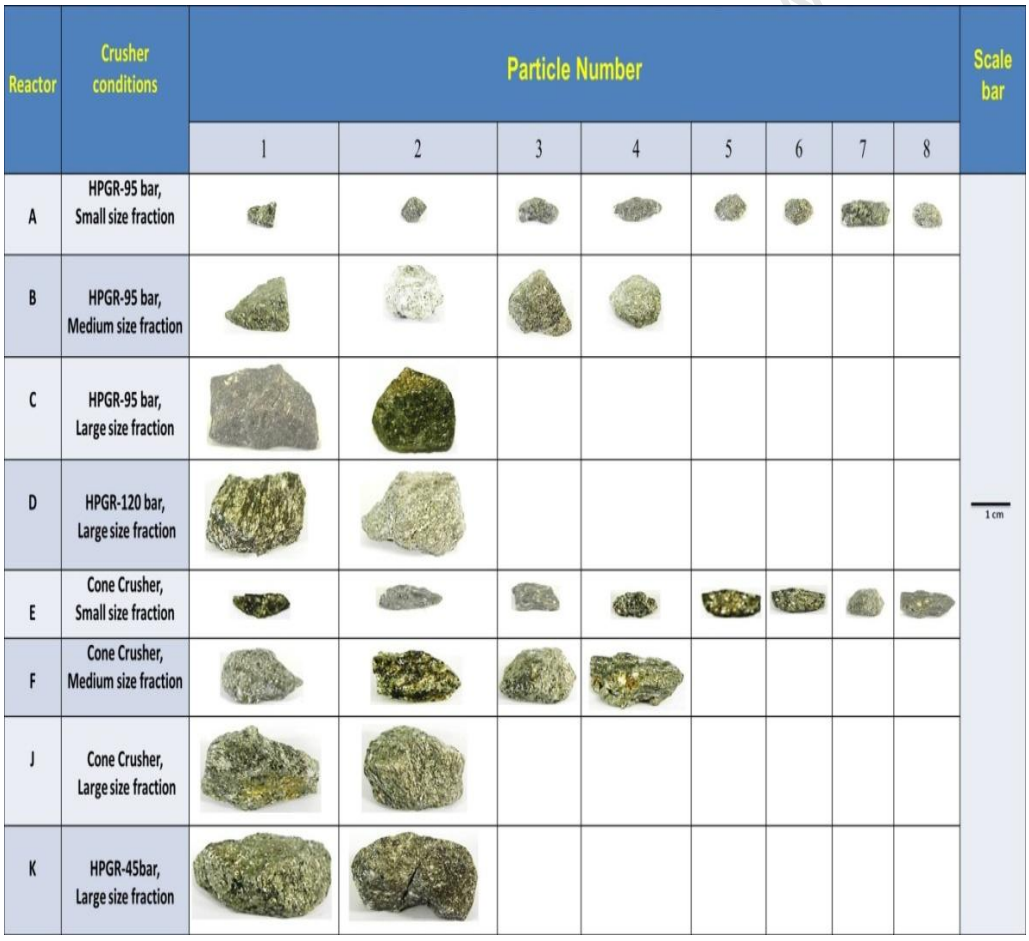

Figure 3.10: All labelled particles before leaching, inside the leach reactors A (HPGR-95bars-Small size fraction), B (HPGR-95bars-Medium size fraction), C (HPGR-95bars-large size fraction), D (HPGR-120bars-large size fraction), E (cone crusher-Small size fraction), F (cone crusher-Medium size fraction), J (cone crusher-large size fraction) and K (HPGR-45bars-large size fraction).

The results were further validated with those measurements obtained using more traditional, although destructive techniques such as SEM/EDS, QEMSCAN and EMPA. During these stoppages, the solution was kept in the reactors and the sample from the solids phases was taken out (and later replaced) by lifting out the basket stack. During stoppages, careful characterisation of the attached microbial population was also conducted.

3.2.4 Microbial cultures and inoculum preparation

After initial chemical leaching (no inoculation, only acidic feed solution supplied) for almost one month, each reactor was inoculated by a mixed culture of mesophilic acidophilic chemolithotrophs at a concentration equivalent of 1.86×10^{10} cell/kg ore. Using qPCR analysis (Dew *et al*., 2011), the culture was identified as predominately *L. ferriphilum* (Figure 3.11). It had previously been adapted to a finely ground sphalerite-containing ore in a stirred batch reactor over a period of two months.

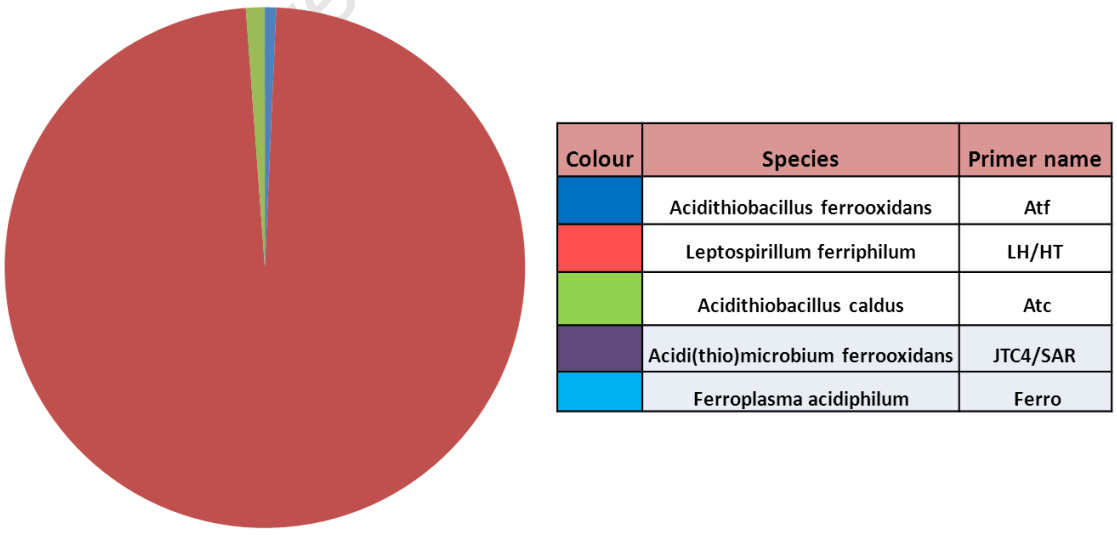

Figure 3.11: The ratio of microorganisms present in the inoculum culture, as determined by qPCR using the primers specified.

3.2.5 Microbial populations during leaching

During the reactor stoppages, the colonisation of the surface of the ore particles by sessile cells was investigated. To achieve this, cell detachment from the ore was carried out according to the methods reported by Chiume *et al*. (2012). Representative ore samples of some 50 g (dry weight) were used with 25 mL detachment medium (acidified detachment medium without Fe^{2+}). Three detachment cycles were performed with the acidified detachment medium and a further two detachment cycles in the presence of 0.4% (v/v) Tween 20.

The relative contributions of previously identified microorganisms to the planktonic and detached sessile microbial populations were monitored by the quantitative real time polymerase chain reaction (qRT PCR), using species-specific primers (or primer sets). The ore-free microbial suspensions were filtered using 0.22 µm cellulose acetate filters, washed and DNA extracted using the High Pure PCR Template Preparation Kit (Roche) as per manufacturer's specifications. The gDNA samples were diluted to 10 ng/µL. Standards of template plasmid DNA were created (0.1-0.00001 ng final DNA concentration) in triplicate with negative controls. One microlitre of gDNA template (10ng/µL) was added to primer containing Mastermix (KAPA Biosystems) as per manufacturer's instructions. The samples and standards were analysed in a qPCR machine (Rotogene 6000, Corbett Life Science), data analysed using software provided, and the primer sets previously described by Dew *et al*. (2011).

4 MINERAL CHARACTERIZATION

In this chapter, the results of ore mineralogy, mineral chemistry, texture and mineral association in the sphalerite ore particles are described and discussed. The complete set of results from the mineral characterization is given in the Appendices.

4.1 Bulk mineralogy

Major minerals identified by QEMSCAN analysis of the feed sample included major sphalerite (16.0 wt %) and pyrite (33.8 wt %) with lesser pyrrhotite, mica and kaolinite. Only minor chalcopyrite and galena occurred, as well as alabandite and arsenopyrite (grouped as other sulfides). Quartz was the main silicate gangue mineral (25.5 wt. %). Table 4.1 shows the bulk mineralogical analysis of the feed.

Table 4.1: Bulk mineralogical composition of the ore sample as determined by QEMSCAN.

Mineral	Amount (wt. %)
Pyrrhotite	1.2
Pyrite	33.8
Sphalerite	16.0
Galena	0.2
Chalcopyrite	< 0.1
Other sufides	3.2
Garnet	0.3
K-Feldspar	0.4
Chlorite	1.7
Kaolinite	2.8
Mica	7.9
Phosphate	2.0
Calcite	< 0.1
Quartz	25.5
Fe oxides/hydroxides	1.9
Others	3.1

As illustrated by several studies (Morey *et al*., 2001; Harmer *et al*., 2007; Chen *et al*., 2010), variations in the mineral chemistry of sphalerite have a profound impact on its behaviour during processing. Mining and processing of the ores according to metal grades alone would not be the preferred option, because low mineral association and impurity within the target mineral grains play an important role during the treatment (flotation or leaching process). This highlights the necessity for conducting a detailed multivariate (i.e. mineralogical, petrographical, mineral chemical) investigation in order to obtain a better understanding of the metallurgical behaviour and/or constraints imparted by the ore. Sphalerite composition and mineral association in the sphalerite ore particles are discussed in the following sections

4.2 Mineral chemistry

The crystal structure of sphalerite has long been recognised to accommodate a broad variety of elements, the most significant of which are Fe and Cd. Many elements enter the sphalerite structure via simple substitution of similar-sized ions ($Zn^{2+} \leftrightarrow Fe^{2+}$, Cd^{2+}, Mn^{2+}, Co^{2+} or $S^{2-} \leftrightarrow Se^{2-}$), or by coupled substitution (e.g., $Zn^{2+} \leftrightarrow Cu^{+}+In^{3+}$). Substitution mechanisms for other elements commonly found in sphalerite (e.g. Sn, Ag, Ga, and Ge) remain less well constrained and for others (e.g., Pb, Tl, As, Sb, and Bi), it is not entirely clear whether they enter the sphalerite structure at all or are almost always present as inclusions of discrete minerals (Cook *et al*., 2009). Consequently, the high degree of stoichiometric variability observed has a pronounced effect on the processing, as high levels of these impurities in some zinc concentrates, such as those produced at Gamsberg, render them unsuitable for processing by traditional Roast-Leach-Electrowinning (RLE) operations (McClung and Viljoen, 2011; Schouwstra *et al*., 2010).

To determine the concentrations of impurities within the sphalerite in the ore sample, mineral chemical studies were done on the samples prepared for QEMSCAN analysis. Samples were analysed for S, Cu, Fe, Zn, Mn, using an electron microprobe. Specifically, 30 individual spot analyses (Table 4.2) were completed for sphalerite. Raw analyses data are given in Appendix III.

The composition of the sphalerite in this study as determined by EPMA is given in Table 4.2 and illustrates that the major impurities in sphalerite composition (Figure 4.1a) are Fe (9.72 ± 0.74 wt. %) and Mn (4.44 ± 1.10 wt. %). The stoichiometric formula of sphalerite based on these major impurities is ($Zn_{0.78}$, $Mn_{0.07}Fe_{0.15}$) S, which is in agreement with McClung and Viljoen (2011). Sphalerite compositions at ~58-60 wt. % Zn are representative of another high Fe sphalerite population which was also described by McClung and Viljoen (2011). Figure 4.1b illustrates that exchange between iron or manganese and zinc occurs in sphalerite, confirming that iron and manganese ions are in fact incorporated in the sphalerite lattice and do not occur as discrete mineral inclusions.

Table 4.2: Average of 30 individual spot analyses for impurity content of sphalerite sample as determined by electron microprobe (wt. %).

Element	S	Cu	Fe	Zn	Mn
Average	34.00	0.03	9.72	52.00	4.44
Standard deviation	0.34	0.06	0.74	1.88	1.10

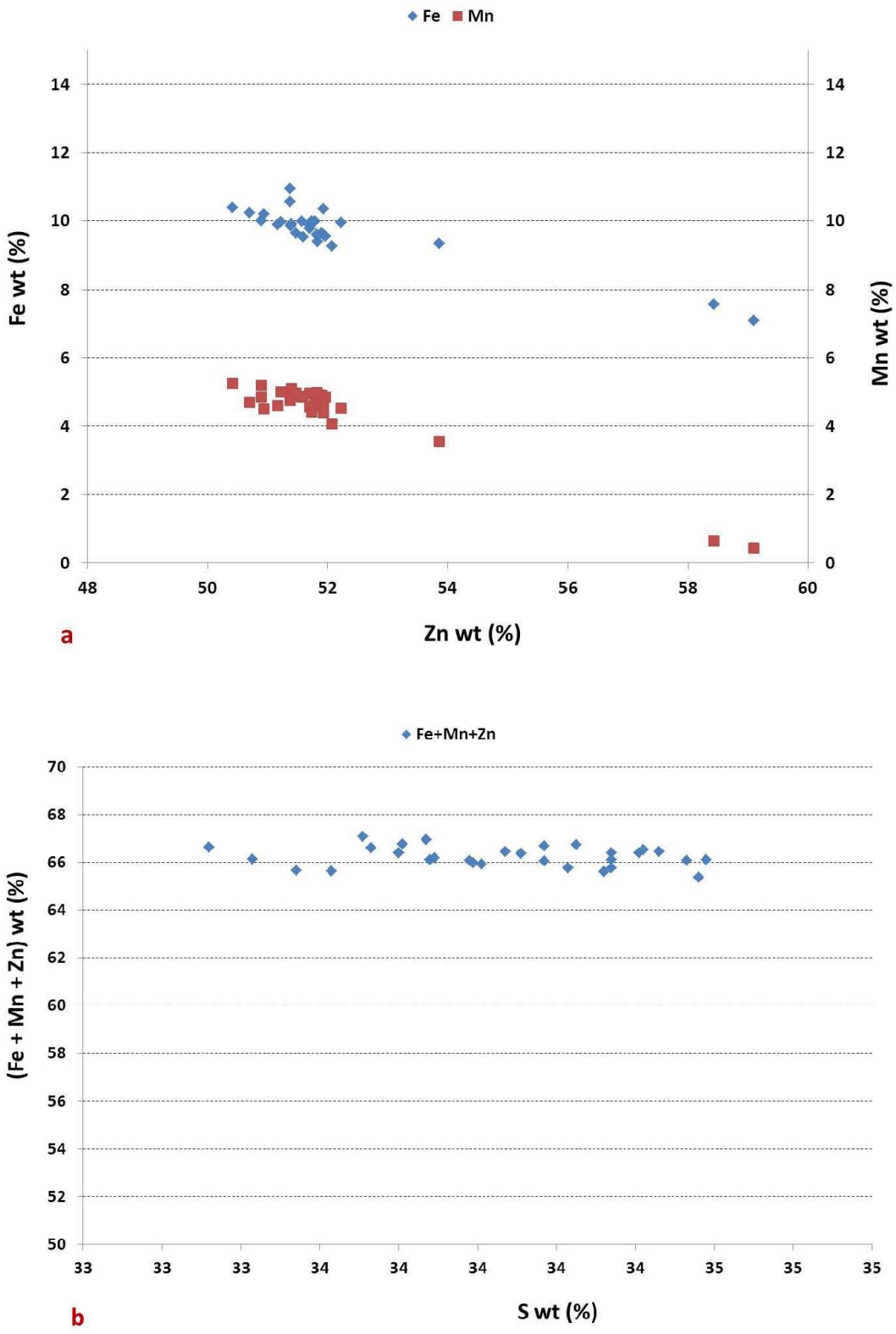

Figure 4.1: Plots of impurity content of sphalerite in the ore sample before leaching, Fe and Mn vs Zn (a) and Fe+Mn+Zn vs S (b).

4.3 Texture and mineral association

Mineral texture and association plays a key role in all mineral processing techniques including heap leaching. In heap leaching, mineral grains need not necessarily be liberated as free grains and only partial exposure of mineral grains may provide sufficient surface front for chemical attack by leaching solution. The sphalerite in this study in general can be divided in two groups based on the grain size and association. The coarse sphalerite grains (≥ 5 mm) were associated with other base metal sulfides and the disseminated fine sphalerite grains (≤ 1 mm) showed a stronger association to the gangue minerals. Unlike other Pb-Zn-Cu ores (e.g. the neighbouring Black Mountain / Broken Hill ores that are enriched in copper (Spry, and Petersen, 1989), sphalerite ore in this study does not show chalcopyrite disease which is the intimate association of very fine chalcopyrite to sphalerite (Barton and Bethke, 1987). Sphalerite in this study can be further classified into six different classes as a result of their comminution and their expected leaching behaviours (Figure 4.2). It should be note that these classes were defined based on the 2D (QEMSCAN) and 3D (X-ray CT) images:

a. Grains located at the surface of particles and exposed to the leach solution (e.g. grain marked A);
b. Grains located close to the surface of particles which become exposed to the leach solutions only after other grains have reacted (e.g. grain marked B);
c. Grains located inside the particles and not connected to the surface (e.g. grain marked C);
d. Grains located inside the particles but connected to the surface via pores or cracks (detectable only in the particles crushed using HPGR) (e.g. grains marked D);
e. Grains with size bigger than 5 mm which could be fully liberated in the small size fraction (-6.75+5.25) mm and thus are completely accessible to the leach solution; (e.g. grains marked E);
f. Fine grains disseminated within the gangue mineral (mostly quartz) that are completely inaccessible to the leach solution (e.g. grain marked F).

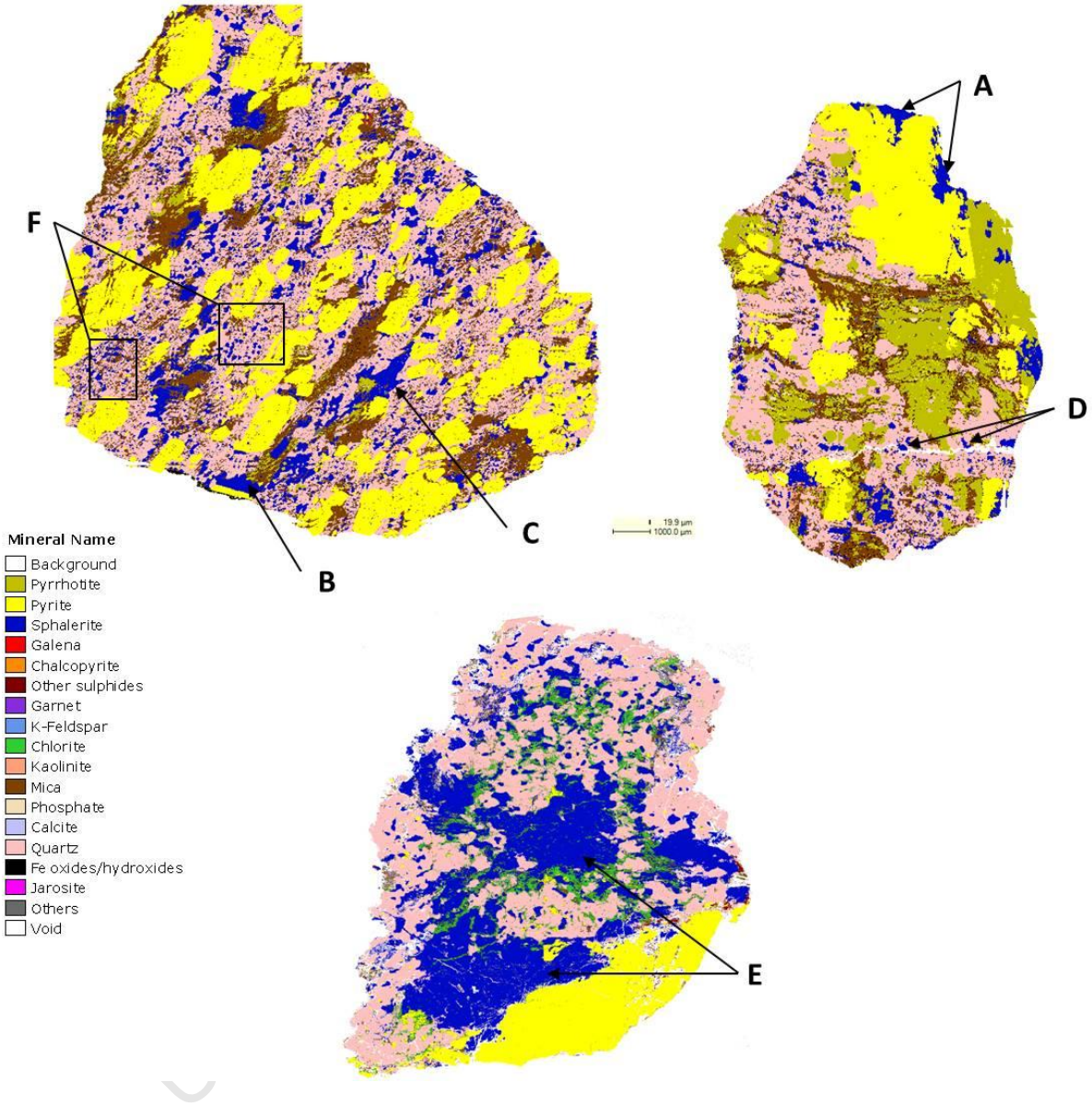

Figure 4.2: QEMSCAN images of three ore particles illustrating the sphalerite distribution.

5 CHARACTERIZATION OF COMMINUTION EFFECTS

The effect of the comminution devices on the ore particle size distribution and crack density are described and discussed in this chapter

5.1 Comminution device and ore particle size distribution

The tests using the cone crusher crushed the feed sample at -40 mm top size down to -25 mm in continuous mode. The HPGR tests were performed at three different pressure settings of 45, 95 and 120 bars, which correspond to the specific grinding forces of 1.42, 3.00 and 3.79 (N/mm^2) respectively (Table 5.1). The grinding force or specific pressure is defined as the total hydraulic force exerted on the rolls divided by the projected area of the rolls, in units of N/mm^2.

Table 5.1: The specific energy and grinding force at the different pressure of HPGR.

Pressure(bars)	F(sp): Specific grinding Force (N/mm^2)	W(sp): Specific Energy (kWh/t)
45	1.42	0.81
95	3.00	1.74
120	3.79	2.16

Figure 5.1 shows the product particle size distribution (PSD), from the HPGR and cone crusher tests. It can be seen that HPGR products from the three pressure settings were finer than the cone crusher product. In the HPGR, contrary to conventional crushing rolls, the particles are broken by compression in a packed particle bed, and not by direct nipping of the particles between the two rolls. This particle bed is created between two choke-fed, counter-rotating rolls. Between these rolls, a particle bed is temporarily

compressed to a density of up to roughly 85% of the solid material density (Celik and Oner, 2006). This compression is achieved by applying high pressure, which was allowed to reach 120 bars in this study, exceeding the compressive strength of the feed material. During this compacting process, the material is ground to a wide particle size distribution with a large proportion of fines, compacted into flakes. The compressive force not only acts on the coarse end of the particle size distribution (PSD), but also throughout the particle bed on both coarse and fine particles, including the fine particles derived from the initially coarser fractions (Apling and Bwalya, 1997; Klymowsky et al., 2002).

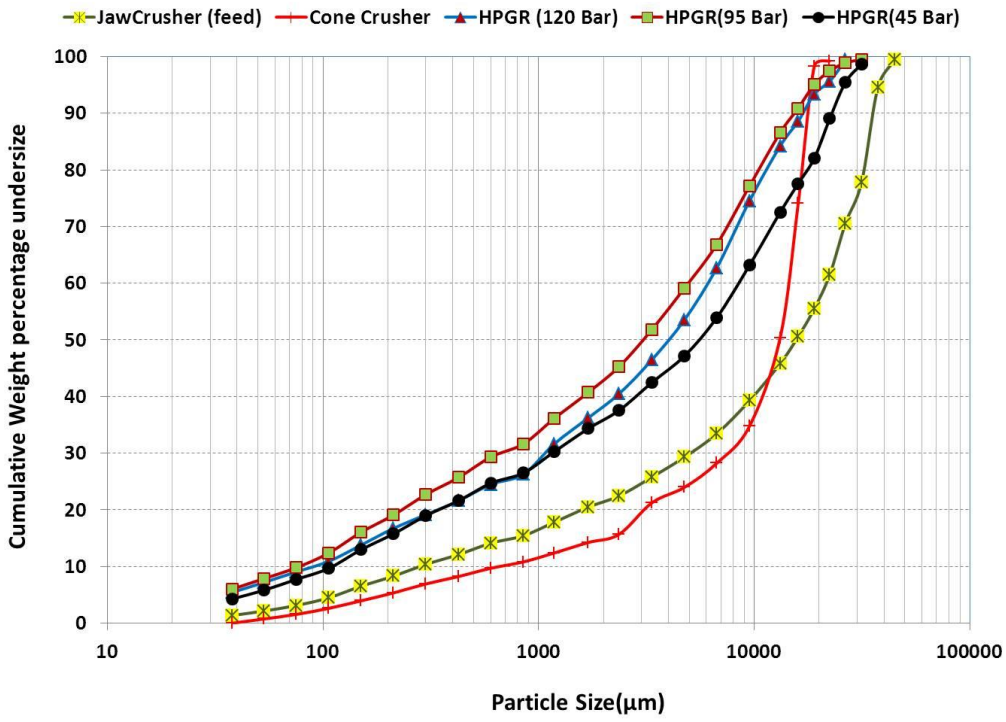

Figure 5.1: Cumulative PSD from the tests performed using Jaw crusher as feed, the cone crusher and three pressure settings of the HPGR.

The specific grinding force was determined to be between 1.42 to 3.79 N/mm^2. Although a finer product size distribution is expected as the pressure increases, the finest product

in this work was obtained when HPGR was operated the pressure setting of 95 bars which corresponded to the specific grinding force of 3.00 (N/mm2). Table 5.1 also shows the specific energy associated with the three pressure settings used in the experimental work. The specific energy is the energy input, which is absorbed per ton of material in units of kWh/t. It is proportional to the applied specific grinding force. The specific energy increased with pressure, which is in agreement with observations from other researchers (Aydoğan et al., 2006, Daniel, 2007). As Table 5.2 shows HPGR required the lowest specific energy consumption and achieved a reduction of 29 % over the cone crusher. Calculation of the cone crusher energy requirements was based on the Bond work index at a sieve size of 150 µm. This coarser screen size provides a lower estimate for the energy requirements of a cone crusher.

Table 5.2: The specific energy of HPGR-95 bars and cone crusher.

Comminution devices	Feed f_{80} (mm)	Product p_{80} (mm)	Specific Energy (kWh/t)
Cone Crusher	32	19	1.91
HPGR -95 bars	32	10	1.74

5.2 Effect of comminution device on formation of crack network

In order to compare the effect of the comminution method on crack network generation, selected sample particles from the different comminution devices (jaw crusher, HPGR and cone crusher) were studied in detail using a combination of optical microscopy, SEM, QEMSCAN and X-ray CT techniques (Figures 5.2 and 5.3). QEMSCAN analysis (Figure 5.4), Mercury Intrusion Porosimetry and BET Physical Gas Adsorption

were also performed for validation purposes, although on different particles from the same sub-samples due to the destructive nature of these techniques.

Photomicrographs and SEM images of the sphalerite particles (Figure 5.2), distinctly show the presence of micro cracks in the ore particles prepared using the HPGR, whereas these are absent in the jaw crusher product, which was the feed to the other two devices, and those prepared with the cone crusher. X-ray CT (Figure 5.3) also confirms this. The presence of these micro cracks suggests that particle bed breakage causes more micro-cracking as opposed to impact breakage. Comparison of the crushed products using HPGR and cone crusher in more ore particles are shown in Appendix IV.

The photographs in Figures 5.2-5.4 reveal that there is a difference in surface texture due to the different modes of grinding. HPGR milled particles have rougher surface texture and show more cracks, as well as generation of fissures on the surface of the particles due to the high loads applied (Celik and Oner, 2006). Quantitative results of porosity from the X-ray CT and QEMSCAN analysis of the samples from large size fraction (average of two particles) and prepared by HPGR were of similar order (~ 0.75 vs 1.1 volume %). Any minor differences between the results can be attributed to the fact that the particles analysed were not identical, and that the QEMSCAN is a 2-D measurement technique as opposed to X-ray CT, which is a 3-D technique. A difference is, however, noted in the porosity of particles prepared by HPGR relative to those from cone crusher (average of two particles from the large size fraction) where no micro-cracks were detected (Table 5.3) at the scale of image resolution (up to 20 µm) achievable with these instruments, which therefore suggests a preferential weakening of the particles prepared by compression breakage (HPGR).

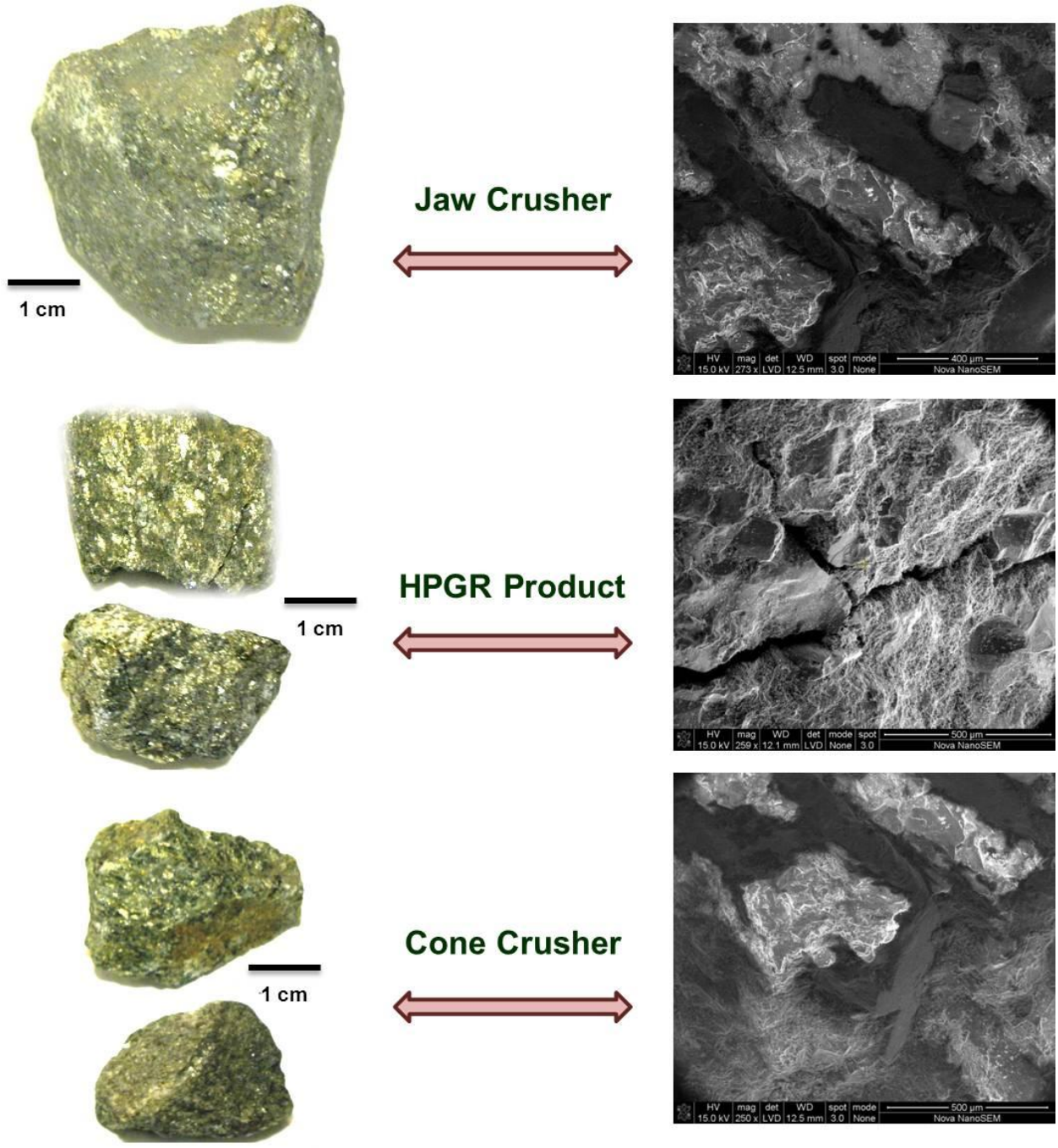

Figure 5.2: Standard optical photomicrograph and SEM photographs of five ore particles compared by different comminution methods (jaw crusher, cone crusher and HPGR). Note the presence of the micro-cracks in the particle prepared by HPGR.

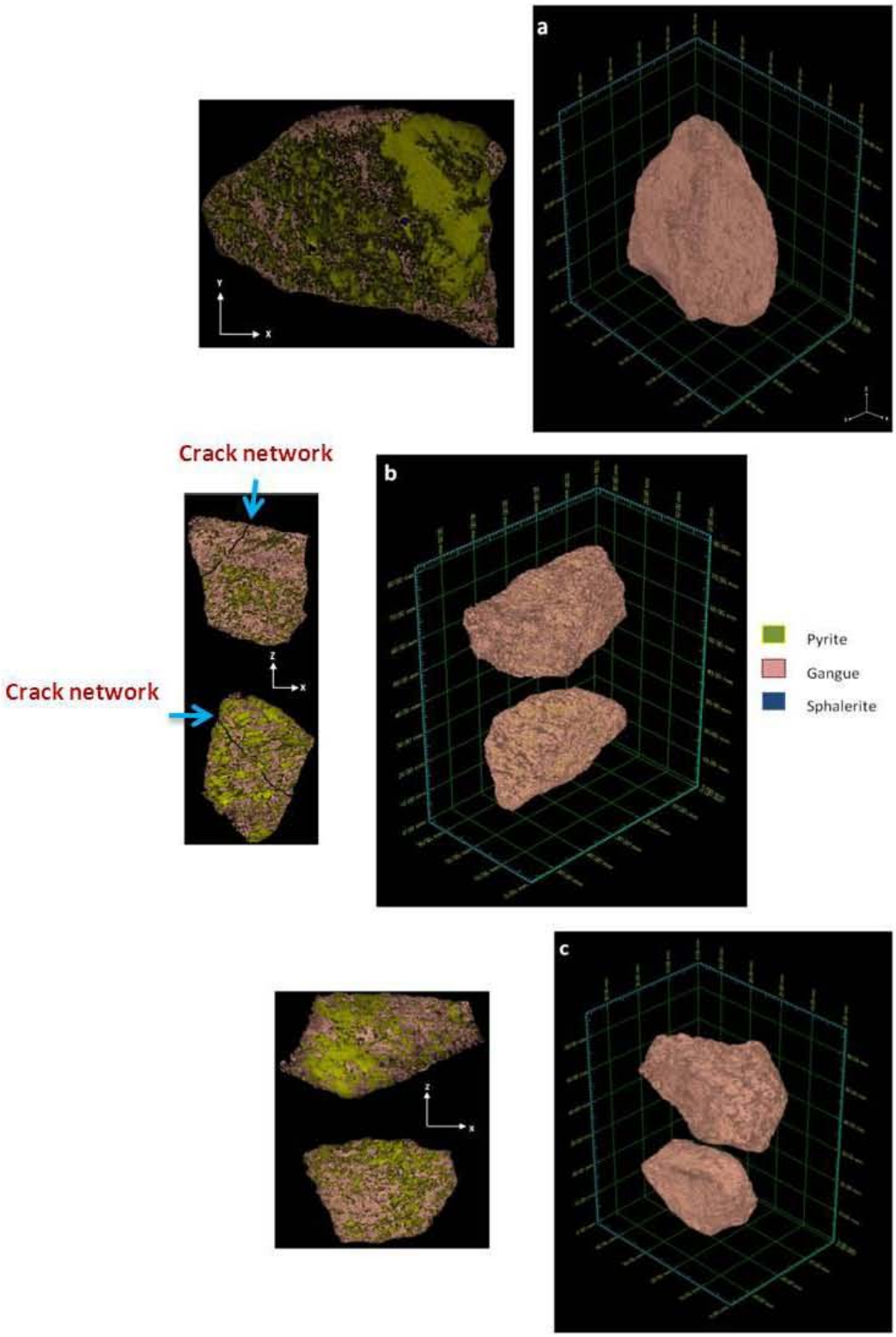

Figure 5.3: 3-D image of several large ore particles (25 mm) prepared by different comminution methods (a. Jaw crusher, b. HPGR and c. cone crusher). 2-D sectioned images of the particles are also shown to reveal the crack network.

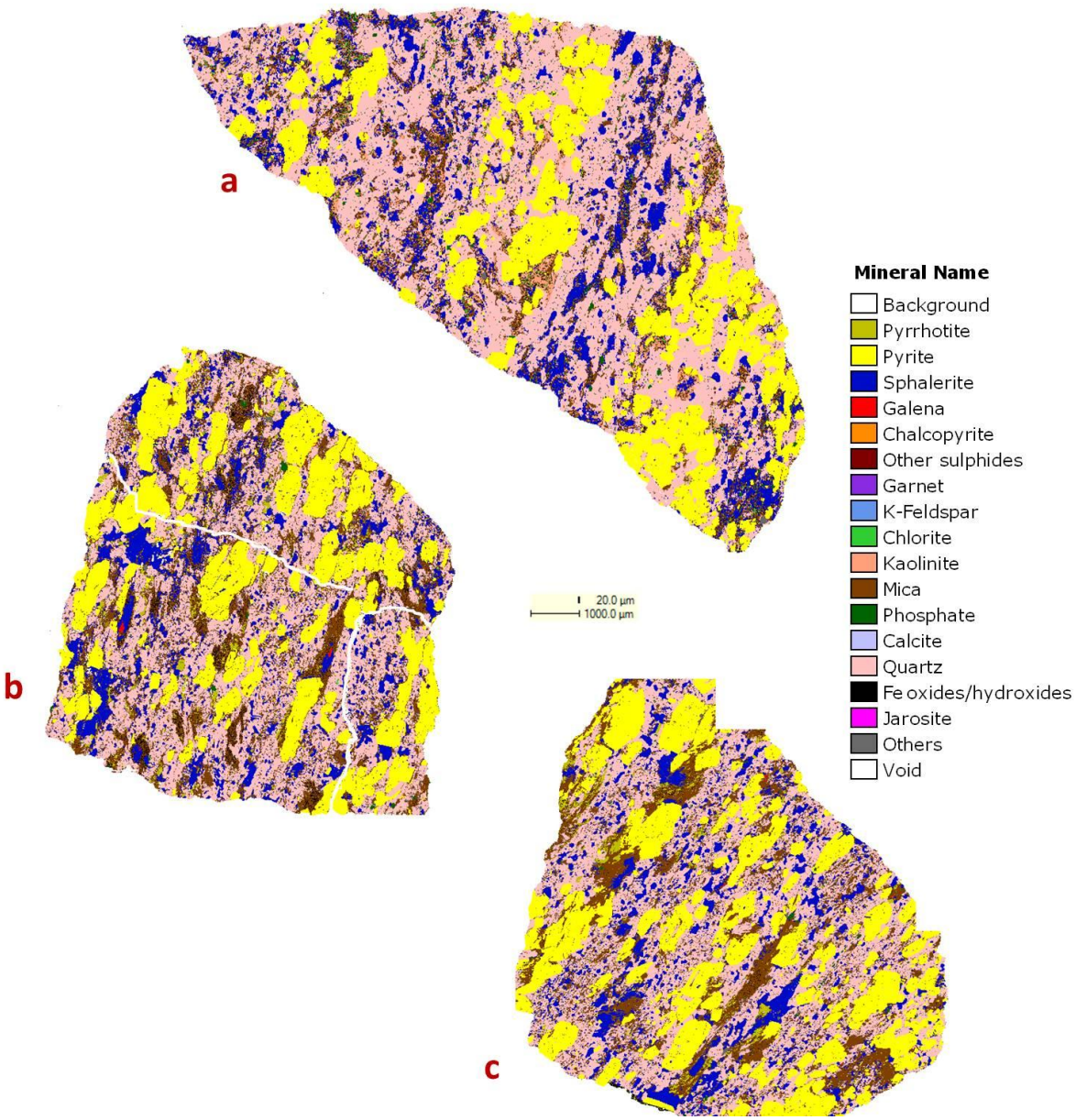

Figure 5.4: QEMSCAN image of one of the large ore particles produced by jaw crusher (a), HPGR (b) and cone crusher (c). Note the presence of the micro-cracks in the particle prepared by HPGR.

Comparison (Table 5.4) of the X-ray CT and QEMSCAN results with more traditional methods (Hg Intrusion Porisimetry and Physical Gas Adsorption (BET)) to measure porosity shows that the values obtained for the average pore diameter and exposed surface area were below the detection limits of either methods for both sets of particles.

The porosity of the bulk sample was however measured, and it is noted to be slightly lower (0.55 %, for HPGR particle) than that determined by X-ray CT (0.75 %, HPGR particle), and QEMSCAN (1.1 %, HPGR particle). This difference can be accounted for by the fact that the bulk sample measurements are influenced by the permeability of the ore and may underestimate the actual porosity, whereas 2-D and 3-D imaging techniques are independent of the connectivity between pores. Once again, a small difference was noted in the porosity measured between samples prepared by HPGR (0.55 % porosity) and cone crusher (0.36 % porosity).

The results of the X-ray CT (Table 5.5) appeared to indicate that more micro-cracks were present in the products obtained from the HPGR operated at the pressure setting of 95 bars. This suggests that for the HPGR device used in this work, the best pressure setting to produce particles with more micro-cracks is around 95 bars. Further increase in pressure did not appear to give a finer product or more micro-cracks, which are favourable for heap leaching.

Table 5.3: Comparison of the particle porosity (%) derived from X-ray CT (3D) and QEMSCAN (2D) measurements (Nd denotes not detected).

Comminution devices	Particle	Particle Porosity (%)	
		X-ray CT	QEMSCAN
Jaw crusher	Particle 1	Nd	Nd
	Particle 2	Nd	
HPGR (95bars)	Particle 1	0.76	1.07
	Particle 2	0.74	
Cone Crusher	Particle 1	Nd	Nd
	Particle 2	Nd	

Table 5.4: Comparison of pore characterization results using mercury intrusion Porosimetry and BET Physical Gas Adsorption methods (LLD denotes the lower limit of detection).

Measurement Technique	**Bulk sample (25g)**			
Mercury Intrusion Porosimetry	Average pore Diameter(nm)		Porosity (%)	
	HPGR	cone crusher	HPGR	cone crusher
	< LLD	< LLD	0.55	0.36
BET Physical Gas Adsorption	Exposed Surface Area (m^2/g)		Micro-pore Volume (cm^3/g)	
	HPGR	cone crusher	HPGR	cone crusher
	< LLD	< LLD	0.0001	0.0001

Table 5.5: Comparison of the particle porosity (%) for three different HPGR pressure settings derived from X-ray CT (3D).

Comminution with HPGR	**Particle**	**Particle Porosity (%)**
45bars	Average of 2 Particle from large size fraction	0.66
95bars	Average of 2 Particle from large size fraction	0.75
120bars	Average of 2 Particle from large size fraction	0.62

6 CHARACTERIZATION OF THE LEACHING PROCESS

In this chapter, the results of the chemical and microbial population dynamics during the leaching experiments are presented. Results of the leaching experiment in the eight reactors are related to the different feed size fractions and different preparation procedure. The effects of crack density and defective areas on microorganism attachment and mineral grain exposure are discussed. Mineral conversion in a single ore particle is investigated and the data has been fitted with the common models. The effects of the different comminution devices and mineral properties on zinc extraction are discussed and a more advanced model to describe particle technology is put forward.

6.1 Chemical dynamics during leaching

As it was described in the chapter 3, after the initial characterization of the ore samples, they were packed into eight leach reactors. The particles were fully immersed in leach solution and the reactor operated in continuous mode. Leaching process was initially chemical leaching (30 days), followed with bioleaching (inoculation on day 31) for 10 months.

The pH of the reactors effluent during the 30 days of chemical leaching with H_2SO_4 at the pH 1.0, increased initially, and then remained constant around pH 1.2 to 1.3 (Figure 6.1). This was due to the high amount of acid soluble gangue minerals in the ore (e.g., pyrrhotite, kaolinite, Fe oxides/hydroxides, and calcite). After inoculation (day 31) with fresh leach solution containing 1 g/L ferrous iron and pH adjusted to 1.50 with concentrated H_2SO_4, a further increase in the pH was observed until day 50 and a maximum of pH 1.8 to 2.5, where after the acid generation from bioleaching countered the gangue leaching and the pH remained around pH 1.3 to 1.5 throughout the remainder of the experiment (Figure 6.1a). Acid is consumed through rapid biooxidation

and regenerated later from sulphur oxidation-the delay of sulphur oxidation is typical and had been discussed, for example by Petersen and Dixon, 2002.

Prior to inoculation, the redox potentials remained in the range of 350 to 380 mV, illustrating the dominance of ferrous iron. The redox potentials reached 500 mV two weeks after inoculation and increased to about 700 mV within one further week and remained stable thereafter (Figure 6.1b), correlating with changes in the relative concentrations of ferrous and ferric iron and the changes in pH as discussed above. The dominance of Fe^{3+} was taken as an indication that strong bioleaching activity was present throughout the run such that mineral leaching was the limiting rate step.

Only once the redox potential is high the pH declines; this indicates that bio-oxidation generates acid (probably from pyrite). Microbes that oxidize ferrous iron to ferric iron are generally thought to be the largest contributors to pyrite oxidation (Murphy and Strongin, 2009). Failing pH after the establishment of high redox potential may also be due to the biooxidation of elemental sulphur. Three distinct types of microbes have been known to oxidizing ferrous iron in different conditions. Acidophiles, such as the bacteria *Acidithiobacillus ferooxidans* and *Leptospirrillum ferrooxidans*, as well as the *Archaeon Ferroplasma*, oxidize iron in environments that have a very low pH (Murphy and Strongin, 2009).

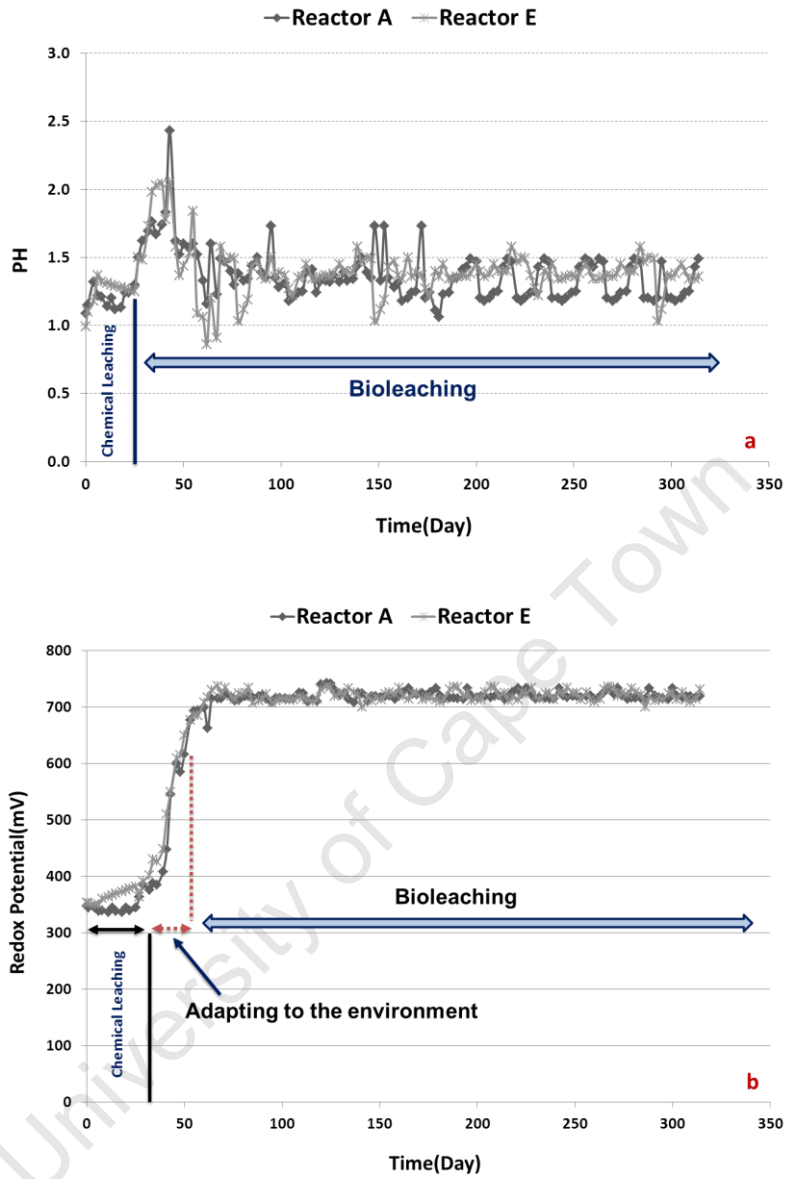

Figure 6.1: Changes of the pH profile (a) and redox potential profile (b) versus time (days) for reactors: A (HPGR-95bars-small size fraction), E (cone crusher-small size fraction) versus time (days).

The primary role of bacteria in the biooxidation process of pyrite is the conversion of aqueous Fe^{2+} into Fe^{3+} and the production of sulfuric acid from the pyritic S_2^{2-} group. The oxidative attack of Fe^{3+} results in the destruction of the sulfide mineral and the solubilisation of its constituents (Rohwerder *et al.*, 2003).

Stable pH and redox potential during the bioleaching process provided a homogenous environment inside the leach reactors. Figures 6.2a and 6.2b show the same trend of pH and Eh for all eight leach reactors. At this condition, the rate of mineral conversion is mostly dependent on the particle properties and mineral association within the particles, which are explained in the following sections.

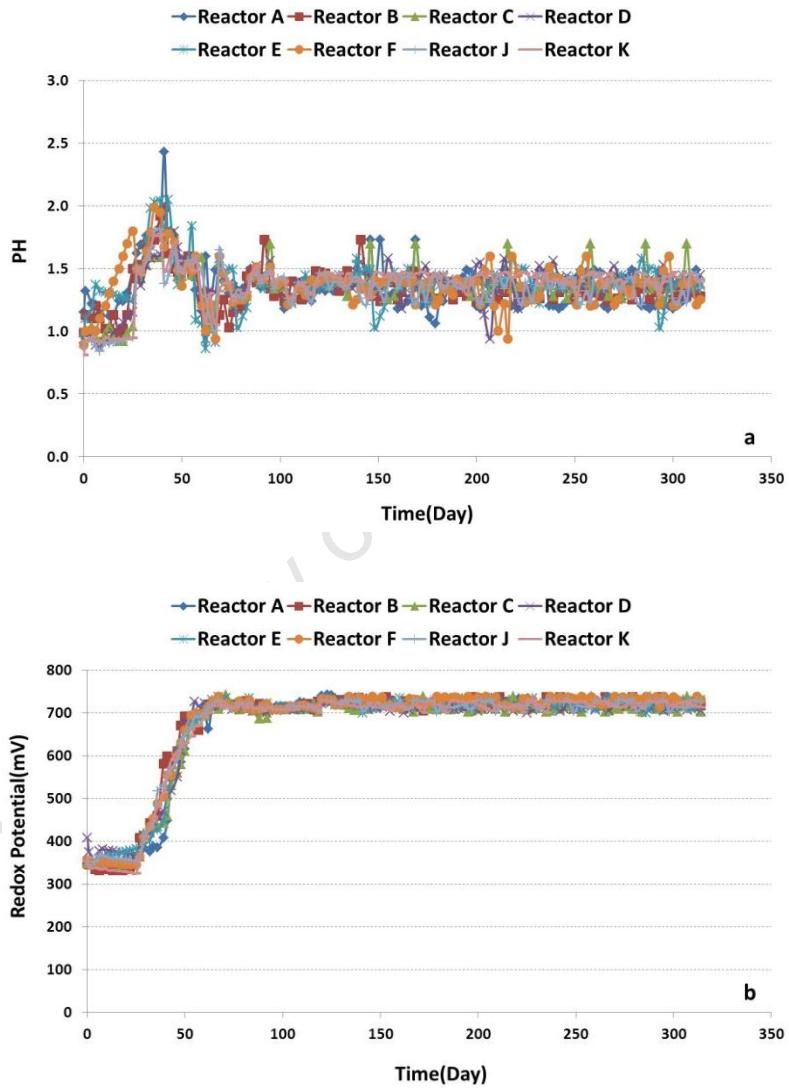

Figure 6.2: Changes of the pH profile (a) and redox potential profile (b) versus time (days) for reactors: A (HPGR-95bars-Small size fraction), B (HPGR-95bars-Medium size fraction), C (HPGR-95bars-large size fraction), D (HPGR-120bars-large size fraction), E (cone crusher-small size fraction), F (cone crusher-medium size fraction), J (cone crusher-large size fraction) and K (HPGR-45bars-large size fraction).

6.2 Zinc extraction

The cumulative extraction trends of zinc into the leach liquors, illustrated in Figure 6.3 for leach reactors A (HPGR-95bars-small size fraction) and E (cone crusher-small size fraction), showed a slow leaching rate during the chemical leaching stage (days 0-30) and the onset of bioleaching (days 30-60) due to the lower availability of Fe^{3+} and, potentially, the dissolution of gangue minerals. On attainment of a redox potential of 700 mV or greater, rapid Zn leaching occurred up to day 170, followed by steady leaching for the remainder of the experiment (to day 314) or until 50-70 % extraction was achieved. Usually, after rapid leaching, metal extraction rates slowed down and a slower constant rate period (part S in the Figure 6.3) followed. This trend is in agreement with other studies (Watling, 2006 and Dreisinger, 2006) (see Figure 2.5). This behaviour was more clear in reactors A (HPGR-95bars-small size fraction) and E (cone crusher-small size fraction) (Figure 6.3). As can be seen on comparison of reactor A to reactor E, reactor A had more Zn extraction during the rapid leaching period. The trend in the other leach reactors almost was the same as reactors A and E (Figure 6.4), and the profiles appear smoother. The leach rates attained were dependent on the size fraction leached, the comminution method and HPGR pressure. Leach rates increased with decreasing particle size. The leach rate of samples of the same size prepared by HPGR exceeded those of the cone crusher (Figure 6.3 and Figure 6.4 a, b).

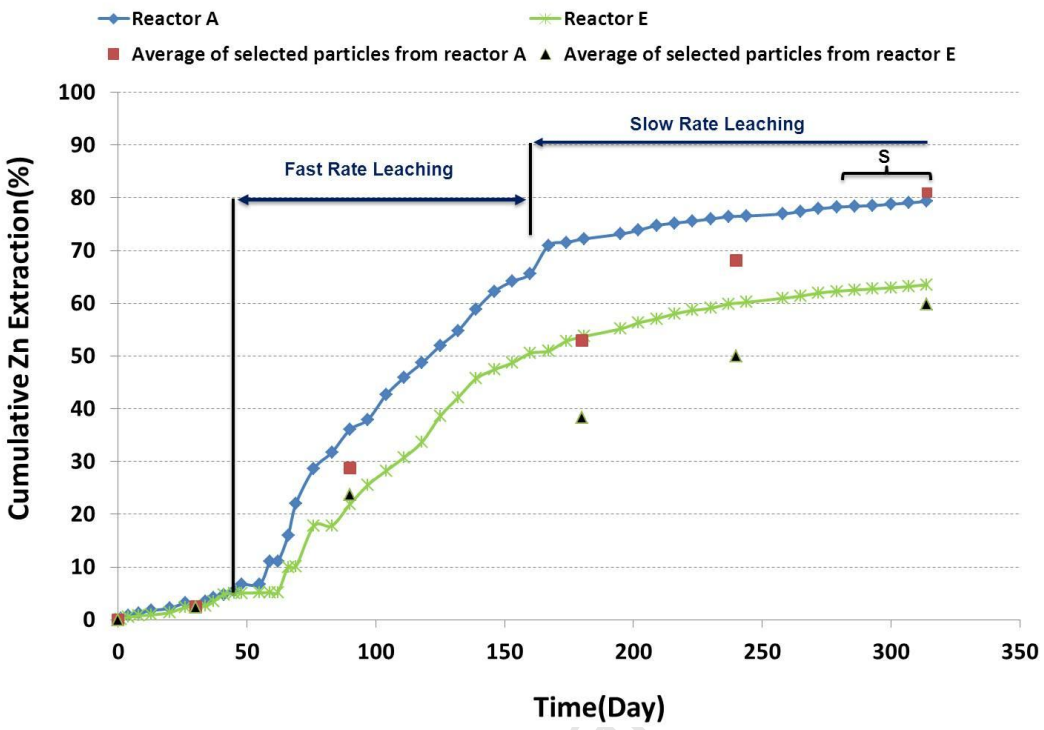

Figure 6.3: Cumulative amount of zinc in the leach liquors from the reactors A (HPGR-95bars-small size fraction) and E (cone crusher-small size fraction). Note that the markers are the average of Zn extraction related to the selected particles from the leach reactors calculated using X-ray CT.

Figure 6.5 shows the cumulative amount of zinc in the leach liquors extracted from the reactors, which were charged with the products obtained from the HPGR operated at the pressure settings of 45, 95 and 120 bars. The pressure setting of 95 bars produced the highest amount of Zn, compared to those products produced by the pressure settings of 45 and 120 bars. This is assumed to be due to the higher micro-crack density present in the products obtained from the HPGR operated at the pressure setting of 95 bars (see Table 5.4).

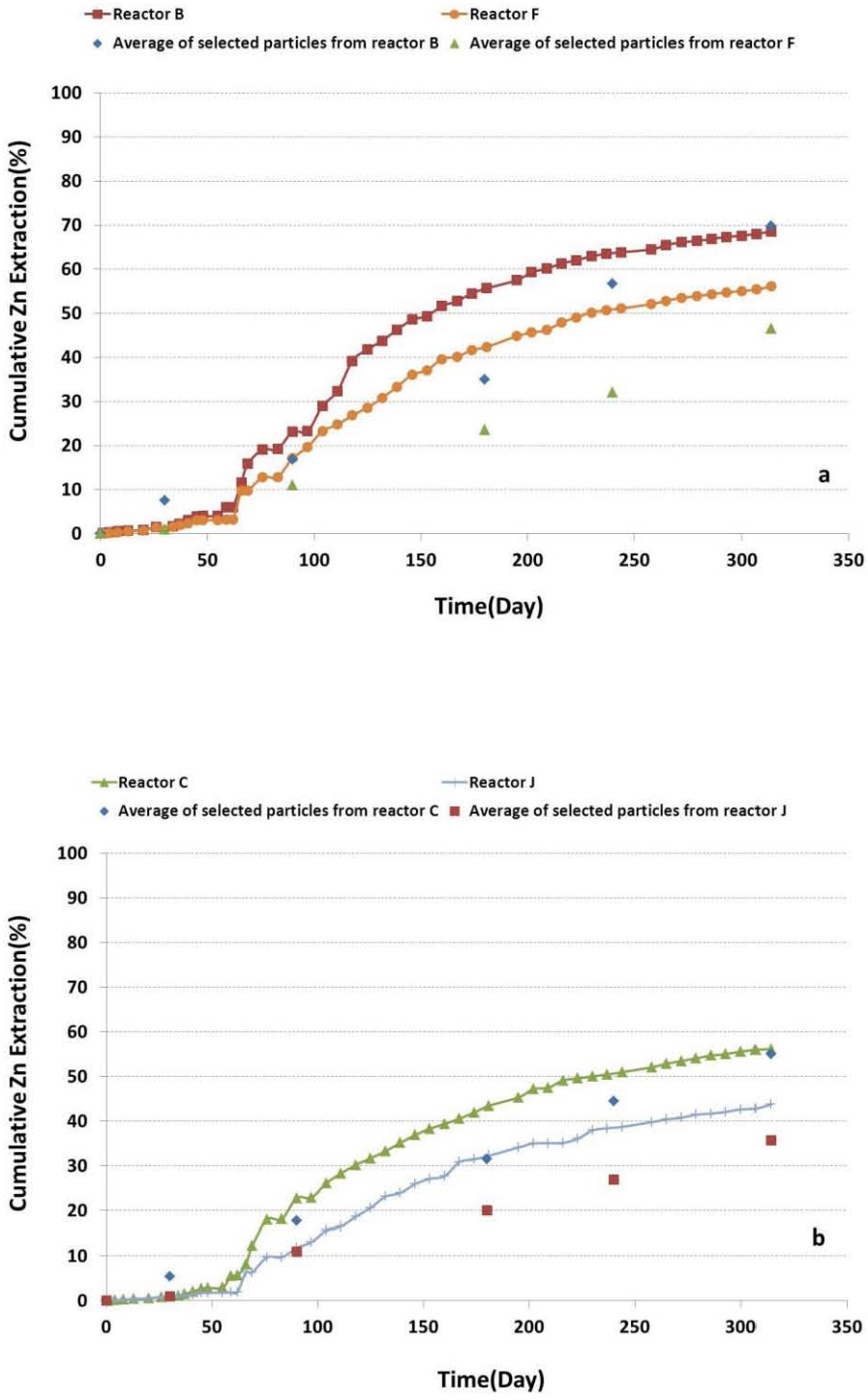

Figure 6.4: Comparison of the cumulative amount of zinc in the leach liquors, a. reactor B (HPGR-95bars-Medium size fraction) and F (cone crusher-Medium size fraction), b. reactor C (HPGR-95bars-large size fraction) and J (cone crusher-large size fraction). Note that the markers are the average of Zn extraction related to the selected particles from the leach reactors calculated using X-ray CT.

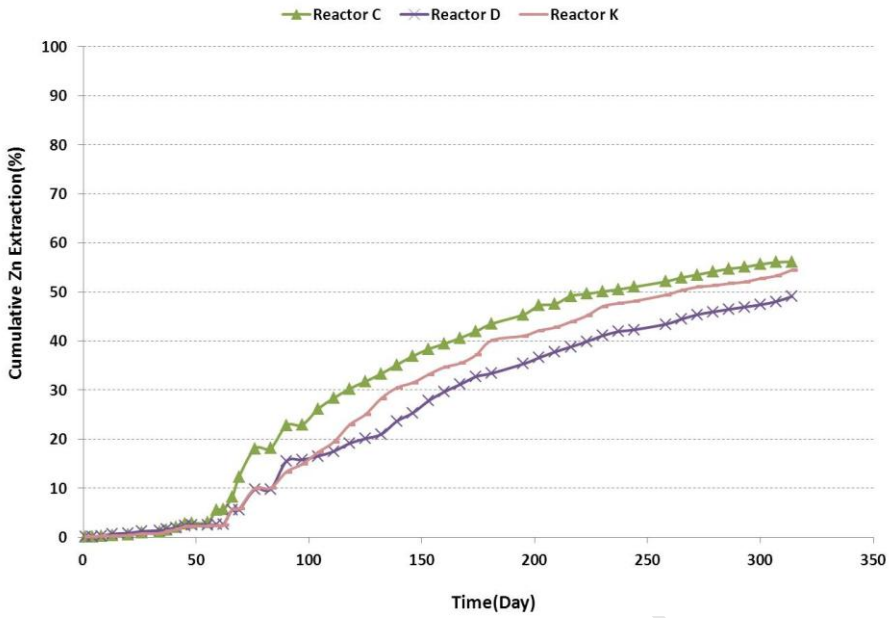

Figure 6.5: Comparison of the cumulative amount of zinc in the leach liquors from the reactor C (HPGR-95bars-large size fraction), D (HPGR-120bars-large size fraction) and K (HPGR-45bars-large size fraction).

Figure 6.6a compares the percentage of zinc extraction over 11 months of leaching from ore crushed by HPGR and cone crusher. This confirms that the leachability of the ores was better for products prepared using the HPGR compared to those from the cone crusher. Figure 6.6b shows higher metal extraction for particles prepared using the HPGR operated at the pressure setting of 95 bars compared to the 45 bars and 120 bars pressure settings. This indicates that there is an optimum operating pressure where the metal extraction rates are higher.

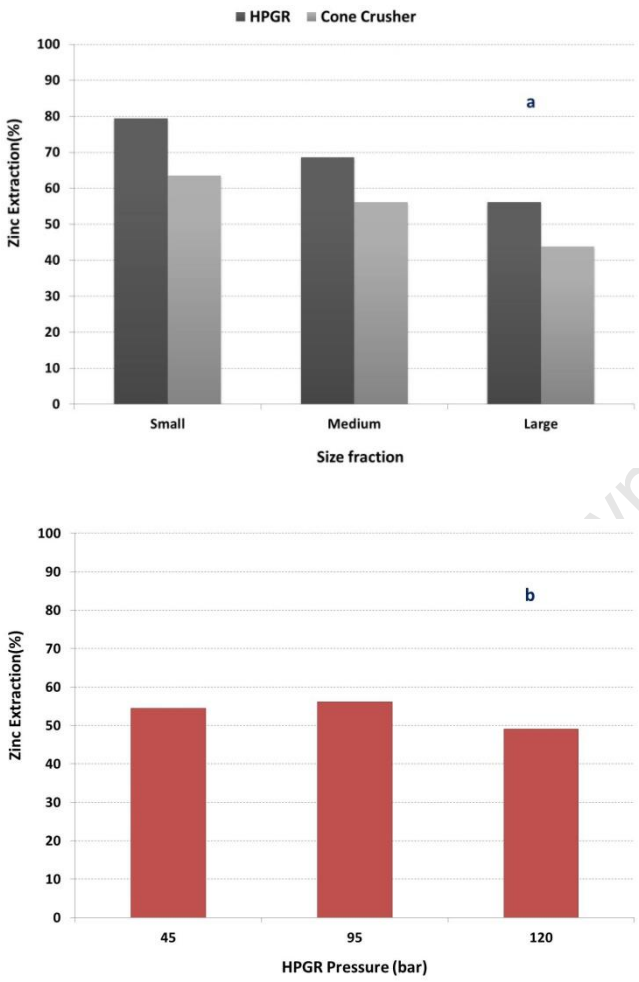

Figure 6.6: Leachability of Zinc for different particle size classes, HPGR product versus cone crusher (a) and HPGR with different pressure (b).

Figure 6.7 shows the concentrations of total Iron (Fe) in the effluent of the reactors. The Fe concentration in solution was high during the chemical leach phase with H_2SO_4 (containing no ferrous iron), with the solution concentrations reaching the highest concentrations in the presence of the smallest particle size and the lowest with the largest particle size. The amount of Fe_{tot} recovered in solution was supplied from the feed solution (1 g/l) during bioleaching and generated from the bio-oxidation of minerals such as pyrite. The Fe_{tot} concentration decreased due to precipitation; this was most notable in the last month of the bioleaching process where the rate of precipitation was more marked relative to the rate of pyrite leaching.

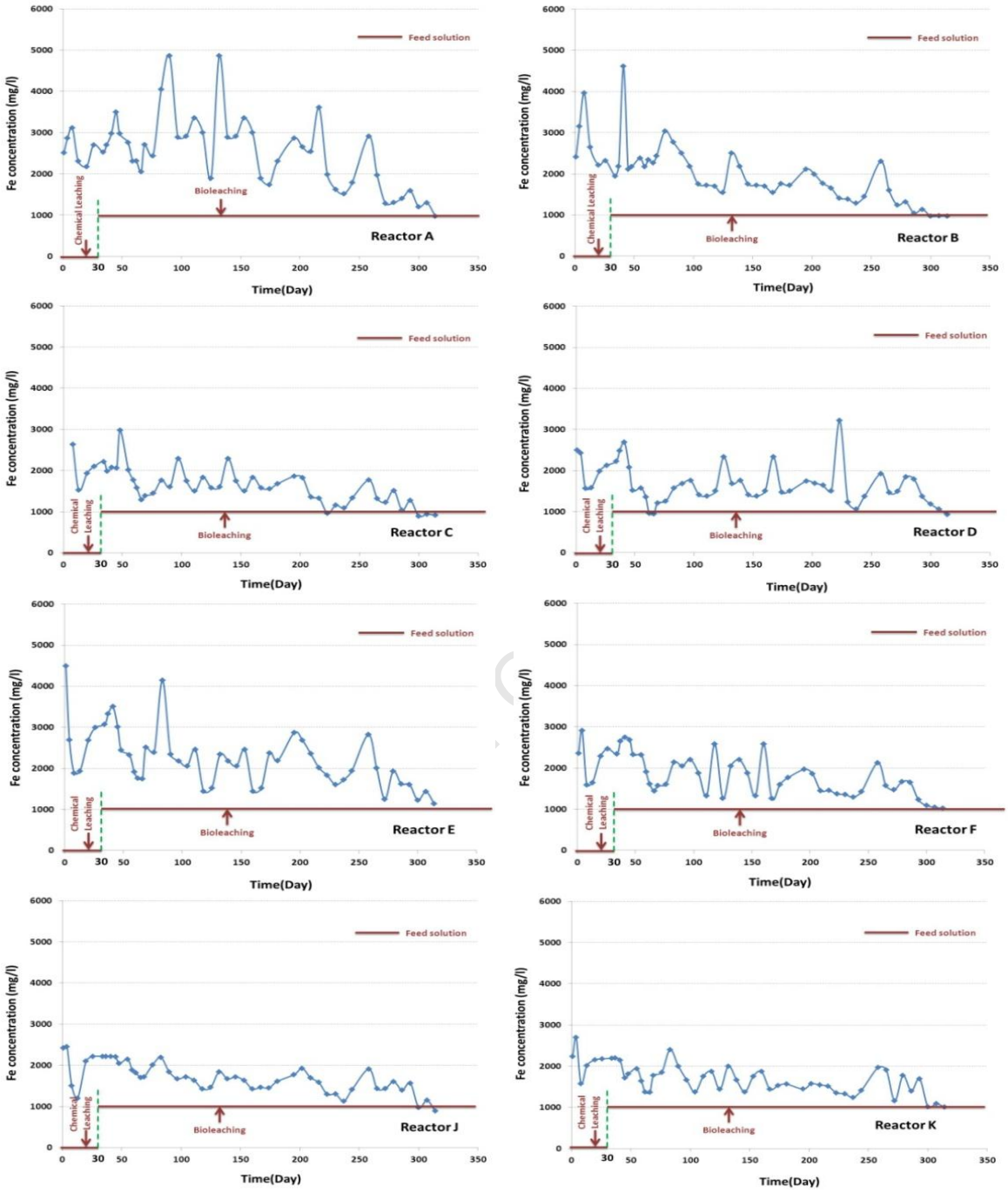

Figure 6.7: Comparison of the amount of total Iron in the leach liquors of the reactors A (HPGR-95bars-Small size fraction), B (HPGR-95bars-Medium size fraction), C (HPGR-95bars-large size fraction), D (HPGR-120bars-large size fraction), E (cone crusher-Small size fraction), F (cone crusher-Medium size fraction), J (cone crusher-large size fraction) and K (HPGR-45bars-large size fraction).

Figure 6.8 shows concentrations of aluminium and magnesium leached from gangue minerals. Garnet (0.3 wt. % of feed sample), K-Feldspar (0.4 wt. % of feed sample), Chlorite (1.7 wt. % of feed sample), Kaolinite (2.8 wt. % of feed sample), Mica (7.9 wt. % of feed sample) and Phosphate mineral group (2.0 wt. % of feed sample) contain aluminium, and magnesium could be in the structure of the Garnet, Chlorite, Mica and Phosphate. The aluminium concentration in solution is high during the initial contact with acidic solution during the chemical leach phase. The solution concentrations were highest in the presence of the smallest particle size and lowest with the highest particle size. No significant aluminium was leached into solution after 40 days, suggesting no further leaching of this gangue mineral. Magnesium was not leached chemically over the first 30 days. It should be noted that some Mg (49 mg/l) was supplied with the feed solution during the bioleaching phase, explaining the sudden rise in Mg after day 30. The decrease in Mg concentration in solution in the late stage of the bioleach suggests precipitation. Solution concentrations of the other metals (Mn and Ca) from gangue minerals has been shown in the appendix V.

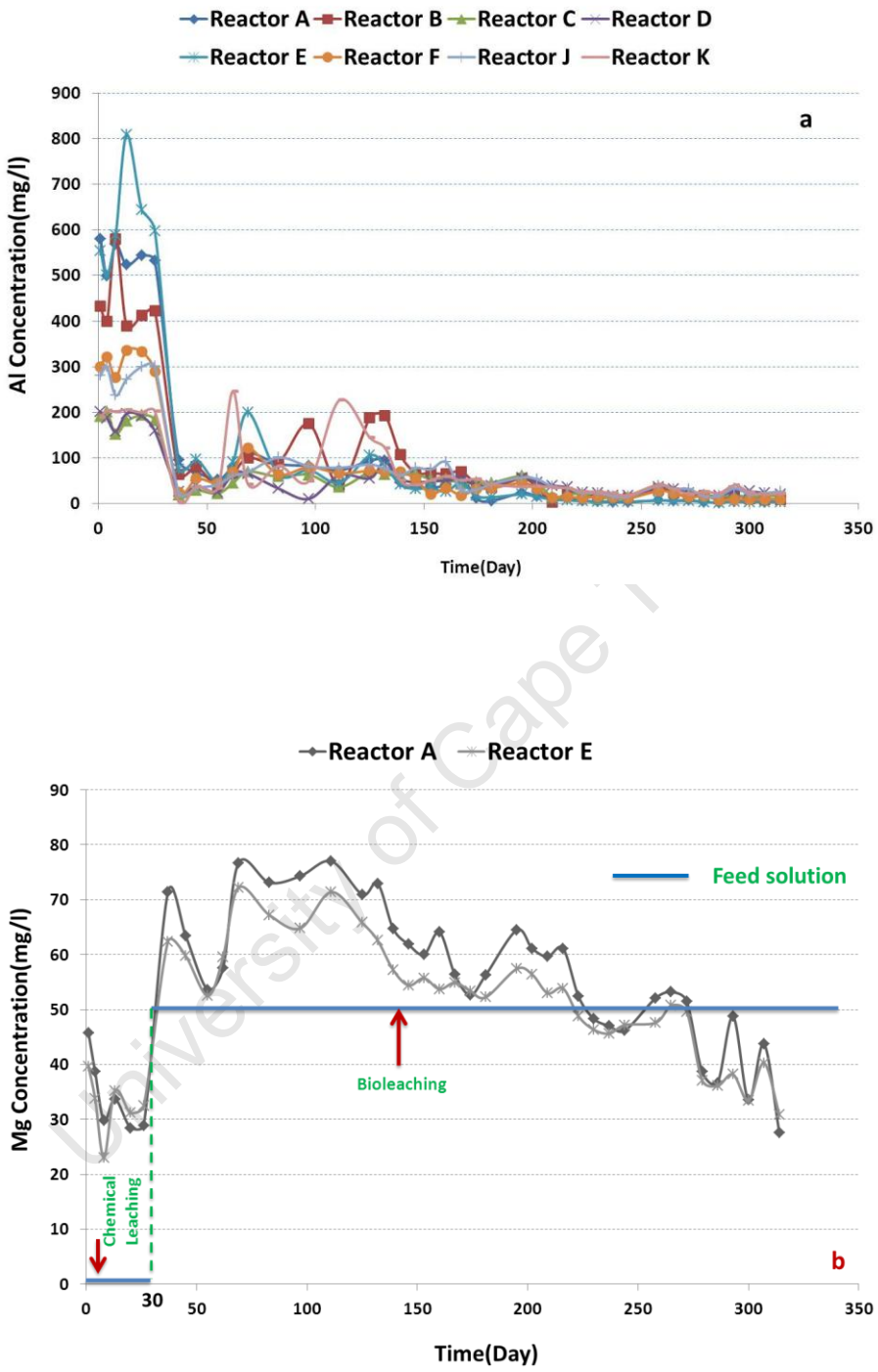

Figure 6.8: Solution concentrations of the metals from gangue minerals, a. Aluminium, b. Magnesium, in the leachate liquors in reactors A (HPGR-95bars-Small size fraction), B (HPGR-95bars-Medium size fraction), C (HPGR-95bars-large size fraction), D (HPGR-120bars-large size fraction), E (cone crusher-Small size fraction), F (cone crusher-Medium size fraction), J (cone crusher-large size fraction) and K (HPGR-45bars-large size fraction).

6.3 Microbial population dynamics during leaching

Comparison of the relative proportions of microorganisms in the PLS and attached to the ore are shown as a function of ore size and method of preparation in Figure 6.9. During 30 to 50 days of operation (after inoculation), *L. ferriphilum* continued to dominate the microbial population, in accordance with the initial inoculum (predominately *L. ferriphilum,* see Figure 3.9), limited inoculation from the ore, high Fe^{3+} concentrations and high redox potential. It is well known that high Fe (III) concentrations inhibit the growth of many microbes, such as *A. ferrooxidans*, whereas *L. ferriphilum* is relatively unaffected by high ferric ion concentrations owing to its excellent ability to scavenge very low Fe^{2+} concentrations (Rawlings *et al*., 1999; Xia *et al*., 2009; Bryan *et al*., 2012).

As described in the section 3.2.5, the relative contributions of previously identified microorganisms to the planktonic and detached sessile microbial populations were monitored by qPCR using species-specific primers (or primer sets). The qPCR data on the abundance of bacteria and archaea attached to the ore sample and in the PLS at Day 50 are shown in Figure 6.10. Across the three different size fractions, particles prepared by HPGR had higher sessile cell concentrations compared to the cone crusher products. This difference is most significant with the largest particle size (Figure 6.10a). Correspondingly, significantly more cells were associated with the PLS in the larger particle size experiments where cone-crushed ore was used (Figure 6.10b). This is an indication that the total surface area or density of preferential surface sites for microbial attachment is less for the cone-crushed rocks than those prepared by HPGR. This shows that the cone crushed surface is less amenable to bacterial attachment and thus favours bioleaching by planktonic cells. After the decrease in the cell concentration in the PLS due to initial attachment to solids, the cell concentration in the PLS from all leach reactors increased till day 50 where after it remained constant and very similar (Figure 6.11).

The stability within the reactors, where the rate of microbial growth equals that removed by solution, is assumed to be the main reason for a steady-state environment.

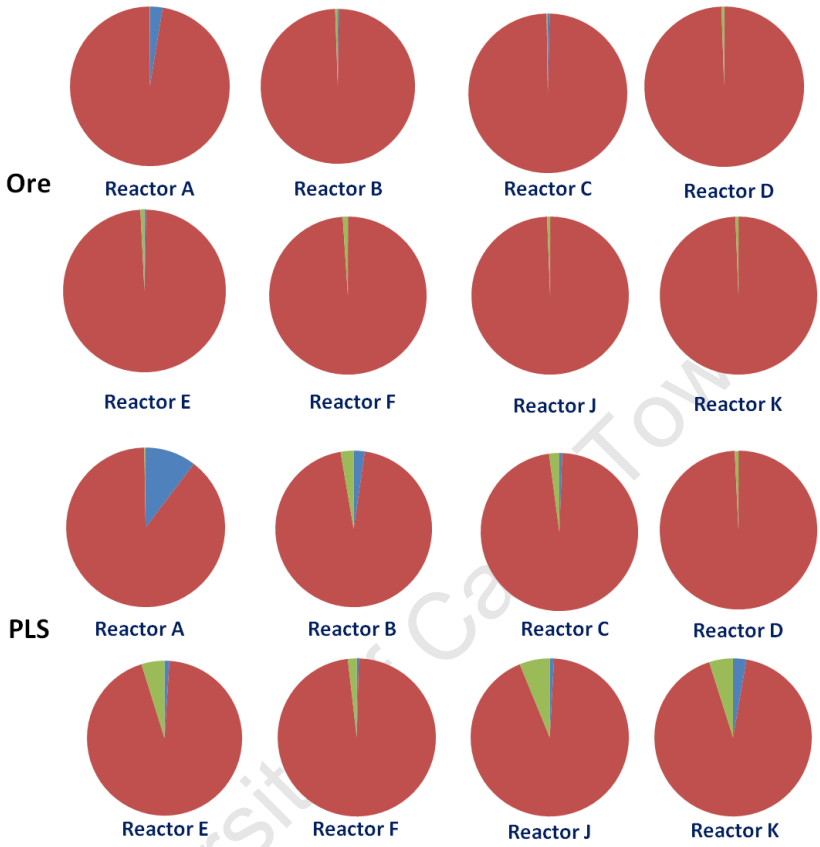

Colour	Species	Primer name
	Acidithiobacillus ferrooxidans	Atf
	Leptospirillum ferriphilum	LH/HT
	Acidithiobacillus caldus	Atc
	Acidi(thio)microbium ferrooxidans	JTC4/SAR
	Ferroplasma acidiphilum	Ferro

Figure 6.9: Comparison of ratios of the microorganisms in the PLS and on the ore during 30 to 50 days of operation in the reactors A (HPGR-95bars-Small size fraction), B (HPGR-95bars-Medium size fraction), C (HPGR-95bars-large size fraction), D (HPGR-120bars-large size fraction), E (cone crusher-Small size fraction), F (cone crusher-Medium size fraction), J (cone crusher-large size fraction) and K (HPGR-45bars-large size fraction).

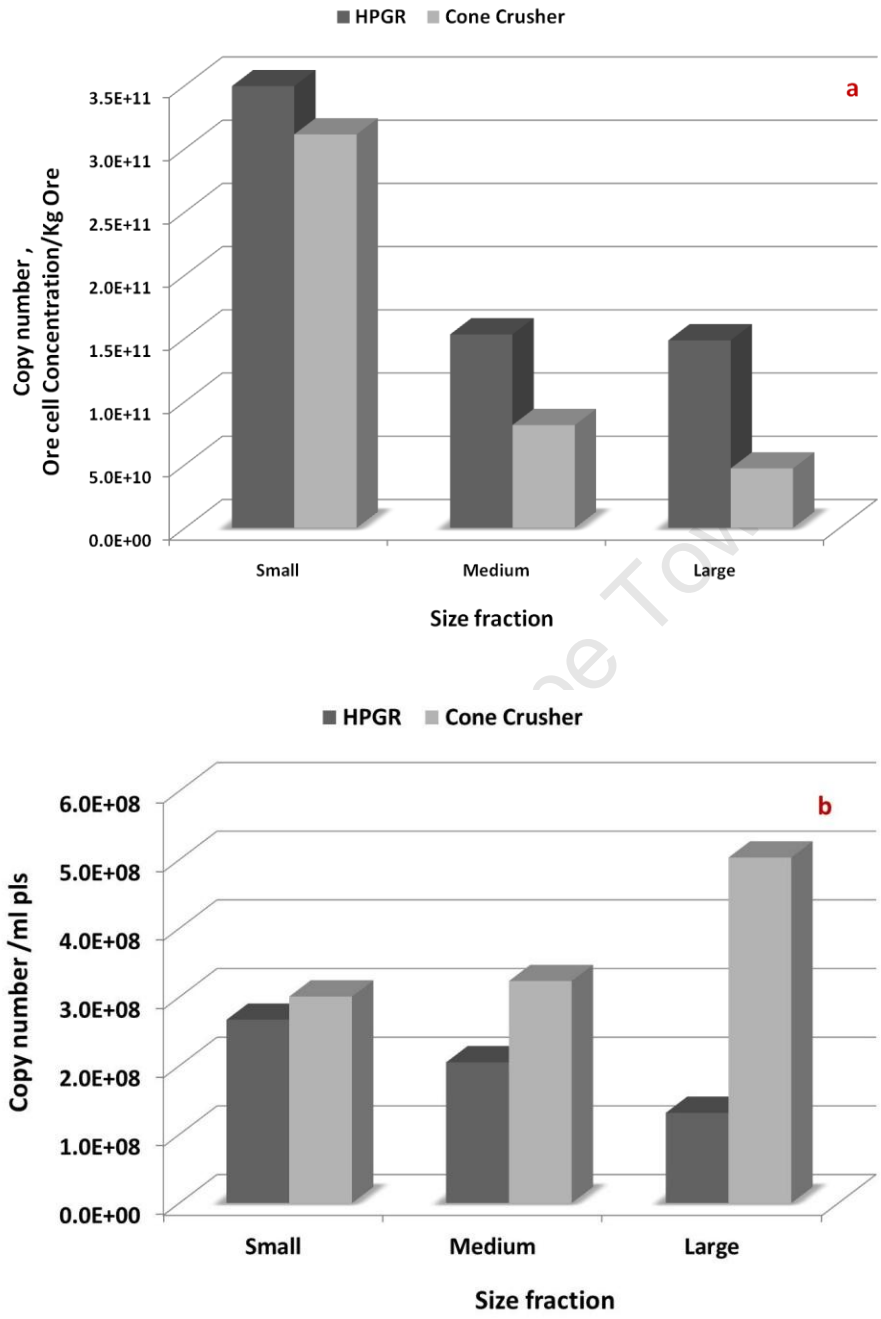

Figure 6.10: *qPCR* growth results of all bacteria and archaea attached to the ore sample (a) and in the PLS (b) ore during 30 to 50 days of operation (after inoculation).

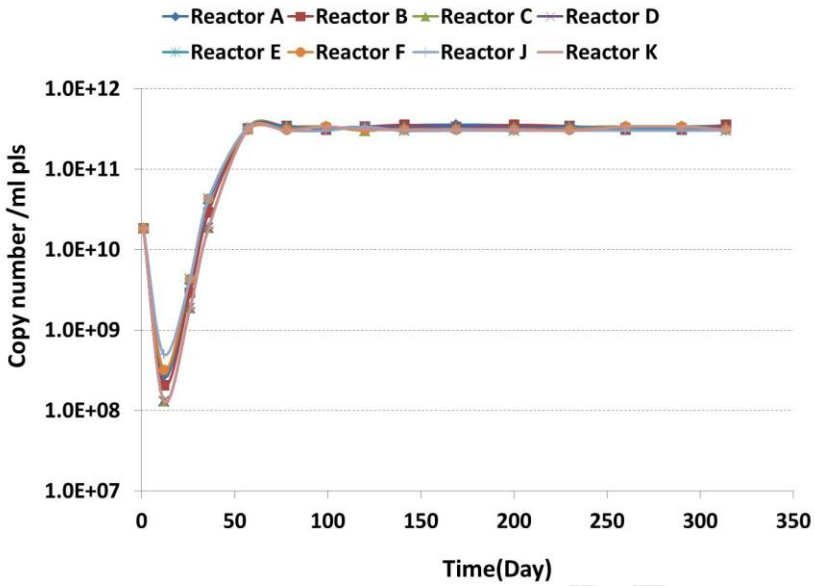

Figure 6.11: Cell concentration in the PLS during the process.

6.4 Microstructures and bacteria distribution

The results show that there is a relationship between attachment and mineral dissolution rate. The higher dissolution rates were most likely due to higher initial microbial attachment to the mineral. Therefore, microbial attachment to mineral surfaces is of great importance in bioleaching because of several positive effects such as the liberation of Fe^{2+} by contact bioleaching of pyrite and oxidation of Fe^{2+} and S_0, which could be accumulated on the mineral sulfide surface (Rodríguez *et al*., 2003).

Attachment of cells at surface defects is apparent in the SEM pictures shown in Figure 6.12 and supported by the work of Africa *et al*. (2010). Attachment was observed to be prevalent in, but not restricted to, the regions containing visible surface defects. The area with a higher density of cracks and irregularities provides nucleation sites for the microorganisms (Figure 6.12a). Microorganisms are unlikely to migrate very deeply into the surface cracks as they are of similar size; ferric iron or acid has to migrate deeper into the particles via the pore network. The reduced ferrous form has to return to the

surface to be re-oxidised by microorganisms. When the micro-cracks are larger than the individual cells, direct attachment of the microorganisms to the sub-surface mineral grains is possible (Figure 6.12b).

The number of these preferential attachment sites depends on the process of particle size reduction. These cracks may not all be on the surface, but only the cracks accessible from the surface can offer attachment sites. Furthermore, these cracks would be expected to be of different sizes and distributed randomly throughout the volume of the particle.

Patterns and footprints of microbial attachment on the mineral surface (Rodríguez et al., 2003; Muñoz et al., 2006), resulting from physico-chemical reaction(s) (Figure 6.12c), provide more holes and defective areas (Figure 6.12d), which can be useful for the diffusion of reagents in and out of the larger particles where the mineral dissolution rate must be considered along with diffusion. Figure 6.13 shows how microbial activities leave footprints on the minerals surface. Further SEM microphotographs are given in Appendix VI.

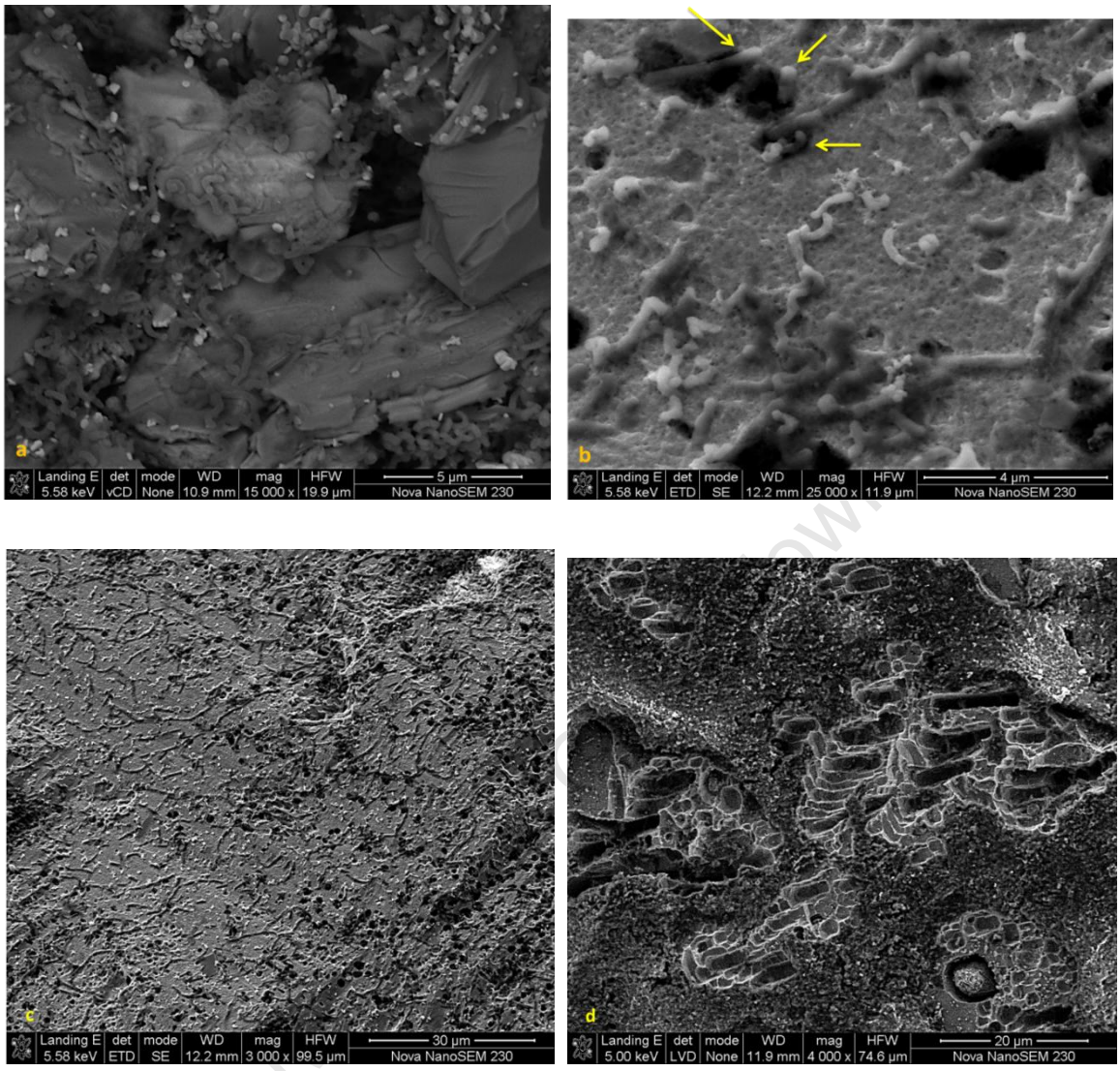

Figure 6.12: SEM microphotograph of the attachment of the microorganism in the particle crushed using HPGR at 95bars pressure setting, cracks and micro-cracks as a nucleation site (a), attachment to the sub-surface of mineral grains shown by yellow arrows (b), patterns of microbial attachment on the particle surface (c), footprints of microbial attachment on the minerals surface (d).

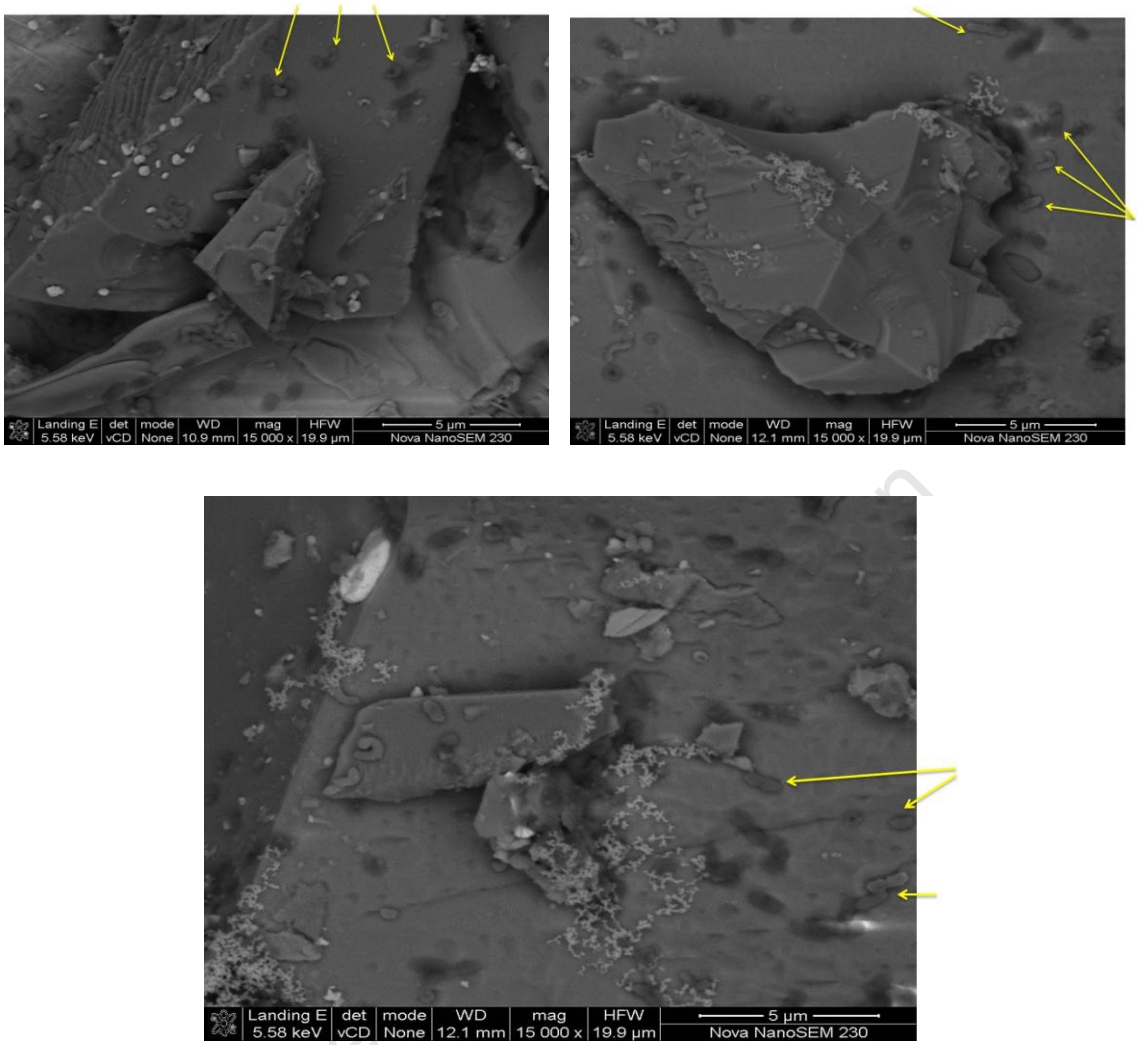

Figure 6.13: SEM microphotograph of the attachment of the microorganism in the different particles crushed using HPGR at 95bars pressure setting; bugs activities leave footprints on the minerals surface shown by yellow arrows.

6.5 Mineral conversion from single ore particles

The overall rate at which a mineral is dissolved from an ore particle is the manifestation of a complex network of individual phenomena, each proceeding at its own intrinsic rate. For finely ground particles, such as those encountered in tank leaching processes, leaching rates are typically controlled by the intrinsic kinetics of mineral breakdown. In heap or dump leaching, however, mineral grains are usually embedded within larger ore

particles or solution-filled agglomerates, and thus accessible only by diffusion through a network of the pores.

Many studies have been done to investigate mineral conversion during the leaching process (Braun *et al*., 1974; Bartlett, 1992; Davis and Ritchie, 1987; Roman, 1974; Shafer *et al*., 1979). Most studies in this regard are based on some key assumptions (particles are spherically symmetric, homogeneously porous environment in the gangue minerals, well distributed mineral grains within gangue matrix and so on), which is not necessarily a realistic image of the mineral physical structure of an ore. Most existing bulk scale models of the process that account for particle scale have been formulated based on these assumptions, and hence they are unlikely to give a real image of the underlying processes. This difficulty is more significant in heap and dump leaching, where ore particle sizes are relatively coarse. This issue has been discussed in detail in the literature review.

In this study, the progress of leaching was followed directly in selected particles from different size fractions using X-ray CT. The reactors were stopped from time to time to investigate the progress of leaching by analysing X-ray CT images of individual tagged particles each time. The results were further validated with those obtained using traditional techniques such as SEM/EDS and QEMSCAN on other particles taken from the same reactor. It should be kept in mind, however, that only few selected particles from each size fraction (eight particles for small, four for medium and two for large size fraction) were analysed using X-ray CT, and are hence not necessarily representative of the overall leach trends. To ensure that results from the analysis of the individual particles are representative, Zn conversions have been compiled from a succession of X-ray CT analyses. These data points are included in Figures 6.3 and 6.4 and can be seen to follow the overall solution leach curve in trend, but not necessarily in extent. Zn conversion data obtained from X-ray CT on the solid particles are lower and there is a kind of underestimate. The fact is that the calculation method when considering the individual particles is not explicit. It is by averaging the zinc grade diminution rate in the selected particles. It should be noted that during the leaching process, attenuation

coefficient of mineral phases would shift to low attenuation coefficient, and changed in the geometry or porosity may be the other causes. To investigate the progression of leaching on the inside of the individual particles, each single selected particle was divided into different shells based on the distance from the centre of particle, as illustrated in Figure 6.14. The concentrations of Zn grains were determined in each shell, each time the particle was analysed, thus allowing determination of the progression of Zn leaching with both time and distance from the surface.

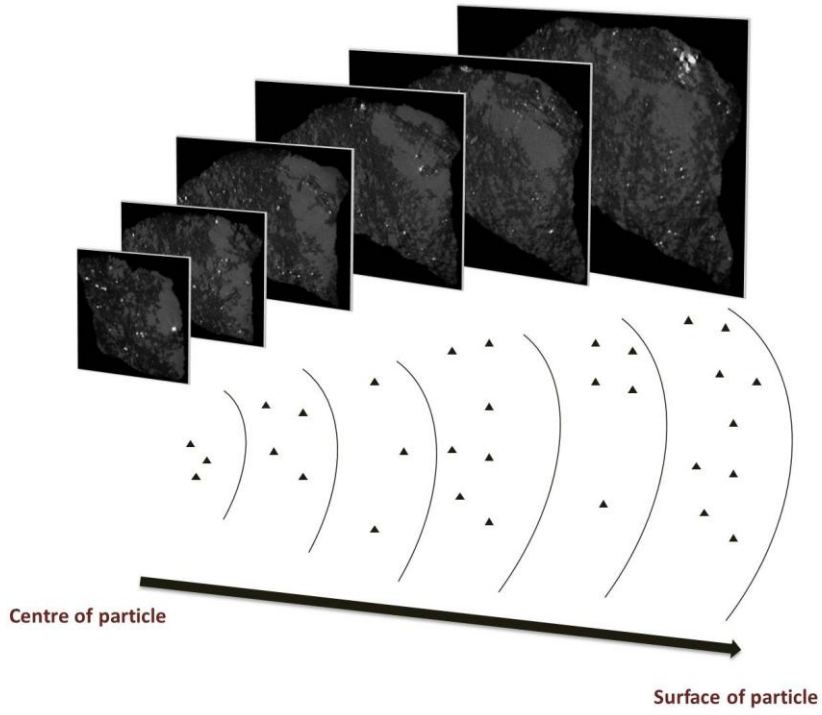

Figure 6.14: An illustration of the division of each single particle into different shells based on the distance from centre of the particle.

Using VGStudio MAX, each shell is defined as a Region of Interest (ROI) and due to the irregular shape of particles; the polygonal surface model tool was used to draw the boundary of each shell, following the shape of each particle. Defining thus the ROI in each, x, y and z, direction of the image and extracting it with the polygonal surface extraction tool provided by the software, allows analysis of each sub-zone as a separate

object in 3-D. Figure 6.15 shows the average Zn grain distribution and Zn grade within selected particles from each size fraction crushed by HPGR at 95bar.

Zn percentage in Figure 6.15 refers to mass percentage of Zn grains located in a given shell. Given that the volumes of the shells are not the same, but become smaller in the centre of the particles, similar percentages of Zn in each shell translate into different zinc grades (or concentrations). As can be seen, counter to a key assumption for using the shrinking core approach, the sphalerite mineral grains are not homogeneously distributed, but tend to be concentrated in the particle centre.

Figure 6.16 shows the average Zn conversion as a function of distance from the centre of the particle in the selected ore particles, produced by the two different comminution devices, and in different size fractions. This analysis clearly shows that leaching from large particles leads to approach complete conversion near the surface, but only partial conversion in the zones that are closer to the centre of particles. The innermost shells of the cone-crushed particles show hardly any conversion at all, especially in the larger particle sizes. After all minerals near the surface are depleted, the leaching front moves from the readily accessible grains on the particle surface to the more inaccessible grains within particles. It should be note that the bump regions for HPGR plots in Figure 6.16 is due to the crack network within the particles crushed using the HPGR, even grains located closer to the centre of a particle could dissolve earlier than those grains that are close to the surface but do not have access to it.

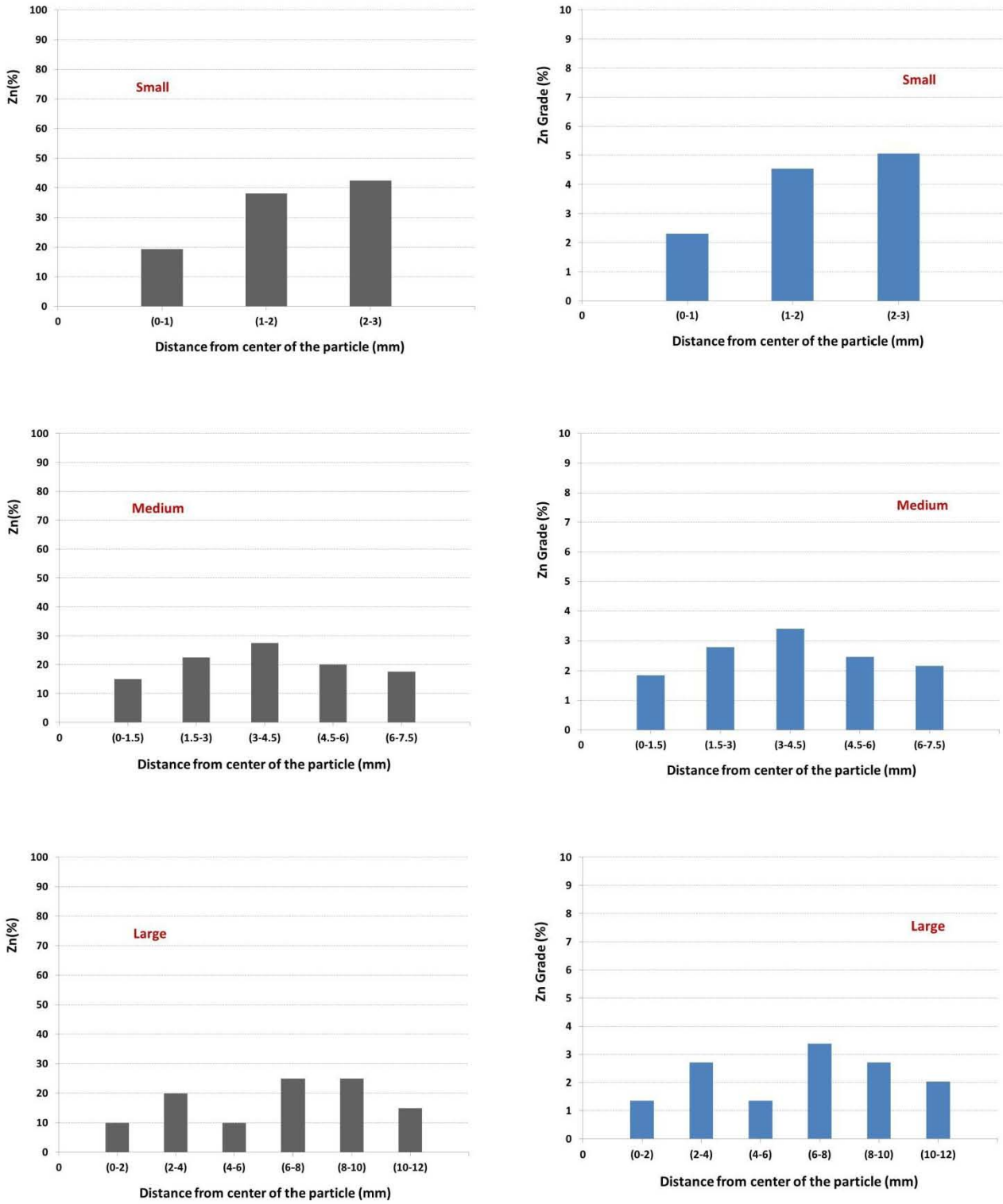

Figure 6.15: Average of Zn distribution (a), and average of Zn Grade (b), within selected particles from each size fraction crushed by HPGR-95bars prior to leaching.

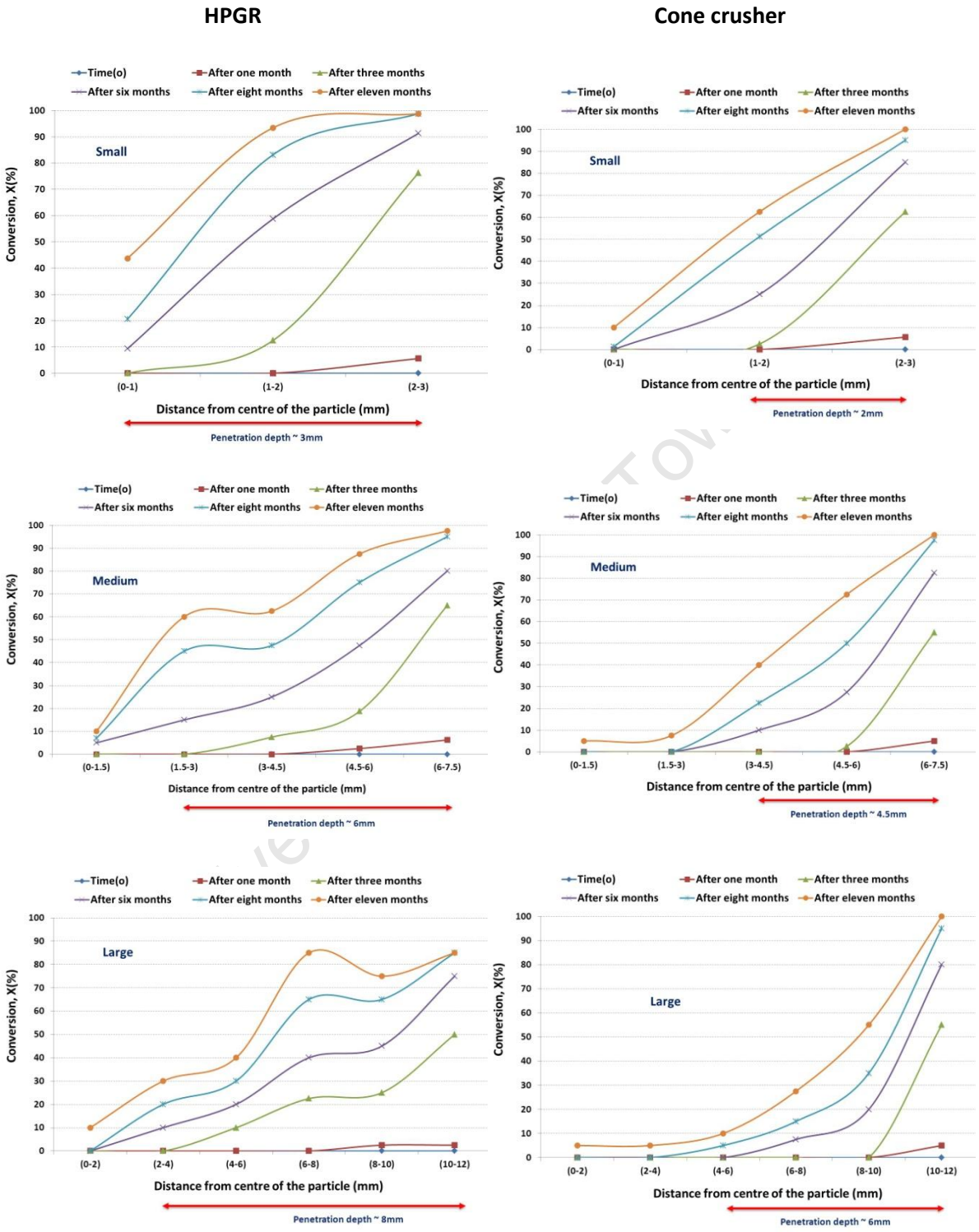

Figure 6.16: Comparison of the average conversion X (Zn) over time (from start of the experiment) from different position within the ore particle crushed by HPGR-95bars and cone crusher in different size fractions. Note the deeper penetration in the particle prepared by HPGR.

6.5.1 Crack density and grain exposure

The solid/liquid contact area, which in low-porosity rocks is mainly a function of the particle size of the material, is a major factor in determining the kinetics of the leaching reactions. Typical to leaching processes is their selectivity with respect to certain minerals or groups of minerals. Leaching reagents are also able to penetrate into microfissures and micropores of the rock mass, thus reducing the need for energy consuming crushing and grinding operations. The optimization of a leaching process thus requires quantitative information on the effect of grain size, as well as on the propagation of the leaching effect inside the mineral grains (Ahonen and Tuovinen 1995).

The rate of reaction of a particle with a reagent in a fluid phase in which it is immersed, such as the reaction environment of the leach reactors in this research, is usually controlled either by molecular diffusion through a boundary layer extending into the fluid or by the reaction at the surface. If the particle contains cracks or holes, which are open to the fluid, the reagent diffuses into the interior of the particle and reacts there. Under steady state conditions, the rates of diffusion and reaction are the same, and this state is maintained by a concentration gradient of the reagent within the holes.

If the chemical reaction is slow, the concentration gradient from bulk into pores is shallow throughout. Under these circumstances, the reaction proceeds on the walls of pore channels at virtually the same rate as on the external surfaces. In other words, the area over which reaction takes place is not the external area but the total area, including that of all open pores (Cariaga *et al*., 2005). As it is not unusual for the internal area to be far greater than the external area, the porosity becomes a dominant factor (Bachu and Cuthiell, 1990; Deschamps *et al*., 2008).

If the chemical reaction at the surface is fast, the concentration gradient is steep and reagent is consumed before it penetrates into the particle. Under these circumstances,

the internal surfaces play no part, and particle size is the important factor as with non-porous particles (Cariaga *et al*., 2005).

As it discussed in the chapter 4, the mineral grains can be classified, according to their accessibility to leach solutions, into different classes. The special mineral grain distribution and their accessibility to leach solutions by cracks and pores, plays a key role in the rate of extraction. Figure 6.17a shows an image of a selected cross-section of one of the labelled large sphalerite ore particles crushed using HPGR-95bar with the grain exposed to the leach solutions at the surface. The same plane after treatment shows that the grains near the surface are largely depleted (Figure 6.17b). Grains exposed to the leach solutions via pores or cracks (yellow colour) (Figure 6.17c, d) also contribute to the rate, in the early stages of leaching.

Figure 6.18 shows an image of the cross-section of one of the labelled large sphalerite ore particles crushed using HPGR at 95bars with the grain exposed to the leach solutions via pores or cracks. Accessibility to leach solutions by cracks accelerates the dissolution of the mineral grains, although they are inside the ore particle.

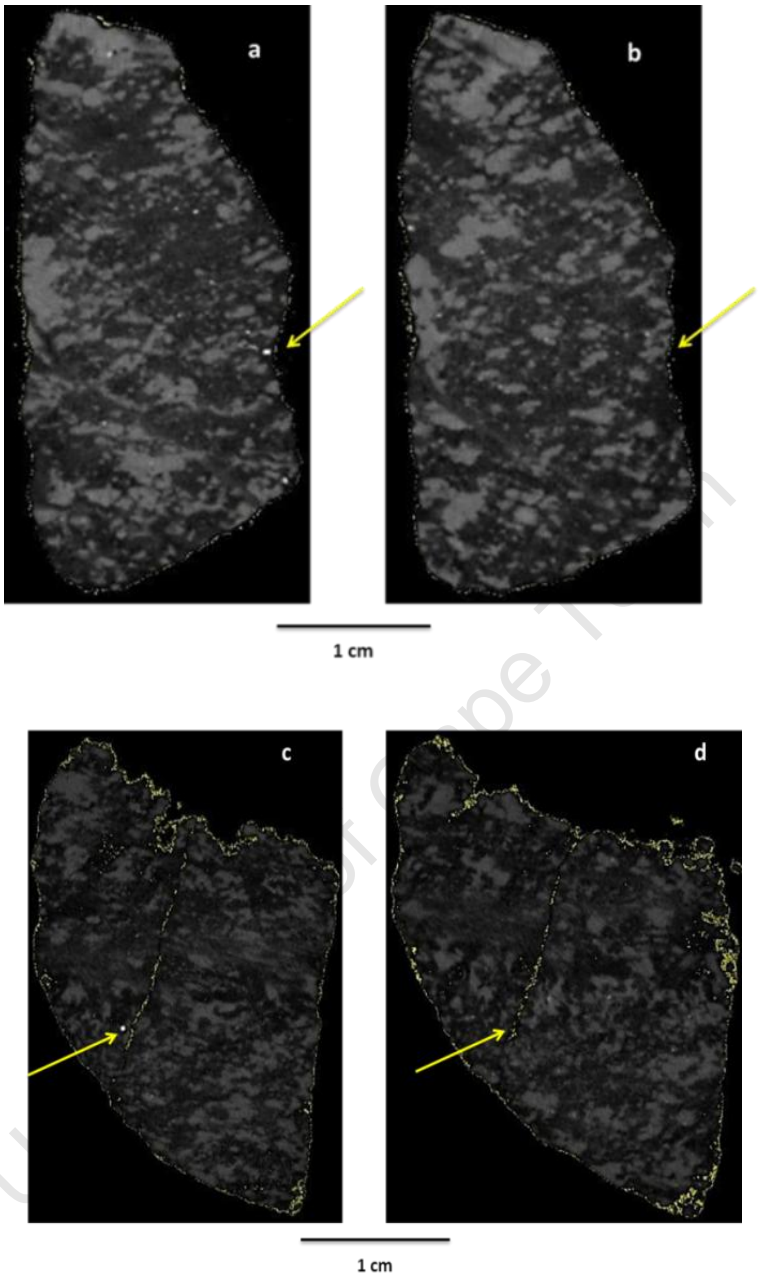

Figure 6.17: Plane images of a single large sphalerite ore particle crushed using HPGR-95 bars, a. grain exposed to the leach solutions at the surface before treatment, b. same plane after treatment, c. grain exposed to the leach solutions via pores or cracks before treatment, d. same plane after treatment.

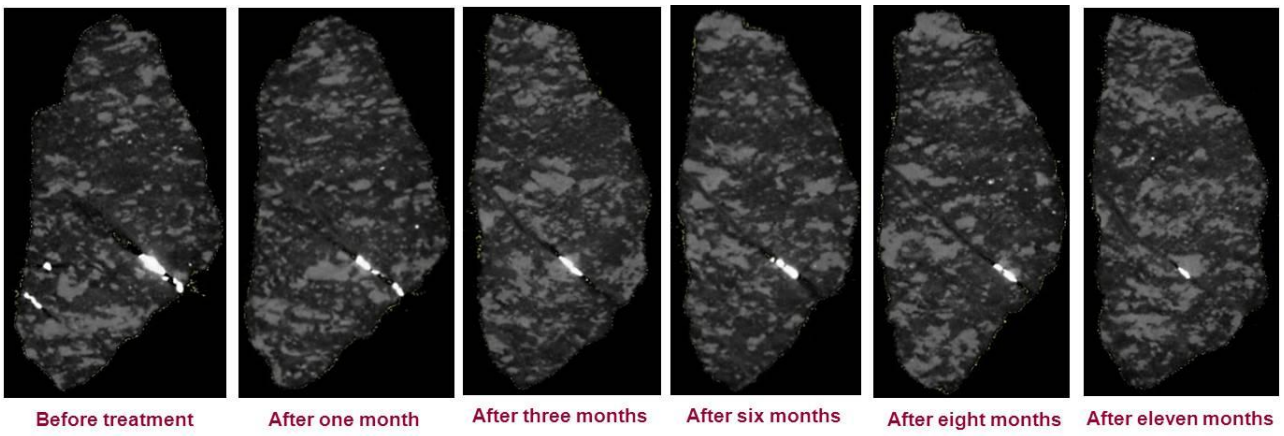

Figure 6.18: Plane images of a sphalerite grain within a single large ore particle crushed using HPGR-95 bar and its accessibility to leach solutions by cracks and pores.

The crack network in the particles crushed by HPGR appeared to increase during the leaching process (Figure 6.19a). This accelerates reagent diffusion into the particles resulting in more metal extraction. However, no significant change was observed in the crack network for the particles crushed using the cone crusher (Figure 6.19b).

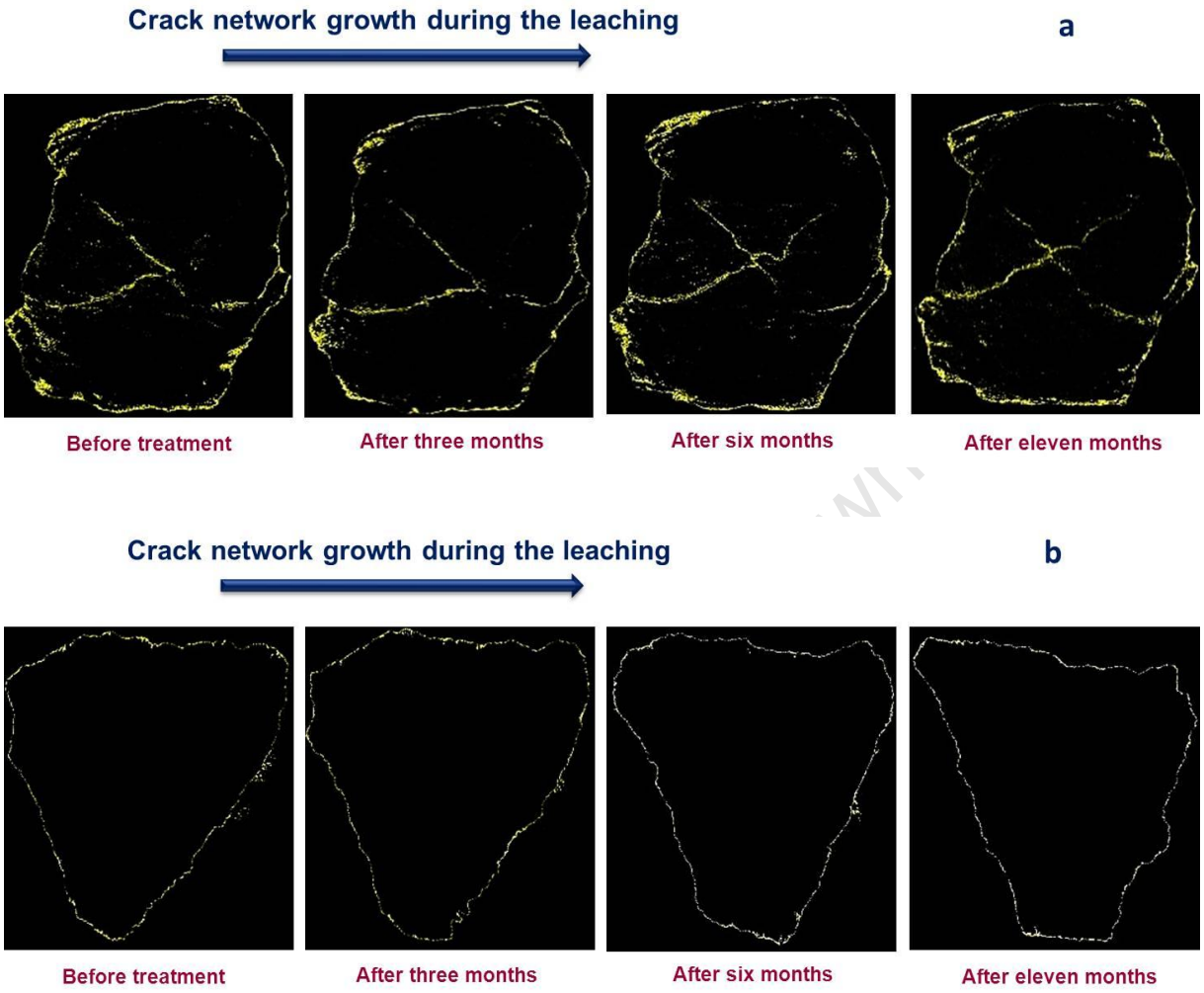

Figure 6.19: Crack network growth during the leaching, a. for the particles crushed by HPGR, b. for the particles crushed by cone crusher.

As previously discussed (see chapter 5), particle characterisation consistently identifies the prevalence of the micro-cracks and higher porosity for particles prepared by compression breakage (HPGR) as compared to conventional crushing by impact breakage .

6.5.2 Crack depth and surface zone

The higher crack density in the particles crushed by HPGR compared to those produced by the cone crusher provides a bigger initial surface zone for reaction. In the HPGR product, the reaction zone covers both the particle surface and subsurface zone, which has access to the surface through cracks. In some particles, even grains close to the centre of the particles can dissolve early if they are connected to particularly deep cracks, such as shown in Figure 6.16. In the case of the cone crusher product, the outer surface of the particle is the main reaction surface and reaction occurs in the subsurface zones to not nearly the same depth as the particles crushed by HPGR. This implies the existence of micro-cracks in these particles, which are not detectable by the visual techniques used here.

Reaction at the surface of particles leads to partial conversion in the coarse particles. After this initially rapid phase, leaching slows down dramatically. This is explained by the fact that after depletion of the easy-to-leach surface minerals, ferric iron or acid has to migrate deeper into the particles via the pore network, and the reduced ferrous form has to return to the surface to be re-oxidised by microorganisms.

Leaching of minerals from whole ore particles, where the key reagent has to migrate from the particle surface, will result in a rim-leaching effect in larger particles. All minerals near the surface are depleted first before the leach front can migrate further into the particle. On the inside of the particle, the rate is controlled by the rate at which ferric iron diffuses into the particle.

Figure 6.16 clearly shows that HPGR-crushed ore leached more rapidly than cone-crushed ore in all particle size classes and to slightly greater depth. 10 percent metal extraction was the criterion for penetration depth. The distance from the particle surface up to the shale where the metal extraction was more than 10%, was considered as penetration depth. Table 6.1 shows the penetration depth (Pd) from Figure 6.16 and average crack depth from the surface of the selected particles of different size fraction

as a function of the crushing device. The crack depth was calculated from analysing the initial X-ray CT images of the particles using the VGStudio Max 2.1 image analysis software. For small size fraction eight particles for medium size fraction four particles and for the large size fraction, two particles were analysed to calculate crack depth.

Table 6.1: The penetration depth (P_d) and average crack depth of the selected particles after crushing in different size fraction (Nd denotes not detected).

Size fraction (mm)	Mean R	Average crack depth (mm)		Penetration depth (P_d) (mm)	
		cone crusher	HPGR	cone crusher	HPGR
Small (-6.75+5.25)	3	Nd	1.08	2	3
Medium (-16+14)	7.5	Nd	3.43	4.5	6
Large (-25+23)	12	Nd	6.35	6	8

It is interesting to note that measured crack and inferred penetration depths for HPGR consistently differ to the order of around 2mm. This is an indication that cracks detectable by X-ray CT are generally larger than those needed for reagent penetration during leaching. It is therefore safe to say that also cone-crushed particles exhibit a network of micro-pores near the surface, even though they are not detectable by X-ray CT. By extension, it is likely that also HPGR crushed particles have a network of such micro-pores deep inside the particles extending beyond the rim of larger pores detectable by X-ray CT.

Furthermore, the results presented in Figure 6.16 indicate that the penetration depth (P_d) is as function of both the comminution mode and the particle size/radius (R). It is clear that prevalence of cracks and particle porosity play key roles in increasing the penetration depth, and as these characteristics are more pronounced in HPGR-crushed particles, the conversion front clearly penetrates more deeply in these.

As can be seen from the trend line equations, the correlation between the penetration depth (P_d) and particle radius (R) is a power law as per Eq. (6.1):

$$p_d = aR^b \qquad \text{Eq. (6.1)}$$

With b=0.7-0.8 more or less the same for the products of the two different comminution devices and the only difference is the value of a, which is 1.4 for the particles crushed using HPGR and 0.8 for particles crushed using cone crusher. The exponential relationship could be related to the mechanics of the crack propagation, with the exponent b as a material related parameter (since it is more or less the same for both sets) and the parameter a, which is related to the comminution mode.

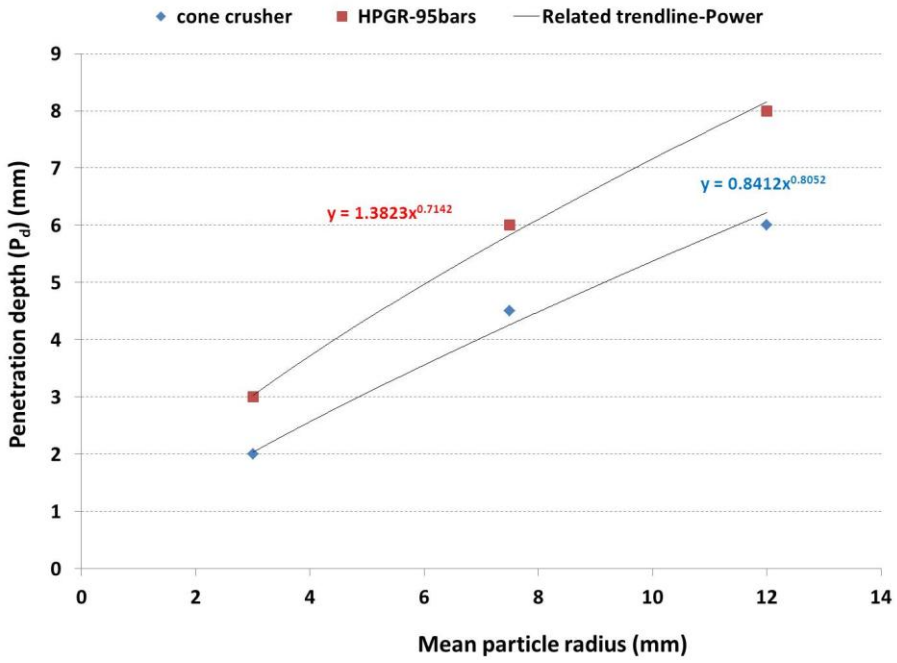

Figure 6.20: The penetration depth (P_d) vs. mean particle radius in the HPGR-95 bars and cone crusher product.

6.5.3 Fitting data with models

6.5.3.1 Shrinking Core Model

The data shown in this section focuses only on the active bioleaching phase and does not consider the first 50 days of treatment, (30 days of chemical leaching and 20 days for adaptation of microorganisms after inoculation). Figure 6.21 shows the application of the diffusion controlled shrinking core model $(1-2/3X-(1-X)^{2/3}$ vs. t) and surface reaction controlled shrinking sphere model $(1-(1-X)^{1/3}$ vs. t) to the leaching of zinc in the leach liquors from the different reactors. The results clearly show that leaching from large particles – contrary to the common assumption – does not follow either of the two models.

In fact, there are three different stages during the leaching process. The first stage is leaching of grains at the surface of the ore particles followed by a second stage, which is leaching of the grains located in the subsurface within the thickness of the penetration depth. The curves in Figure 6.21 indicate a clear inflection point after which the slope changes. This point lies between days 120 and 150, independent of size and comminution method. It is postulated that this point relates to the depletion of mineral grains on the surface of particles, thereafter penetration of reagent (Figure 6.22a) dissolves grains which are located in the shallow surface layer (particles crushed using cone crusher) and surface layer with a bigger penetration depth (particles crushed using HPGR).

In the cracked rim, there is a rapid penetration of leaching reagent through the crack network, but slow leaching from zones between cracks, , which explains why the profiles in the Figure 6.16 are quite flat, especially in the particles crushed using HPGR. The particles in all size fractions crushed using HPGR have a higher specific surface area (per unit mass of particles) and relatively bigger penetration depth, resulting in the dissolution of a larger number of grains during the first stage and higher total Zn extraction at the end of this stage (see Figures 6.3 and 6.4).

This second stage is a combination of diffusion and reaction, which proceeds up to a certain penetration depth, thereafter a much slower mechanism governs leaching from the deeper core. In fact, this transition point is the beginning of a third stage where the overall leaching rate decreases dramatically until there is an almost linear relationship between conversion of the target mineral grains and time. This is shown schematically in Figure 6.22b. It should be noted that there is not enough data for this third phase leaching from the core of the particles to decide what mechanism this follows. The trend in Figures 6.3 and 6.4 indicate the last stage of leaching can be approximated as linear. Given the time-scale of heap leaching, a linear model to describe this residual leaching is acceptable.

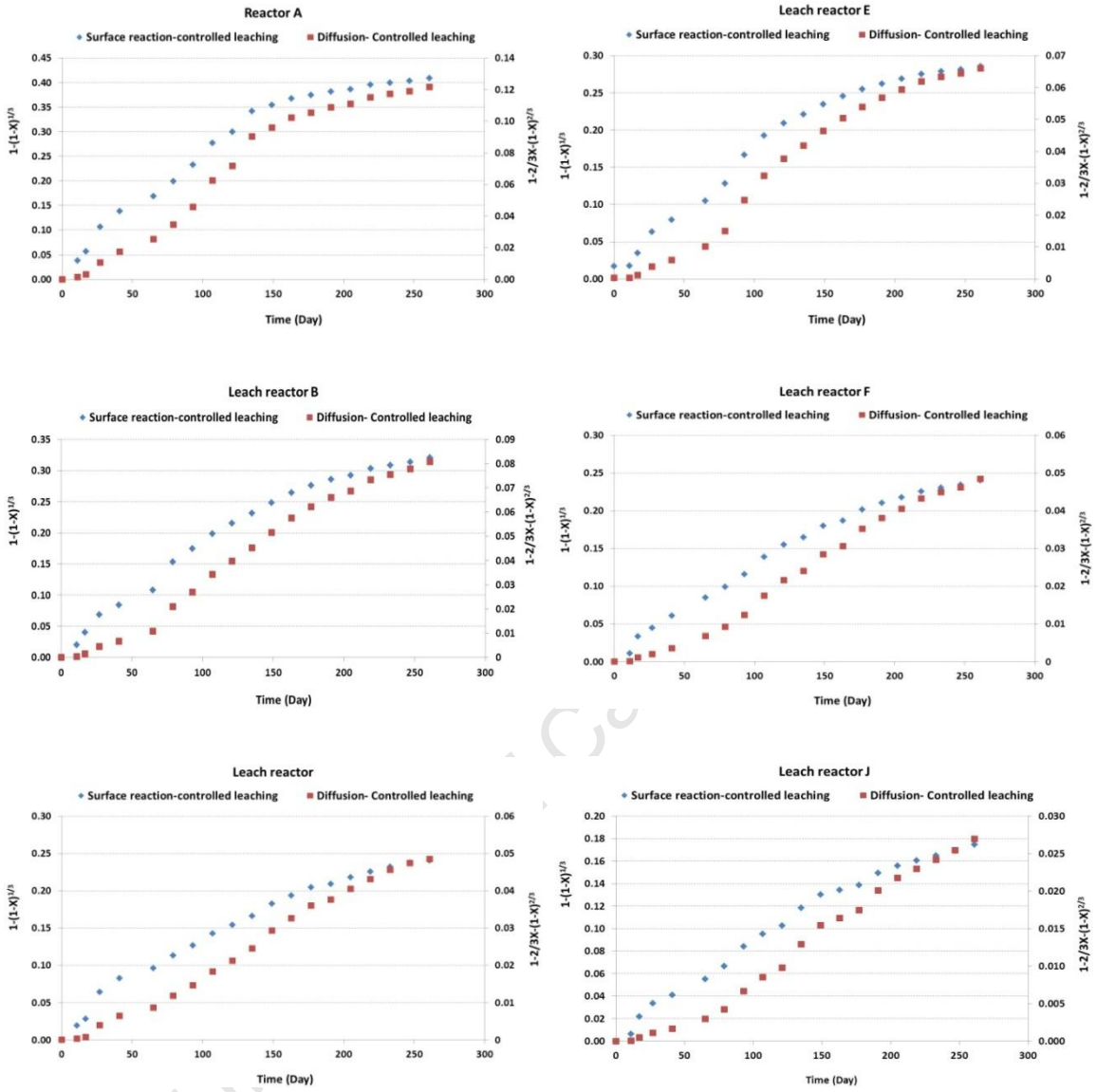

Figure 6.21: Application of the shrinking core model and shrinking sphere model to the leaching of zinc in the leach liquors from the reactors A (HPGR-95bars-Small size fraction), E (cone crusher-Small size fraction), B (HPGR-95bars-Medium size fraction), F (cone crusher-Medium size fraction), C (HPGR-95bars-large size fraction) and J (cone crusher-large size fraction).

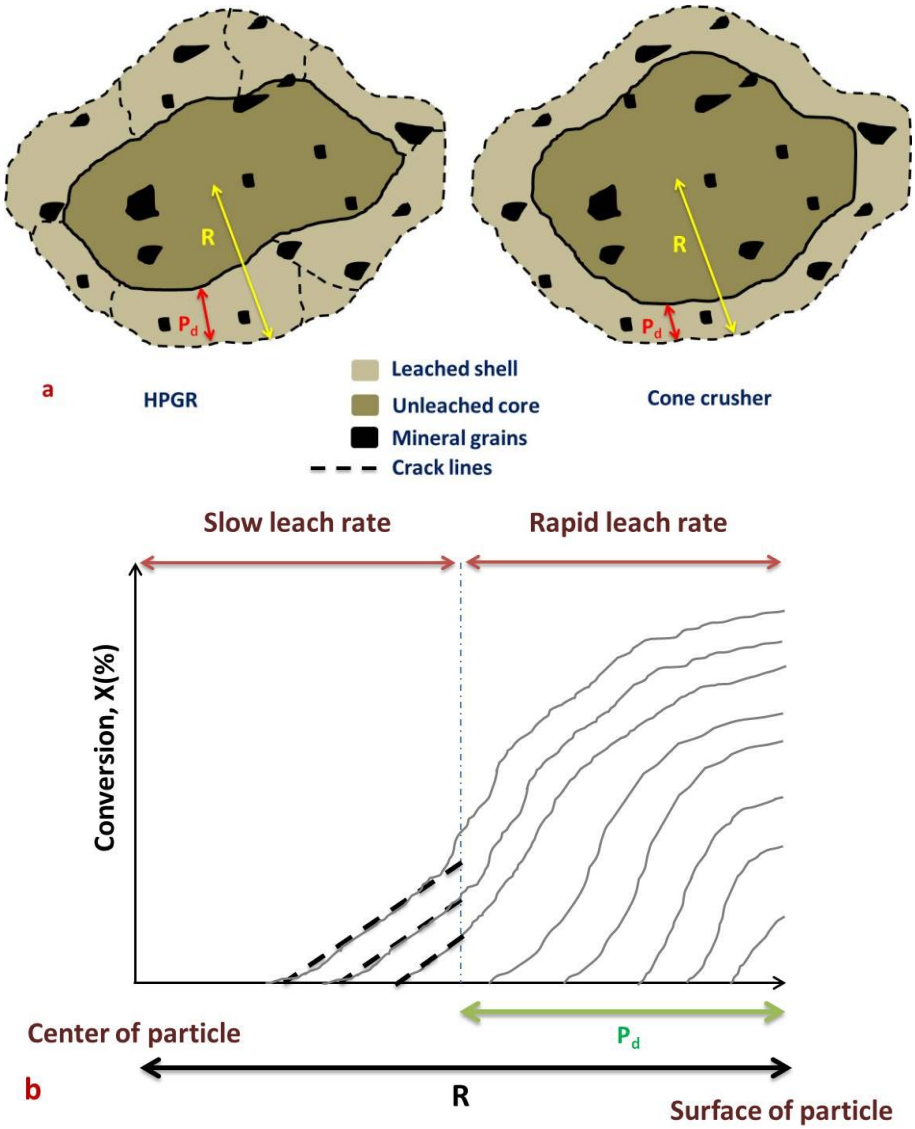

Figure 6.22: Schematic cross section of a large particle, a. partially leached particle with the effective penetration depth (P_d), b. two different leach regime.

6.5.3.2 Reaction-diffusion Model

As discussed, the second stage of the leaching process is a combination of diffusion and reaction. Modelling a simplified reaction-diffusion system in spherical coordinates and how the predicted trends fit with experiments data will be discussed here. For this, consider a porous, structurally uniform, spherical ore particle of radius R which is

submerged in a lixiviant solution, and which contains small amounts of solid reactant evenly distributed along the pore walls. The solid reactant ($B_{(s)}$), is dissolved by a single reagent ($A_{(aq)}$) according to the formula (6.2):

$$A_{(aq)} + B_{(s)} \rightarrow dissolved\ products \qquad \text{Eq. (6.2)}$$

Since every reaction within the particle involves the consumption of reagent A, under these conditions, the transient simultaneous diffusion-reaction of species A through a spherical domain is described by

$$D_{Ae}\left[\frac{\partial^2 C_A}{\partial r^2} + \frac{2}{r}\frac{\partial C_B}{\partial r}\right] + S_A = \frac{\partial C_A}{\partial t} \qquad \text{Eq. (6.3)}$$

where D_{Ae} is the effective diffusivity of reagent A within the particle pores. It should be noted that C_A is the volumetric concentration of reagent A in solution and C_B is the volumetric concentration of the solid B in the particle. To convert to a mass concentration, the mean particle density needs to be introduced, but this is ignored here for simplicity of the discussion. For the source term SA, the reaction of solute A with solid B is assumed to follow simple first order kinetics in terms of both A and B, i.e.

$$S_A = \left(\frac{1-\varepsilon}{\varepsilon}\right)\frac{dC_B}{dt} = -kC_A C_B \qquad \text{Eq. (6.4)}$$

Where k is the corresponding rate constant and ε represents the porosity of the solid particle. With the following boundary conditions:

$$r = 0:\ N_A = -D_{Ae}\frac{\partial C_A}{\partial r}\Big|_{r=0} = 0 \qquad \text{Eq. (6.5)}$$

$$r = R: N_A = -D_{Ae}\frac{\partial C_A}{\partial r}\Big|_{r=R} = k_C(C_{AR} - C_{Ab}) \qquad \text{Eq. (6.6)}$$

where k_C is the corresponding rate constant, C_{AR} is the concentration of the reagent A at the particle radius R and C_{Ab} is the concentration of the reagent A in the bulk solution external to the particles. This can be discretised by dividing the r-axis of the sphere into a number (N) of equal spaced intervals Δr, with the centre becoming node 0 and the surface (at r=R) node N. Then, for all internal nodes 0 < n < N:

$$D_{Ae}\left[\frac{C_A^{n+1}-2C_A^n+C_A^{n-1}}{\Delta r^2}+\frac{2}{n\Delta r}\,\frac{C_A^{n+1}-C_A^{n-1}}{2\Delta r}\right]-kC_A^nC_B^n=\frac{C_A^{n,t+\Delta t}-C_A^{n,t}}{\Delta t} \qquad \text{Eq. (6.7)}$$

And for the boundaries:

$$n=0: \quad D_{Ae}\frac{6}{\Delta r^2}(C_A^1-C_A^0)-kC_A^0C_B^0=\frac{C_A^{0,t+\Delta t}-C_A^{0,t}}{\Delta t} \qquad \text{Eq. (6.8)}$$

It should be noted that the derivation of this equation is in fact based on a finite volume approach applied to the centre of the particle.

$$n=N: \quad D_{Ae}\frac{3C_A^N-4C_A^{N-1}+C_A^{N-2}}{2\Delta r}=k_c(C_{Ab}-C_A^N) \qquad \text{Eq. (6.9)}$$

This assumes that there is a convective mass transfer resistance at the surface of the particles, which can be determined from relevant Sherwood number correlations (as function of fluid properties and pore velocities in a packed bed). If the external mass transfer can be assumed not to be limiting, a sufficiently large value for k_c is chosen. For the concentration of solid species B, we need to determine at each node n= 0…N-1:

$$-\mathrm{k}C_A^nC_B^n=\frac{1-\varepsilon}{\varepsilon}\,\frac{C_B^{n,t+\Delta t}-C_B^{n,t}}{\Delta t} \qquad \text{Eq. (6.10)}$$

The unsteady state problem is solved starting with an arbitrary initial condition (usually all $C_A^n = 0$; $C_B^n = C_B^{ini}$) and recalculating each set of equations for each node. In the present case, this was done on an Excel spread sheet. It is important to note that, in order to ensure numerical stability Δt must be chosen such that:

$$\frac{D_{Ae}}{\Delta r^2}<0.5 \qquad \text{Eq. (6.11)}$$

Figure 6.23 shows the simulated conversion X (Zn) over time from different position within the ore particle in different size fractions using Eq. (6.10) and Table 6.2 summarizes the parameters involved.

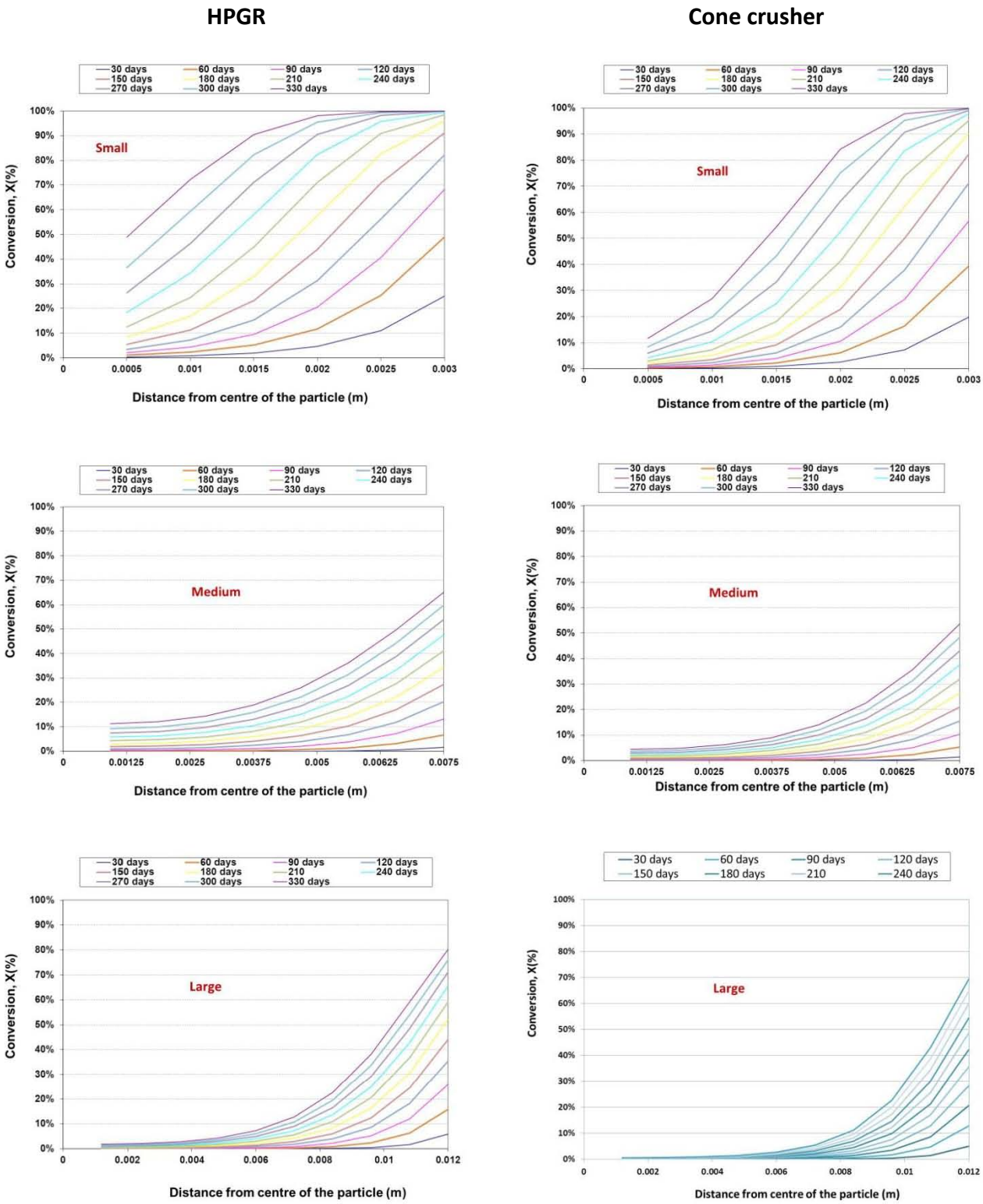

Figure 6.23: The simulated conversion X (Zn) over time from different position within the ore particle crushed by HPGR-95bars and cone crusher in different size fractions using the1st order particle diffusion-reaction model.

Table 6.2: Parameters values used in Figure 6.22.

Parameters	HPGR			Cone crusher		
	Small	Medium	Large	Small	Medium	Large
$D_{Ae}(m^2/s)$	10^{-10}	10^{-10}	10^{-10}	10^{-10}	10^{-10}	10^{-10}
N	6	8	10	6	8	10
$K(s^{-1})$	10^{-4}	10^{-5}	10^{-5}	10^{-4}	10^{-5}	10^{-5}
R (m)	0.003	0.0075	0.012	0.003	0.0075	0.012
C_B^{ini} (mol B/g ore)	4	4	4	6	6	6
C_{Ab} (mol A/cm^3)	100	100	100	100	100	100
ε	0.01	0.018	0.01	0.01	0.018	0.018
Da	0.11	0.18	0.07	0.11	0.18	0.07

Figure 6.24 shows comparison of the measured conversion X (Zn) and simulated conversion X (Zn) over time from leach reactor A (HPGR-95bars-small size fraction) and leach reactor J (cone crusher-large size fraction). As it can be seen, there is a good agreement between the trends predicted by the first order particle diffusion-reaction model and the average conversion X (Zn) over time from different position within the ore particle evaluated with the X-ray CT. Any deviation would be due to the fact that this simulated model is based on the certain over-simplified assumptions, such as homogeneous porosity, structurally uniform, spherical ore particle, and it ignores the inner core into which crack do not penetrate.

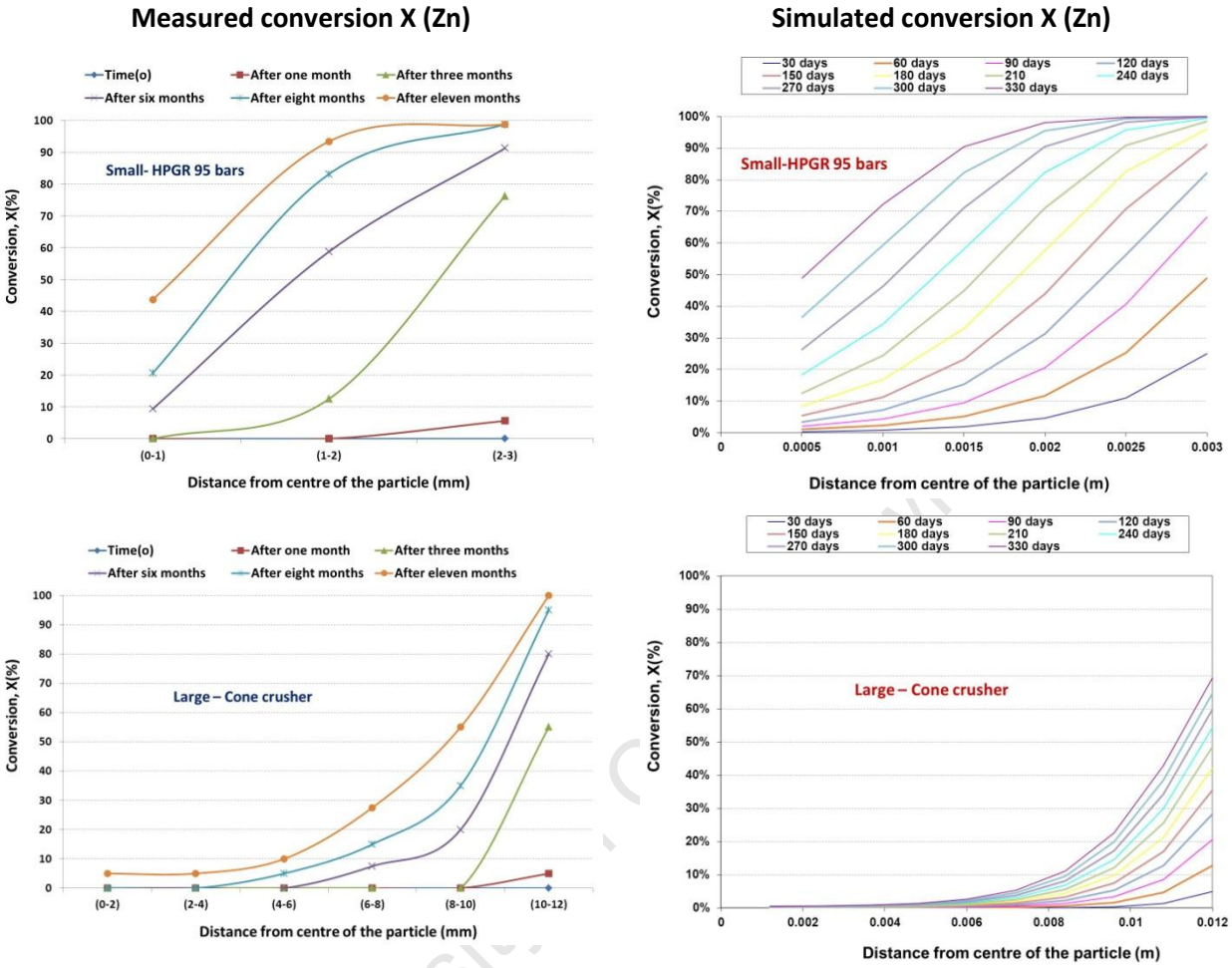

Figure 6.24: Comparison of the measured conversion X (Zn) and simulated conversion X (Zn) over time from leach reactor A (HPGR-95bars-small size fraction) and leach reactor J (cone crusher-large size fraction).

Figure 6.25 shows the simulated solution concentrations of reagent A over time from different position within the ore particle crushed by HPGR-95bars and cone crusher in different size fractions. As can be seen the trend is similar to the simulated conversion X (Zn) over time, but it is important to note that concentration profiles in the medium and small size fractions are flat towards the centre indicating that this system is more mixed reaction-diffusion controlled than purely diffusion controlled as is the common assumption. The Damkohler numbers (Da) calculated for these model systems confirm this. As given in the Table 6.2 if Da>10, the system is reaction controlled, for Da<0.1 it is diffusion controlled and it is mixed reaction-diffusion controlled if 0.1 <Da<10.

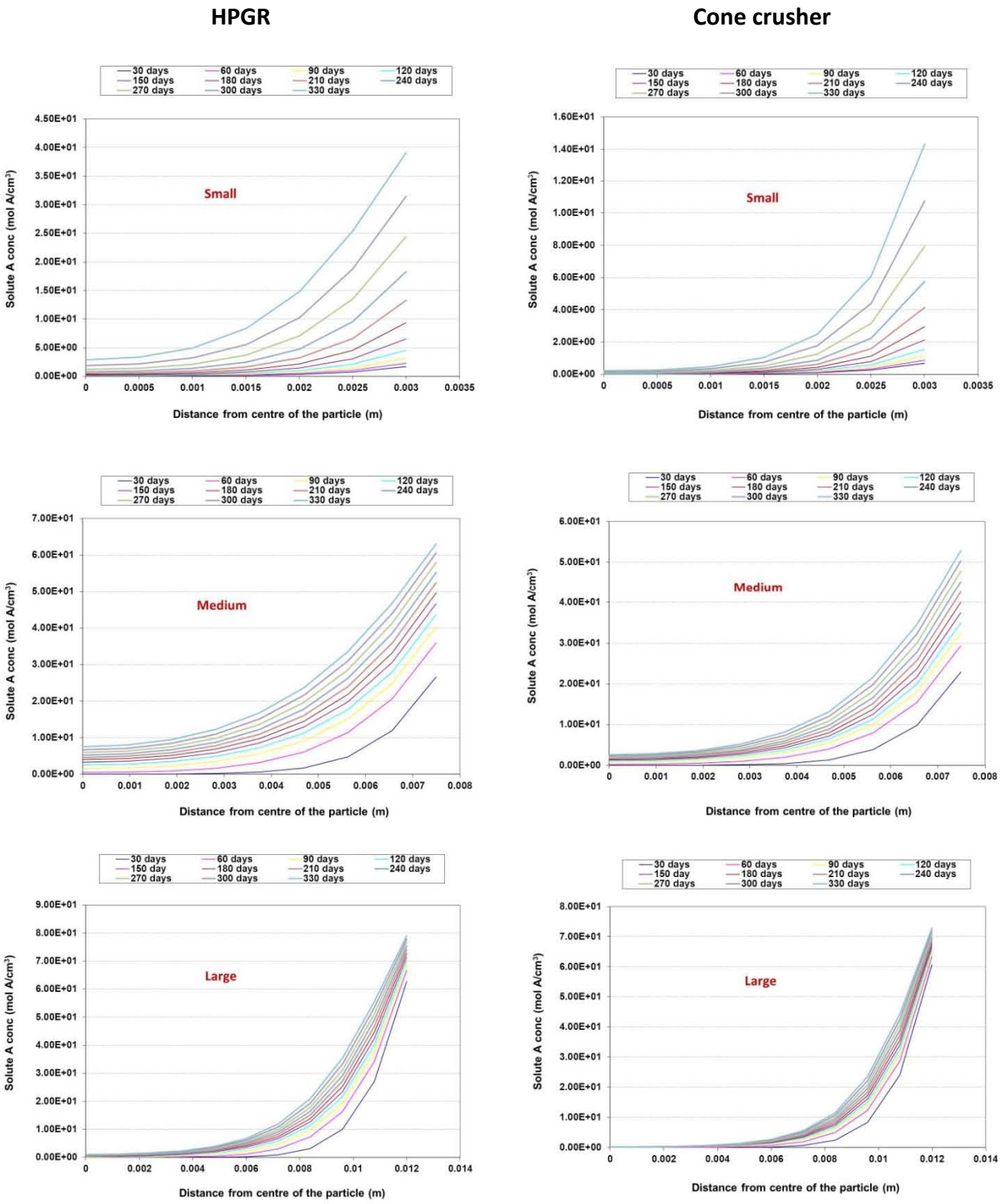

Figure 6.25: The simulated solution concentrations of A over time from different position within the ore particle crushed by HPGR-95bars and cone crusher in different size fractions using the1st order particle diffusion-reaction model.

6.5.3.3 K- φ Model

Although the explicit diffusion-reaction model can capture the key reaction trends reasonably well, it is for modelling purposes somewhat cumbersome, as it would require solution of the set of equations (6.7) to (6.10) for all particle size classes at each time step. As a simplification, the intrinsic kinetics of leaching can generally be described by a rate expression of the following form (Bouffard, 2003; Bouffard and Dixon, 2001):

$$\frac{dx}{dt} = k(T).f(c_i).w(1-X) \qquad \text{Eq. (6.12)}$$

where k (T,d_0) is a rate constant, which is a function of temperature (*i.e.*, Arrhenius's law) and initial mineral grain size (or surface area), $f(C)$ is a function of solution composition and can be more complex, ranging from the concentration of a single reagent, such as acid in the case of oxide dissolution, to a complex function of the concentrations and/or concentration ratios of several reagents, such as ferric and ferrous in the case of sulfide oxidation. w (1–X) is a function of the fraction of unreacted mineral, which represents the changing topology of the mineral surface over the course of leaching. Often, for finely ground particles, w (1–X) conforms to some well-known form, such as the shrinking sphere or shrinking core model. A simple general form for the topological rate term can be given as follows (Bouffard, 2003):

$$w(1-X) = k(1-X)^{\varphi} \qquad \text{Eq. (6.13)}$$

where φ is equal to or greater than 2/3 (the shrinking sphere model) and may be as high as 3 when the distribution of effective grain size is particularly wide. For each particle size fraction, Eq. (6.12) can be written as the following equation, assuming temperature, particle size and chemical condition are all fixed.

$$\frac{dx}{dt} = K(1-X)^{\varphi} \qquad \text{Eq. (6.14)}$$

Eq. (6.14) can be integrated to yield:

$Kt = \frac{(1-X)^{1-\varphi}-1}{\varphi-1}$ $\varphi \neq 1$ or

$$X(t) = 1 - (1 + K(\varphi - 1)t)^{\frac{1}{1-\varphi}} \quad \varphi \neq 1; \; t_{lim} = \frac{1}{K(1-\varphi)} \text{ if } \varphi < 1 \qquad \text{Eq. (6.15)}$$

If φ < 1, the function X(t) will reach the value 1 after a finite time, t_{lim}, as indicated. For any values of t larger than this limiting time, X(t) = 1, and the function defined above is no longer valid. For φ > 1, X(t) = 1 for t → ∞.

Table 6.3 shows K and ϕ values obtained by minimisation of mean squared error (MSE) using Eq. (6.15), for the selected particles from different size fractions crushed using HPGR-95 bars and cone crusher. Leach reactors and modelling data using K-ϕ model have been given in the appendix VII.

Table 6.3: Obtained K and **φ** values for leach reactors from different size fractions crushed using HPGR-95 bars and cone crusher.

Size fraction (mm)	K (day^{-1})		φ	
	HPGR	cone crusher	HPGR	cone crusher
Small (-6.75+5.25)	0.012	0.007	1.59	1.88
Medium (-16+14)	0.007	0.005	1.65	2.00
Large (-25+23)	0.006	0.003	2.45	2.15

As given in Table 6.3, in both comminution devices the value for K decreases with increasing particle size. This was expected; since K represents the initial (surface) rate and with increasing particle sizes the specific surface area declines. In all three sizes classes for those particles that were crushed using HPGR, the value of K is bigger than that crushed using a cone crusher, which indicates the larger effective initial surface in the particles crushed using HPGR. Figure 6.26 shows the relationship between K and

mean particle radius (R). According to the trend lines, the correlation between K and particle radius (R) can be represented by a power law as per Eq. (6.16):

$$K = \mathrm{c}\mathrm{R}^{\mathrm{d}} \qquad \text{Eq. (6.16)}$$

With d≈(-0.5) almost the same for the products of the two different comminution devices, the only difference is the value of c, which is 0.021 for the particles crushed using HPGR and 0.014 for particles crushed using a cone crusher. The difference in the K values is due to specific surface area in different size fraction and product of different comminution devices. In this context, it is interesting to note that the ratios of values of a in Eq. (6.1) ($a_{HPGR}/a_{cone\ cerusher}$ = 1.6) and those for the values c in Eq. (6.16) ($c_{HPGR}/c_{cone\ cerusher}$ = 1.5) compare closely, suggesting that the rate parameter K is indeed closely linked to the crack network created by the different comminution devices.

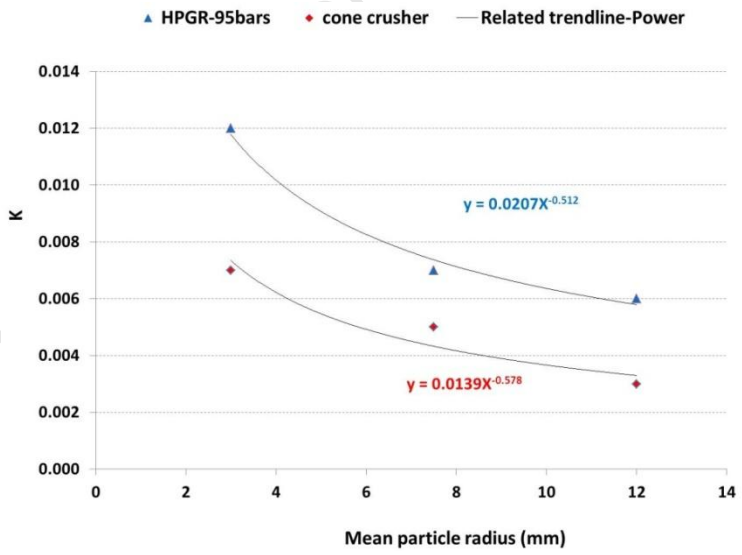

Figure 6.26: Relationship between K and mean particle radius.

Figure 6.27 shows a comparison of the conversion X (Zn) for the leach reactors vs. time for experimental data and the fitted curve obtained for K and φ values from different size fractions.

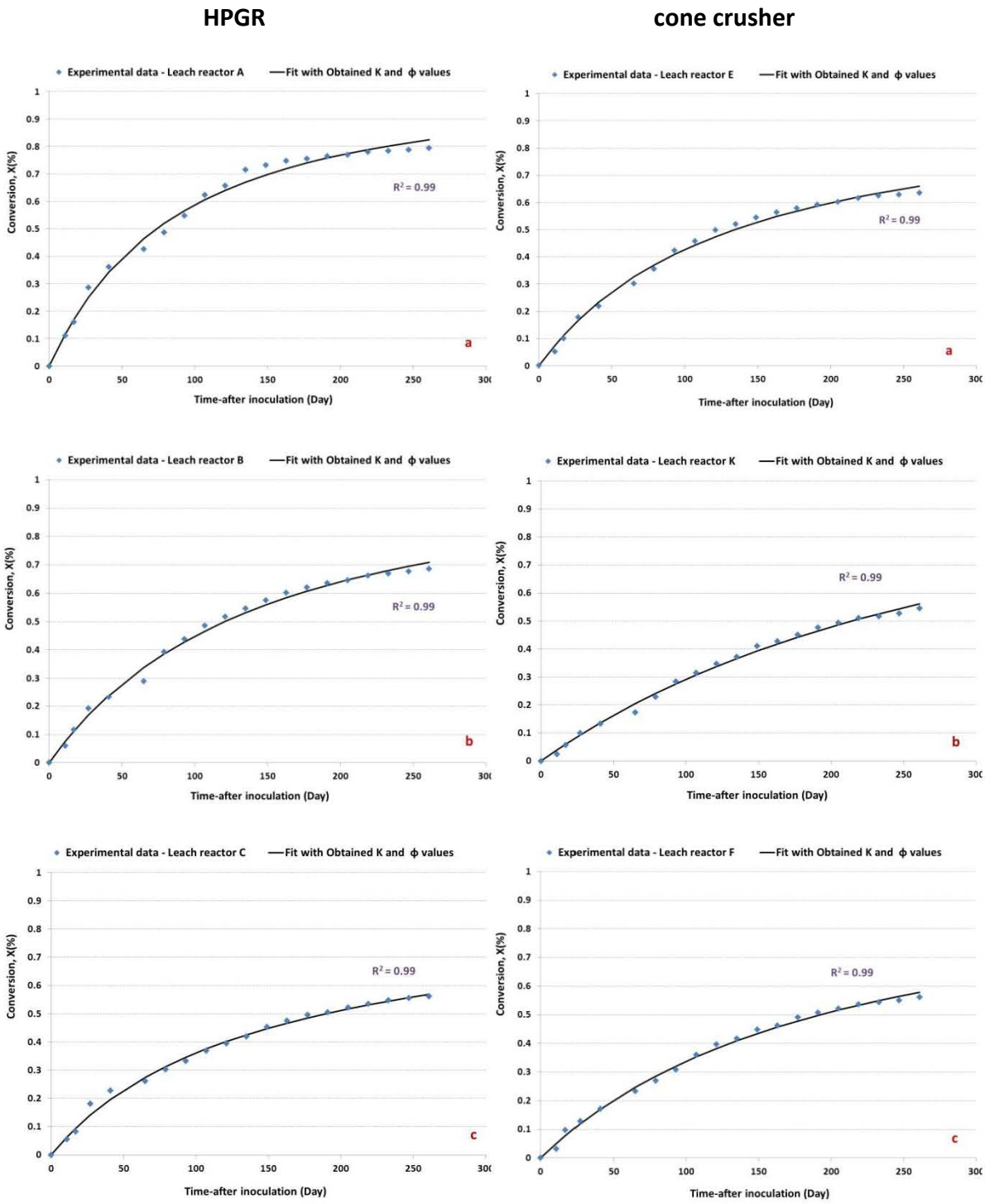

Figure 6.27: Comparison of the conversion X (Zn) vs. time for experimental data and fit curve for obtained K and φ values for leach reactors from different size fractions crushed using HPGR-95bars and cone crusher (a. Small, b Medium and c. Large).

6.5.3.4 Extended K-φ Model

As discussed, in fitting data with the shrinking core and shrinking sphere models there are clearly three different stages during the leaching process - leaching of grains at the surface, leaching up to penetration depth and very slow leaching phase from the core. While the fits shown in Figure 6.27 are generally good, there is clearly an indication that modelled curve and experimental data begin to diverge from each other towards the end of the leach, where the proposed third phase, deep particle leaching becomes dominant. The model over-predicts the rate of leaching, which, although marginal here, could lead to significant mis-predictions of the rate of leaching from large particles in the long run.

Therefore, an alternative analysis was considered in extension of the model presented in Eq. (6.15). Here it is assumed that there is a readily leachable fraction (α) of Zn in the ore, which is accessible through the pore network and a poorly leachable fraction (1-α), which is locked within zones that are not cracked. The readily leachable fraction (α) varies with particle size and comminution method and is likely to be related to the penetration depth (P_d) discussed earlier, relating to the size un-cracked core. In this case, the general topology model needs to be adjusted that it applies only to the leachable fraction (α) as follows:

$$\frac{dx}{dt} = K(1 - \frac{X}{\alpha})^{\varphi} \qquad \text{Eq. (6.17)}$$

Where X remains the overall fractional Zn conversion (i.e. relative to total Zn content). This equation can be integrated to yield:

$$\frac{Kt}{\alpha} = \frac{(1-\frac{X}{\alpha})^{1-\varphi}-1}{\varphi-1} \quad \varphi \neq 1 \qquad \text{or}$$

$$X(t) = \alpha\left[1 - \left(1 + (\varphi - 1)\frac{Kt}{\alpha}\right)^{\frac{1}{1-\varphi}}\right] \quad \varphi \neq 1; \quad t_{lim} = \frac{\alpha}{K(1-\varphi)} \quad \text{if } \varphi < 1 \qquad \text{Eq. (6.18)}$$

where the limiting time t_{lim} applies for φ < 1, as discussed for Eq. (6.15).

Finally, after depletion of the leachable fraction (α), the reaction proceeds further at a very slow rate, probably related to the solid-state diffusion of reacting species that occurs at diffusivities orders of magnitude smaller than that assumed for a porous matrix. From the data in Figures 6.3 and 6.4, it appears that leaching towards the end proceeds in a more or less linear fashion and to account for this in the model, we add a simple linear term to above equation:

$$X(t) = \begin{cases} \alpha\left[1-\left(1+(\varphi-1)\frac{Kt}{\alpha}\right)^{\frac{1}{1-\varphi}}\right]+\beta t & t \le \frac{\alpha}{K(1-\varphi)} \text{ if } \varphi<1;\ \text{all t, if } \varphi>1 \\ \alpha+\beta t & t > \frac{\alpha}{K(1-\varphi)} \text{ if } \varphi<1 \end{cases} \quad \text{Eq. (6.19)}$$

Table 6.4 shows K and φ values obtained by minimisation of mean squared error (MSE) using Eq. (6.19), for the leach reactors data from different size fractions crushed using HPGR-95 bars and cone crusher. Leach reactors and modelling data using K-ϕ model have been given in the appendix VII.

Table 6.4: Obtained K and φ values for leach reactors data from different size fractions crushed using HPGR-95 bars and cone crusher.

Size fraction (mm)	K (day^{-1})		φ		α		B (day^{-1})	
	HPGR	cone crusher	HPGR	cone crusher	HPGR	cone crusher	HPGR	cone crusher
Small	0.011	0.005	0.793	0.217	0.789	0.418	0.00E+00	8.64E-04
Medium	0.007	0.003	0.793	0.284	0.643	0.322	1.79E-04	9.30E-04
Large	0.005	0.002	0.710	0.252	0.565	0.225	1.15E-06	8.10E-04

Comparing Table 6.4 to the Table 6.3 shows that the values for K remain roughly the same and follow the same trends as shown in Figure 6.28. This is expected as K describes the initial slope of the leach curves, which remain the same regardless of the model used. Thus K can still be modelled with Eq. (6.16), with the model parameters of d≈(-0.5) almost the same for the products of the two different comminution devices, and c,

which is 0.02 for the particles crushed using HPGR and 0.01 for particles crushed using a cone crusher.

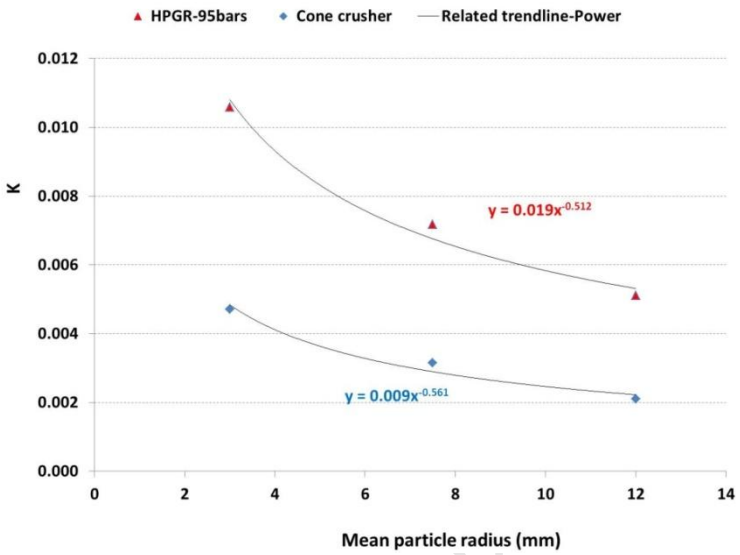

Figure 6.28: Relationship between K and mean particle radius.

The values for φ completely change with the introduction of the readily leachable fraction (α) and always are below 1. As given in the Table 6.4, φ does not significantly change with particle size and can directly be related to crushing mode. The small value of φ for cone crusher indicates that the leaching is nearly linear, i.e. that exposed mineral is mostly near the surface, which relates to the much lower α value found for this comminution mode.

Figure 6.29 shows the relationship between the readily leachable fraction (α) and fractional penetration volume $(P_d/R)^3$, which could be perceived as the volumetric portion of the particle that is accessible to reagent. As the trend line shows, the correlation follows almost perfect linear fits, further confirming the link between the penetration depth and leach behaviour. Leachable fraction (α) can thus be described as per Eq. (6.20):

$$\alpha = \alpha_0 + \alpha_1 \left(\frac{p_d}{R}\right)^3 \qquad \text{Eq. (6.20)}$$

The connection between P_d and R already described in Eq. 6.1.

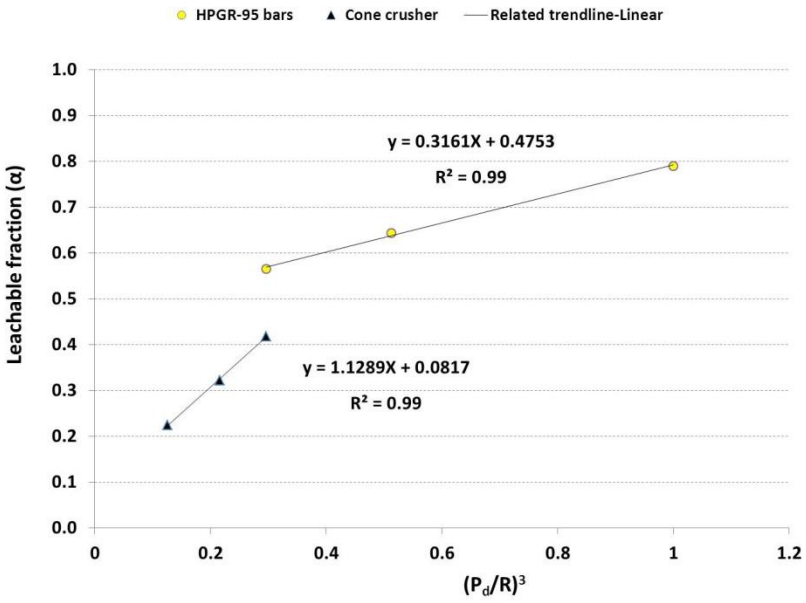

Figure 6.29: The relationship between the readily leachable fraction (α) and fractional penetration volume $(P_{d/}R)^3$.

The values close to zero for β in Table 6.4, indicates that after depletion of the leachable fraction (α), the reaction proceeds further at a very slow rate, which is almost negligible. This indicates that metal extraction from the uncracked zones within the particles takes a very long time and probably follows a solid-state diffusion mechanism. In terms of extraction in a heap leaching context this portion of leaching from large particles is essentially beyond economic recovery.

Figure 6.30 shows a comparison of the conversion X (Zn) for leach reactors vs. time for experimental data and the fitted curve obtained for K and φ values from different size fractions. As can be seen there is near perfect fit compared to the Figure 6.26.

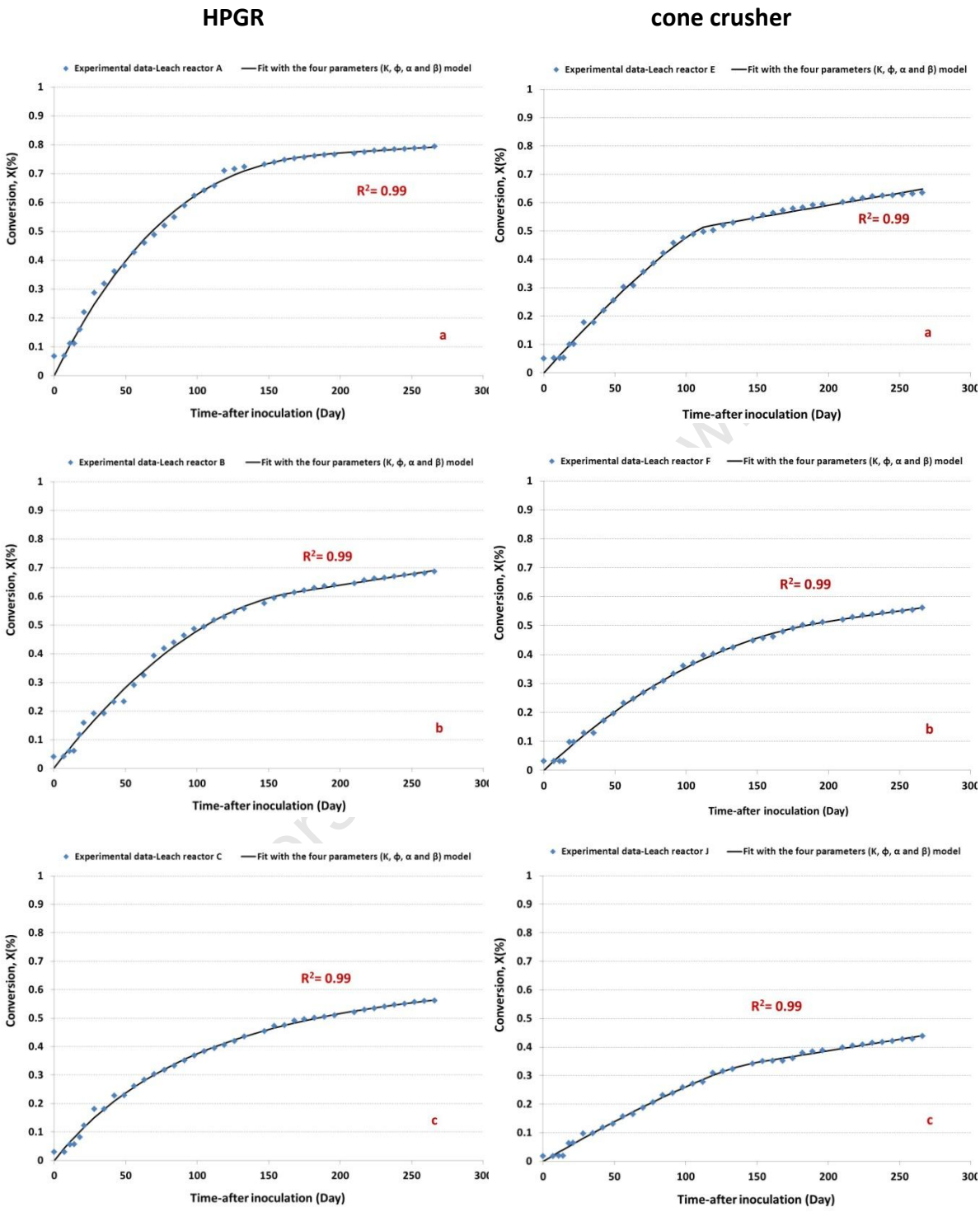

Figure 6.30: Comparison of the conversion X (Zn) vs. time for experimental data and fit curve of 4-parameter model with obtained K and φ values for leach reactors from different size fractions crushed using HPGR-95bars and cone crusher (a. Small, b Medium and c. Large).

6.5.1 Model Summary and Discussion

Following the leaching process in the selected particles from different size fractions with X-ray CT and other techniques provided a clear image of the effective parameters in leaching from large particle in course of heap leaching.

Table 6.5 summarizes the core model parameters from Eq. (6.19) and how they relate to the other variable such as the comminution mode, the penetration depth (P_d) and mean particle radius (R). This indicates that the mineral conversion (X) in general could be written in the following equation as a generic model:

$$X(t) = f(\text{comminution mode}, R, t) \qquad \text{Eq. (6.21)}$$

i.e. only comminution mode and particle radius remain as true variables in a heap leach system, which makes modelling of the reaction process straightforward.

Table 6.5: Final rate model (Eq. (6.18)) and summary the core model parameters. Note mean particle radius (R) is in [mm].

Final rate model	$X(t) = \begin{cases} \alpha\left[1-\left(1+(\varphi-1)\frac{Kt}{\alpha}\right)^{\frac{1}{1-\varphi}}\right]+\beta t \\ \alpha+\beta t \end{cases}$	
Core model parameters		
Equation for parameters	**Values**	
	HPGR	**Cone Crusher**
$\alpha = \alpha_0 + \alpha_1\left(\frac{p_d}{R}\right)^3$	α_0 = 0.48 α_1 = 0.32	α_0 = 0.08 α_1 = 1.13
$p_d = aR^b$ [mm]	a = 1.38 b = 0.71	a = 0.84 b = 0.80
$K = cR^d$ [day^{-1}]	c = 0.019 d = - 0.51	c = 0.009 d = - 0.56
φ	~ 0.75	~ 0.25
β [day^{-1}]	10^{-4}	$9{\cdot}10^{-4}$

The derivation of the various model parameters listed in Table 6.5 follows from a systematic analysis of the progression of leaching overall and within individual particles. It has clearly shown that leaching rate and extent are linked to the mode of comminution via the formation of a network of cracks and micro-pores in the outer rim of the particle. Penetration depth (P_d) of this network can be related to particles size via a power relationship, with the exponent very similar for the methods tested here, indicating a connection, possibly to the mechanics of crack formation. Crack density within the cracked rim could not be determined, but closely relates to the model parameter φ, which represents the 'remoteness' of mineral grains from the nearest crack or pore. Again it is interesting to note that the value of φ is more or less constant for the two comminution methods, independent of particle size, but substantially different between the two methods. This points to a very different nature of cracks formed by the two methods: Relatively deep cracks with relatively few micro-fissures created by HPGR; and a denser network of micro-fissures with few cracks near the surface created by the cone crusher. This is also borne out by both physical observation and pore size analysis presented in Table 6.1 and in chapter 5.

This interpretation is further supported by the leachable fraction (α) parameter, which shows a direct relationship with the relative particle volume of the cracked rim, $(p_d/R)^3$. This correlation is much stronger for the cone crusher than the HPGR (the value of α_1 is 3.5 times larger), which would make sense if the former mode resulted in a dense network of micro-pores as opposed to a less dense network of larger cracks for the latter. However, the tools available to this study do not allow a closer characterisation of the nature and extent of micro-pores created by the two different comminution methods. This would certainly be of great interest in a follow-up study, also with a view to maximising the leachibility of an ore, while minimising the amount of crushing that is needed to prepare it for heap leaching.

Finally, the nature of 'residual' leaching from the uncracked portion of particles merits further exploration. While the leach data generated in the present study was insufficient to characterise this more closely, the extremely slow rates indicated ($\beta < 10^{-3}$ 1/d for the

cone crusher and $<10^{-4}$ 1/d for the HPGR material) point at a process with a rate constant several orders of magnitude slower than the principal reaction/diffusion processes studied here. It is well possible that this could relate to solid-state diffusion phenomena through zones, which have remained unaffected by any cracks or micro-fissures. It could, however, also be related to passivation effects through mineral associations as discussed in the next Section. Careful long-term studies could reveal more about this process, but from a practical heap leaching point of view, this mode of leaching refers to the portion of mineral that less likely to be recovered economically. The principal focus must therefore remain on preparing an ore charge, which minimises the occurrence of this slow-leaching phase.

6.6 Mineral association and zinc extraction

It was furthermore noted that access to a mineral grain is necessary for it to leach but that mineral association, target mineral composition and precipitation are rate-limiting factors. These variable factors are not easy to be formulated due to their natural complexity. A complete discussion in this regards, is given in the following sections.

6.6.1 Galvanic Effect

Galvanic interactions between metal sulfide minerals are known to have a significant influence on chemical mineral processing methods such as flotation and hydrometallurgy (Ahonen and Tuovinen, 1995). In hydrometallurgy, galvanic interactions have been studied for several leaching and bioleaching systems. In these systems, the galvanic interactions were shown to substantially increase the leaching of one or both of the minerals that constitute the galvanic cell, depending on the electrochemical characteristics of the minerals and on the occurrence of the distinct sulfides contained in the concentrates (Arce *et al*., 2002; Liu and Zhou, 2008; Urbano *et al*., 2007).

For semiconductive minerals, such as sulfides, direct contact of different minerals with dissimilar rest potentials initiates the galvanic effect. This effect has been modelled with galvanic cells through the redox reactions, where the mineral with the higher rest potential acts as the cathode, which is galvanically protected, while the mineral with the lower rest potential acts as an anode and its dissolution is favoured through electronic interactions. These interactions occur between sulfides, involving the flow of electrons from grains with a higher potential to grains with lower potentials, modifying the Fermi level of both minerals (Arce *et al*., 2002).

Galvanic interactions depend on the mineralogical association between the phases present in the ore sample. The presence of strong oxidizing ions, such as Fe^{3+}, present in solution results in enhanced corrosion current density of galvanic interaction between sulfides, with higher concentrations of strongly oxidizing ions leading to increased corrosion current density. Even if there is a large quantity of non-oxidizing and non-reducing ions, the corrosion current density will not significantly change (Cruz *et al*., 2005).

The electrochemical behaviour of sulfide minerals is characterized by their rest-potential (Arce et al., 2002). A list of rest-potentials for the minerals encountered in this work is found in Table 6.6. The values vary depending on the origin of the mineral but the order generally remains consistent:

Pyrite > Chalcopyrite > Sphalerite > Pyrrhotite > Galena

Table 6.6: Literature rest potential values (Kocabag, 1985).

Mineral	Rest potential vs. SHE (Volts)
Pyrite	0.66
Chalcopyrite	0.56
Sphalerite	0.46
Pyrrhotite	0.31
Galena	0.28

To illustrate the importance of the order, consider two sulphides in contact in electrolyte. The sulfide with the lower rest-potential acts as the anode and undergoes oxidation by giving up electrons (Eq. (6.20)) to the sulfide with the higher rest-potential acting as the cathode. The Me in Eq. (6.20) stands for metal (e.g., zinc, copper, lead, etc.). The final electron acceptor is commonly oxygen, which is reduced to hydroxide (OH^-) (Eq. (6.21)). Another electron acceptor is ferric iron (Fe^{3+}), which is reduced to ferrous iron (Fe^{2+}) (Eq. (6.22)) (Rao and Finch, 1988; Ahonen and Tuovinen, 1995). This electrochemical process is known as galvanic interaction.

$$MeS \rightarrow Me^{2+} + S^o + 2e^- \qquad \text{Eq. (6.20)}$$

$$\frac{1}{2}O_2 + H_2O + 2e^- \rightarrow 2OH^- \qquad \text{Eq. (6.21)}$$

$$Fe^{3+} + e^- \rightarrow Fe^{3+} \qquad \text{Eq. (6.22)}$$

Since pyrite is a dominant sulfide mineral in the ore sample (34 wt. %), the role of the pyrite on the leaching of sphalerite is of importance, and merits study.

A physical representation of galvanic interaction is illustrated in Figure 6.31 for pyrite and sphalerite. From Table 6.6, the rest-potential of pyrite (0.66 V) is higher than that of sphalerite (0.46 V) and, therefore, electrons flow from sphalerite, the anodic mineral, to pyrite, the cathodic mineral. As the anode, sphalerite is oxidized (Eq. (6.20)) and the cathodic reaction is either reduction of oxygen on the surface of pyrite (Eq. (6.21)) or reduction of ferric iron (Eq. (6.22)).

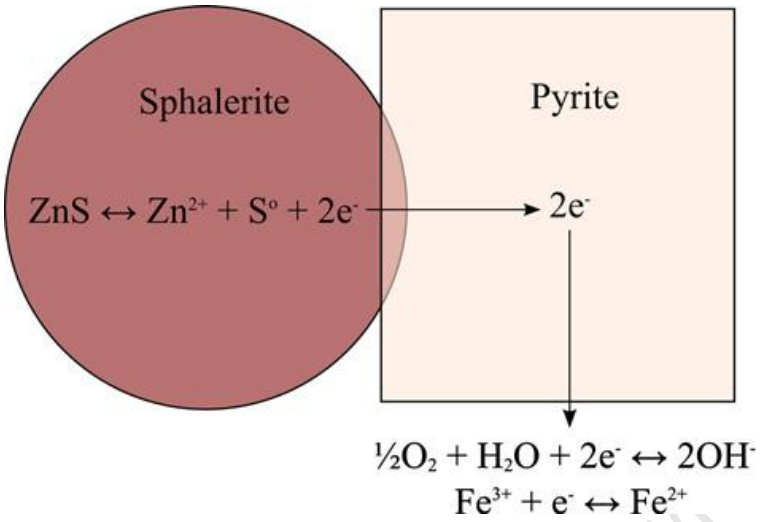

Figure 6.31: Schematic of galvanic interaction mechanism between pyrite and sphalerite.

This indicates that during bioleaching a galvanic current would flow from sphalerite to pyrite when they are in contact with one another. Figure 6.32 derived from the X-ray CT analysis, shows two areas of sphalerite associated with pyrite prior to leaching. After 6 months of treatment, the sphalerite has completely reacted. The sphalerite surface association to pyrite (i.e. % of the sphalerite grain perimeter) is illustrated in Figure 6.33 for the 8 different reactors prior to and after the leach experiment. The results show an overall decrease in the association of sphalerite to pyrite consistent with the selective oxidation of sphalerite relative to pyrite. The discrepancies in the data for reactors B and J are attributed to the statistical representativity of the coarse particles analysed.

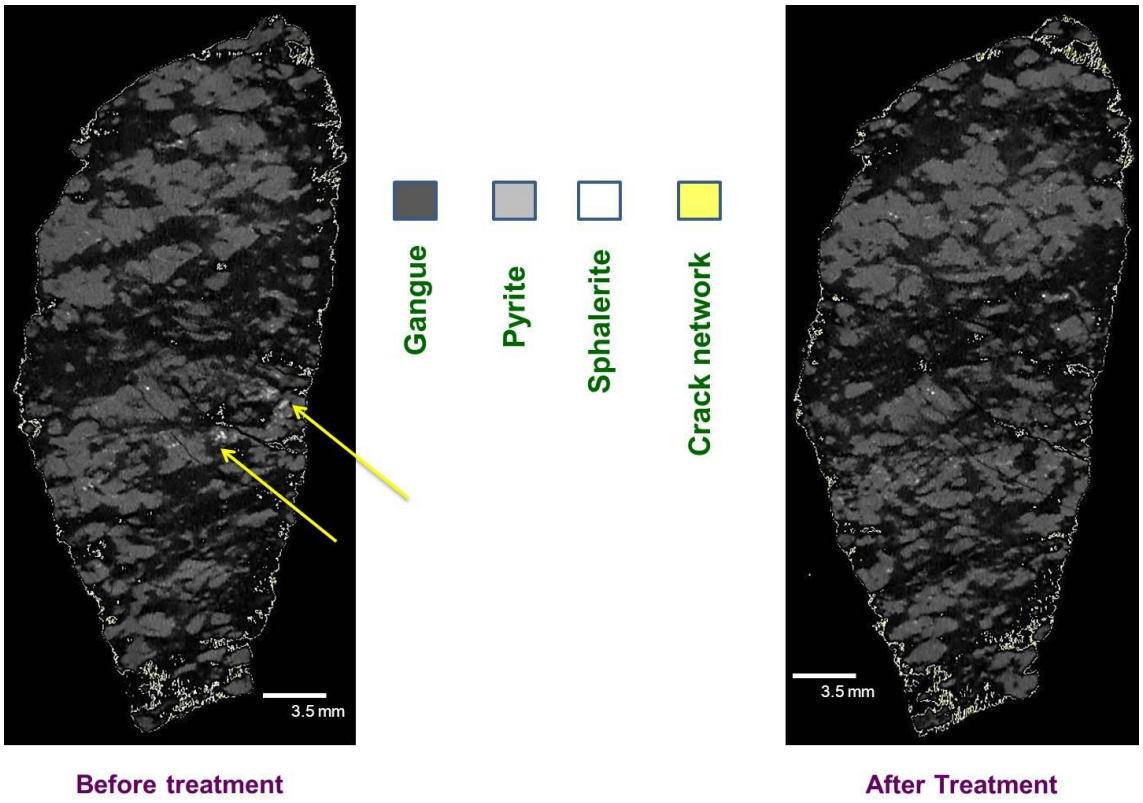

Figure 6.32: X-ray CT analysis results for the trend of depletion of the sphalerite association with pyrite in the ore particles before and after six months treatment.

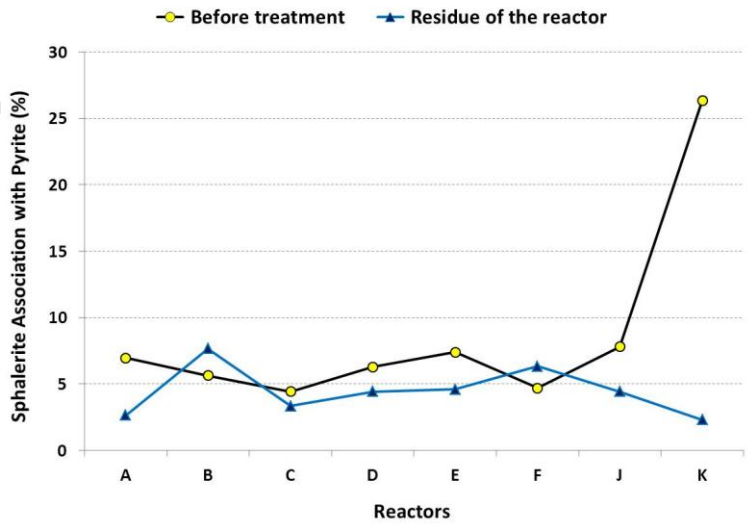

Figure 6.33: QEMSCAN analysis results for the trend of the sphalerite association with pyrite in the leach reactors before and after leaching process.

The QEMSCAN particle images in Figure 6.34 similarly show a decrease in the association of sphalerite to pyrite during the course of the leach experiment. Note that sphalerite contained in the residue is completely associated with the gangue minerals.

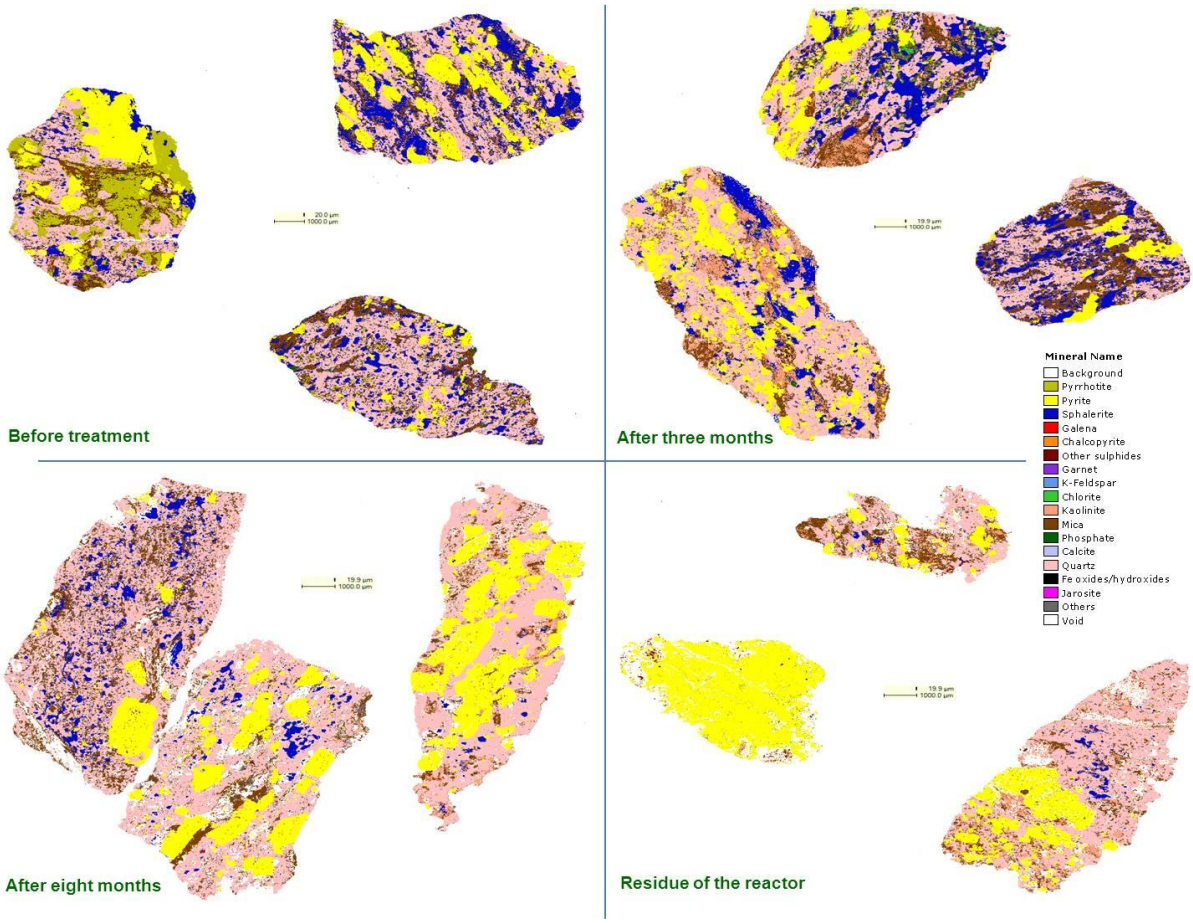

Figure 6.34: QEMSCAN analysis results for the trend of depletion of the sphalerite association with pyrite in the ore particles before, during and after treatment.

6.6.2 Precipitation

Jarosite precipitation is an important phenomenon that is observed in many bacterial cultures. In the bacterial leaching of sulfide minerals, ferric iron is the key oxidizing agent

and soluble iron species are the main determinants of redox potential. Active iron oxidizing bacteria, such as *Acidithiobacillus ferrooxidans* and *Leptospirillum ferrooxidans*, maintain high Fe^{3+}/Fe^{2+} ratios due to continued oxidation as part of their respiratory process. During bioleaching, monovalent cations (e.g., K^+ and Na^+) released from the alteration of silicate phases (e.g., Mica as a potassium aluminium silicate) present in the ore may promote the precipitation of ferric iron mainly as K-jarosite, which is controlled by pH (Ahonen and Tuovinen, 1995).

The limited extraction of metals has often been attributed to the formation of these secondary phases during bioleaching (Ahonen and Tuovinen, 1995; Harmer *et al*., 2007). Jarosite caused an obstruction to mineral-microbe contact by forming a mass transfer barsrier to nutrients, oxygen, and carbon dioxide. Precipitation of iron hydroxide and jarosite phases in the leaching system may suppress the metal solubilisation by preventing contact between the leaching agent and the mineral. The solubility of iron species is defined by their concentration in solution and pH. Thus, the optimization of these parameters may greatly improve the metal recovery (Malik *et al*., 2004).

Jarosite precipitation during the leaching process was found to be minor. This would be as expected given the stable environment (stable redox potential and pH) in the leach reactors and the relatively low pH maintained. However, within the last month of leaching, evidence of precipitation was found. SEM images of selected samples in the Figure 6.35 show the progress of this phenomenon. EDS used for elemental analysis showed significant Fe, K, and S in the precipitation areas indicative of Fe (III)-hydroxysulfates. Table 6.7 shows the semi-quantitative elemental analysis of precipitation on the surface of ore particles (A, B and C crushed using HPGR at 95bars pressure setting), determined by EDS. It should be noted that elemental analysis of precipitation on the surface of ore particles in both cone crusher and HPGR products was same.

This was supported by the QXRD that showed the precipitation of Jarosite ($KFe_3(SO_4)_2(OH)_6$) up to 2 wt.% and Schwertmannite ($Fe_{16}O_{28}(SO_4)4H_{16}$) up to 5 wt.%.

These minerals were not detected by QEMSCAN most likely due to a combination of factors such as sample preparation, edge effect, soft texture, as well as the composition and discrimination of these phases from other ferric hydroxide species. A sulfide ore/concentrate should contain sufficiently high iron since the provision/availability of sufficient soluble iron in bioleaching environment is essential for the bacteria to generate ferric iron and efficiently drive the extraction of zinc from the complex sulfides (Deveci *et a*l., 2004). The change in leaching from the readily accessible grains on the particle surface to the more inaccessible grains within particles is the main reason in this for precipitation.

During the leaching process, microorganisms regenerate ferric oxidant form the sufficient ferrous iron (Fe^{2+}) in the solution environment (1g/L in the media and dissolved from the ore). Slow oxidation rate of Zn during the last month of treatment in this study, affected balance of Fe^{2+} and Fe^{3+} ions concentration in the solution environment. High concentration of insoluble Fe^{3+}, due to the lack of demand precipitates as ferric hydroxide or precipitate as Fe(III)-hydroxysulfates such as jarosites or schwertmannite. However, as there was no perceptible shift in solution potential at this time (see Figure 6.2) it would be more likely that the leaching shifted from sphalerite to pyrite, thus causing a significant increase in the supply of Fe^{3+}.

In addition to the obstruction role of precipitation to mineral-microbe contact, the formation and dissolution of iron-hydroxysulfate minerals such as jarosite and schwertmannite can influence the mobility of metals and radionuclides in the environment. Jarosite can incorporate lead, mercury, copper, zinc, silver, and radium by substitution for structural K^{+1} or Fe^{+3}, and anions such as chromate, arsenate, and selenate by substitution for SO_4^{-2}.

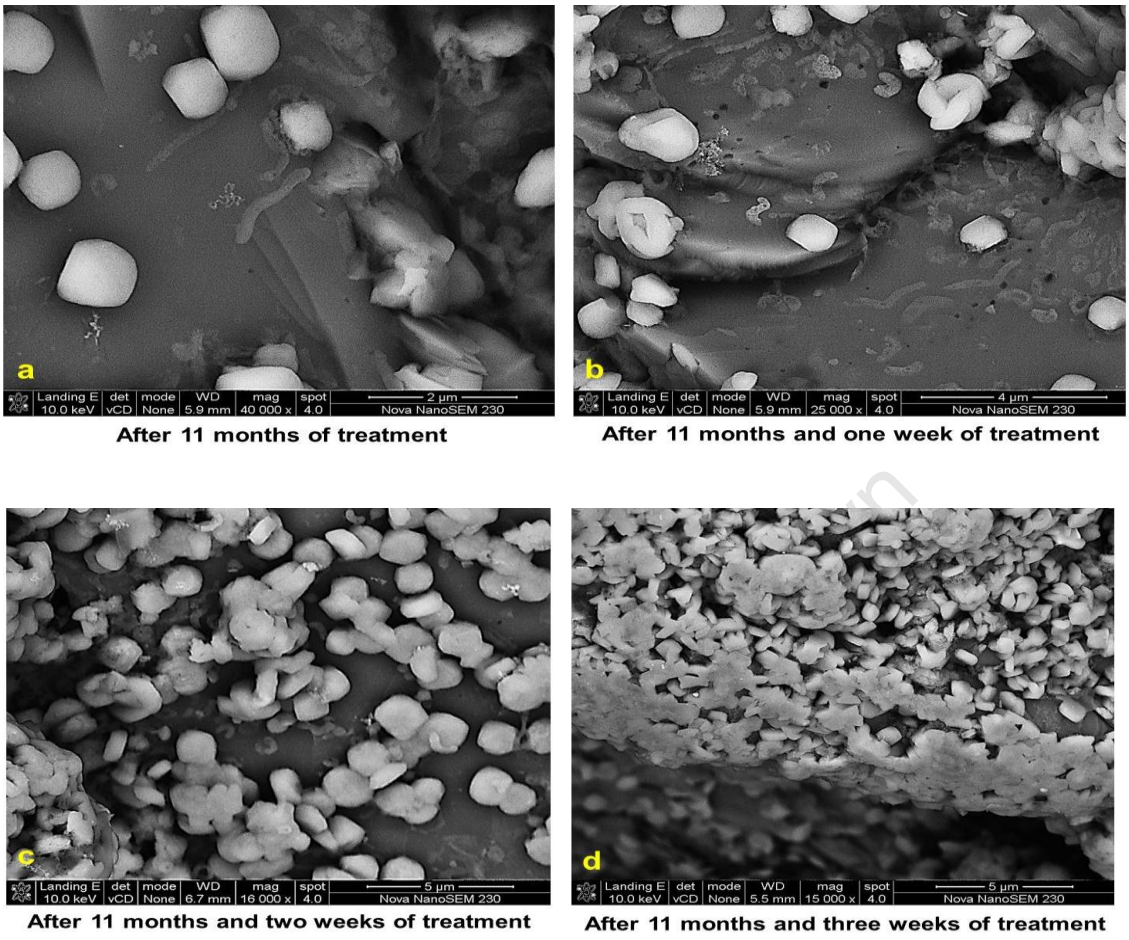

Figure 6.35: Growth trend of precipitation on the surface of particles from a to d.

Table 6.7: Semi-quantitative elemental analysis of the precipitate on the surface of ore particles (A, B and C crushed using HPGR at 95bars pressure setting) determined by EDS. (Nd denotes not detected).

Element	(wt. %)		
	A	B	C
O	> 20	> 20	> 20
Al	< 5	< 5	< 5
Si	10-20	10-20	10-20
S	5-10	< 5	< 5
K	< 5	< 5	< 5
Fe	< 5	< 5	< 5
Zn	Nd	Nd	Nd

6.6.3 Sphalerite composition

Characterization of the residue of the leach reactors indicated that there are areas within the ore particles where although sphalerite grains are accessible to the solution, they remain unreacted. Figure 6.36 shows unreacted sphalerite grains at the surface (Figure 6.36a) or in subsurface regions, which are accessible from the surface by cracks and pores (Figure 6.36b).

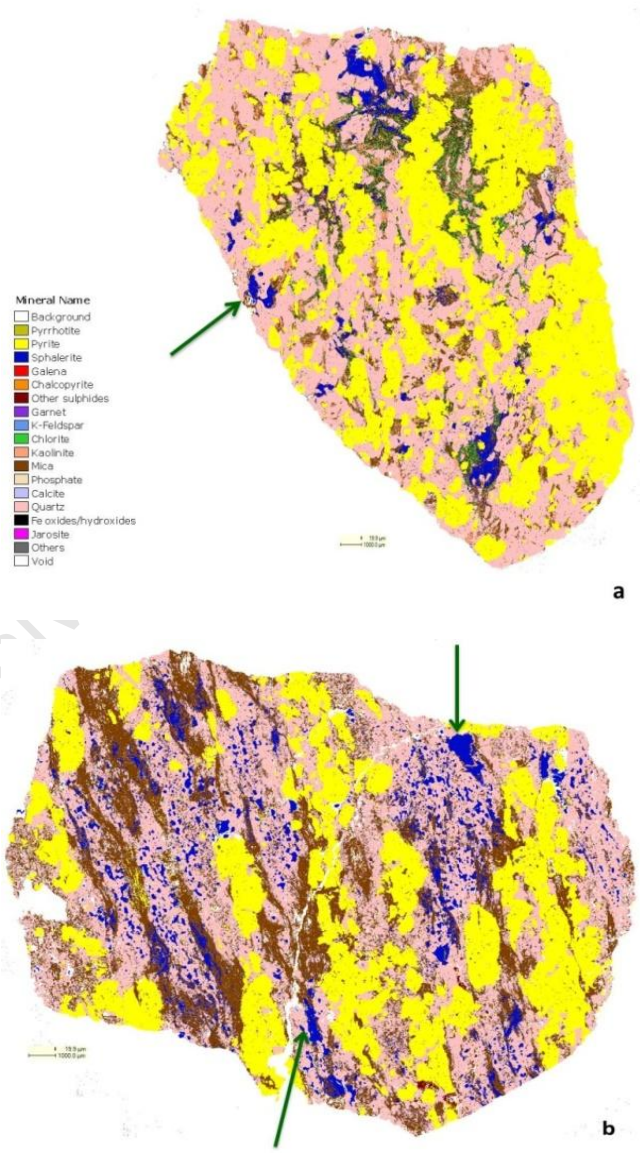

Figure 6.36: Unreacted sphalerite grains, at the surface of the cone-crushed particle (a) and subsurface of HPGR crushed particle, accessible to the solution by crack (b).

These results indicate that accessibility to the reagent is necessary but not necessarily enough and a variety of mineralogical conditions can hamper or prevent leaching of an ore. Further investigations were done in these areas using EMPA to determine if any compositional variation or chemical zoning within the sphalerite could explain the behaviour.

Figures 6.37 to 6.40 show elemental maps of Zn, S, Fe, Mn and Cd and the accompanying QEMSCAN images of unreacted sphalerite within the residue of particles prepared by HPGR (Figures 6.37 and 6.38) and cone crusher (Figure Figures 6.39 and 6.40). The QEMSCAN images of particles prepared by HPGR (small size fraction) have sphalerite with an associated void, most likely due to the prior dissolution of sphalerite. In contrast, particles prepared by cone crusher do not show this feature, which is consistent with the lower final zinc extraction.

Elemental maps show little true compositional variation within individual sphalerite grains. Associated spot analyses show that after eleven months of leaching treatment, sphalerite composition remains the same as the feed (see table 4.2 in chapter 4). This shows a homogeneous and impervious environment within individual sphalerite grains. Sphalerite grains in the ore particles dissolve with varying size with constant density. During the leaching process, the radius gradually decreases with time, while the particle interior does not undergo much compositional change. In cases where the chemical reaction at the surface is much slower than the diffusion of reagents through the diffusion layer, the leaching becomes reaction controlled. This reaction trend in the mineral grain scale is in agreement with a shrinking sphere model. Back-scattered electron (BSE) and EMPA of elemental mapping for different areas of HPGR and cone crusher products have been shown in the appendix III.

Impurities within the sphalerite in the ore sample can also be rate-limiting factors in large particle leaching. Several previous studies (e.g. Morey *et al*., 2001; Harmer *et al*., 2007; Chen *et al*., 2010) have shown that variations in the mineral chemistry of sphalerite have a profound impact on its behaviour during processing. High levels of

these impurities in some zinc concentrates, such as those produced at Gamsberg zine mine, may render them unsuitable for processing by traditional Roast-Leach-Electrowinning (RLE) operations (McClung and Viljoen, 2011; Schouwstra *et al*., 2010). Therefore, the effect of the significant Fe and Mn contamination of sphalerite in this study needs evaluation. Although there is little Fe and Mn compositional variation within this sphalerite, it is compositionally quite different to pure ZnS and so the effects described in the following are considered significant.

It is well known that Fe influences both the sphalerite band gap and reactivity (Harmer *et al*., 2007). The result of study by Weisener *et al*. (2004) showed that the greater the concentration of Fe in the sphalerite, the greater the surface concentration of oxidised sulfur species observed. It appears likely that the elemental sulphur formed remains highly porous thus allowing the reactants and products to diffuse through or between the localised regions without significant diffusion control. The activation energies are consistent with a solid diffusion-controlled leach reaction rate. The activation energies for both Zn and Fe dissolution are dependent on the sphalerite Fe concentration and decrease with increasing Fe concentration (Harmer *et al*., 2007; Weisener *et al*., 2004). This could be due to the availability of ferrous ions for ferric ion oxidation, which would increase the oxidation of zinc. This acceleration of the dissolution arising from the presence of Fe within the sphalerite could also be explained from the semiconduction and electrochemistry viewpoint. The iron content within sphalerite has the effect of narrowing the band gap energy, and consequently, the rate of dissolution of sphalerite is therefore directly proportional to the concentration of constitutional iron impurity in the solid. The iron content hence, formed a narrow impurity band within the forbidden band gap of the sphalerite, which energetically favoured the transfer of electron between the d-orbital band and the oxidant than the transfer of electrons between the valence band and the oxidant. Since sphalerite occurs as ferrous sphalerite, when iron substitutes for zinc, sphalerite dissolution generates acid instead of being acid consuming, due to hydrolysis of the ferric phases (Harmer *et al*., 2007, Schouwstra *et al*., 2010).

Although the elemental maps of sphalerite show little compositional variation in Mn, the presence of Mn within the ore in sphalerite, discrete FeMn silicates (pyroxmangite), Mn garnet (spessartine and almandine) and alabandite (MnS) would be associated with higher order oxidation products that may form refractory compounds of zinc and manganese. This could be a possible reason for unreacted sphalerite grains at the surface of the particle in the Figures 6.37 to 6.40.

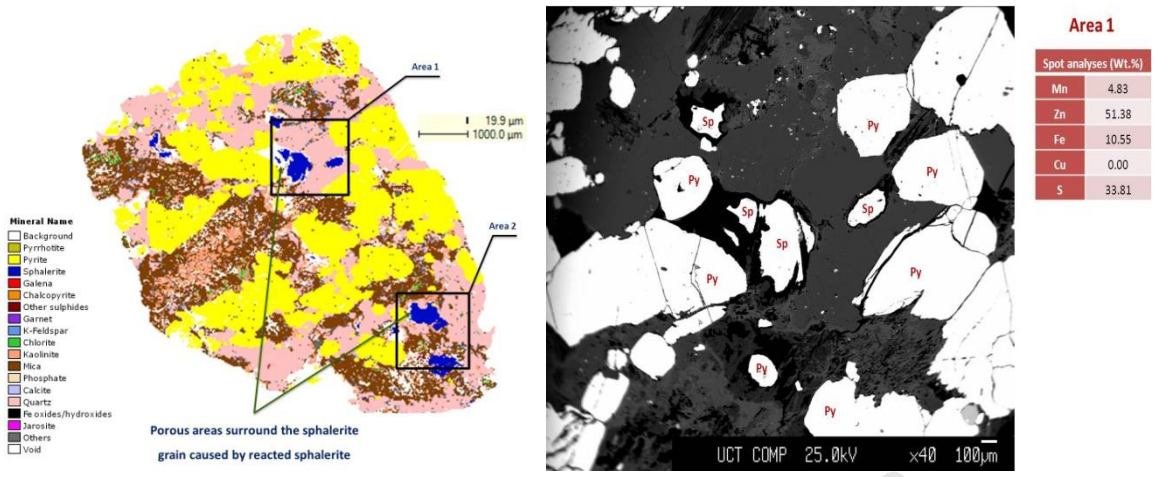

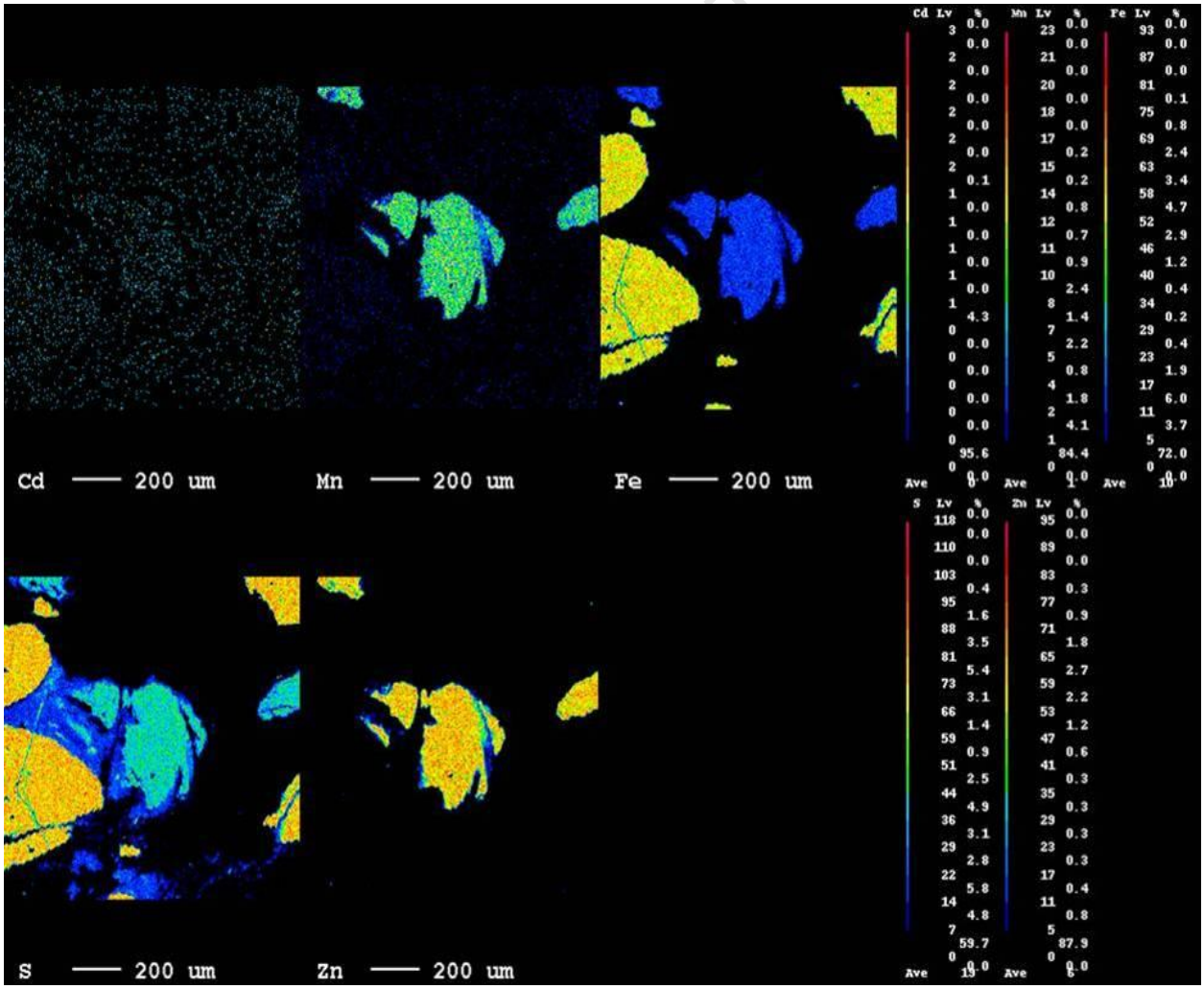

Figure 6.37: Back-scattered electron (BSE) and EMPA of elemental mapping for an area of the HPGR product from the leach reactor A (HPGR-95bars-small size fraction).

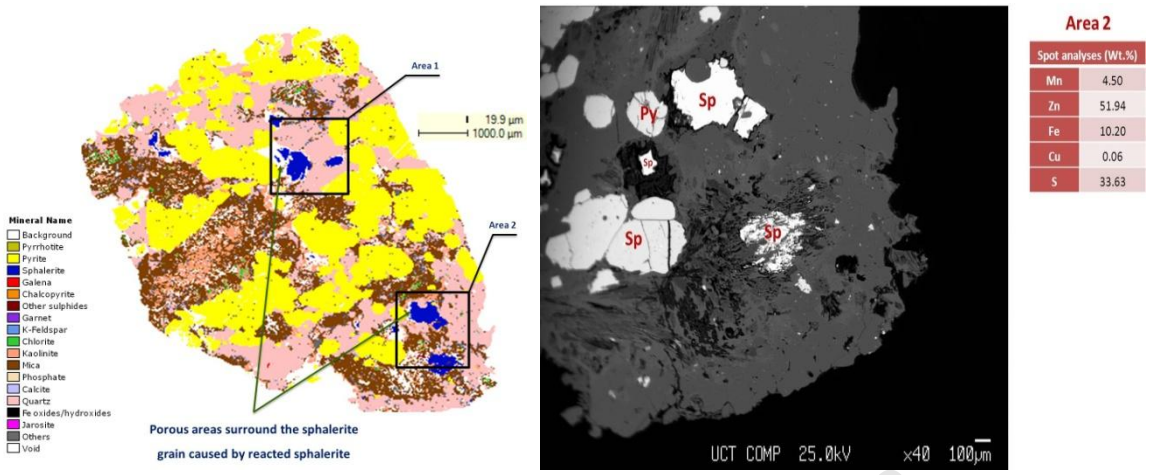

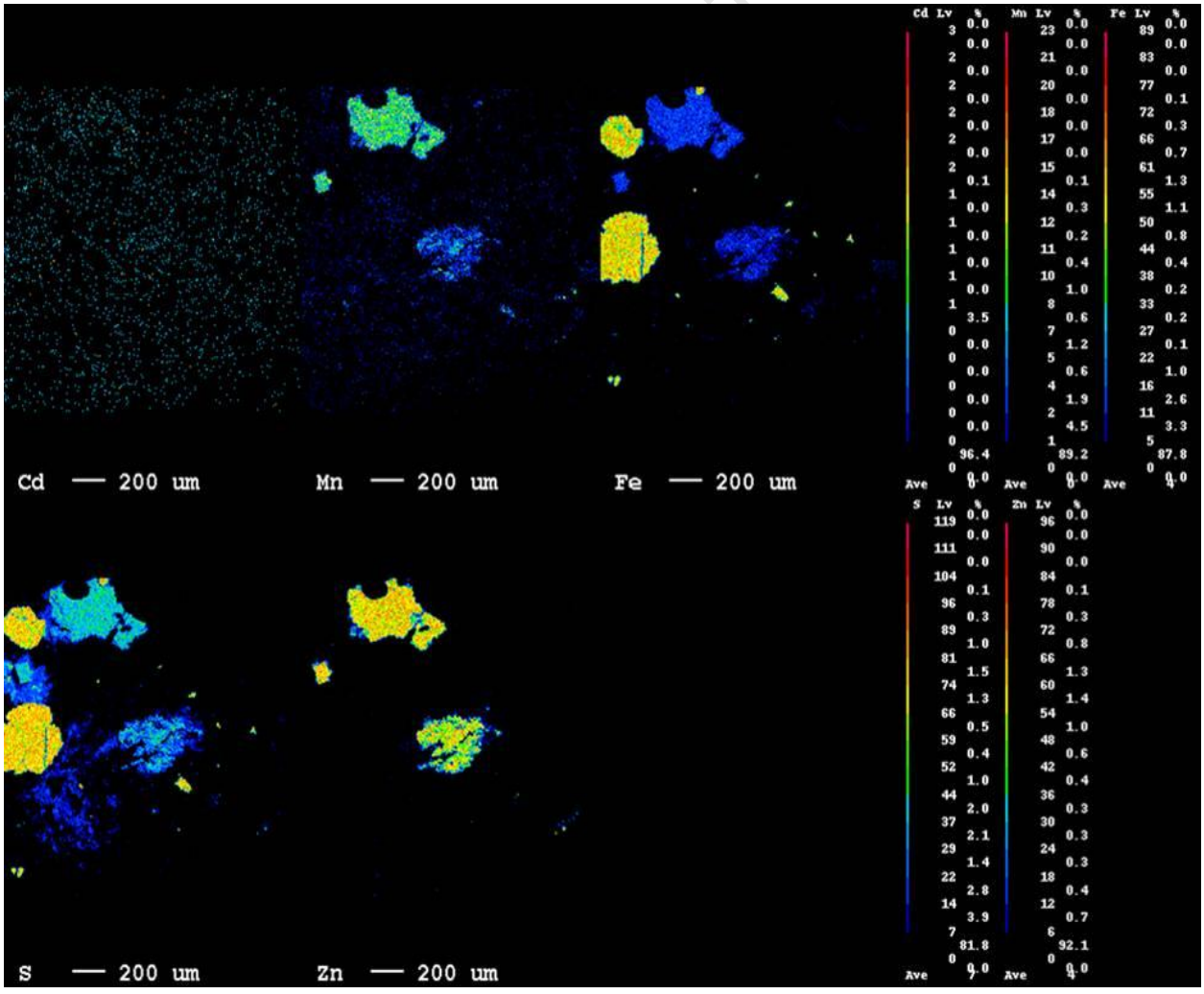

Figure 6.38: Back-scattered electron (BSE) and EMPA of elemental mapping for an area of the HPGR product from the leach reactor A (HPGR-95bars-small size fraction).

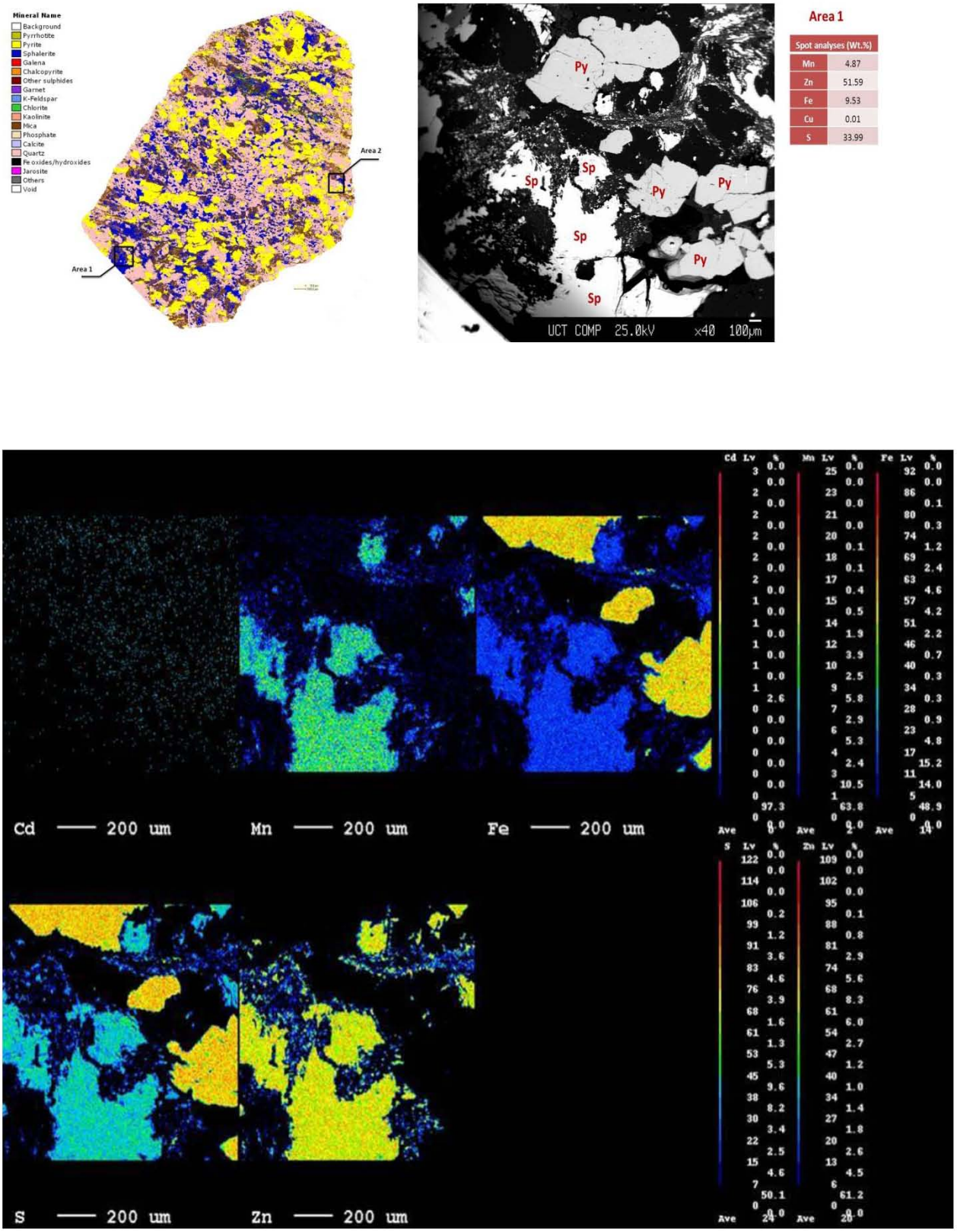

Figure 6.39: Back-scattered electron (BSE) and EMPA of elemental mapping for an area of the cone crusher product from the leach reactor J (cone crusher-large size fraction).

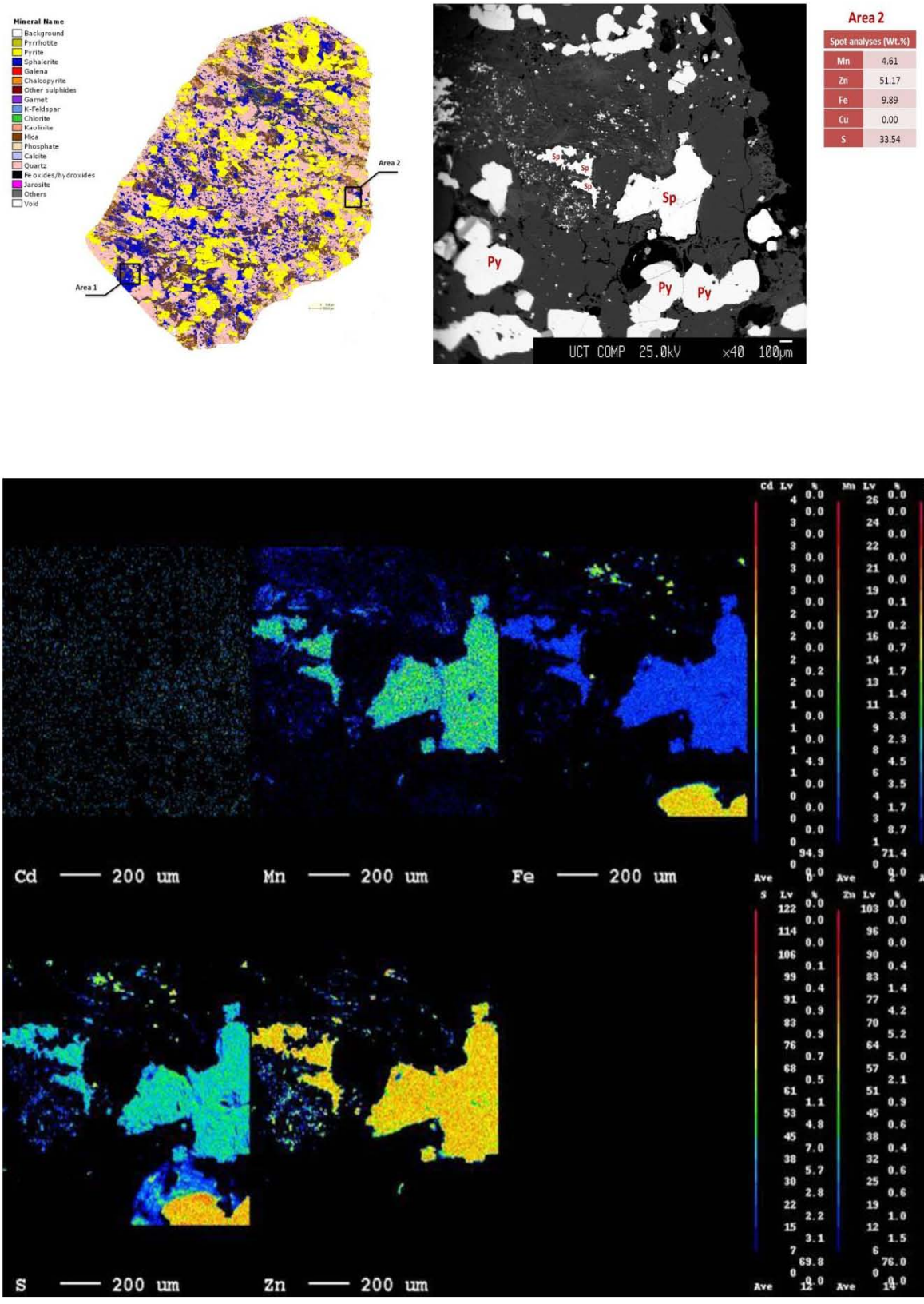

Figure 6.40: Back-scattered electron (BSE) and EMPA of elemental mapping for an area of the cone crusher product from the leach reactor J (cone crusher-large size fraction).

6.6.4 Association with gangue minerals

Characterization of the residue of the leach reactors indicated that most of the unreacted sphalerite grains occurred either as fine grains disseminated within the quartz (Figure 6.41a) or associated with mica (Figure 6.41b). As described in the sphalerite texture, fine grains disseminated within the gangue mineral (mostly quartz) are completely inaccessible to the leach solution. This indicates that diffusion of the reagent through the dense network of quartz to dissolve the disseminated fine sphalerite grains is practically impossible. For mica however, areas do exist where sphalerite is accessible to the solution, but the sphalerite grains still remain unreacted. Sphalerite grains associated with mica in the area shown in the Figure 6.41b are in the range of the penetration depth (see section 6.5.2) and theoretically must dissolve during the process. This suggests that some element of the association of sphalerite to mica is inhibiting the dissolution of sphalerite.

Mica is a common constituent of rocks, which during weathered forms secondary minerals such as vermiculite and interstratified mica/vermiculite, according to the environmental conditions. During weathering, mica minerals typically lose K from the interlayer positions and are transformed to expansible minerals such as vermiculite (Leonard and Sweed, 1970).

Dissolution and structural alteration of mica could be mediated by proton attack and bacterial oxidation of ferrous iron during the bioleaching process (Bigham et al., 2001). According to the results of the research by Bigham et al. (2001) and Bhatti et al. (2011), mica weathering was found to proceed via two pathways depending upon experimental conditions. At pH 2–3 in the presence of Fe^{3+}, K was preferentially stripped from the interlayer regions of phlogopite to form jarosite. Subsequent replacement of K by hydrated cations yielded expansible phases including vermiculite and interstratified vermiculite/phlogopite. Under these conditions, bacteria facilitated the weathering through the oxidation of Fe^{2+} to Fe^{3+}. At pH 1.5-2, the solubility product of jarosite was not exceeded, and preferential removal of K from the mica interlayer was diminished.

Consequently, the formation of expansible layer silicate phases was halted and weathering proceeded by chemical dissolution mediated by proton attack of the mineral structure. It should be noted that the biological systems might also act as nutrient sinks and thereby enhance the structural alteration of mica through removal of interlayer K (Bhatti et al., 2012).

The formation of minor jarosite from the alteration of mica during the course of the 11 months of leaching would shield the surface of the sphalerite grains, thereby inhibiting sphalerite dissolution. Quantitative XRD confirmed the presence of minor jarosite during the leach experiment.

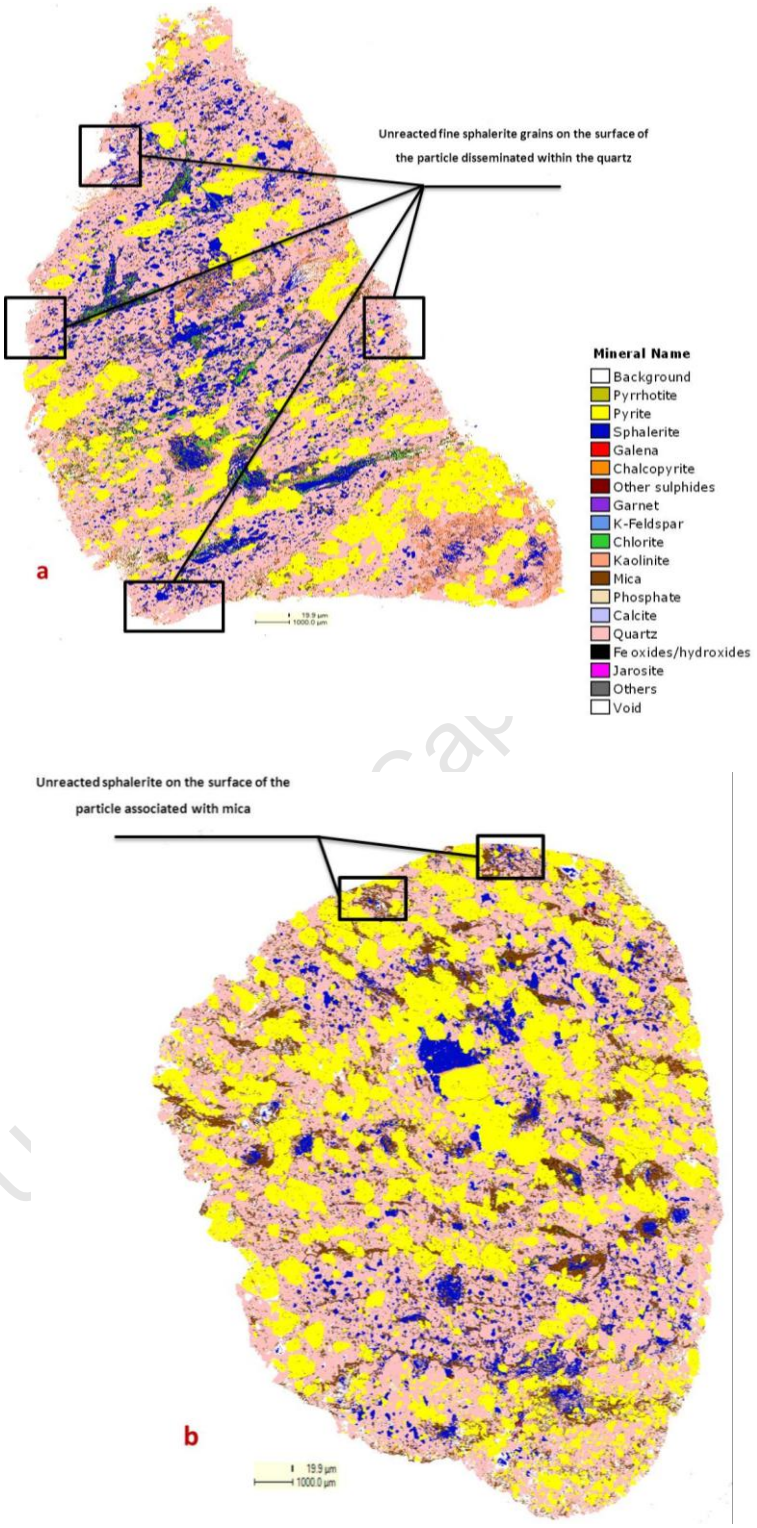

Figure 6.41: Unreacted sphalerite grains, fine grains disseminated within the quartz (a), associated with mica (b).

The sphalerite surface association to mica and quartz (i.e. % of the sphalerite grain perimeter) is illustrated in Figures 6.32 for the 8 different reactors prior to and after the leach experiment. The results show an overall increase in the association of sphalerite to Mica and quartz. This indicates that sphalerite grains association to mica and quartz remain unreacted and there is a preferential leaching of sphalerite grains associated with pyrite. The discrepancies in the data are attributed to the statistical representativity of the coarse particles analysed.

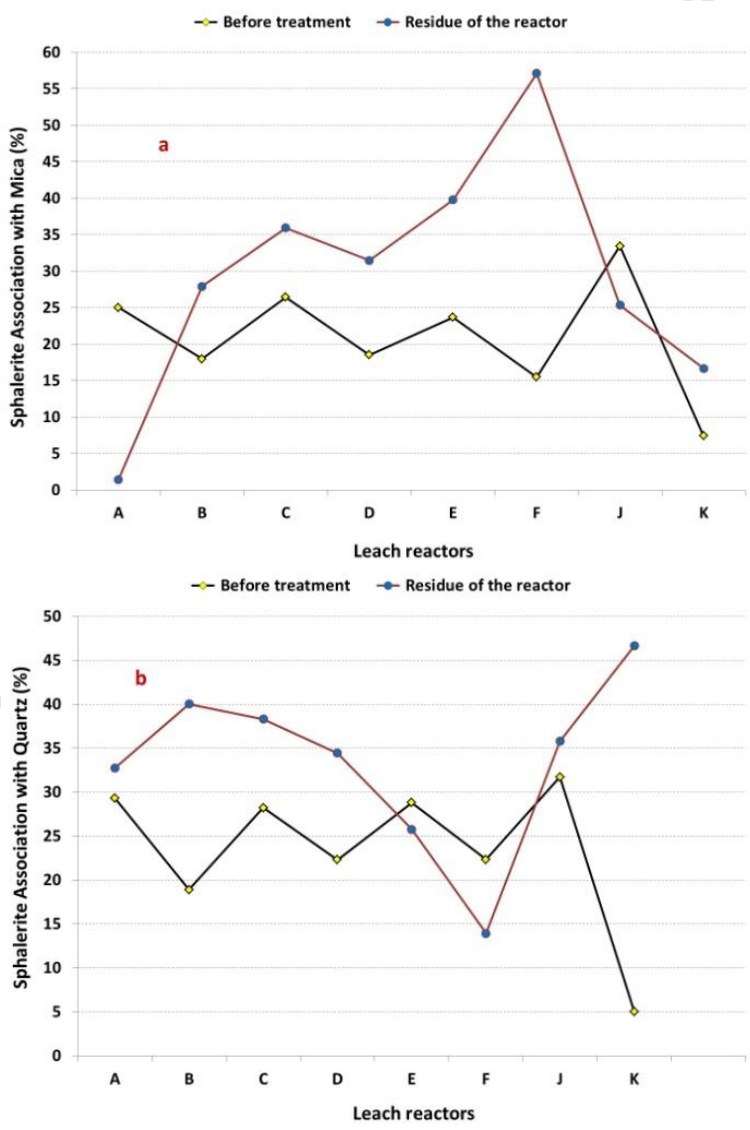

Figure 6.42: QEMSCAN analysis results for the trend of the sphalerite association with Mica (a) and quartz (b) in the leach reactors before and after leaching process.

6.7 Effect of HPGR product on percolation of heap leaching

In this study, similar size fractions for the ore were selected from the products of the material crushed using the HPGR and cone crusher and subjected to leaching tests. The micro-fracturing observed in the feed prepared using the HPGR could be the major reason for difference in the zinc extraction in each of the size fractions evaluated. The results obtained in this work showed that a 10 to 15% additional zinc leach extraction is possible (see Figure 6.6).

The HPGR products for at all pressure settings were finer than that of the cone crusher (see chapter 5). It is known that the presence of excess fines in heap leaching operations may cause low recovery due to reduced heap permeability and/or channelling of lixiviant flow. These problems are mitigated to some extent by agglomeration pre-treatment prior to heap leaching (Kodali *et al*., 2011; Yang *et al*., 2008). In this work, the feed material to the leach reactors had the same selection of the sieve ranges for both the HPGR and cone crusher tests. Eight reactors were prepared and fed with particles in specific size classes produced using either the HPGR or the cone crusher given in Table 3.3. Evaluation of the leach reactors residue indicated significant changes in the PSD compared to the feed as shown in Figures 6.43 to 6.45 for different size fractions of HPGR and cone crusher products.

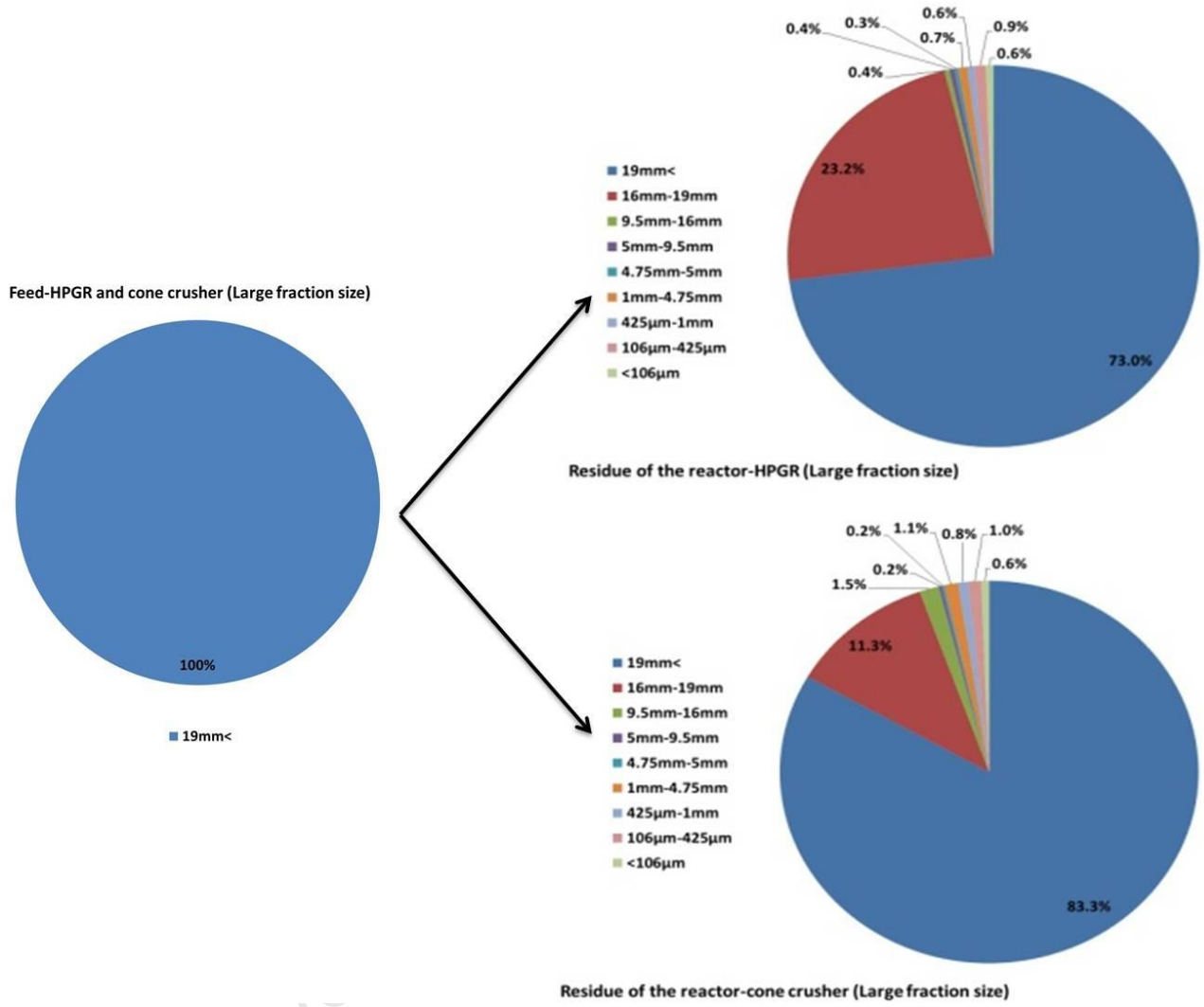

Figure 6.43: Changes in the PSDs of the HPGR and cone crusher products after 11 months leaching process in of the large size fraction.

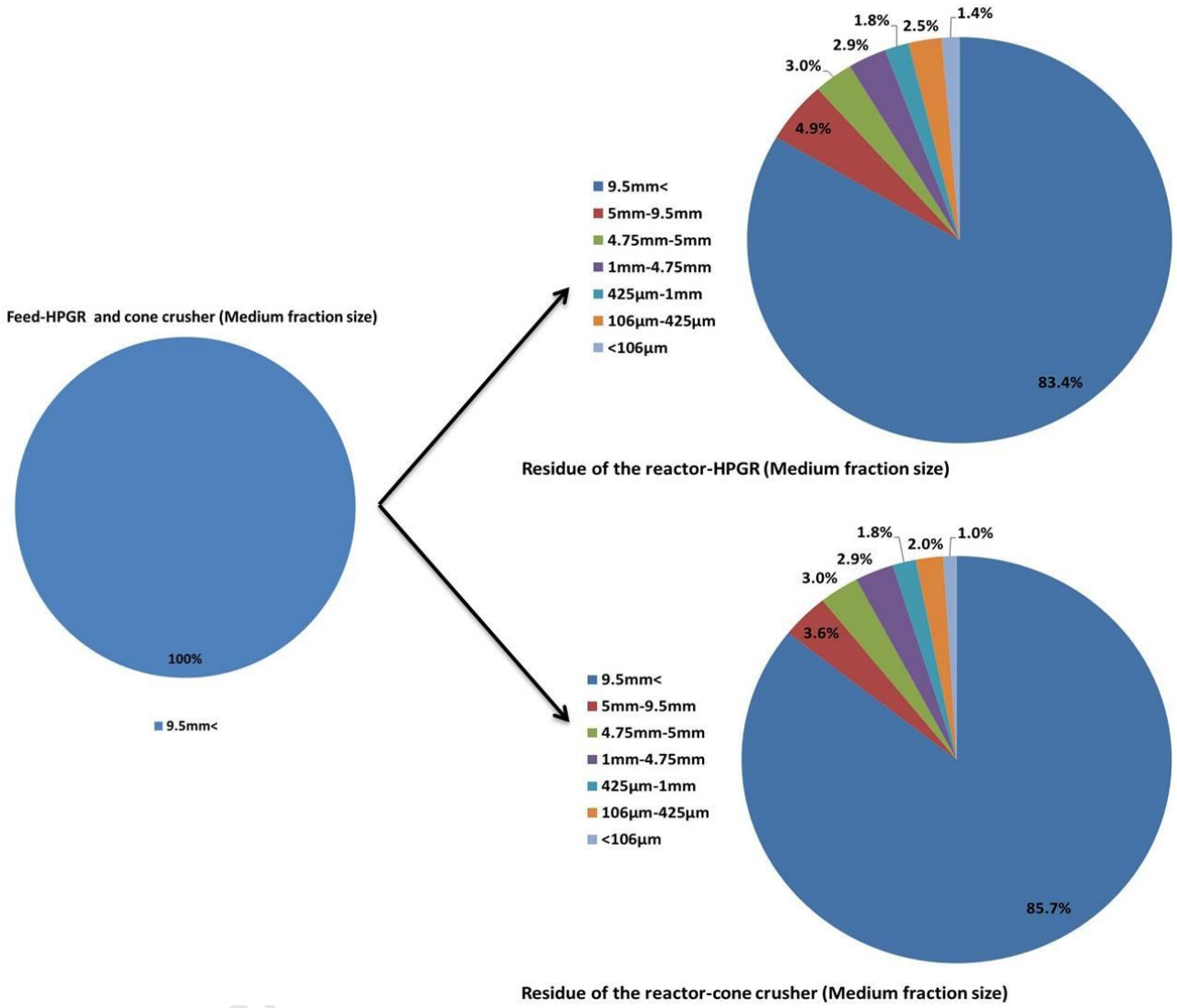

Figure 6.44: Changes in the PSDs of the HPGR and cone crusher products after 11 months leaching process in of the medium size fraction.

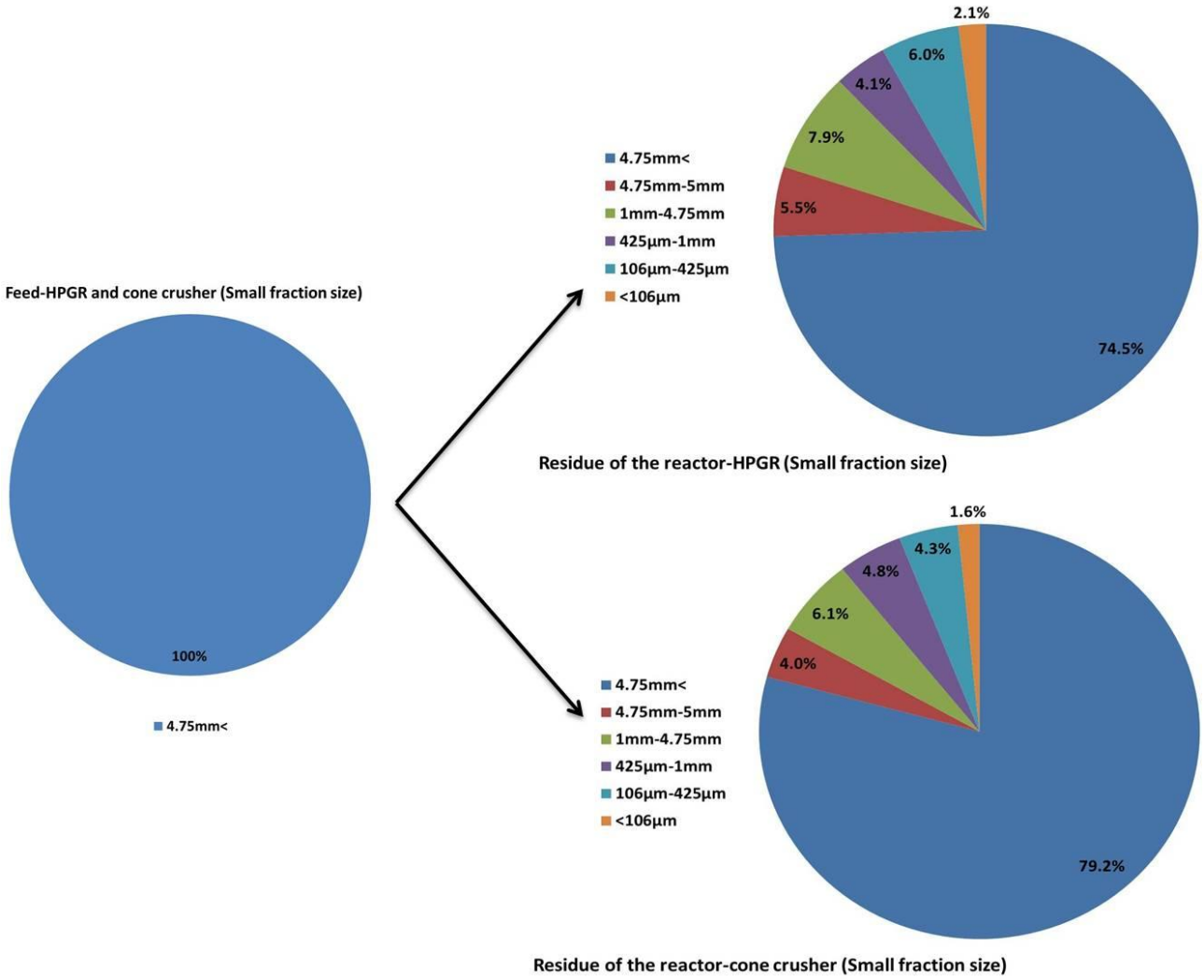

Figure 6.45: Changes in the PSDs of the HPGR and cone crusher products after 11 months leaching process in of the small size fraction.

Although the reactors were fed with specific size fractions, the residue had a size distribution containing even some fines. Results presented in the Figures 6.43-6.45 show that the residues from the reactors leaching the material prepared using the HPGR product contained more fine particles than the reactors, which were fed by cone crusher product. Table 6.8 shows that these differences were in order of 10.3% in large size fraction, 2.3% in the medium size fraction and 4.7 % in the small size fraction. High fine particle fraction in the residue of the leach reactors related to the particles crushed by HPGR could be due to the active crack network growth observed during the leaching.

Since the surface of ore particles and their inner micro pores or cracks are damaged after reacting with sulfuric acid, some fine particles would be produced. The initial crack network in the particles crushed by HPGR increases during the leaching process, which splits each single particles to two or more new ore particles and produces a particles size distribution different to the initial reactor feed.

Table 6.8: Changes in the PSDs after 11 months leaching process in all three size fractions.

Size fraction	Before treatment		Residue of reactors	
	HPGR	cone crusher	HPGR	cone crusher
Large	0% < 23mm		27.0% < 23mm	16.7% < 23mm
Medium	0% < 14mm		16.6% < 14mm	14.3% < 14mm
Small	0% < 5.25 mm		25.5% < 5.25 mm	20.8% < 5.25 mm

However, after leaching, under the combined action of multiple factors, such as hydraulic power, gravity and chemical reactions, newly formed fine particles flow downwards through the pore space among coarse particles and deposited at local areas and an extremely small amount of fine particles are transported out of the reactor by the solution (Kodali *et al*., 2011; Yang *et al*., 2008). Since in this study the solution reagent was introduced to the leach reactors from the bottom and there were basket frames at different level inside the leach reactors (see chapter 3), there was no fine particles transportation out of the reactor. Thus, the ore particles size would have been redistributed in different levels of leach reactors.

The most fundamentally important aspect of heap leaching is permeability of the leach and even percolation of the lixivant solution throughout all the ore. Excessive amounts of the fines generated during the leaching process mostly with the product of HPGR, and

their mobilization would result in reduced permeability as the leaching process progresses, which could have a negative effect on percolation especially over long periods of heap leaching operation. It would also prevent a uniform flow of the solution through the heaps.

7 CONCLUSIONS AND RECOMMENDATIONS

In conclusion then, the work presented in this thesis has shed considerable light on the phenomena occurring inside the solid body of large particles in the course of bioleaching. A comprehensive literature review indicated that the actual progression of leaching within large particles has never been explored systematically and no model used to describe leaching from large particles is based on actual physical observation. Based on this problem statement and a literature review on the current understanding of such processes the following hypotheses were formulated:

- Leaching from large particles occurs only at the surface and in subsurface regions, which are accessible from the surface by cracks and pores.
- The cracks produced by comminution with HPGRs rather than conventional impact crushers significantly promote subsurface leaching.

In order to effectively understand and formulate models for (bio) leaching from large particles, fundamental study of the rate controlling factor(s) was deemed important. The subject of this research was to understand more clearly the diffusion-reaction phenomena of reagents through large particles and to provide true and reliable physical parameters to formulate the relevant modelling approaches to large particle leaching. A combination of standard optical microscopy, SEM, QEMSCAN and X-ray CT techniques were used for the characterization of crack networks and mineral dissemination in the ore particles before and during leach tests to allow conclusions to be drawn of how and where mineral dissolution progresses with time.

In this study, large particle size classes (+23/-25, +14/-16, +5.25/-6.75 mm) were prepared from a sphalerite ore from the Northern Cape, South Africa, by two different methods of comminution (HPGR and cone crusher). Physical and chemical characterization of selected ore particles was done. The ore samples were then leached in continuous flooded packed bed leach reactors. The reactors were stopped from time

to time to investigate the progress of leaching and the colonisation of the surface of the ore particles by sessile cells. The progress of leaching was investigated by analysing individual tagged particles using X-ray CT scanning at regular intervals during leaching. The results were validated using traditional destructive techniques such as SEM/EDS, EMPA and QEMSCAN. It must be stressed that the number of particles thus analysed is not statistically significant and that all deductions based on analysing these must be seen as indicative only.

Unique to this study, X-ray CT has been used for 3D characterization of crack and mineral dissemination in the large ore particles for the first time. In order to distinguish between the different minerals, a dual energy scanning procedure was developed, giving both density and effective atomic number of the scanned mineral. Using this technique, together with 3D image analysis software, sectioned 2D images in different orientation and at different position could be obtained with speed, high accuracy and without the need for laborious sample preparation, and the scanned sample could be returned to the leach reactor for further leaching.

7.1 Mineral characterization

Major minerals identified by QEMSCAN analysis of the feed sample included sphalerite (16.0 wt. %) and pyrite (33.8 wt. %) with lesser pyrrhotite, mica and, kaolinite. Only minor chalcopyrite and galena occurred, as well as alabandite and arsenopyrite (grouped as other sulfides). Quartz was the main silicate gangue mineral (25.5 wt. %). The major impurities in sphalerite are Fe (9.72 ± 0.74 wt. %) and Mn (4.44 ± 1.10 wt. %). The stoichiometric formula of sphalerite based on these major impurities is $(Zn_{0.78}, Mn_{0.07}Fe_{0.15})$ S.

The sphalerite in this study can in general can be divided in two groups, based on the grain size and association. The coarse sphalerite grains (≥ 5 mm) were associated with other base metal sulfides and the disseminated fine sphalerite grains (≤ 1 mm) showed a

stronger association to the gangue minerals. Sphalerite in this study can be further classified into six different classes as a result of their comminution and their expected leaching behaviours:

g. Grains located at the surface of particles and exposed to the leach solution;
h. Grains located close to the surface of particles which become exposed to the leach solutions only after other grains have reacted;
i. Grains located inside the particles and not connected to the surface;
j. Grains located inside the particles but connected to the surface via pores or cracks (detectable only in the particles crushed using HPGR);
k. Grains with size bigger than 5 mm which could be fully liberated in the small size fraction (-6.75+5.25) mm and thus are completely accessible to the leach solution;
l. Fine grains disseminated within the gangue mineral (mostly quartz) that are completely inaccessible to the leach solution.

7.2 Effect of comminution device on crack network and on zinc extraction

The tests were performed using the cone crusher with feed sample at -40 mm top size and crushed down to -25 mm in continuous mode. The HPGR tests were performed at three different pressure settings of 45, 95 and 120 bars, which correspond to the specific grinding forces of 1.42, 3.00 and 3.79 (N/mm^2) respectively. The particle size distribution (PSD) of HPGR products from the three pressure settings were finer than the cone crusher product, with the finest product obtained when HPGR was operated the pressure setting of 95 bars.

In order to compare the effect of the comminution method on crack network generation, selected sample particles from different comminution devices (Jaw crusher, HPGR and cone crusher) were studied in detail, using a combination of standard optical microscopy, SEM, and X-ray CT techniques. QEMSCAN analysis, Mercury Intrusion

Porosimetry and BET Physical Gas Adsorption were also performed for validation purposes.

Quantitative results from the X-ray CT and QEMSCAN analysis of the samples prepared by HPGR were similar (~ 0.75 vs 1.1 %) and any minor differences between the results can be attributed to the fact that the particles analysed were not identical, and that the QEMSCAN is a 2-D measurement technique as opposed to X-ray CT that is a 3-D technique.

Combination of the results of standard optical microscopy, SEM, QEMSCAN and X-ray CT techniques for a comparison of the effect of comminution method on crack network generation, confirmed that HPGR produces particles with a significantly higher density of crack and micro-cracks compared to conventionally crushed products. Although no cracks were detected in the particles prepared by cone crusher, the leach tests indicated, however, that reagent penetration into cone crushed particles was nevertheless possible and it therefore has to be assumed that there exist micro-pores which are not detectable using the techniques employed in this study.

Due to the larger ore particle sizes encountered in heap leaching, the mineral grain distribution and their accessibility to leach solutions by cracks and micro-pores, plays a key role in determining the rate of extraction. The implications of the prevalence of the micro-cracks and higher porosity for particles prepared by HPGR, as compared to cone crushing, is that the larger particles prepared by the HPGR are more likely to be amenable to leaching, since the presence of these micro-cracks provides an additional surface-front of valuable mineral grains for chemical attack by the leaching solution, and a higher prevalence of attachment sites for microorganisms, which would provide for regeneration of ferrous to ferric iron as leach reagent closer to the mineral surface and increase metal recovery.

Comparison of the percentage of zinc extraction of a sphalerite ore over 11 months of leaching from ore crushed by HPGR and cone crusher confirmed that the leachability of the ores was consistently better after high pressure grinding and had a 10 to 15%

additional zinc leach extraction. Higher metal extraction of HPGR ore prepared at 95 bars pressure shows further that preparation at this pressure is the optimum compared to tests using ore crushed at 45 and 120 bars. This indicates that there is an optimum operating pressure where the metal extraction rates are higher, although the three pressures tested did not allow determination of the optimum pressure with any accuracy.

It was furthermore noted that although accessibility to the reagent is necessary, a variety of mineralogical conditions such as mineral association (galvanic interactions), sphalerite composition (concentrations of impurities-e.g. Fe, Mn) and precipitation are the rate-limiting factors.

7.3 Mineral conversion from single ore particles

Investigation of mineral conversion from single ore particles indicated that leaching from large particles occurs leading to near complete conversion close to the surface, but only partial conversion in the grains that are close to the centre of particles. After all minerals near the surface are depleted, leaching regime changes from the readily accessible grains on the particle surface to the more inaccessible grains within particles. Crack and porosity play key role in determining the penetration depth to which reaction is likely to proceed into the ore particles.

In the HPGR product, the reaction zone covers both the particle surface and a significant subsurface rim, which has access to the surface through cracks. In some particles, even grains close to the centre of the particles can dissolve early if they are connected to particularly deep cracks. In the case of the cone crusher product, the outer surface of the particle is the main reaction surface and reaction occurs in the subsurface zones to not nearly the same depth as the particles crushed by HPGR. This implies the existence of micro-cracks in these particles, which are not detectable by the visual techniques used here.

The concept of penetration depth (P_d) was introduced to describe the distance from the surface of a given particle class to which significant progression of leaching was found. In the cracked rim, there is a rapid penetration of leaching reagent through the crack network, but slow leaching from zones between cracks. The results indicated that the penetration depth (P_d) is as function of both the comminution mode and the particle size. It is clear that prevalence of cracks and particle porosity play key roles in increasing the penetration depth, and as these characteristics are more pronounced in HPGR-crushed particles, the conversion front clearly penetrates more deeply in these. A power law as per Eq. (6.1) can describe the correlation between the penetration depth (Pd) and particle radius (R):

$$p_d = aR^b \qquad \text{Eq. (6.1)}$$

With b=0.7-0.8 in a similar range for the products of the two different comminution devices and hence likely to be independent of crushing mode.

7.4 Fitting data with models

Application of the shrinking core and shrinking sphere models showed that leaching from large particles – contrary to common assumption – does not follow either of the two models. In fact, there are three different stages during the leaching process. The first stage is leaching of grains at the surface of the ore particles followed by a second stage, which is leaching of the grains located in the subsurface within the thickness of the penetration depth. A third stage relates to very slow, linear leaching from uncracked zones within the particle, especially the inner core.

Application of a simplified reaction-diffusion system in spherical coordinates showed that there is a good agreement between the trends predicted by a first order particle diffusion-reaction model and the average conversion X (Zn) over time from different position within the ore particle evaluated by direct observation using X-ray CT. This

analysis indicated that this system is more under mixed reaction-diffusion control than under pure diffusion control as is the common assumption.

Values obtained for the rate constant K in the general intrinsic kinetics equation of leaching indicated that in both comminution devices the value for K decreases with increasing particle size. This was expected; since K represents the initial (surface) rate and with increasing particle sizes the specific, surface area (per unit mass of particles) declines. In all three sizes classes for those particles that were crushed using HPGR, the value of K is bigger than that crushed using a cone crusher, which indicates the larger effective surface in the particles crushed using HPGR. A power law as per Eq. (6.16) can represent the correlation between K and particle radius (R):

$$K = \mathrm{cR}^{\mathrm{d}} \qquad \text{Eq. (6.16)}$$

With d≈ (-0.5) almost the same for the products of the two different comminution devices and thus expected to be independent of crushing mode.

An alternative analysis was considered in extension of the intrinsic kinetics equation of the leaching. It is assumed that there is a readily leachable fraction (α) of Zn in the ore, which is accessible through the pore network and a poorly leachable fraction (1-α), which is locked within zones that are not cracked. The general topology model needs to be adjusted that it applies only to the leachable fraction (α) as follows:

$$\frac{dX}{dt} = \mathrm{K}.\left(1 - \frac{X}{\alpha}\right)^{\boldsymbol{\varphi}}$$

Where X remains the overall fractional Zn conversion (i.e. relative to total Zn content).

If a simple linear term (βt) is added to account for the very slow rate at which the reaction proceeds after depletion of the leachable fraction (α), the following overall kinetic equation can be formulated:

$$X(t) = \begin{cases} \alpha\left[1 - \left(1 + (\varphi - 1)\frac{Kt}{\alpha}\right)^{\frac{1}{1-\varphi}}\right] + \beta t & \\ \alpha + \beta t & t > \frac{\alpha}{K(1-\varphi)} \text{ if } \varphi < 1 \end{cases} \quad \text{Eq. (6.19)}$$

The values for φ were ~ 0.75 for the HPGR product and around ~ 0.25 for the cone crusher products and barely change with particle size. The small value of φ for the cone crusher indicates that the leaching is nearly linear, i.e. that exposed mineral is mostly near the surface, which was clearly confirmed by the X-ray CT analysis.

The correlation between the readily leachable fraction (α) and fractional penetration volume $(P_d/R)^3$ follows almost perfect linear trends, further confirming its connection with the extent of the crack and pore network. The very small values estimated for the residual leach rate β indicate that leaching from the uncracked zones (especially at the centre of larger particles) proceeds substantially more slowly and probably follows a different mechanism (solid-state diffusion). In terms of extraction in a heap leaching context this portion of leaching from large particles is essentially beyond the point of economic recovery.

7.5 Implications

Given that unique to heap leaching is the relatively coarse particle size distribution, the major technical challenge is to expose the mineral grains within the ore to the reagent, be it acid, ferric ions or bacteria and oxygen. It has been shown as one of the outcomes of this study that one possible approach to improving recovery in the heap is to introduce fractures into large ore particles, so increasing the surface area available for lixiviant attack. Extensive cracking can be induced in a number of ways; for example using HPGR as investigated in this work, which produces particle with high crack density. Although HPGR shows definite promise in the present case, the larger amounts of fines produced already during crushing could constitute problems with heap permeability. Furthermore, the significant amount of crepitation (i.e. splintering off fines) observed

with the HPGR material during the 11 months leach tests could potentially acerbate the fines problem during percolation further.

In addition, it is clear that large particles >10mm will always have slow leaching from the particle cores (the dynamics of which has not entirely clarified in this work), that perhaps suggests a shift in focus to heap leaching with smaller particles is needed.

Investigation of the residue of the reactors indicated that particle size and accessibility to the reagent is necessary, but a variety of mineralogical conditions can hamper or prevent leaching of an ore, even if well crushed. This therefore calls for systematic mineralogical characterisation of the ore to be incorporated in the heap design process.

By directly observing the leaching of individual ore particles, and the effect of key parameters in terms of crack networks and mineralogy of the ore sample, this research has provided new insights into the underlying mechanisms and the rate-limiting factors on metal extraction, which should give rise to further exploration, possibly with a statistically more significant sample of particles analysed. This work has set out a systematic approach to assess a particular ore in this regard and should set the route forward for systematic design of efficient heap leach operations.

7.6 Future perspectives

The work presented in this thesis has identified a number of aspects, which would merit further investigation in follow up studies. Some of these are listed in the following.

- In this study, X-ray CT was adapted for the major minerals in the zinc ore sample but future improvement and research need to be done to make X-ray CT as versatile a tool as QEMSCAN and MLA for mineral characterization, but in 3D. This kind of approach would be a turning point and revolutionary in process mineralogy, and consequently it will be of benefit to improve the mineral processing techniques used for feed preparation for heap leaching with large ore particles.

- In heap leach applications, the major technical challenge is to expose the mineral grains within the ore to the lixiviant. One possible approach to improving recovery in the heap is to introduce fractures into large ore particles, so increasing the surface area available for lixiviant attack. Extensive cracking can be induced in a number of ways, such as microwave heating of ores and using HPGR for preparing the ore. The results from the tests performed to compare the crack density and metal extraction rate between the particles prepared using the HPGR and cone crusher, are investigated in this study. Further research need to be done to find the right technique with reasonable justification from both technical and economic aspects.

- As discussed, different comminution devices produce different density of cracks and micro-cracks (not detectable using the techniques employed in this study), and crack depth and penetration were related to particle size. A study needs to be done to discern the mode of micro-fissure formation in different cracking modes and their particular relationship to particle size. In addition, one should look at ways to detect such micro-fissures e.g. Focused Ion Beam SEM applications as used in the oil and gas industry for imaging Nano-pore structures, which plays a key role in the diffusion of reagent to the centre of the large ore particles.

- It was furthermore noted that access to a mineral grain is necessary for it to leach but that mineral association (Galvanic effect), target mineral composition (impurity) and precipitation are the rate-limiting factors and play key role in the leaching rate. This highlights the necessity for conducting a detailed multivariate (i.e. mineralogical, petrographical, mineral chemical) investigation in order to obtain a better understanding of the metallurgical behaviour and/or constraints imparted by the ore.

- Excessive amounts of fines were generated during HPGR crushing and the subsequent leaching testwork, and their mobilization would have negative effects on the permeability during the process and could have a negative effect on percolation especially over long periods of heap leaching operation. Further research need to be done to investigate the applicability of HPGR in preparing of the feed for heap from both a technical and economical perspective.

- This study has proposed an appropriate assessment and modelling approach to large particle leaching. This approach needs to be further evaluated and substantiated by similarly systematic experiments using different ore types.

8 REFERENCES

Acevedo, F., 2002, Present and future of bioleaching in developing countries. Electronic Journal of Biotechnology, 52-56.

Africa, C. J., Harrison, S. T. L., Becker, M. and van Hille, R. P., 2010, In situ investigation and visualisation of microbial attachment and colonisation in a heap bioleach environment: the novel biofilm reactor, Minerals Engineering, 23, 486-491.

Ahonen, L., Tuovinen, O. H., 1995, Bacterial leaching of complex sulfide ore samples in bench-scale column reactors. Hydrometallurgy, 37, 22-36.

Al-Harahsheh, M. ,Kingman, S. b., Bradshaw, S., 2006, The reality of non-thermal effects in microwave assisted leaching systems?, Hydrometallurgy, 84, 1-13.

Apling, A. and Bwalya, M. 1997, Evaluating high pressure milling for liberation enhancement and energy saving, Minerals Engineering, 10, 1013-1022.

Arce, E. M., González, I., 2002, A comparative study of electrochemical behaviour of chalcopyrite, chalcocite and bornite in sulphuric acid solution, Int. J. Miner. Process, 67, 17-28.

Bachu, S. and Cuthiell, D., 1990, Effects of core-scale heterogeneity on steady state and transient fluid flow in porous media: numerical analysis. International Journal of Rock Mechanics and Mining Sciences Geomechanics Abstracts, 27, 341-352.

Baláž, P., Kušnierová, M., Varencova, V.I. and Mišura, B., 1994, Mineral properties and bacterial leaching of intensively ground sphalerite and sphalerite- pyrite mixture. International Journal of Mineral Processing, 40, 273-291.

Barstlett, R. W., 1992, Simulation of ore heap leaching using deterministic models, Hydrometallurgy, 29, 231-243.

Barston, P. B., Bethke P. M., 1987, Chalcopyrite disease in sphalerite: Pathology and epidemiology, American Mineralogist, 72, 451-467.

Bartlett, R.W., 1992. Simulation of ore heap leaching using deterministic models, Hydrometallurgy, 29, 231-243.

Bhatti, T.M., Bigham, J. M., Vuorinen, A., Tuovinen, O. H., 2011, Weathering of phlogopite in simulated bioleaching solutions, International Journal of Mineral Processing, 98, 30-34

Bhatti, T.M., Bigham, J. M., Vuorinen, A., Tuovinen, O. H., 2012, Chemical and bacterial leaching of metals from black schist sulfide minerals in shake flasks, International Journal of Mineral Processing, 110-111, 25-29.

Bigham, J. M., Bhatti, T.M., Vuorinen, A., Tuovinen, O. H., 2001, Dissolution and structural alteration of phlogopite mediated by proton attack and bacterial oxidation of ferrous iron, Hydrometallurgy , 59, 301-309.

Boespflug, X., Long, B.F.N., Occhietti, S., 1995. CAT-scan in marine stratigraphy: a quantitative approach. Marine Geology 122, 281-301.

Boon, M., 2001, The mechanism of 'direct' and 'indirect' bacterial oxidation of sulfide minerals. Hydrometallurgy, 62, 67-70.

Bouffard, S. C. and Dixon, D. G., 2001, Investigative study into the hydrodynamics of heap leaching processes. Metallurgical and Materials Transactions B., 32, 763-776.

Bouffard, S. C., 2003, Understanding the Heap Biooxidation of Sulfidic Refractory Gold Ores. PhD Dissertation University of British Columbia, 2003.

Brandl, H., Bosshard, R., Wegmann, M., 2001, Computer-munching microbes: metal leaching from electronic scrap by bacteria and fungi, Hydrometallurgy 59, 319-326.

Braun, R. L., Lewis, A. E. and Wadsworth, M. E., 1974, In-place leaching of primary sulfide ores: Laboratory leaching data and kinetics model. Metallurgical and Materials Transactions B., 5, 1717-1726.

Brierley, C.L., 2008, How will biomining be applied in future? Transactions of Nonferrous Metals Society of China, 18, 1302-1316.

Bryan C.G., Davis-Belmar C., van Wyk N., Dew D., Rautenbach G. and Harrison S.T.L., 2012, The effect of CO_2 availability on the growth, iron oxidation and CO_2 fixation rates of pure cultures of *Leptospirillum ferriphilum* and *Acidithiobacillus ferrooxidans*. *Biotechnology and Bioengineering* (in press). Doi: 10.1002/bit.24453.

Cariaga, E., Conchac, F. and Sepúlveda, M., 2005, Flow through porous media with applications to heap leaching of copper ores. Chemical Engineering Journal, 111, 151-164.

Carlsson, E. and Büchel, G., 2005, Screening of residual contamination at a former uranium heap leaching site, Thuringia, Germany. Chemie der Erde-Geochemistry, 65, 75-95.

Celik, I.B., Oner, M., 2006, The influence of grinding mechanism on the liberation characteristics of clinker minerals, Cement and Concrete Research, 36, 422-427.

Chandraprabha, M., Modak, J., Natarajan, K., Raichur A., 2003, Modelling and analysis of biooxidation of gold bearing pyrite-arsenopyrite concentrates by Thiobacillus ferrooxidans. Biotechnology Progress, 19, 54-65.

Chen, J.H., Chen, Y., LI, Y. G., 2010, Effect of vacancy defects on electronic properties and activation of sphalerite (110) surface by first-principles, Trans. Nonferrous Met. Soc. China, 20, 502-506.

Chiume, R., Minnaar, S.H., Ngoma, I.E., Bryan, C., and Harrison, S. T. L., 2012, Microbial Colonisation in Heaps for Mineral Bioleaching and the Influence of Irrigation Rate, currently under review.

Clark, D.A., Norris, P.R., 1996, Oxidation of mineral sulfides by thermophilic microorganism, Minerals Engineering, 9, 1119-1125.

Coles, M.E., Hazlett, R.D., Spanne, P., Soll, W.E., Muegge, E.L., Jones, K.W., 1998, Pore level imaging of fluid transport using synchrotron X-ray microtomography. Journal of Petroleum Science and Engineering, 19, 55-63.

Cook, N.J., Ciobanu, C.L., Pring, A., Skinner W., Shimizu, M., Danyushevsky, L., Eidukat, B.S., Melcher, F., 2009, Trace and minor elements in sphalerite: A LA-ICPMS study, Geochimica et Cosmochimica Acta, 73, 4761-4791.

Cruz, R., Luna-Sánchez, R.M., Lapidus, G.T., González, I., Monroy, M., 2005, An experimental strategy to determine galvanic interactions affecting the reactivity of sulfide mineral concentrates, Hydrometallurgy, 78, 198-208.

Dai, X. and Jeffrey, M.I., 2006, The effect of sulfide minerals on the leaching of gold in aerated cyanide solutions. Hydrometallurgy, 82, 118-231.

Daniel, M. J., 2007, Energy efficient mineral liberation using HPGR technology, PhD thesis, University of Queensland.

Davis, G. B. and Ritchie, A. I. M., 1987, A model of oxidation in pyritic mine wastes: part 1 equations and approximate solution. Applied mathematical modelling, 11, 417-422.

De Beer, F.C., Coetzer, M., Fendeis, D. and Silva, A.D.C.E., 2004, Neutron radiography and other NDE tests of main rotor helicopter blades, Applied Radiation and Isotopes, 61, 609-616.

Demir, L., Sahin, M., 2009, Determination of mass attenuation coefficients, effective atomic and electron numbers for some natural minerals, Radiation Physics and Chemistry 78, 760-764.

Deschamps, T., Benzaazoua, M., Bussière, B., Aubertin, M. and Belem, T., 2008, Microstructural and geochemical evolution of paste tailings in surface disposal conditions. Minerals Engineering, 21, 341-364.

Devasia, P., Natarajan, K.A., Sathyanarayan, D.N., Rao, G.R., 1993, Surface chemistry of Thiobacillus ferrooxidans relevant to adhesion on mineral surfaces, Appl Environ Microbiol, 59, 4051-4055.

Deveci, H., Akcil, A. and Alp, I., 2004, Bioleaching of complex zinc sulfides using mesophilic and thermophilic bacteria: comparative importance of pH and iron, Hydrometallurgy, 73, 293-310.

Dew, D. W., Rautenbach, D., Harvey, I., Truelove, J., and van Hille, R. P., 2011, High Temperature Heap Leaching of Chalcopyrite: Method of Evaluation and Process Model Validation , International Conference on Percolation leaching: The status globally and in southern Africa, 8-9 November 2011 , Misty Hills, Muldersdrift, South Africa, 221-236.

Dixon, D. G., 2000, Analysis of heat conservation during copper sulfide heap leaching. Hydrometallurgy, 58, 27-33.

Dixon, D.G., and Petersen, J., 2003, Comprehensive Modelling Study of Chalcocite Column and Heap Bioleaching; in Copper-Volume VI: Hydrometallurgy of Copper (Book 2), P.A. Riveros, D. Dixon, D. Dreisinger, J. Menacho (eds.), CIM, Montreal, Canada, 493-516.

Dreisinger, D., 2006, Copper leaching from primary sulfides: Options for biological and chemical extraction of copper, Hydrometallurgy, 83, 10-21.

Evans, K.A. and Banwart, S.A., 2006, Rate controls on the chemical weathering of natural polymineralic material. I. Dissolution behaviour of polymineralic assemblages determined using batch and unsaturated column experiments Applied Geochemistry, 21, 352-363.

Fandrich, R., Gu, Y., Burrows, D., Moeller, K., 2007, Modern SEM-based mineral liberation analysis, Int. J. Miner. Process., 84, 310-320.

Garcia, D., Lin, C.L. and Miller, J.D., 2009, Quantitative analysis of grain boundary fracture in the breakage of single multiphase particles using X-ray microtomography procedures. Minerals Engineering, 22, 236-243.

Gehrke, T., Telegdi, J., Thierry, D., Sand, W., 1998, Importance of extracellular polymeric substances from Thiobacillus ferrooxidans for bioleaching. Appl. Environ. Microbial, 64, 2743-2747.

Gerke, H. H., Molson, J. W. and Frind, E. O., 1998, Modelling the effect of chemical heterogeneity on acidification and solute leaching in overburden mine spoils. Journal of Hydrology, 209, 166-176.

Gottlieb, P., 2008, The revolutionary impact of automated mineralogy on mining and mineral processing. In: Wang Dian Zuo, Sun Chuan Yao, Wang Fu Liang, Zhang Li Cheng, Hang Long, (Eds.), The XXIV International Mineral Processing Congress, 165-174.

Hansford, G.S., 1997, Recent development in modelling the kinetics of bioleaching. In In: Rawlings DE, ed. Biomining: Theory, Microbes and Industrial Processes. Springer-Verlag, Berlin, 151-175.

Hansford,G.S., Vargas, T., 2001, Chemical and electrochemical basis of bioleaching processes, Hydrometallurgy 59, 135-145.
Haque, K.E., 1999, Microwave energy for mineral treatment processes- a brief review. International Journal of Minerals Processing, 57, 1-24.

Harmer, S.L., Goncharova, L.V., Kolarova, R., Lennard, W.N., Munoz-Marquez, M.A., Mitchell, I.V., Nesbitt, H.W., 2007, Surface structure of sphalerite studied by medium energy ion scattering and XPS , Surface Science, 601, 352-361.

Harneit, K., Göksel, A., Kock, D., Klock, J.-H., Gehrke, T. and Sand, W., 2006, Adhesion to metal sulfide surfaces by cells of Acidithiobacillus ferrooxidans, Acidithiobacillus thiooxidans and Leptospirillum ferrooxidans. Hydrometallurgy, 83, 245-254.

Helle, S., Kelm, U., Barsrientos, A., Rivas, P. and Reghezza, A., 2005, Improvement of mineralogical and chemical characterization to predict the acid leaching of geometallurgical units from Mina Sur, Chuquicamata, Chile. Minerals Engineering, 18, 1334-1353.

Herrero, D., Arias, P.L., Güemez, B., Barsrio, V.L., Cambra, J.F., Requies, J., 2010, Hydrometallurgical process development for the production of a zinc sulfate liquor suitable for electrowinning, Minerals Engineering, 23, 511-517.

Hsih, C. S., Wen, S. B. and Kuan, C. C., 1995, An exposure model for valuable components in crushed particles, International Journal of Mineral Processing, 43, 145-153.

http://electrochem.cwru.edu/encycl/art-m02-metals.htm

http://www.goldenqueen.com/gall07.htm

Jones, D.A., Kingman, S.W., Whittles, D.N., Lowndes, I.S., 2005, Understanding microwave assisted breakage. Minerals Engineering, 18, 659-669.

Kingman, S.W., Jackson, K., Bradshaw, S.M., Rowson, N.A., Greenwood, R., 2004, An investigation into the influence of microwave treatment on mineral ore comminution, Powder Technology, 146, 176-184.

Kingman, S.W., Rowson, N.A., 1998. Microwave treatment of minerals-a review. Minerals Engineering 11, 1081-1087.

Kirjavainen, V. and Heiskanen, K., 2007, Some factors that affect beneficiation of sulfide nickel-copper ores. Minerals Engineering, 20, 629-641.

Klymowsky, R., Patzelt, N., Knecht, J. and Burchardt, E., 2002, Selection and sizing of high pressure grinding rolls, Mular, A.L., Halbe, D., and Barsratt, D.J. (Eds.), Mineral Processing Plant

Design, Practice, and Control, Society for mining, metallurgy, and exploration, Inc. (SEM), Littleton. Colorado, USA, 636-668.

Knackstedt, M., Middleton, J., Turner, M., Butcher, A., Jaime, P., Botha, P., Shrestha, P., 2010, 4D Characterization of Cu Leach Residue Samples using 3D Imaging & Analysis (Digital core) Technology, Process Mineralogy Conference, 10–12 November, Cape Town, South Africa.

Kocabag, D., 1985, The effect of grinding media and galvanic interactions upon the flotation of sulfide minerals. Complex Sulfides, Process Symposium, 5, pp. 81-97.

Kodali, P., Depci, T., Nikhil Dhaw ,N., Wang, X., Lin, C.L., Miller, J. D., 2011, Evaluation of stucco binder for agglomeration in the heap leaching of copper ore, Minerals Engineering, 24, 886-893.

Leahy, M.J., Davidson, M.R. and Schwarz, M.P., 2007, A model for heap bioleaching of chalcocite with heat balance: Mesophiles and moderate thermophiles. Hydrometallurgy, 85, 24-39.

Lefebvre, R., Hockley, D., Smolensky, J. and Gélinas, P., 2001, Multiphase transfer processes in waste rock piles producing acid mine drainage: 1: Conceptual model and system characterization. Journal of Contaminant Hydrology, 52, 137-151.

Leonard, R.A, Weed, S.B., 1970, Mica weathering rate as related to mica type and composition, Clays and Clay Minerals, 18, 187-195.

Liddell, K. C., 2005, Shrinking core models in hydrometallurgy: What students are not being told about the pseudo-steady approximation, Hydrometallurgy, 79, 62-72.

Lin, C.L. and Miller, J.D., 2005, 3D characterization and analysis of particle shape using X-ray microtomography (XMT). Powder Technology, 154, 61-73.

Liu, Q., Li, H., Zhou, L., 2008, Galvanic interactions between metal sulfide minerals in a flowing system: Implications for mines environmental restoration, Applied Geochemistry, 23, 2316-2323.

López Pérez, R., Miguel Nieto, J. and Ruiz de Almodóvar, G., 2007, Utilization of fly ash to improve the quality of the acid mine drainage generated by oxidation of a sulfide-rich mining waste: Column experiments. Chemosphere, 67, 1637-1645.

Malik, A., Dastidar, M. G. and Roychoudhury, P. K., 2004, Factors limiting bacterial iron oxidation in biodesulphurization system. International Journal of Mineral Processing, 73, 34-42.

Malmström, M. E., Berglund, S. and Jarsjö, J., 2008, Combined effects of spatially variable flow and mineralogy on the attenuation of acid mine drainage in groundwater, Applied Geochemistry, 23, 1419-1422.

Mazuelos, A., Palencia, I., Romero, R., Rodríguez, G. and Carranza, F., 2001, Ferric iron production in packed bed bioreactors: influence of pH, temperature, particle size, bacterial support material and type of air distributor. Minerals Engineering, 14, 507-512.

McClung, C.R., Viljoen, F., 2011, A detailed mineralogical assessment of sphalerite from the Gamsberg zinc deposit, South Africa: The manganese conundrum, Minerals Engineering, 24, 930-938.

Mehta, A.P. and Murr, L.E., 1983, Fundamental studies of the contribution of galvanic interaction to acid-bacterial leaching of mixed metal sulfides. Hydrometallurgy, 9, 235-342.

Mellado, M. E., Cisternas, L. A. and Gálvez, E. D., 2009, An analytical model approach to heap leaching. Hydrometallurgy, 95, 33-42.

Miller, G., 2003, Ore geotechnical effects on copper heap leach kinetics, TMS (The Minerals, Metals and Materials Society), 329-342.

Miller, J. D., Lin,C. L., Garcia, C. and Arias, H., 2003, Ultimate recovery in heap leaching operations as established from mineral exposure analysis by X-ray microtomography. International Journal of Mineral Processing, 72, 331-342.

Moreno, L., Martinez, J. and Casas, J., 1999, Modelling of bioleaching copper sulfide ores in heaps or dumps. Process Metallurgy, 9, 443-453.

Morey, M.S., Grano, S.R., Ralston, J., Prestidge, C.A., Verity, B., 2001, The electrochemistry of Pb activated sphalerite in relation to flotation, Minerals Engineering, 14, 1009-1017.

Muñoz, J. F., Rengifo, P. and Vauclin, M., 1997, Acid leaching of copper in a saturated porous material: Parameter identification and experimental validation of a two-dimensional transport model, Journal of Contaminant Hydrology, 27, 11-23.

Muñoz, J.A., Blázquez, M.L., González, F., Ballester, A., Acevedo, F., Gentina, J. C., González, P., 2006, Electrochemical study of enargite bioleaching by mesophilic and thermophilic microorganisms, Hydrometallurgy 84, 175-186.

Murphy, R., Strongin, D. R., 2009, Surface reactivity of pyrite and related sulfides, Surface Science Reports, 64, 1-45.

Nicol, M., Miki, H., Rautenbach, D., Velasques, L., van Buuren, L., 2011, The development of heap leaching in chloride solution for primary and secondary copper minerals, International Conference on Percolation leaching: The status globally and in southern Africa, 8-9 November 2011 ,Misty Hills, Muldersdrift, South Africa, 221-236.

Ogbonna, N., Petersen, J. and Laurie, H., 2006, An agglomerate scale model for the heap bioleaching of chalcocite, The Journal of the South African Institute of Mining and Metallurgy, 106, 433-442.

Olubambi, P.A., Ndlovu, S., Potgieter, J.H. and Borode, J.O., 2007, Effects of ore mineralogy on the microbial leaching of low grade complex sulfide ores. Hydrometallurgy, 86, 96-112.

Otte, O., 1988, Polycom high pressure grinding principles and industrial application, Third Mill Operators' Conference, Cobars NSW, AusIMM: pp 131-136.

Padilla, G. A., Cisternas, L. A. and Cueto, J. Y., 2008, On the optimization of heap leaching. Minerals Engineering, 21, 673-683.

Pantelis, G., Ritchie, A. I. M. and Stepanyants, Y. A., 2002, A conceptual model for the description of oxidation and transport processes in sulphidic waste rock dumps. Applied Mathematical Modelling, 26, 751-769.

Park, J. Y. and Levenspiel, O., 1977, The crackling core model for the multistep reaction of solid particles. Chemical Engineering Science, 32, 233-243.

Petersen, J and Dixon, D.G., 2002, Systematic modelling of heap leaching processes for optimisation and design. Proceedings of the EPD Congress and Fundamentals of Advanced Materials for Energy Conversion. TMS, 757-771.

Petersen, J., 2010, Modelling of bioleach processes: Connection between science and engineering. Hydrometallurgy, 104, 404-409.

Petersen, J., and Dixon, D.G., 2007, Modelling and optimization of heap bioleach processes, In Biomining, Rawlings, D.E. and Johnson D.B. (Eds.), Springer, Berlin, 153-175.

Petersen, J., and Dixon, D.G., 2007, Modelling zinc heap bioleaching. Hydrometallurgy, 85, 127-136.

Pogliani, C., Donati, E., 1999, The role of exopolymers in the bioleaching of a non-ferrous metal sulfide. J. Ind. Microbiol. Biotech, 22, 88-92.

Pownceby, M.I., MacRae, C.M. and Wilson, N.C., 2007, Mineral characterisation by EPMA mapping. Minerals Engineering, 20, 444-461.

Pradhan, K.C., Nathsarma, K., Srinivasa, R., Sukla, L.B. and Mishra, B.K., 2008, Heap bioleaching of chalcopyrite: A review. Minerals Engineering, 21, 355-362.

Prosser, A.P., Box, J.C., 1983. Simulation of the mineralogical and chemical aspects of heap and dump leaching as an aid to ore-proc. Australasian Institute of Mining and Metallurgy.

Raghavan, R., Upadhyay, R.N., 1999, Innovative hydrometallurgical processing technique for industrial zinc and manganese process residues, Hydrometallurgy, 51, 207-226.

Rao, S.R., Finch, J.A., 1988, Galvanic interaction studies on sulphide minerals. Canadian Metallurgical Quarterly 27, 253-259.

Rattanasak, U., Kendall, K., 2005, Pore structure of cement/pozzolan composites by X-ray microtomography. Cement and Concrete Research 35, 637-640.

Rawlings, D. E., Tributsch H. and Hansford, G. S., 1999, Reasons why '*Leptospirillum*'-like species rather than Thiobacillus ferrooxidans are the dominant iron-oxidizing bacteria in many commercial processes for the biooxidation of pyrite and related ores", Microbiology, 145, 5-13.

Rawlings, D., 2005, Characteristics and adaptability of iron and sulphur-oxidising microorganisms used for the recovery of metals from minerals and their concentrates", Microbial Cell Factories, 4, 312-322.

Rawlings, D., Dew, D. and du Plessis, C. 2003, Biomineralization of metal-containing ores and concentrates, TRENDS in Biotechnology, 21, 39-44.

Remeysen, K., Swennen, R., 2008, Application of microfocus computed tomography in carbonate reservoir characterization: possibilities and limitations. Marine and Petroleum Geology, 25, 486-501.

Rodríguez, Y., Ballester, A., Luisa, B., González, M., Angel, M. J., 2003, Study of Bacterial Attachment During the Bioleaching of Pyrite, Chalcopyrite, and Sphalerite, Geomicrobiology Journal, 20,131-141.

Rohwerder, T., Gehrke, T., Kinzler, K. and Sand, W., 2003, Bioleaching review part A: Progress in bioleaching: fundamentals and mechanisms of bacterial metal sulfide oxidation, Applied Microbiology & Biotechnology, 63, 239-248.

Roman, R.J. and Olsen, C., Theoretical scale-up of heap leaching. Solution Mining Symposium, AIME. 1974, 211-229.

Rossi, G., 1990, Biohydrometallurgy. McGraw-Hill, New York.

Sand, W., Gehrke, T., 2006, Extracellular polymeric substances mediate bioleaching/ biocorrosion via interfacial processes involving iron (III) ions and acidophilic bacteria", Research in Microbiology 157, 49-56.

Sand, W., Gehrke, T., Jozsa, P. G., Schippers, A., 1999, Direct versus indirect bioleaching. In: Amils, R., Ballester, A. (Eds.), Biohydrometallurgy and the Environment toward the Mining of the 21st Century, Part A. Elsevier, Amsterdam, 27-49.

Sandström, Å. and Petersson, S., 1997, Bioleaching of a complex sulfide ore with moderate thermophilic and extreme thermophilic microorganisms, Hydrometallurgy, 46, 181-188.

Santos, M.C. S., Machado, M. R., Correia, M. J.N., Reis, M. T.A., Ismael, M. R. C., Carvalho, J.M.R. 2010,Ferric sulfate/chloride leaching of zinc and minor elements from a sphalerite concentrate, Minerals Engineering, 23, 606-615.

Sasaki, K., Nakamuta, Y., Hirajima, T., Tuovinen, O.H., 2009, Raman characterization of secondary minerals formed during chalcopyrite leaching with Acidithiobacillus ferrooxidans, Hydrometallurgy 95, 153-158.

Schönert, K. and Lui, J., 1996, Modelling of inter-particle breakage. International Journal of Mineral Processing, 44, 101-115.

Schönert, K., 1988, A first survey of grinding with high-compression roller mills, International Journal of Mineral Processing, 22, 401-412.

Schouwstra, R., De Vaux, D., Hey, P., Malysiak, V., Shackleton, N., Bramdeo, N., 2010, Understanding Gamsberg-A geometallurgical study of a large stratiform zinc deposit , Minerals Engineering, 23, 960-967.

Senanayake, G., 2007, Review of rate constants for thiosulfate leaching of gold from ores, concentrates and flat surfaces: Effect of host minerals and pH, Minerals Engineering, 20, 5-14.

Shafer, J.L., White, M.L., Caenepeel, C.L., 1979. Application of the shrinking core model for copper oxide leaching. In: AIME Transactions AIME.

Shakir, K., Aziz, M., Beheir, S. B., 1992, Studies on uranium recovery from a uranium bearing phosphatic sandstone by a combined heap leaching-liquid-gel extraction process. 1 Heap leaching, Hydrometallurgy, 31, 29-40.

Sidborn, M., Casas, J. Martínez, J. and Moreno, L., 2003, Two-dimensional dynamic model of a copper sulfide ore bed, Hydrometallurgy, 71, 67-81.

Silva, G.D., 2004, Relative importance of diffusion and reaction control during the bacterial and ferric sulfate leaching of Zinc sulfide , Hydrometallurgy 73, 313-324.

Silverman, M. P., Ehrlich, H. L., 1964, Microbial formation and degradation of minerals. Adv Appl Microbiol, 6, 181-183.

Solymar, M. and Fabricius, I. L., 1999, Image analysis and estimation of porosity and permeability of Arnager Greensand, Upper Cretaceous, Denmark. Physics and Chemistry of the Earth, 24, 587-599.

Spry, P. G. , Petersen, E. U., 1989, Zincian högbomite as an exploration guide to metamorphosed massive sulphide deposits, Mineralogical Magazine, 53, 263-969.

Sracek, O., Gélinas, P., Lefebvre, R. and Nicholson, R. V., 2006, Comparison of methods for the estimation of pyrite oxidation rate in a waste rock pile at Mine Doyon site, Quebec, Canada. Journal of geochemical exploration, 91, 99-112.

Strömberg, B. and Banwart, S., 1999, Experimental study of acidity-consuming processes in mining waste rock: some influences of mineralogy and particle size. Applied Geochemistry, 14, 1-13.

Suzuki, I., Microbial leaching of metals from sulfide minerals. Biotechnology Advances, 2001, 19, 119-129.

Thiel, R. and Smith, M. E., 2004, State of the practice review of heap leach pad design issues, Geotextiles and Geomembranes, 22, 555-571.

Toniazzo, V., Lazaro, I., Humbert, B., Mustin, C., 1999, Bioleaching of pyrite by Thiobacillus ferrooxidans: fixed grains electrode to study superficial oxidized compounds, Earth and Planetary Science, 328, 535-540.

Tributsch, H., 2001, Direct versus indirect bioleaching, Hydrometallurgy, 59, 177-185.

Tromans, D. and Meech, J. A., 1999, Enhanced dissolution of minerals: Microtopography and mechanical activation. Minerals Engineering, 12, 609-616.

Tromans, D., Meech, J. A., 2002, Enhanced dissolution of minerals: Conjoint effects of particle size and microtopography, Minerals Engineering 15, 263-269.

Tsakiroglou, C.D., Payatakes, A.C., 2000, Characterization of the pore structure of reservoir rocks with the aid of serial sectioning analysis, mercury porosimetry and network simulation. Advances in Water Resources, 23, 773-789.

Ubaldini, S., Veglió, F., Toro, L. and Abbruzzese, C., Biooxidation of arsenopyrite to improve gold cyanidation: study of some parameters and comparison with grinding. International Journal of Mineral Processing, 1997, 52, 65-71.

Unlanda, G. and Szczelina, P., 2004, Coarse crushing of brittle rocks by compression. International Journal of Mineral Processing, 74, 209-223.

Urbano, G., Meléndez, A.M., Reyes, V.E., Veloz, M.A. and González, I., 2007, Galvanic interactions between galena-sphalerite and their reactivity International Journal of Mineral Processing, 82, 148-159.

Van Geet, M., Swennen, R. and Wevers, M., 2000, Quantitative analysis of reservoir rocks by microfocus X-ray computerised tomography, Sedimentary Geology, 132, 25-36.

Van Geet, M., Swennen, R., David, P., 2001, Quantitative coal characterisation by means of microfocus X-ray computer tomography, colour image analysis and back-scattered scanning electron microscopy, International Journal of Coal Geology 46, 11-25.

Van Geet, M., Volckaert, G. and Roels, S., 2005, The use of microfocus X-ray computed tomography in characterising the hydration of a clay pellet/powder mixture, Applied Clay Science, 29, 73-87.

Vegliò, F., Trifoni, M., Pagnanelli, F. and Toro, L., 2001, Shrinking core model with variable activation energy: a kinetic model of manganiferous ore leaching with sulphuric acid and lactose. Hydrometallurgy, 60, 167-179.

Velardo, A., Giona, M., Adrover, A., Pagnanelli, F. and Toro, L., 2002, Two-layer shrinking-core model: parameter estimation for the reaction order in leaching processes. Chemical Engineering Journal, 90, 231-240.

Watling, H.R., 2006, The bioleaching of sulfide minerals with emphasis on copper sulfides-A review, Hydrometallurgy, 84, 81-102.

Weisener, C. G., Smart, R. St.C., Gerson, A. R., 2004, A comparison of the kinetics and mechanism of acid leaching of sphalerite containing low and high concentrations of iron, Int. J. Miner. Process, 74, 239-249.

Xia, L., Dai, S., Yin, C., Hu, Y., Liu, J., Qiu, G., 2009, Comparison of bioleaching behaviours of different compositional sphalerite using *Leptospirillum ferriphilum*, *Acidithiobacillus ferrooxidans* and *Acidithiobacillus caldus*, J Ind Microbiol Biotechnol, 36, 845-851.

Yang, B.H., Wu, A.-X., Jiang, H.C. and Chen, X.S., 2008, Evolution of permeability of ore granular media during heap leaching based on image analysis. Transactions of Nonferrous Metals Society of China, 18, 426-433.

APPENDICES

Appendix I: Ore sample characterization using XRF and QEMSCAN

Chemical assay of the leach reactors feed in the different before treatment using XRF (%)								
	Leach reactors							
	A	B	C	D	E	F	J	K
SiO_2	34.88	35.23	36.07	36.86	34.30	37.54	36.81	36.25
TiO_2	0.30	0.30	0.30	0.30	0.28	0.33	0.31	0.28
Al_2O_3	7.15	7.06	7.04	7.12	6.73	7.46	7.53	7.51
Fe_2O_{3r}	2.81	0.16	1.83	0.43	2.83	3.56	0.94	2.07
MnO	0.55	0.46	0.51	0.41	0.54	0.53	0.50	0.47
MgO	0.62	0.60	0.54	0.50	0.54	0.66	0.55	0.55
CaO	0.30	0.27	0.21	0.33	0.29	0.35	0.28	0.22
Na_2O	0.00	0.00	0.00	0.00	0.00	0.00	0.00	0.00
K_2O	0.85	0.89	0.80	0.70	0.83	0.91	0.98	0.91
P_2O_5	0.22	0.22	0.17	0.26	0.22	0.24	0.23	0.19
Cr_2O_3	0.04	0.05	0.05	0.04	0.05	0.04	0.04	0.03
NiO	0.00	0.00	0.00	0.00	0.00	0.00	0.00	0.00
S	21.17	22.41	21.03	21.53	21.91	19.65	21.15	20.78
Zn	11.90	12.36	13.53	12.64	11.57	11.67	12.80	12.01
Pb	0.57	0.35	0.22	0.32	0.51	0.39	0.10	0.52
Cu	0.01	0.01	0.01	0.01	0.02	0.02	0.01	0.01
Fe-sul	18.25	19.50	17.17	18.29	19.32	16.58	17.78	17.72
Total	99.64	99.87	99.51	99.75	99.94	99.91	99.99	99.52
Fe-sul	Fe estimated present in sufides							
Fe_2O_{3r}	Fe residual present in oxides and/or silicates							

Chemical assay of the residue of leach reactors using XRF (%)								
	Leach reactors							
	A	B	C	D	E	F	J	K
SiO_2	55.42	46.24	42.91	42.18	48.66	45.08	42.76	41.09
TiO_2	0.53	0.40	0.40	0.34	0.39	0.34	0.38	0.36
Al_2O_3	14.08	11.35	12.11	10.83	12.22	10.56	12.07	10.72
Fe_2O_{3r}	7.27	7.69	7.27	6.80	9.28	7.53	7.53	7.47
MnO	0.16	0.20	0.21	0.27	0.20	0.15	0.26	0.33
MgO	0.50	0.40	0.43	0.54	0.42	0.43	0.45	0.52
CaO	0.03	0.05	0.16	0.12	0.04	0.06	0.13	0.14
Na_2O	0.25	0.55	0.87	0.98	0.31	0.70	1.10	1.35
K_2O	1.93	1.53	1.31	1.29	1.53	1.35	1.38	1.11
P_2O_5	0.06	0.07	0.15	0.12	0.07	0.08	0.14	0.14
Cr_2O_3	0.04	0.05	0.03	0.04	0.06	0.06	0.04	0.05
NiO	0.00	0.00	0.00	0.00	0.00	0.00	0.00	0.00
S	9.39	15.10	16.08	17.02	13.13	16.21	15.65	17.03
Zn	2.16	4.19	5.87	6.53	1.92	4.22	6.83	7.75
Pb	0.49	0.43	0.15	0.13	0.64	0.25	0.42	0.17
Cu	0.01	0.02	0.02	0.01	0.02	0.02	0.01	0.02
Fe-py	7.18	11.29	11.46	12.00	10.52	12.27	10.65	11.48
Total	99.51	99.57	99.43	99.21	99.42	99.31	99.82	99.74

Mineral analysis results for bulk sample of leach reactors feed using QEMSACN							
	Element	Combined	Size fractions				
			-150/+125	-125/+90	-90/+63	-63/+38	-38
Chemical Assay (%)	Al	2.43	4.14	2.79	2.13	2.19	1.53
	Ca	0.21	0.22	0.20	0.18	0.24	0.23
	Cu	0.16	0.18	0.27	0.13	0.10	0.08
	Fe	20.07	12.90	14.21	22.36	23.51	26.23
	Mg	0.73	0.96	0.91	0.65	0.67	0.50
	Mn	0.24	0.12	0.28	0.24	0.21	0.30
	Pb	0.19	0.05	0.09	0.15	0.30	0.38
	S	25.30	17.58	19.74	27.33	28.65	31.95
	Si	14.52	16.06	18.07	14.02	12.21	11.22
	Ti	0.18	0.17	0.15	0.18	0.18	0.23
	Zn	10.15	12.26	12.38	8.75	9.23	8.70
Mineral Mass (%)	Mineral	Combined	-150/+125	-125/+90	-90/+63	-63/+38	-38
	Pyrrhotite	1.16	1.02	0.97	1.13	1.47	1.14
	Pyrite	33.80	18.54	22.52	38.53	39.61	47.71
	Sphalerite	15.98	19.40	19.55	13.77	14.49	13.65
	Galena	0.22	0.05	0.11	0.18	0.34	0.44
	Chalcopyrite	0.04	0.05	0.02	0.03	0.06	0.06
	Other sufides	3.19	2.27	2.32	3.58	4.08	3.01
	Garnet	0.28	0.24	0.28	0.37	0.20	0.23
	K-Feldspar	0.44	0.55	0.53	0.41	0.38	0.33
	Chlorite	1.72	1.58	3.06	1.36	1.04	0.98
	Kaolinite	2.78	4.93	3.11	2.15	2.65	2.24
	Mica	7.85	10.39	9.96	6.88	7.14	4.85
	Phosphate	2.01	6.04	0.79	1.74	2.53	1.34
	Calcite	0.03	0.03	0.02	0.03	0.04	0.04
	Quartz	25.54	26.35	31.72	25.24	21.32	20.23
	Fe oxides/hydroxides	1.92	3.56	1.44	1.94	2.01	1.56
	Jarosite	0.00	0.00	0.00	0.00	0.00	0.00
	Others	3.06	4.99	3.61	2.68	2.63	2.19
	Void	0.00	0.00	0.00	0.00	0.00	0.00

Mineral analysis results for the selected particle of the leach reactors using QEMSACN (before treatment)								
	Leach reactors							
	A	B	C	D	E	F	J	K
Mineral Mass (%)								
Pyrrhotite	10.50	2.98	0.08	0.07	0.05	1.30	0.05	0.17
Pyrite	26.17	34.21	33.21	43.47	41.27	29.18	23.72	55.16
Sphalerite	17.51	15.21	15.35	11.04	14.09	17.23	23.28	5.60
Galena	0.04	0.30	0.03	0.07	0.14	0.12	0.08	0.19
Chalcopyrite	0.01	0.01	0.01	0.01	0.01	0.01	0.01	0.00
Other sufides	0.14	0.15	0.07	0.07	0.15	0.07	0.13	0.23
Garnet	0.03	0.04	0.05	0.16	0.05	0.02	0.14	0.17
K-Feldspar	0.76	0.88	0.36	0.68	0.81	0.74	0.45	0.22
Chlorite	0.13	0.18	0.68	0.52	0.40	2.38	0.65	4.88
Kaolinite	1.02	0.50	3.75	3.96	2.07	0.13	2.15	0.25
Mica	13.25	15.68	8.98	12.40	11.53	12.09	14.40	6.97
Phosphate	0.60	0.36	0.43	0.36	0.37	0.33	0.58	0.60
Calcite	0.00	0.00	0.00	0.01	0.21	0.00	0.00	0.00
Quartz	27.96	26.17	34.91	24.87	26.29	32.76	31.44	20.12
Fe oxides/hydroxides	0.50	1.92	1.17	1.14	0.71	2.60	1.46	3.97
Jarosite	0.00	0.00	0.00	0.00	0.00	0.00	0.00	0.00
Others	1.38	1.41	0.91	1.17	1.86	1.03	1.45	1.45
Void	0.00	0.00	0.00	0.00	0.00	0.00	0.00	0.00
Mineral Volume (%)								
Pyrrhotite	7.96	2.25	0.06	0.06	0.04	0.96	0.04	0.14
Pyrite	18.32	23.83	22.53	31.02	29.55	19.81	15.94	42.00
Sphalerite	15.13	13.09	12.87	9.73	12.43	14.45	19.31	5.27
Galena	0.02	0.14	0.02	0.04	0.07	0.05	0.03	0.10
Chalcopyrite	0.01	0.01	0.01	0.01	0.01	0.01	0.01	0.00
Other sufides	0.10	0.10	0.05	0.05	0.10	0.05	0.09	0.17
Garnet	0.02	0.04	0.04	0.14	0.04	0.02	0.12	0.16
K-Feldspar	1.03	1.20	0.48	0.94	1.13	0.99	0.59	0.33
Chlorite	0.17	0.23	0.87	0.70	0.54	3.06	0.83	7.00
Kaolinite	1.38	0.67	4.89	5.44	2.84	0.17	2.78	0.36
Mica	15.72	18.58	10.49	15.34	14.10	14.00	16.55	9.04
Phosphate	0.66	0.40	0.46	0.42	0.43	0.36	0.62	0.71
Calcite	0.00	0.00	0.00	0.01	0.28	0.00	0.00	0.00
Quartz	37.23	34.73	45.12	33.80	35.65	42.35	40.17	28.90
Fe oxides/hydroxides	0.57	2.18	1.14	1.16	0.77	2.54	1.58	4.23
Jarosite	0.00	0.00	0.00	0.00	0.00	0.00	0.00	0.00
Others	1.34	1.26	0.79	1.10	1.84	0.94	1.29	1.47
Void	0.34	1.28	0.18	0.05	0.18	0.27	0.06	0.12

Mineral analysis results for the selected particle of the leach reactors using QEMSACN (After 2 months)								
	Leach reactors							
	A	B	C	D	E	F	J	K
Mineral Mass (%)								
Pyrrhotite	0.06	0.25	0.12	0.15	0.41	0.09	0.11	0.24
Pyrite	27.06	39.62	35.60	33.57	60.75	34.22	9.32	23.91
Sphalerite	19.18	18.89	13.99	8.86	5.94	21.09	32.46	21.28
Galena	0.03	0.04	0.01	0.04	0.09	0.05	0.01	0.09
Chalcopyrite	0.00	0.00	0.01	0.01	0.01	0.02	0.00	0.02
Other sufides	0.14	0.18	0.18	0.09	0.39	0.10	0.09	0.03
Garnet	0.12	0.00	0.01	0.05	0.09	0.02	0.03	0.02
K-Feldspar	0.94	0.35	0.23	0.79	0.32	0.13	0.48	0.72
Chlorite	0.83	0.06	0.90	0.52	1.85	1.58	0.18	2.72
Kaolinite	6.08	2.28	1.91	0.12	0.83	8.89	5.71	0.44
Mica	14.90	16.64	9.77	21.72	8.69	3.69	19.19	21.87
Phosphate	0.18	0.46	0.43	0.22	0.09	0.73	0.11	0.34
Calcite	0.00	0.00	0.00	0.00	0.01	0.00	0.00	0.00
Quartz	28.73	19.47	34.05	32.52	19.06	27.81	30.34	24.96
Fe oxides/hydroxides	0.40	0.50	1.82	0.54	0.85	0.90	0.64	1.94
Jarosite	0.00	0.00	0.00	0.00	0.06	0.00	0.00	0.00
Others	1.34	1.26	0.97	0.80	0.56	0.68	1.31	1.40
Void	0.00	0.00	0.00	0.00	0.00	0.00	0.00	0.00
Mineral Volume (%)								
Pyrrhotite	0.04	0.20	0.09	0.11	0.34	0.07	0.08	0.18
Pyrite	18.05	28.86	24.43	22.35	45.98	23.74	5.97	15.94
Sphalerite	15.73	16.88	11.86	7.29	5.56	18.06	25.64	17.55
Galena	0.01	0.02	0.01	0.02	0.05	0.02	0.01	0.04
Chalcopyrite	0.00	0.00	0.01	0.01	0.01	0.01	0.00	0.02
Other sufides	0.09	0.13	0.12	0.06	0.28	0.07	0.05	0.02
Garnet	0.10	0.00	0.01	0.04	0.09	0.02	0.02	0.02
K-Feldspar	1.21	0.49	0.31	1.03	0.48	0.17	0.60	0.93
Chlorite	1.04	0.08	1.16	0.65	2.64	2.07	0.22	3.42
Kaolinite	7.77	3.17	2.52	0.16	1.21	11.86	7.03	0.56
Mica	17.16	20.46	11.38	25.36	11.30	4.42	21.24	25.12
Phosphate	0.19	0.52	0.47	0.24	0.12	0.80	0.11	0.36
Calcite	0.00	0.00	0.00	0.00	0.01	0.00	0.00	0.00
Quartz	36.11	26.73	44.42	41.22	27.31	36.65	37.00	31.73
Fe oxides/hydroxides	0.42	0.59	1.99	0.55	0.89	0.74	0.68	1.99
Jarosite	0.01	0.00	0.00	0.00	0.07	0.00	0.00	0.00
Others	1.23	1.35	0.92	0.65	0.57	0.60	1.11	1.30
Void	0.84	0.50	0.31	0.28	3.10	0.71	0.24	0.79

Mineral analysis results for the selected particle of the leach reactors using QEMSACN (After 5 months)								
	Leach reactors							
	A	B	C	D	E	F	J	K
Mineral Mass (%)								
Pyrrhotite	0.60	0.21	3.95	0.53	0.03	0.15	0.17	1.98
Pyrite	54.92	12.41	24.31	44.10	35.03	15.81	20.29	34.28
Sphalerite	1.37	12.08	17.61	3.54	2.01	10.76	39.26	15.08
Galena	0.15	0.03	0.10	0.02	0.46	0.01	0.04	0.16
Chalcopyrite	0.11	0.05	0.03	0.04	0.06	0.02	0.03	0.02
Other sufides	1.23	0.17	0.45	0.09	8.32	1.79	0.84	0.69
Garnet	0.00	0.29	0.01	0.01	0.00	0.04	0.10	0.02
K-Feldspar	0.51	1.19	0.89	0.20	1.10	1.22	0.13	0.43
Chlorite	0.03	4.44	0.04	0.66	0.07	2.72	5.32	0.35
Kaolinite	5.21	5.32	3.76	6.12	4.10	10.45	0.31	4.77
Mica	7.37	11.56	21.07	8.72	10.41	12.54	2.86	12.85
Phosphate	0.03	0.28	0.29	0.25	0.03	0.49	0.41	0.36
Calcite	0.01	0.01	0.00	0.01	0.00	0.00	0.01	0.00
Quartz	24.20	49.59	25.52	32.62	36.77	39.85	28.31	27.11
Fe oxides/hydroxides	0.14	0.95	0.18	1.38	0.01	2.07	0.85	0.45
Jarosite	0.02	0.00	0.01	0.00	0.00	0.00	0.01	0.01
Others	4.11	1.41	1.77	1.69	1.57	2.09	1.06	1.42
Void	0.00	0.00	0.00	0.00	0.00	0.00	0.00	0.00
Mineral Volume (%)								
Pyrrhotite	0.44	0.13	2.86	0.39	0.02	0.10	0.13	1.48
Pyrite	37.54	7.14	16.25	29.94	22.56	9.68	13.54	23.64
Sphalerite	1.16	8.59	14.53	2.97	1.60	8.10	32.39	12.82
Galena	0.07	0.01	0.05	0.01	0.20	0.00	0.02	0.07
Chalcopyrite	0.09	0.03	0.03	0.03	0.05	0.01	0.02	0.02
Other sufides	0.78	0.09	0.28	0.06	4.88	1.00	0.52	0.44
Garnet	0.00	0.21	0.01	0.01	0.00	0.03	0.09	0.02
K-Feldspar	0.68	1.33	1.15	0.26	1.38	1.45	0.17	0.58
Chlorite	0.04	4.82	0.05	0.85	0.08	3.13	6.70	0.46
Kaolinite	6.86	5.89	4.83	7.99	5.08	12.25	0.40	6.31
Mica	8.67	11.35	24.28	10.17	11.54	13.19	3.37	15.14
Phosphate	0.04	0.26	0.31	0.27	0.03	0.47	0.41	0.40
Calcite	0.01	0.01	0.00	0.01	0.00	0.00	0.01	0.00
Quartz	31.45	54.25	32.47	42.17	44.86	46.19	35.77	35.48
Fe oxides/hydroxides	0.13	0.75	0.19	1.43	0.01	1.67	0.64	0.50
Jarosite	0.03	0.00	0.01	0.00	0.00	0.00	0.01	0.01
Others	3.90	1.05	1.66	1.58	1.31	1.63	0.97	1.34
Void	8.11	4.07	1.05	1.85	6.40	1.10	4.85	1.27

Mineral analysis results for the selected particle of the leach reactors using QEMSACN (After 9 months)								
	Leach reactors							
	A	B	C	D	E	F	J	K
Mineral Mass (%)								
Pyrrhotite	0.74	0.35	1.83	1.61	0.74	0.71	0.68	0.21
Pyrite	50.29	30.44	21.35	35.76	42.31	42.10	37.27	28.53
Sphalerite	3.65	1.02	9.22	11.87	1.49	3.80	2.54	13.83
Galena	0.01	0.06	0.23	0.22	0.74	0.23	0.05	0.04
Chalcopyrite	0.04	0.08	0.17	0.04	0.05	0.07	0.07	0.04
Other sufides	0.66	0.26	0.24	0.20	0.32	0.39	0.44	0.09
Garnet	0.02	0.04	0.00	0.01	0.05	0.02	0.18	0.04
K-Feldspar	0.12	2.51	1.49	0.41	0.98	1.16	1.99	0.37
Chlorite	0.02	0.33	0.00	0.49	0.14	0.09	1.34	1.70
Kaolinite	0.09	0.25	1.05	4.72	3.12	1.59	0.21	7.30
Mica	2.11	15.11	15.92	12.48	18.60	26.31	19.74	5.24
Phosphate	0.04	0.05	0.02	0.31	0.04	0.09	0.29	0.22
Calcite	0.00	0.00	0.01	0.00	0.00	0.01	0.01	0.01
Quartz	13.85	48.19	46.45	30.32	29.42	21.27	33.54	40.40
Fe oxides/hydroxides	27.34	0.09	0.04	0.27	0.06	0.38	0.30	0.75
Jarosite	0.00	0.00	0.00	0.01	0.00	0.04	0.01	0.00
Others	1.03	1.21	1.96	1.30	1.93	1.76	1.34	1.22
Void	0.00	0.00	0.00	0.00	0.00	0.00	0.00	0.00
Mineral Volume (%)								
Pyrrhotite	0.65	0.23	1.21	1.18	0.52	0.52	0.48	0.15
Pyrite	40.29	18.64	13.08	24.23	27.45	28.65	24.18	18.23
Sphalerite	3.42	0.77	6.96	9.92	1.19	3.19	2.04	10.92
Galena	0.00	0.03	0.10	0.10	0.32	0.10	0.02	0.02
Chalcopyrite	0.04	0.06	0.13	0.03	0.04	0.06	0.06	0.03
Other sufides	0.51	0.15	0.14	0.13	0.20	0.26	0.27	0.06
Garnet	0.02	0.03	0.00	0.01	0.04	0.01	0.14	0.03
K-Feldspar	0.19	2.99	1.77	0.54	1.24	1.53	2.51	0.46
Chlorite	0.03	0.38	0.00	0.63	0.17	0.11	1.64	2.05
Kaolinite	0.13	0.30	1.24	6.14	3.89	2.07	0.26	8.97
Mica	2.87	15.91	16.74	14.34	20.90	30.73	22.01	5.80
Phosphate	0.05	0.05	0.02	0.33	0.05	0.10	0.30	0.22
Calcite	0.01	0.00	0.02	0.00	0.00	0.01	0.01	0.01
Quartz	20.90	55.88	53.90	38.90	36.15	27.45	41.21	49.05
Fe oxides/hydroxides	22.02	0.07	0.03	0.29	0.05	0.37	0.26	0.59
Jarosite	0.00	0.00	0.00	0.01	0.00	0.04	0.02	0.00
Others	1.05	0.96	1.37	1.21	1.61	1.54	1.13	1.00
Void	7.83	3.55	3.29	2.00	6.18	3.24	3.46	2.41

Appendix II: Analysing of X-ray CT images of individual tagged particles

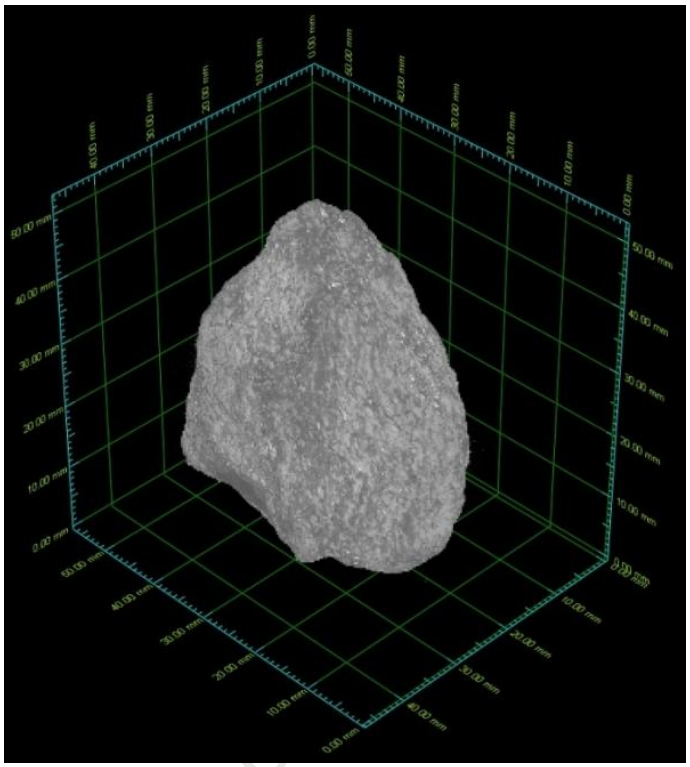

3-D image of a single ore particle (40 mm) where the different grey levels represent the different minerals.

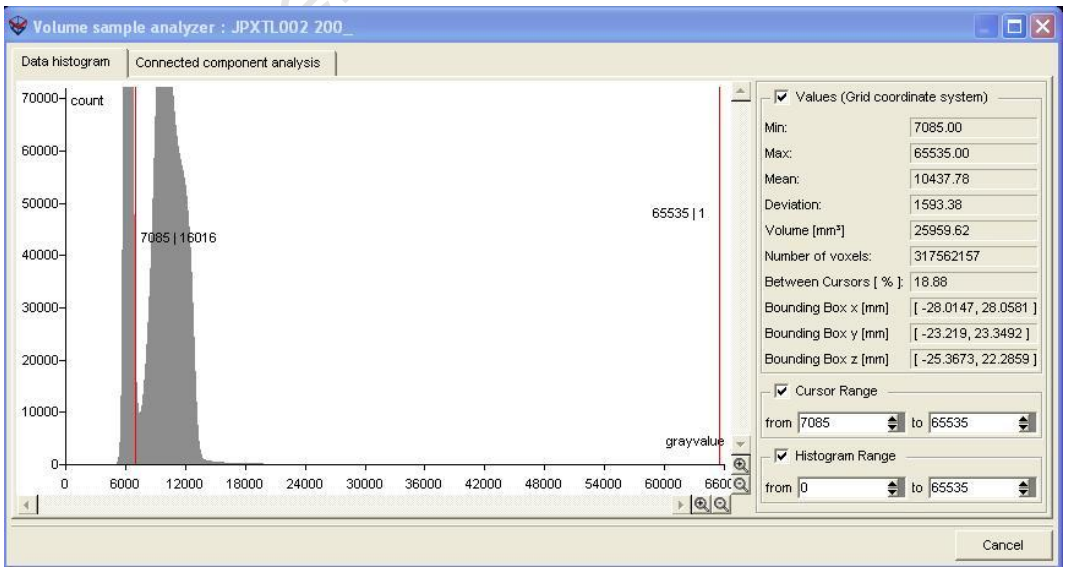

Volume sample analyser for measuring the volume of the selected ore particle base on grey value.

Phase segmentation

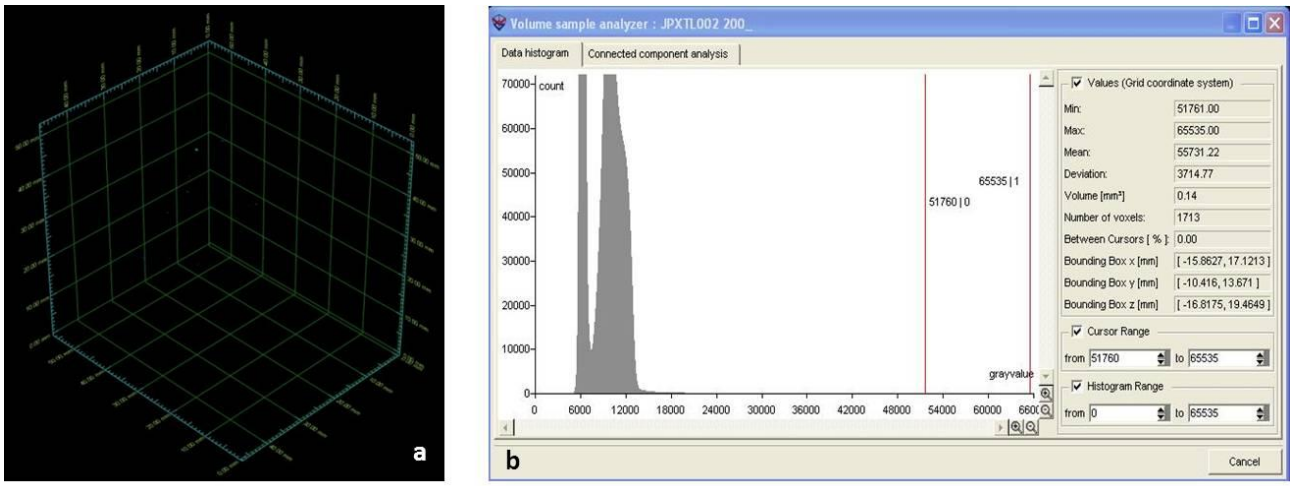

a. Single ore particle virtually processed to extract all minerals other than galena, b. Volume sample analyser for measuring the volume of the galena grains within the selected ore particle.

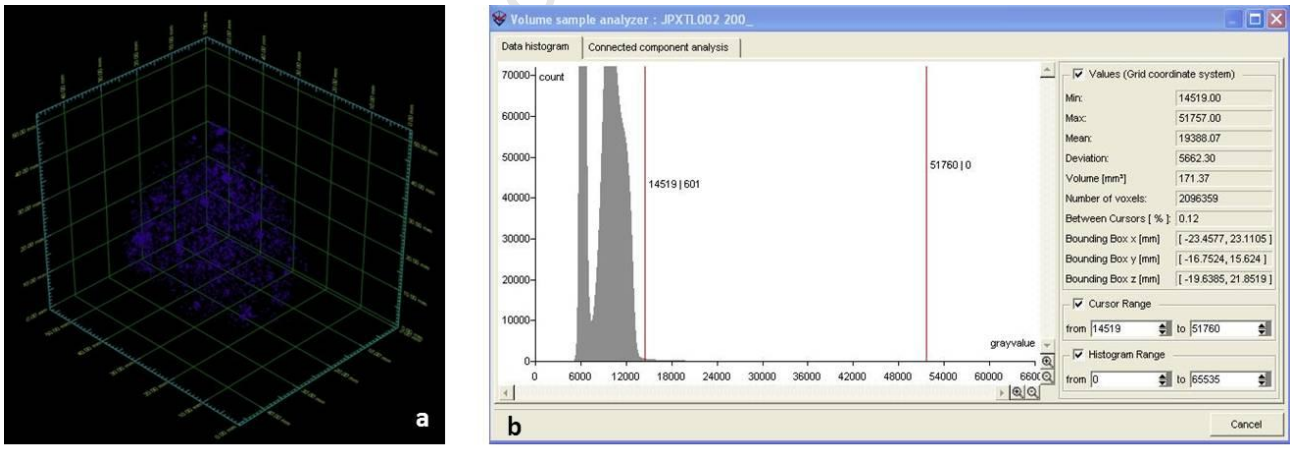

a. Single ore particle virtually processed to extract all minerals other than sphalerite, b. Volume sample analyser for measuring the volume of the galena grains within the selected ore particle.

Phase segmentation

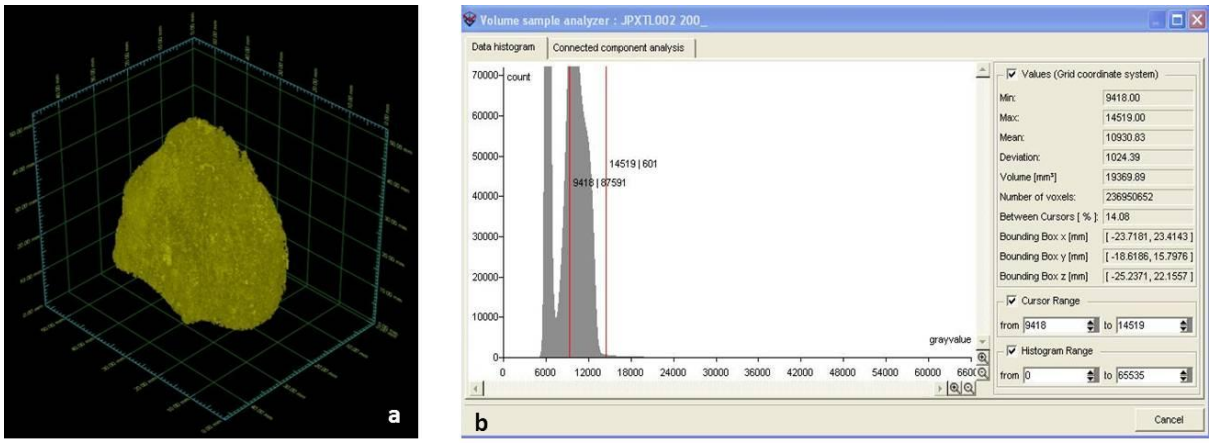

a. Single ore particle virtually processed to extract all minerals other than pyrite, b. Volume sample analyser for measuring the volume of the galena grains within the selected ore particle.

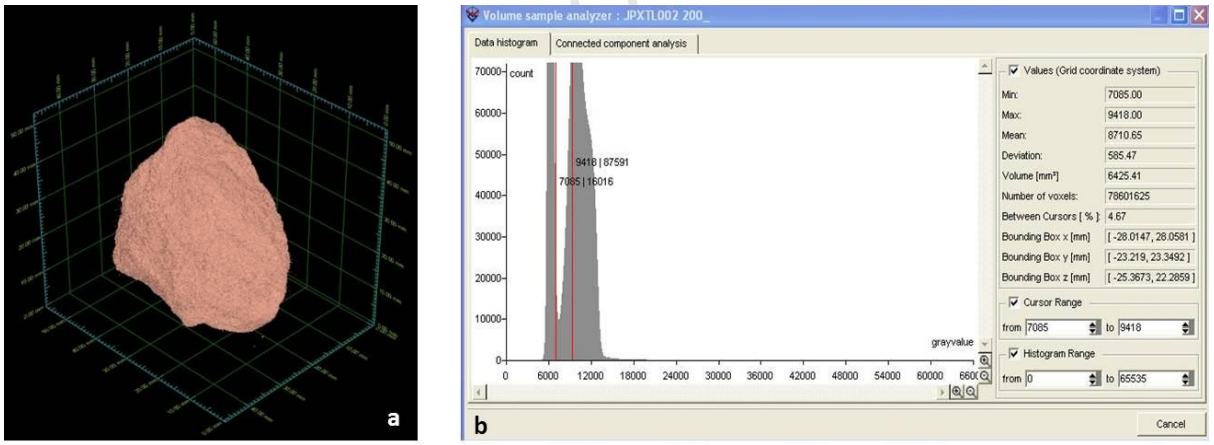

a. Single ore particle virtually processed to extract all minerals other than gangue minerals, b. Volume sample analyser for measuring the volume of the galena grains within the selected ore particle.

Plane images of the single ore particle

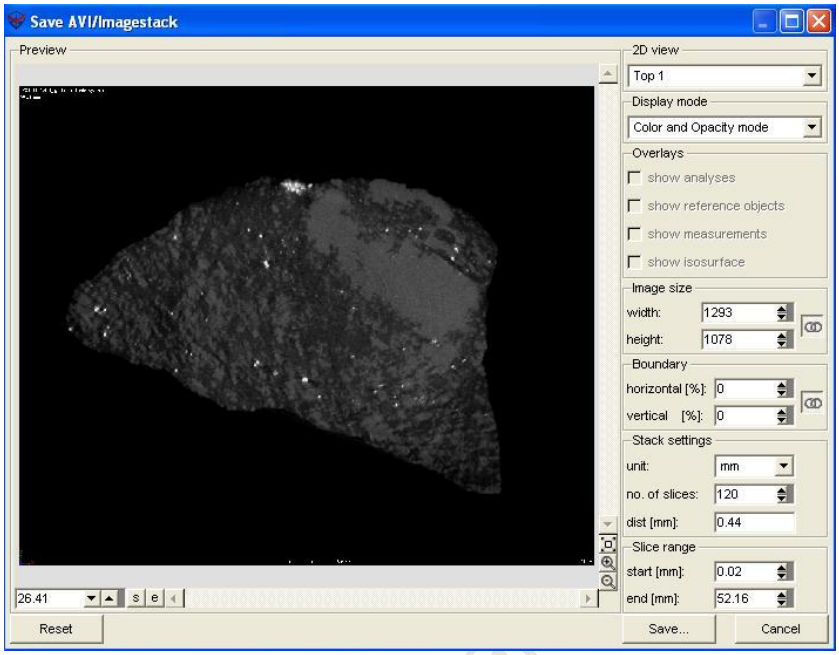

Image stacks management -2D view from top.

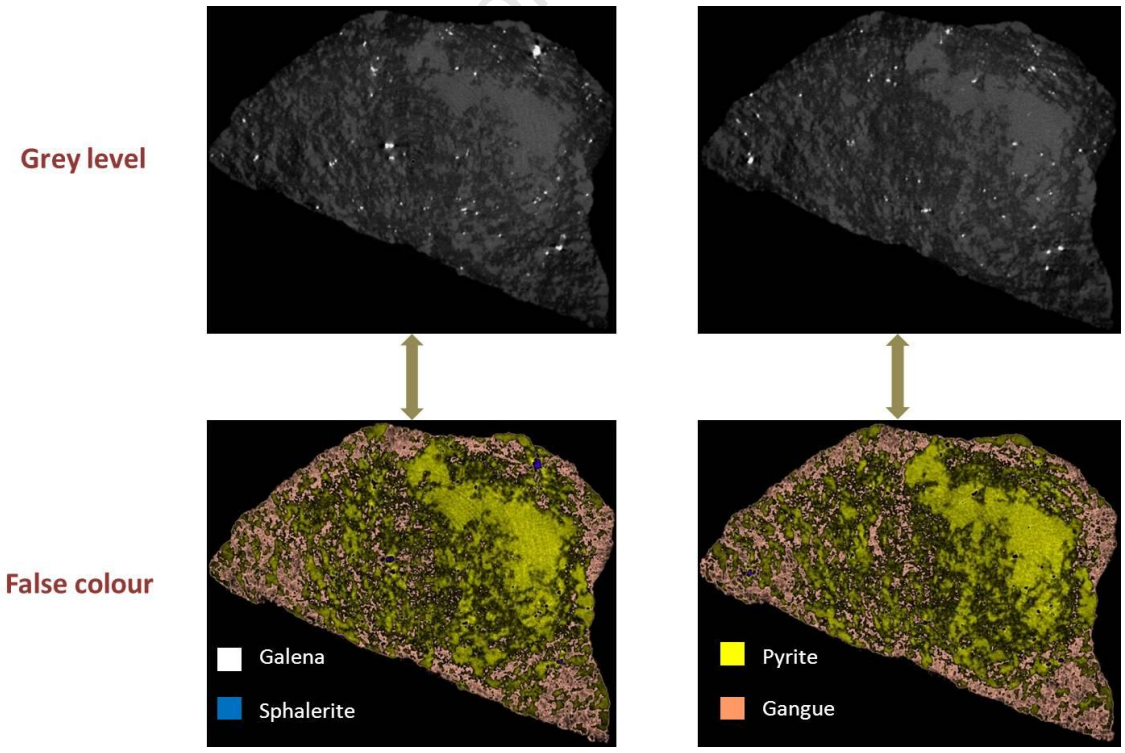

Tow Plane images of the ore particle with grey level and false colour representation to reveal textual details of the ore particles reveal textual details of the ore particles.

Plane images of the single ore particle

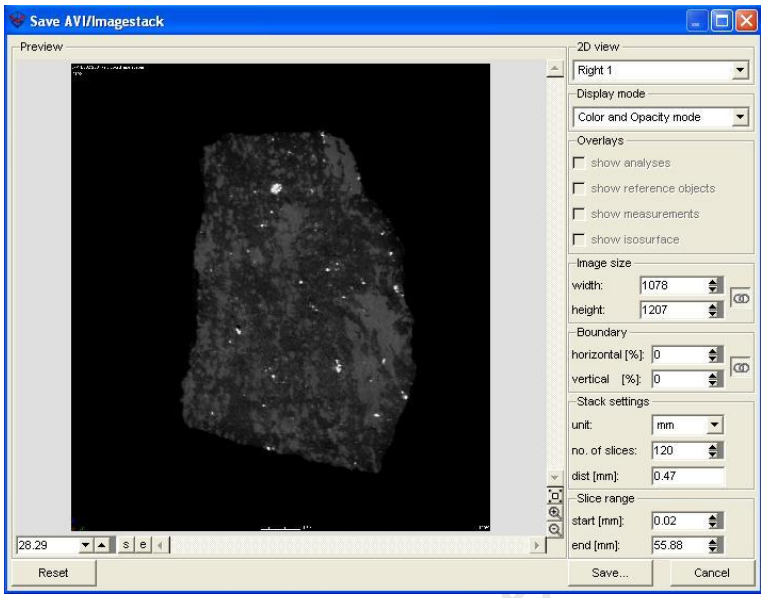

Image stacks management -2D view from right.

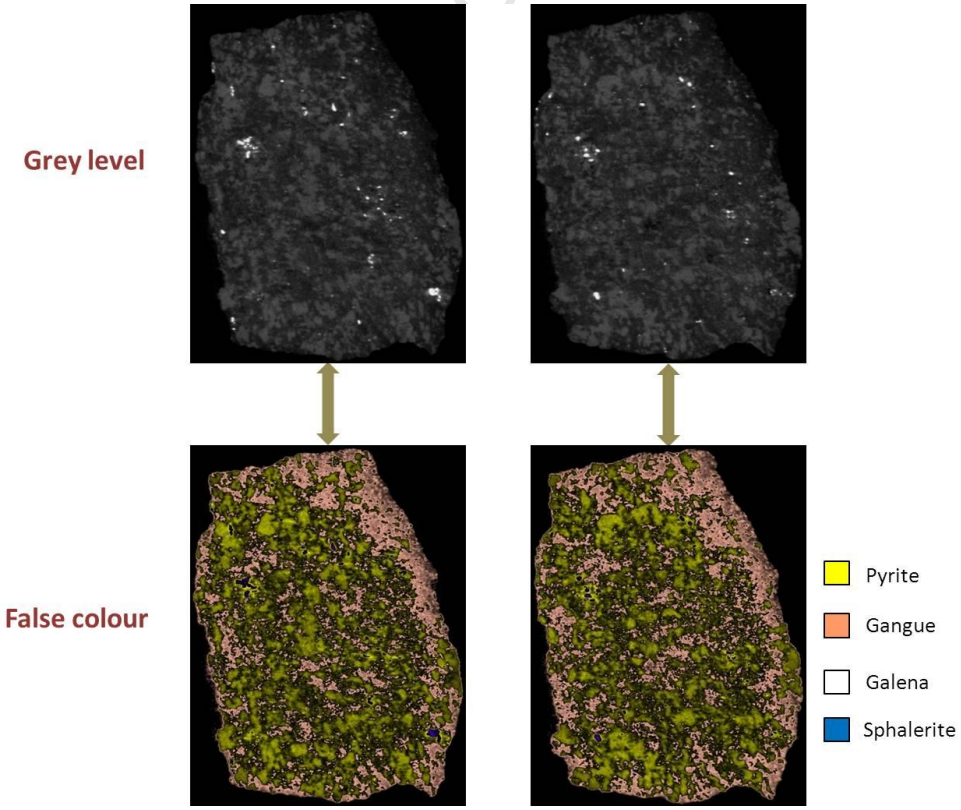

Tow Plane images of the ore particle with grey level and false colour representation to reveal textual details of the ore particles reveal textual details of the ore particles.

Plane images of the single ore particle

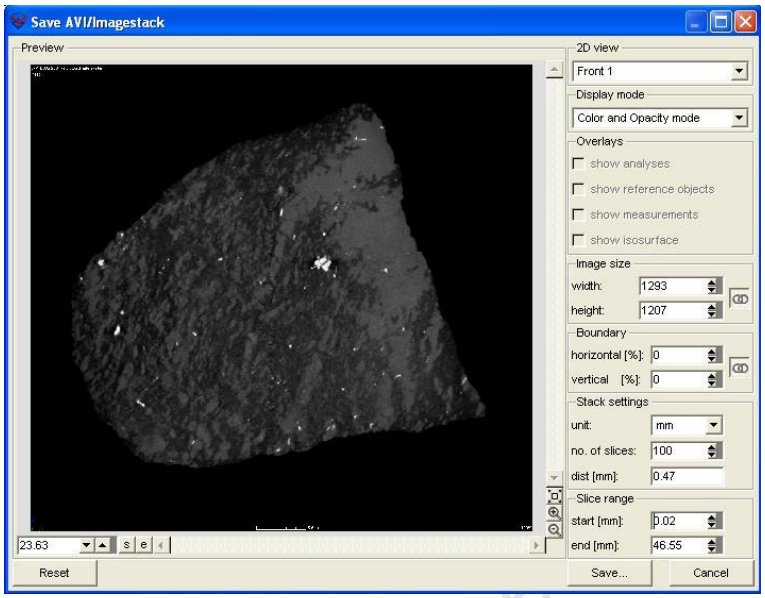

Image stacks management -2D view from front.

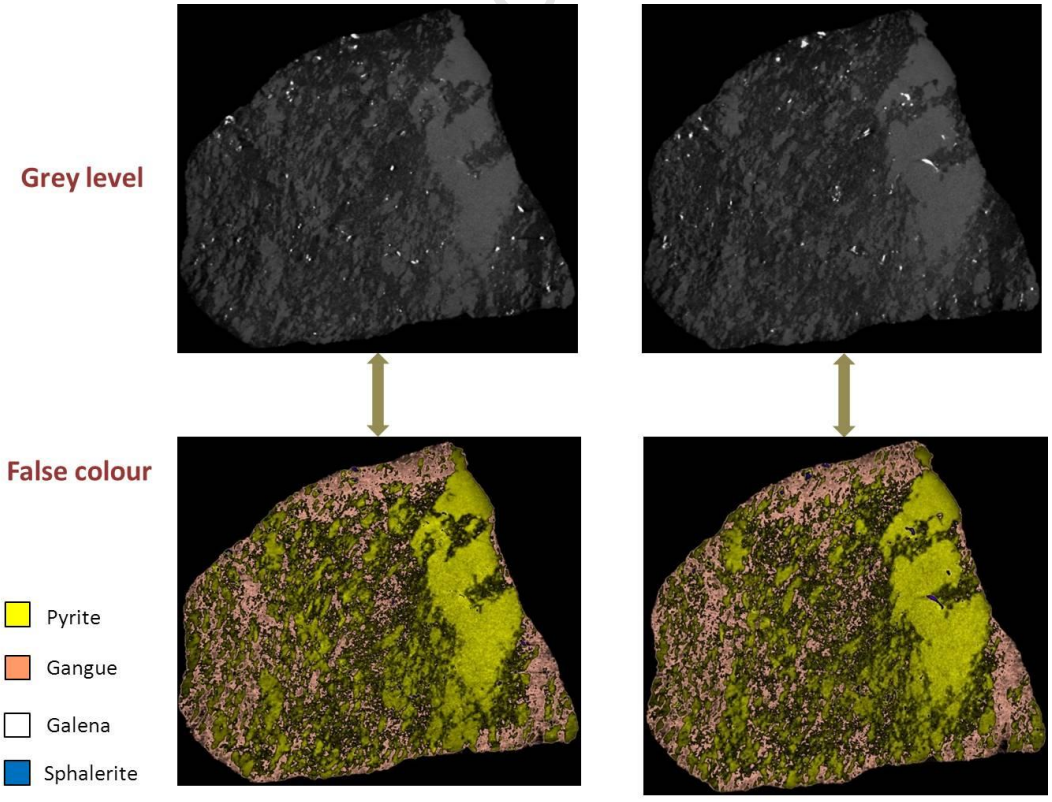

Tow Plane images of the ore particle with grey level and false colour representation to reveal textual details of the ore particles reveal textual details of the ore particles.

Appendix III: Back-scattered electron (BSE) and Electron Microprobe Analysis (EMPA) of elemental mapping

30 individual spot analyses for impurity content of sphalerite sample as determined by electron microprobe (wt. %).

No.	S	Cu	Fe	Zn	Mn	Fe+Mn	Fe+Mn+Zn
1	33.81	0.00	10.55	51.38	4.83	15.38	66.76
2	33.63	0.06	10.20	50.94	4.50	14.70	65.64
3	33.99	0.01	9.53	51.59	4.87	14.40	65.99
4	33.54	0.00	9.89	51.17	4.61	14.50	65.67
5	33.87	0.00	10.35	51.93	4.67	15.02	66.95
6	33.71	0.02	10.94	51.38	4.76	15.70	67.08
7	34.34	0.01	10.01	50.90	4.85	14.86	65.76
8	34.23	0.00	9.38	51.83	4.56	13.94	65.77
9	34.01	0.00	9.60	51.93	4.40	14.00	65.93
10	34.34	0.00	10.01	50.90	5.20	15.21	66.11
11	34.34	0.01	9.98	51.57	4.85	14.83	66.40
12	34.42	0.04	9.99	51.79	4.75	14.74	66.53
13	34.25	0.01	9.34	53.86	3.54	12.88	66.74
14	34.58	0.06	9.84	51.39	4.89	14.73	66.12
15	33.73	0.01	7.10	59.09	0.43	7.53	66.62
16	33.32	0.04	7.57	58.43	0.64	8.21	66.64
17	34.56	0.00	9.25	52.07	4.06	13.31	65.38
18	34.53	0.02	10.39	50.42	5.26	15.65	66.07
19	34.41	0.00	9.91	51.40	5.10	15.01	66.41
20	34.32	0.36	10.23	50.70	4.69	14.92	65.62
21	34.07	0.05	9.63	51.90	4.91	14.54	66.44
22	33.98	0.04	9.57	51.83	4.69	14.26	66.09
23	34.46	0.03	9.78	51.70	4.96	14.74	66.44
24	34.17	0.01	9.63	51.47	4.96	14.59	66.06
25	34.11	0.00	9.54	51.97	4.86	14.40	66.37
26	34.17	0.02	9.94	52.23	4.52	14.46	66.69
27	33.80	0.02	9.60	51.82	4.99	14.59	66.41
28	33.88	0.03	9.86	51.70	4.56	14.42	66.12
29	33.89	0.03	9.97	51.22	5.01	14.98	66.20
30	33.43	0.04	9.98	51.74	4.41	14.39	66.13

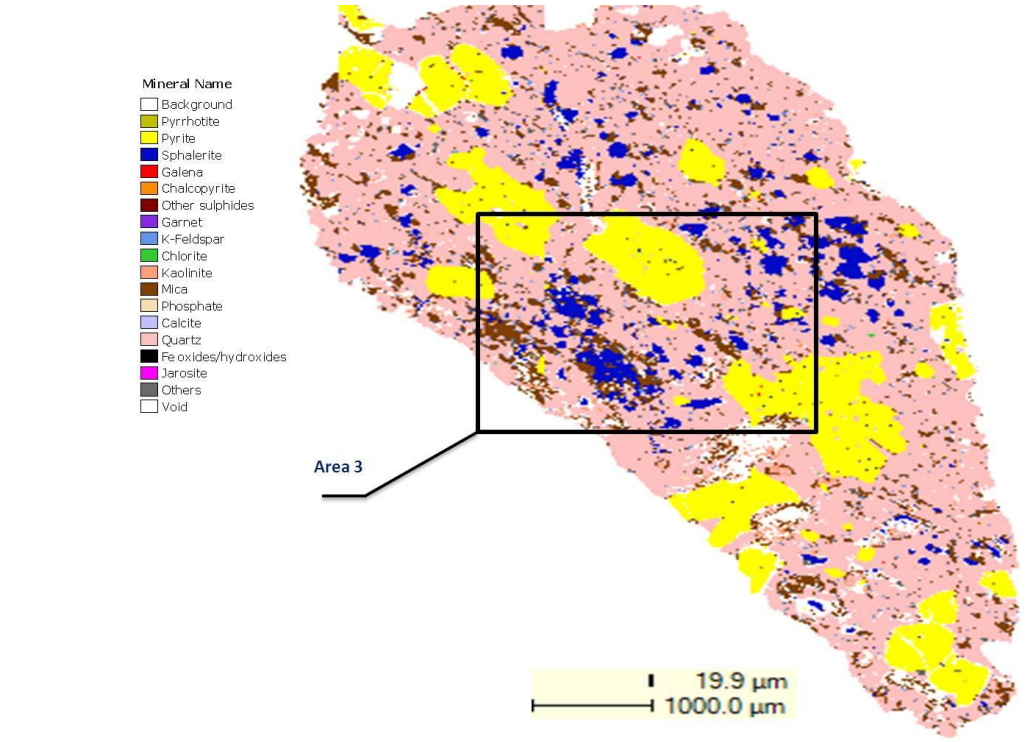

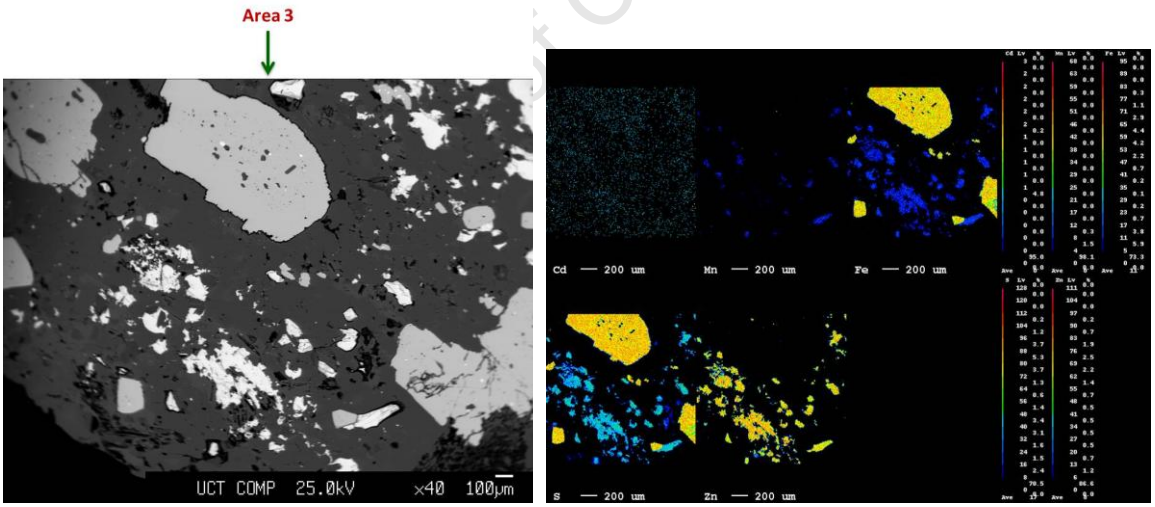

Back-scattered electron (BSE) and EMPA of elemental mapping for an area of a particle produced by HPGR.

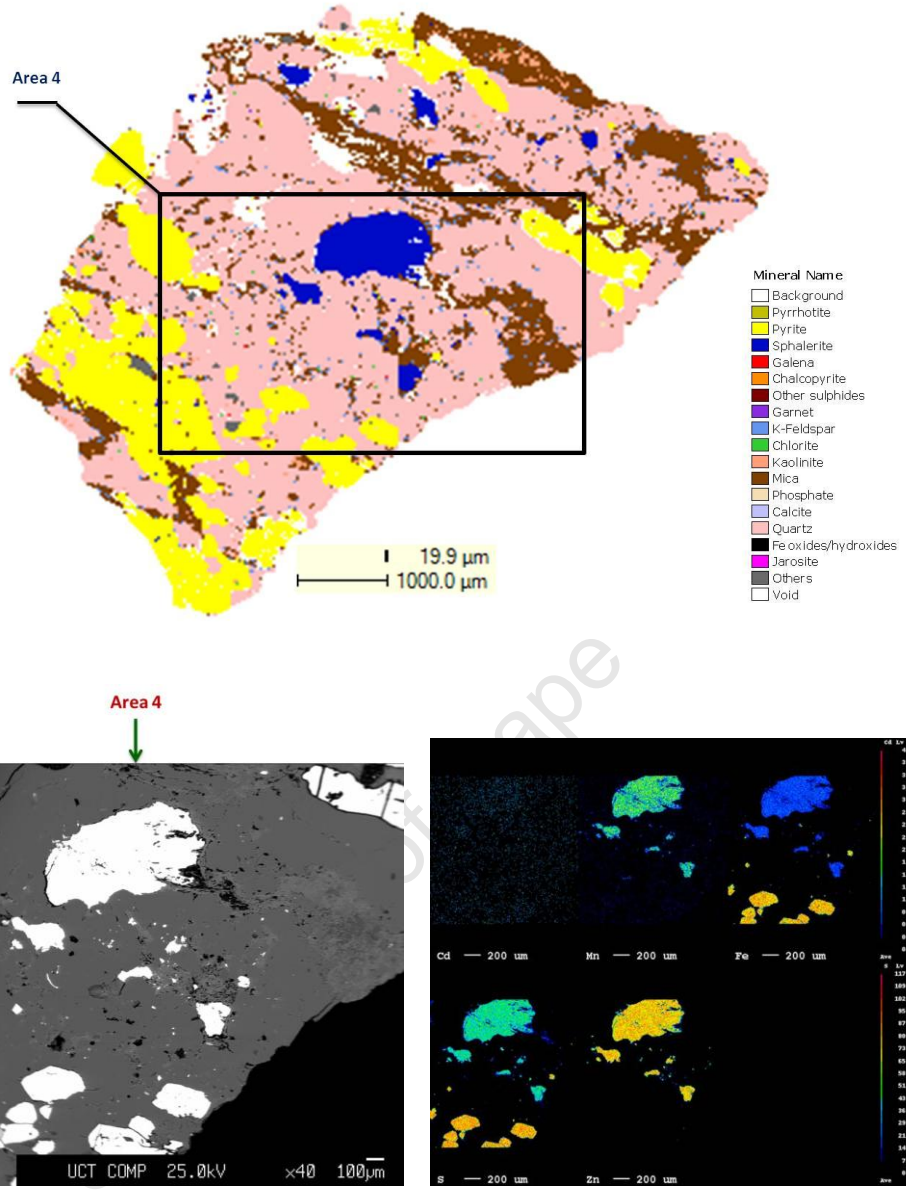

Back-scattered electron (BSE) and EMPA of elemental mapping for an area of a particle produced by HPGR.

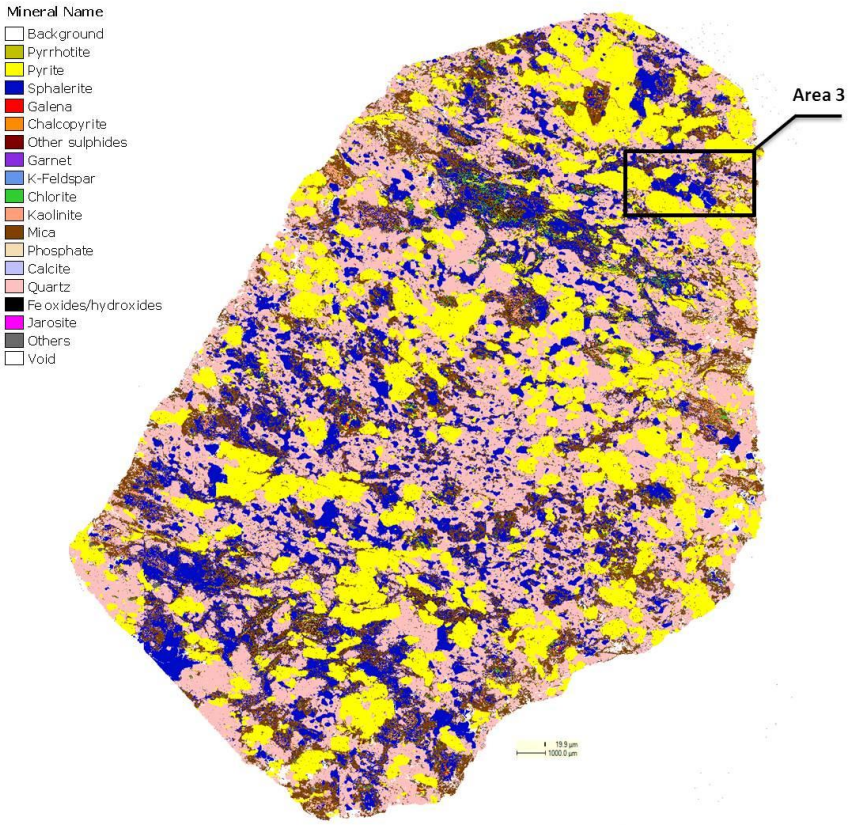

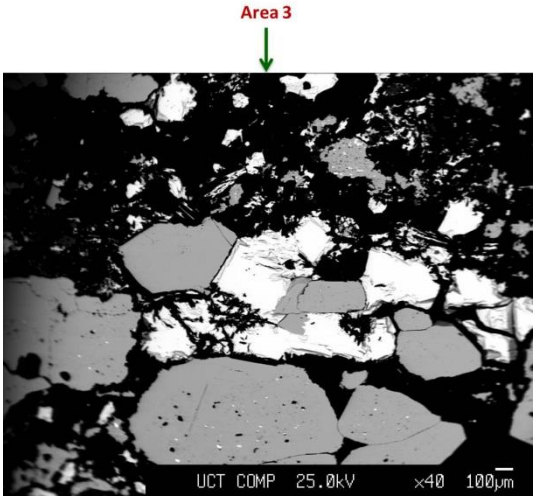

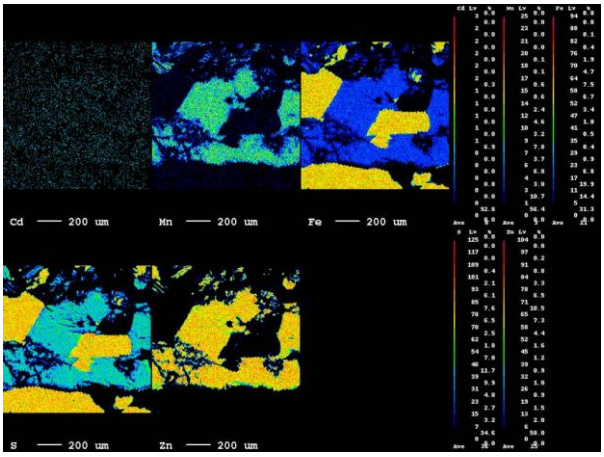

Back-scattered electron (BSE) and EMPA of elemental mapping for an area of a particle produced cone crusher.

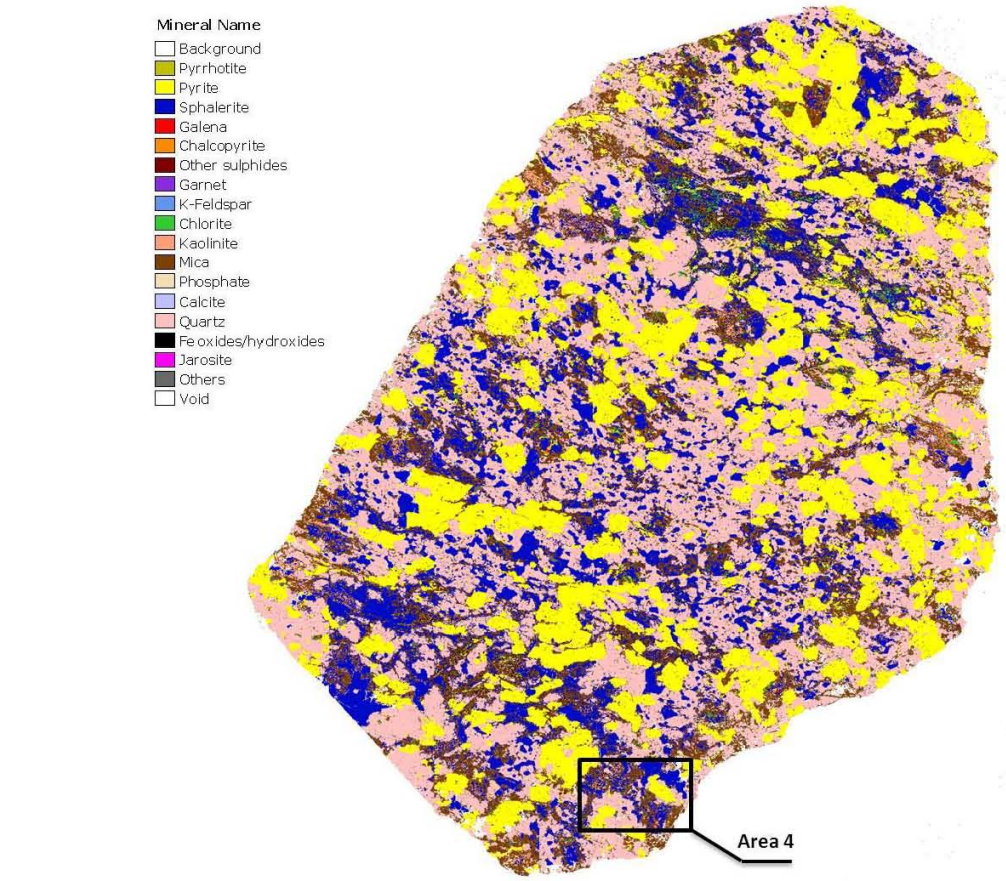

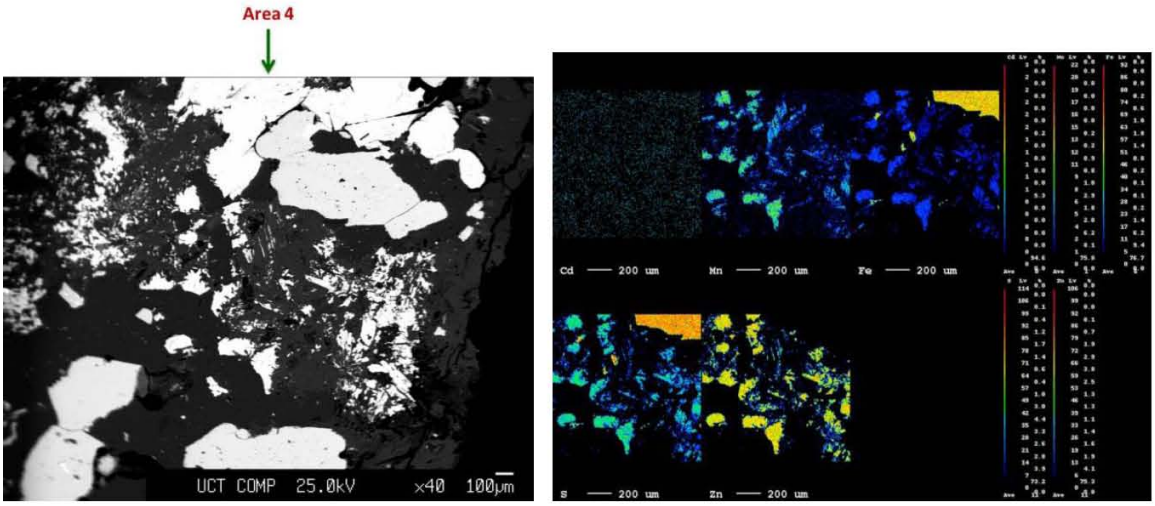

Back-scattered electron (BSE) and EMPA of elemental mapping for an area of a particle produced cone crusher.

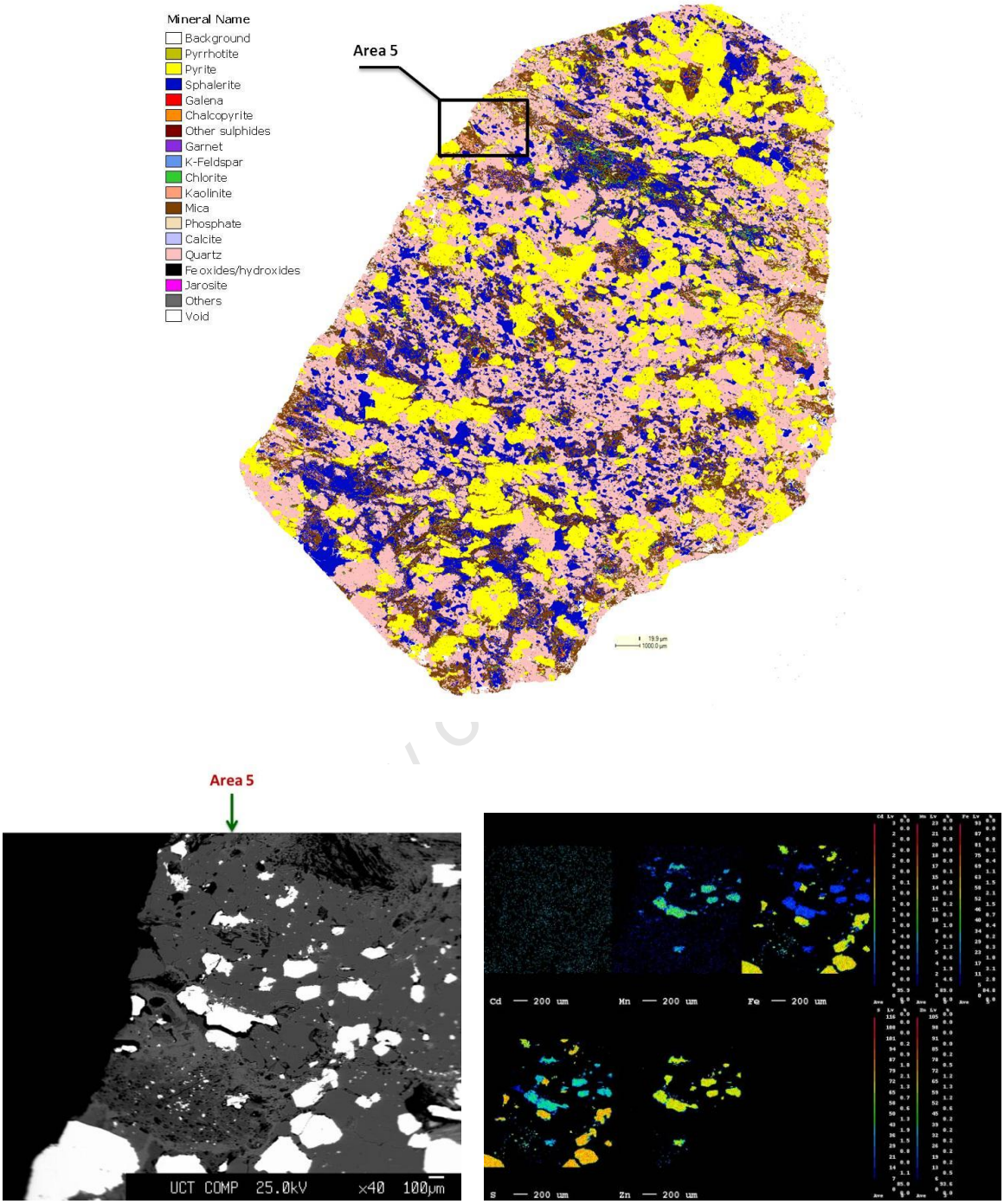

Back-scattered electron (BSE) and EMPA of elemental mapping for an area of a particle produced cone crusher.

Appendix IV: Comparison of crushed products- Microscopic and QEMSCAN.

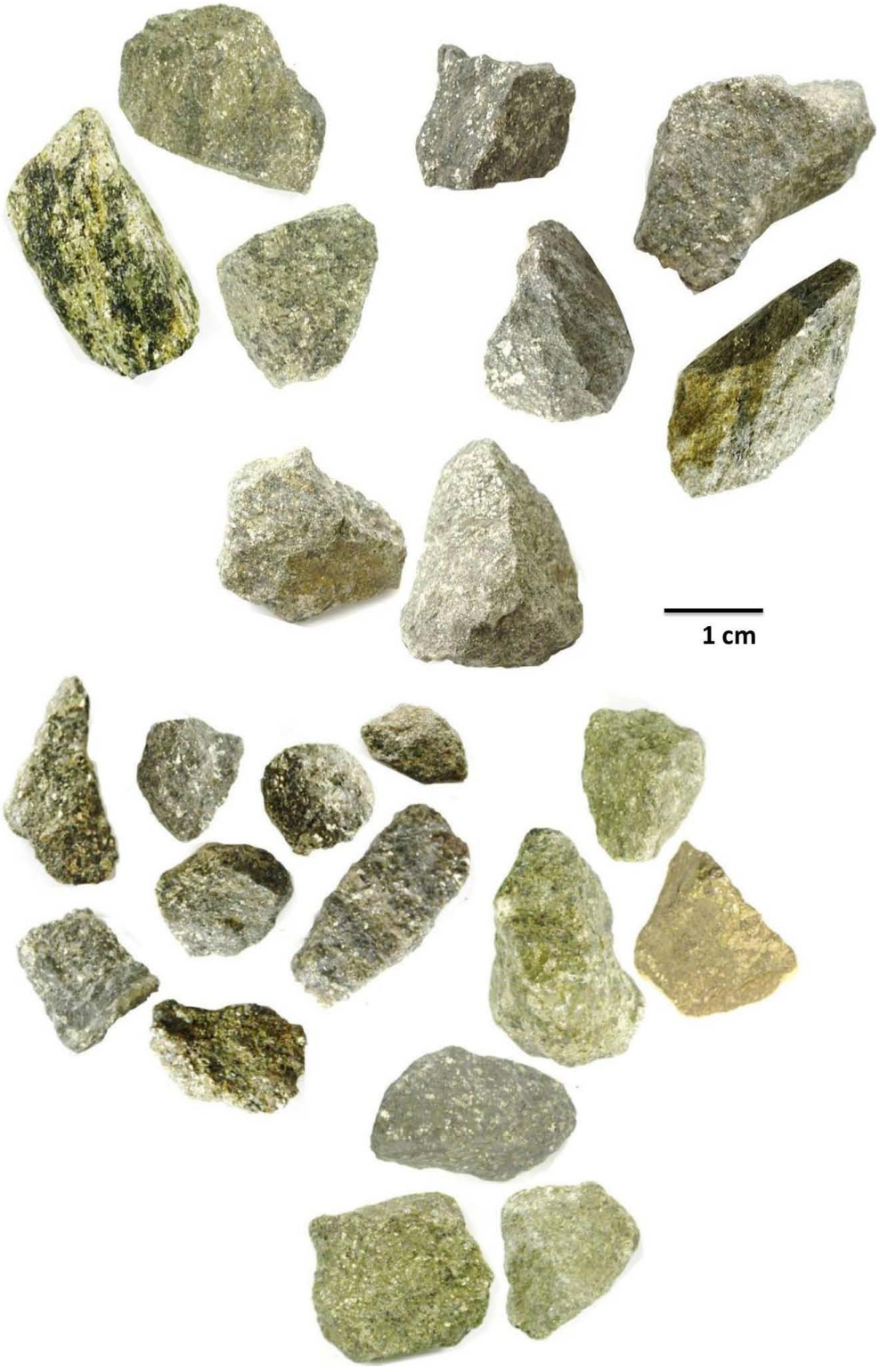

Ore particles produced using cone crusher.

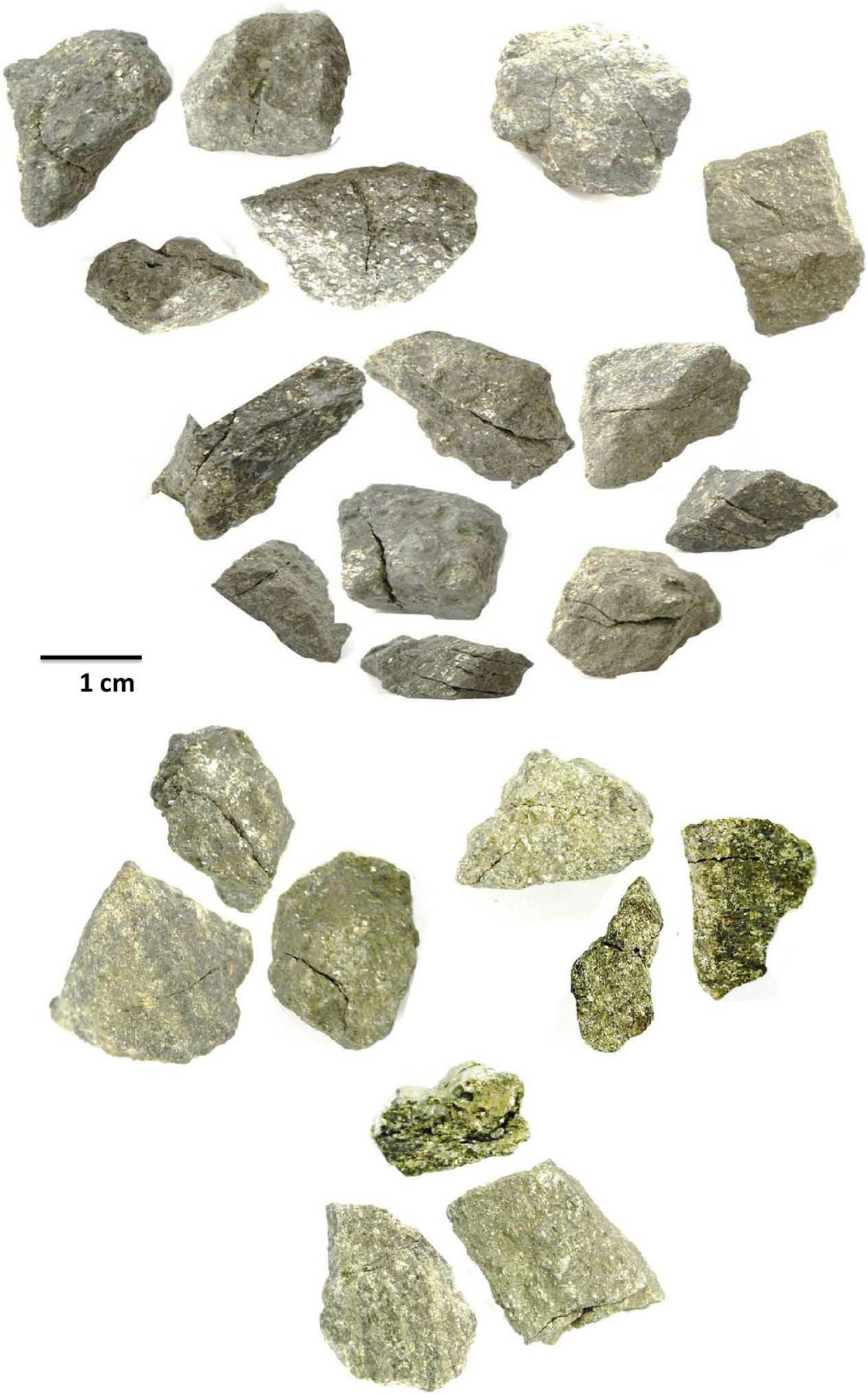

Ore particles produced using HPGR.

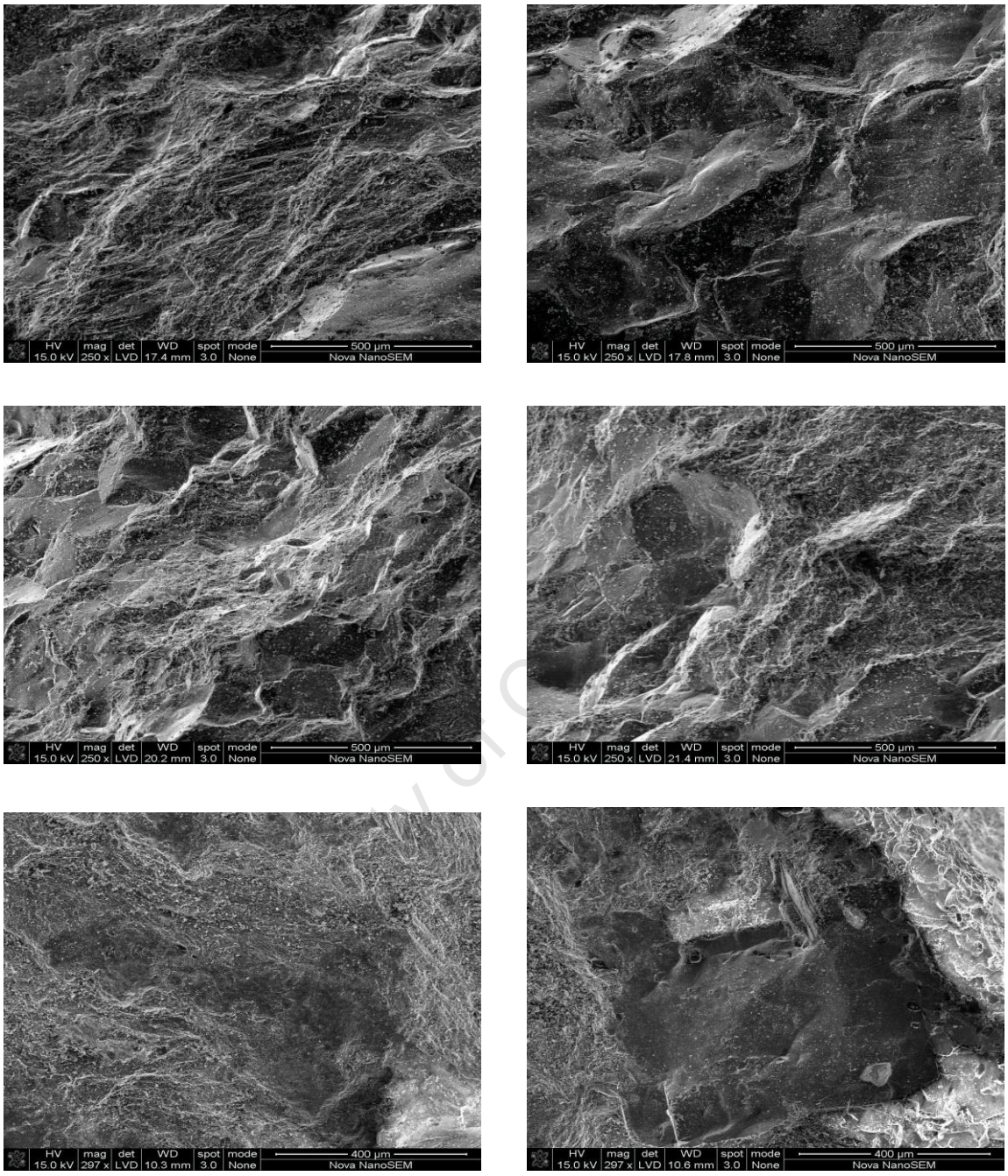

SEM microphotograph of the ore particles produced using cone crusher (to be continued on the next page).

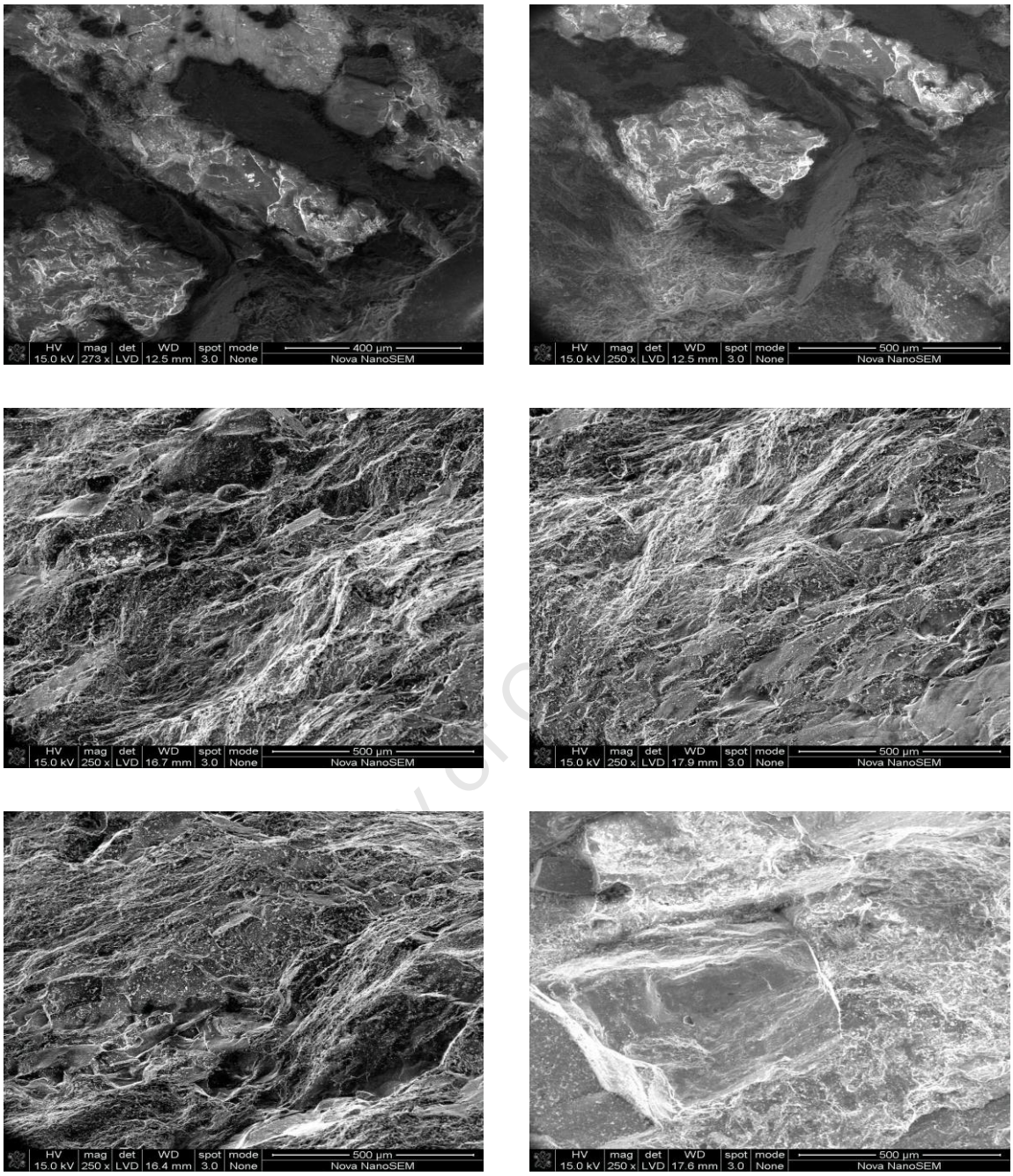

SEM microphotograph of the ore particles produced using cone crusher (to be continued on the next page).

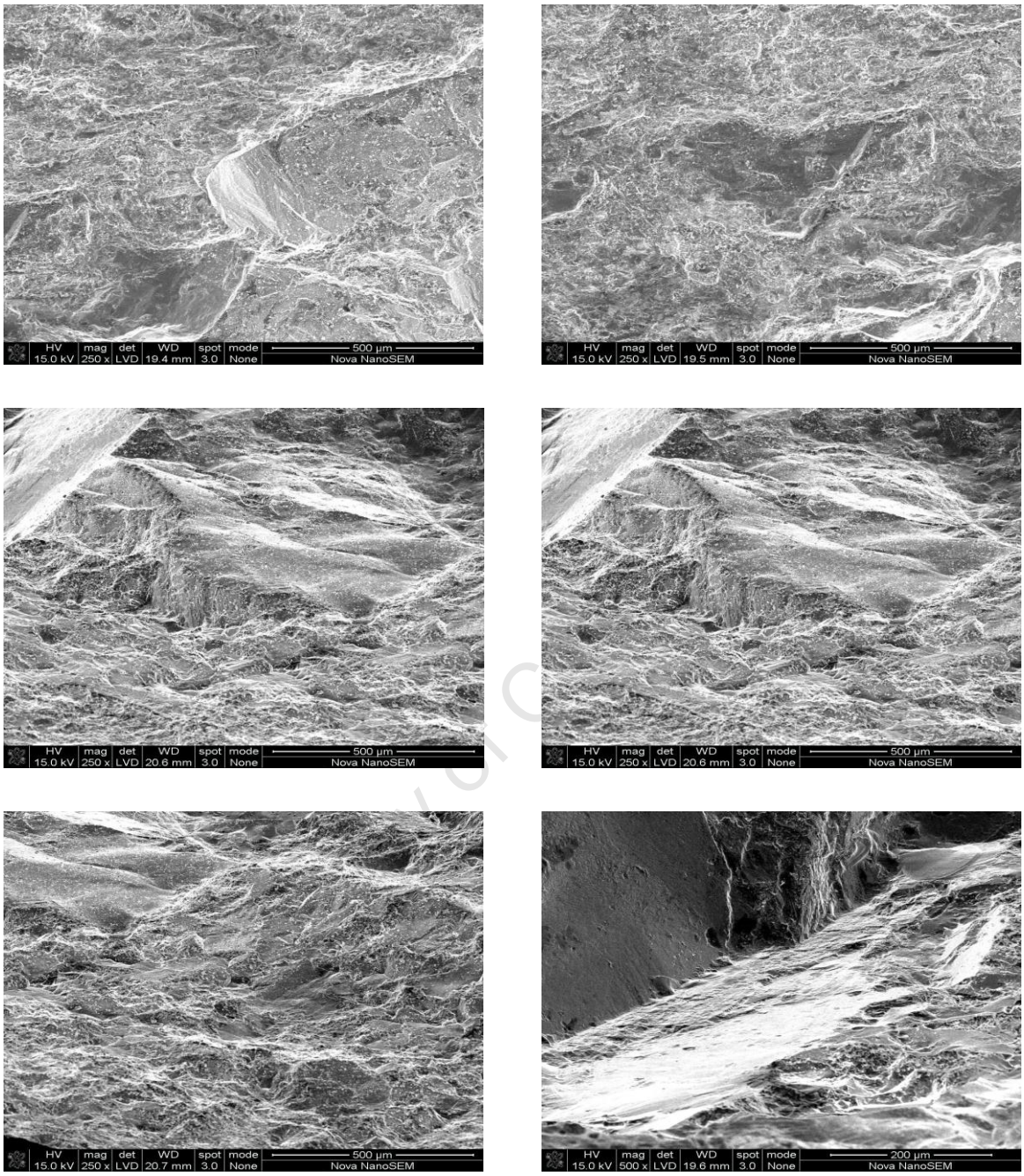

SEM microphotograph of the ore particles produced using cone crusher.

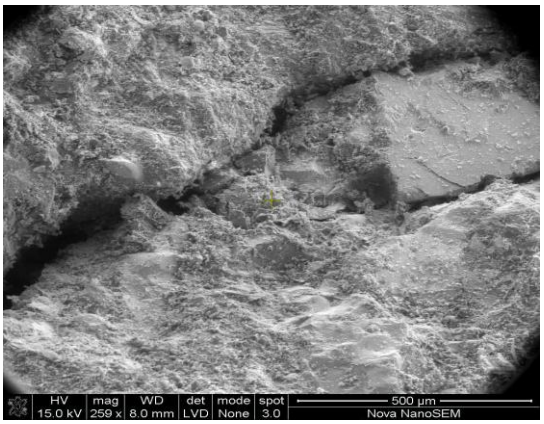

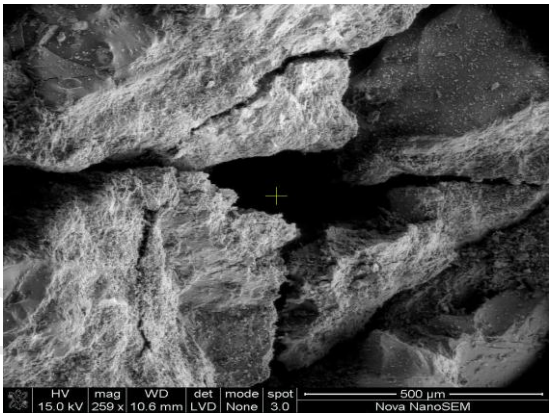

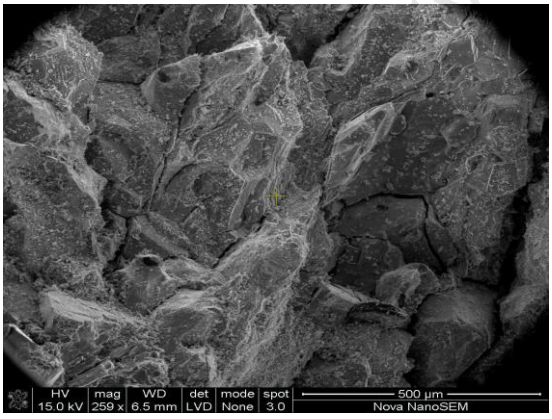

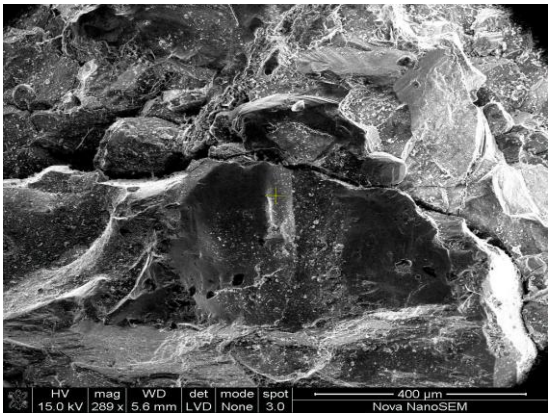

SEM microphotograph of the ore particles produced using HPGR (to be continued on the next page).

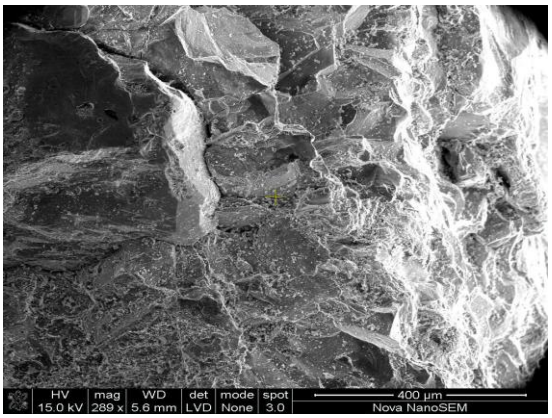

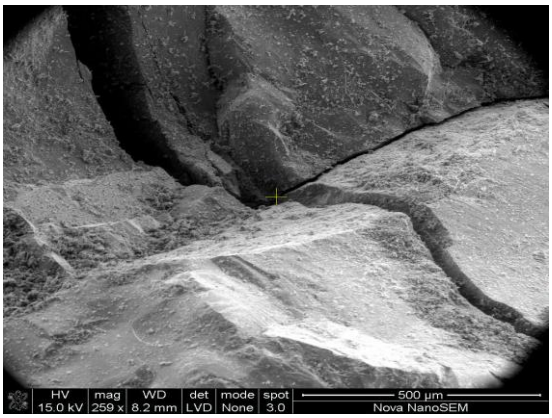

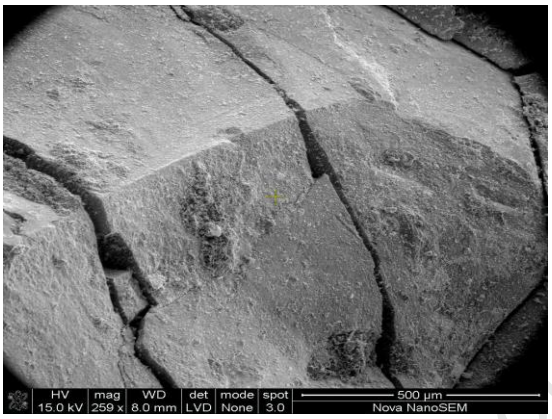

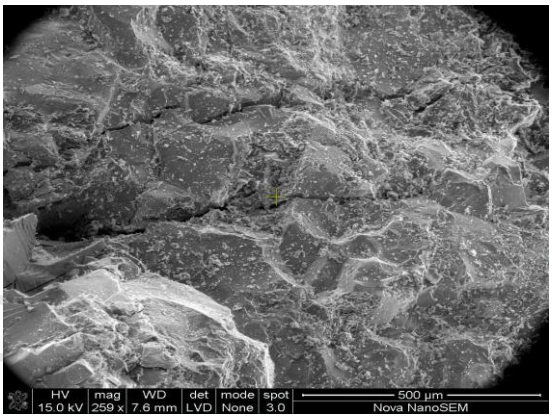

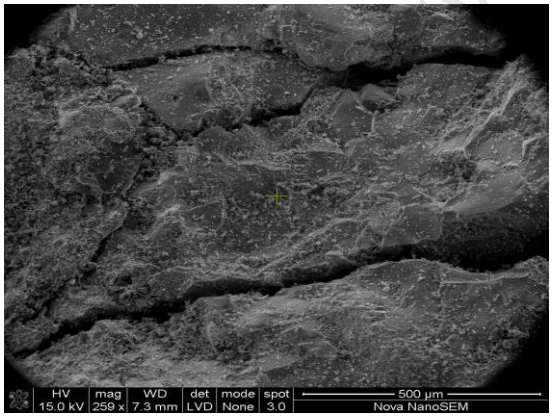

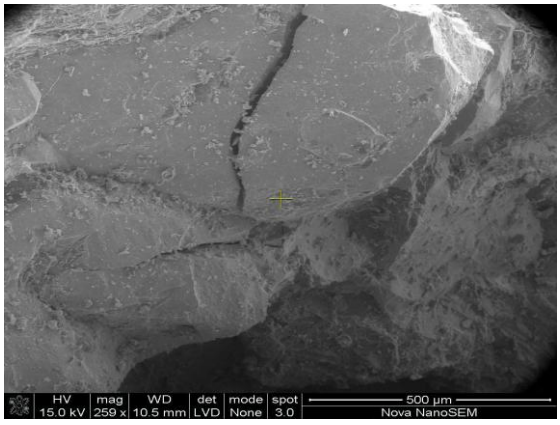

SEM microphotograph of the ore particles produced using HPGR (to be continued on the next page).

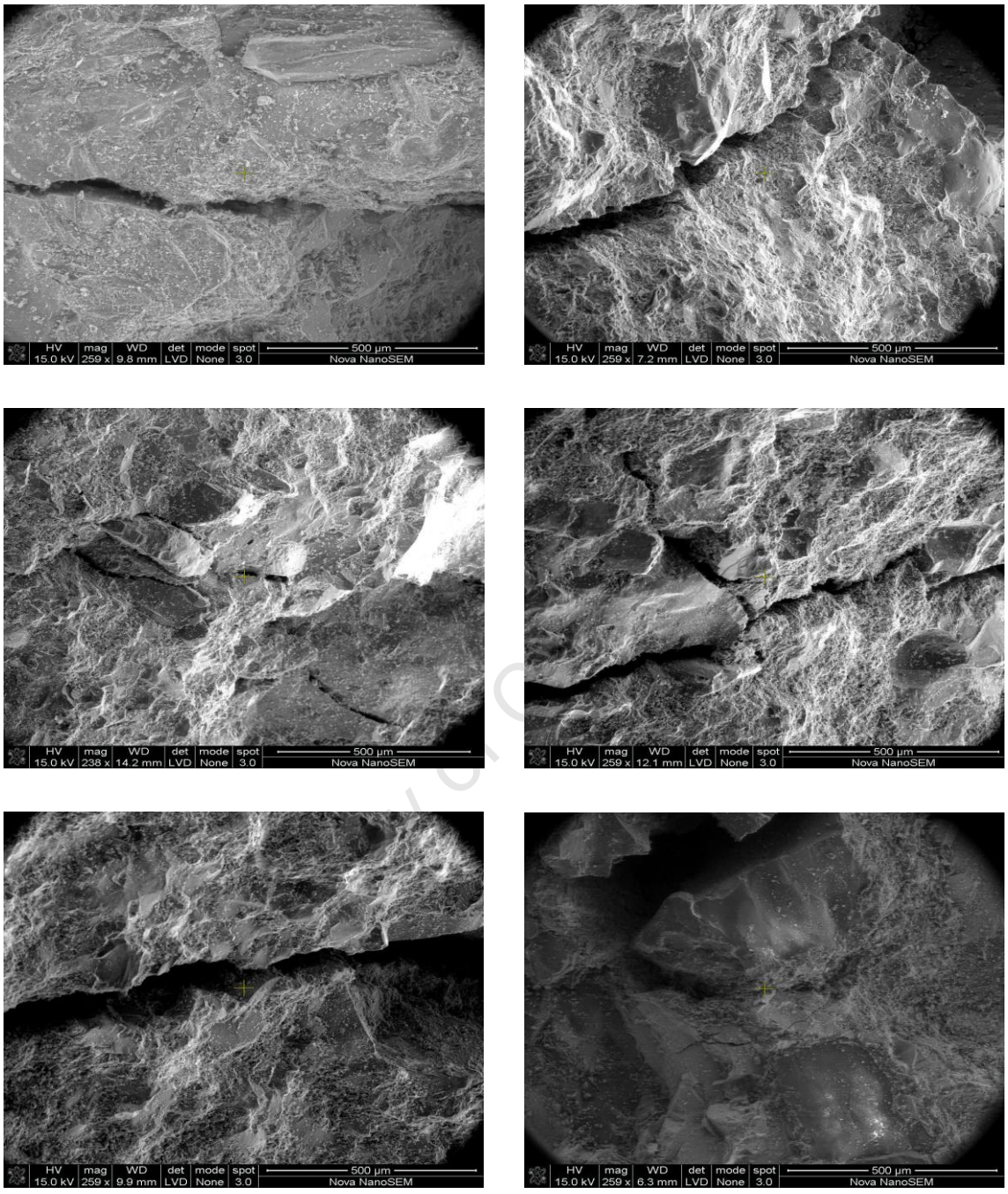

SEM microphotograph of the ore particles produced using HPGR.

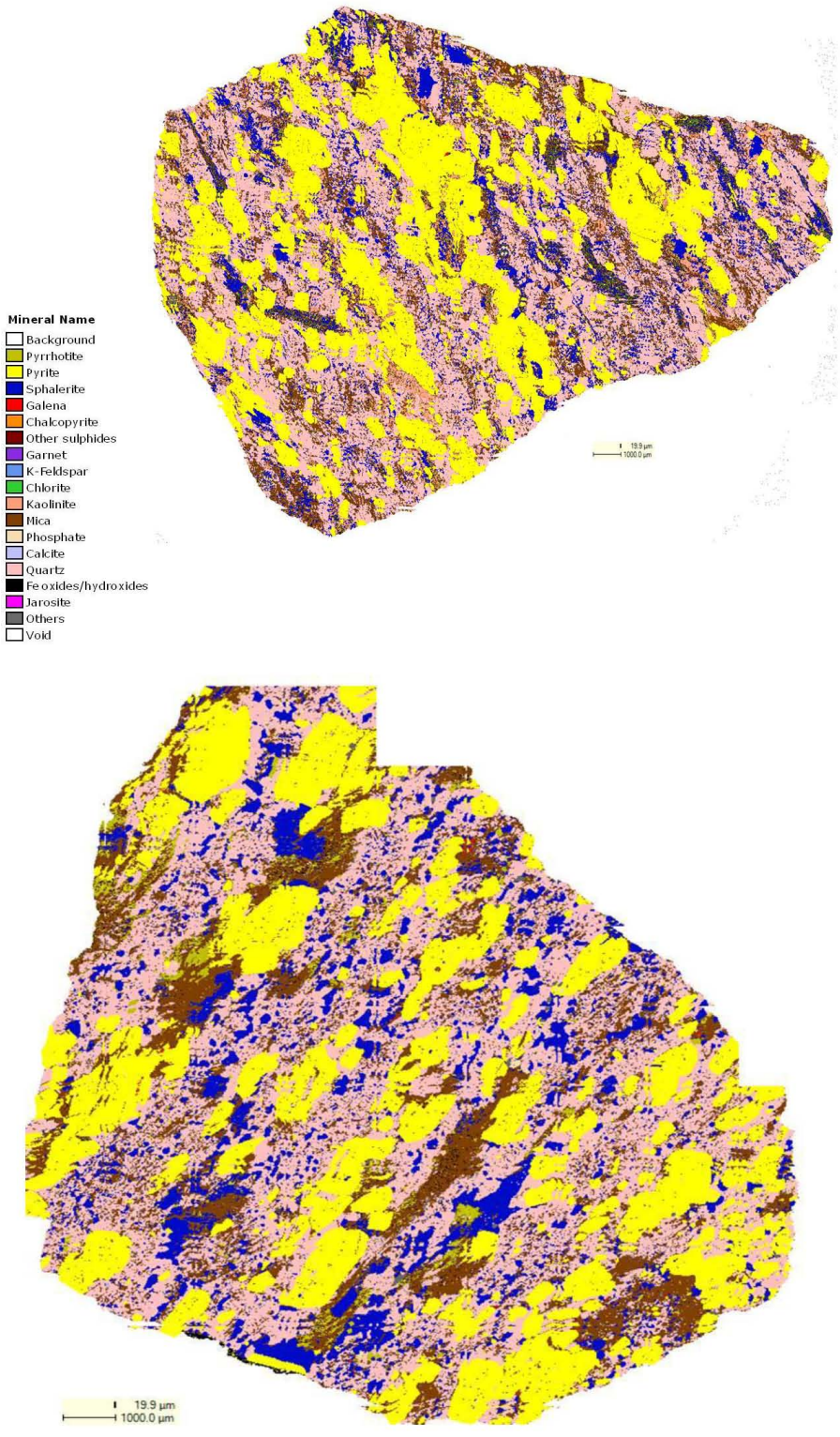

QEMSCAN image of the ore particles produced by cone crusher (to be continued on the next page).

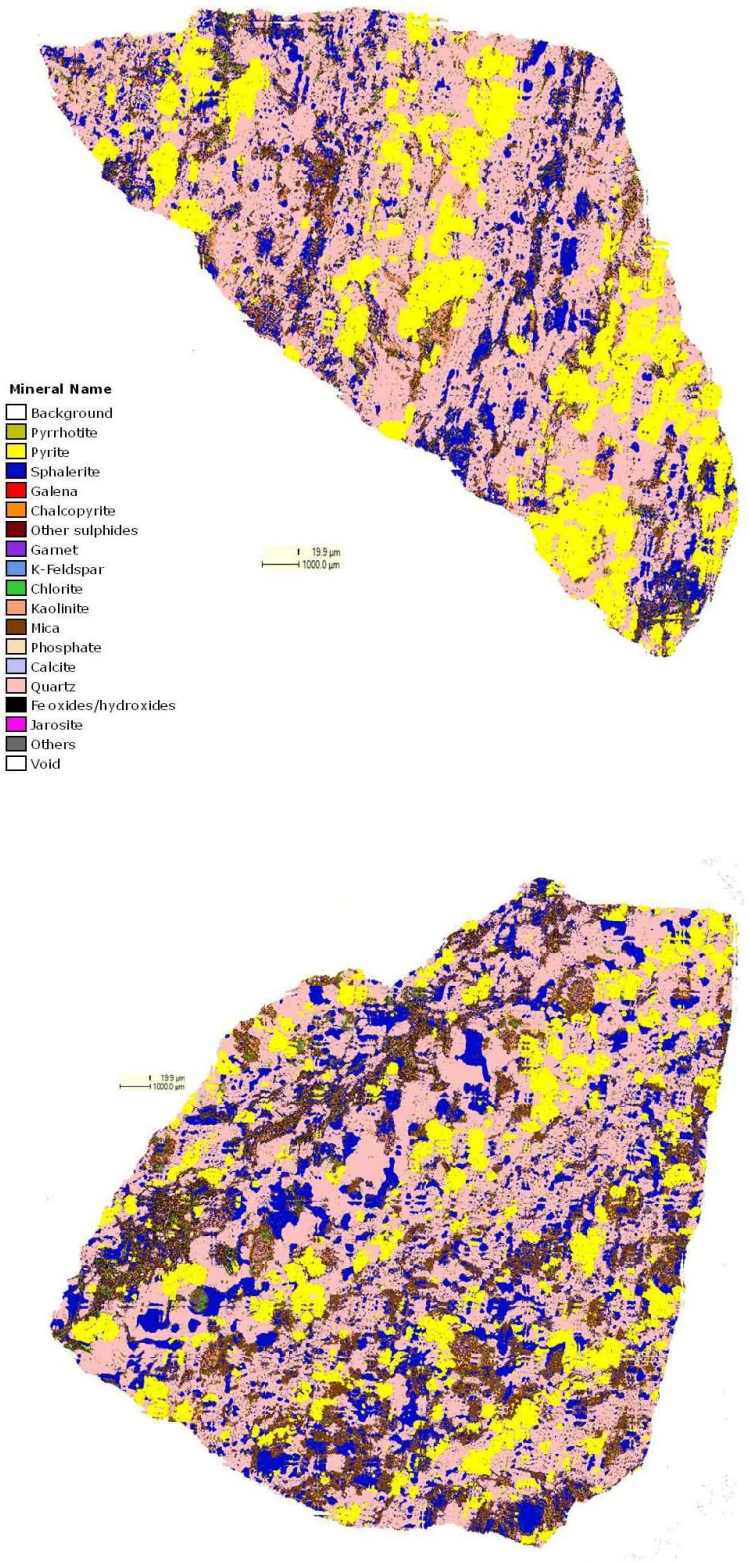

QEMSCAN image of the ore particles produced by cone crusher.

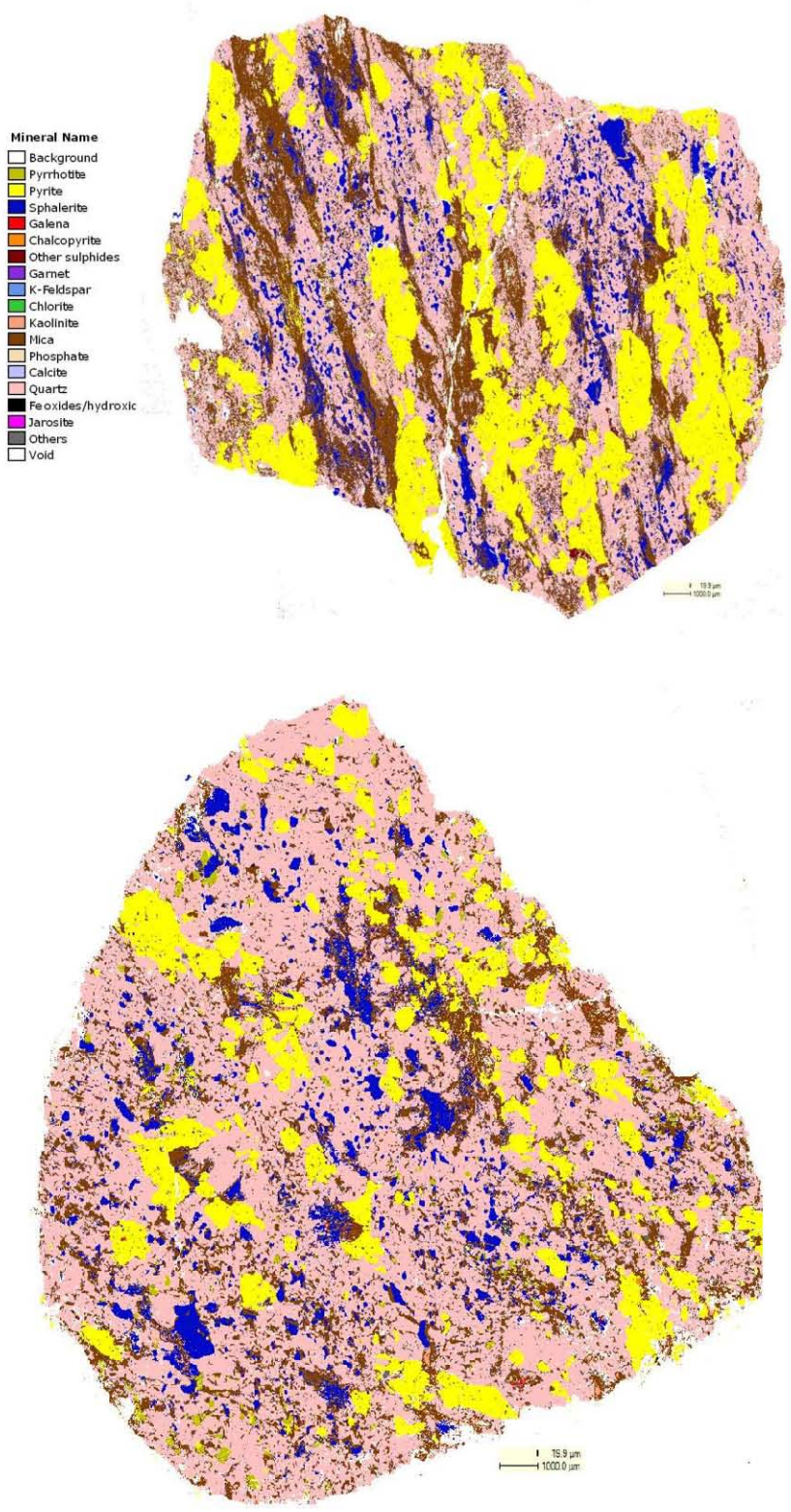

QEMSCAN image of the ore particles produced by HPGR (to be continued on the next page).

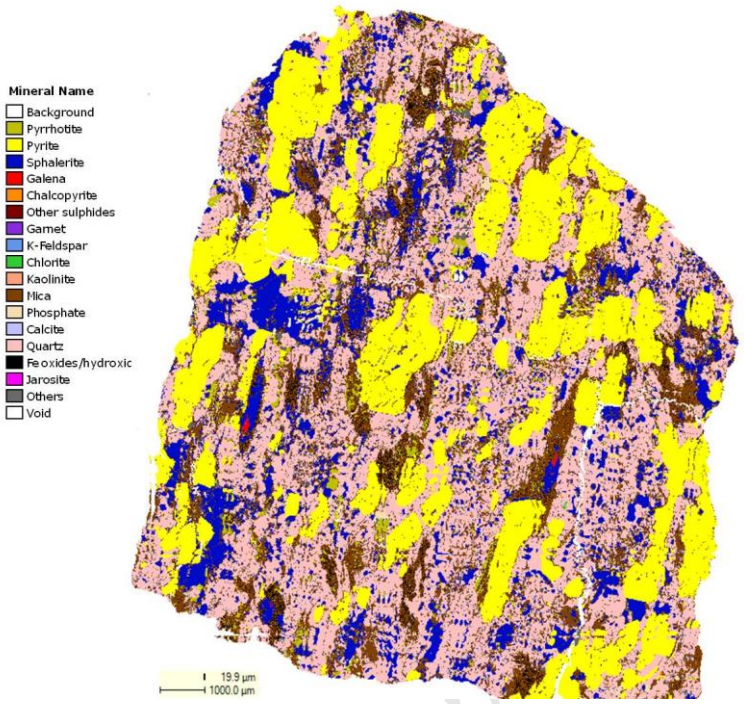

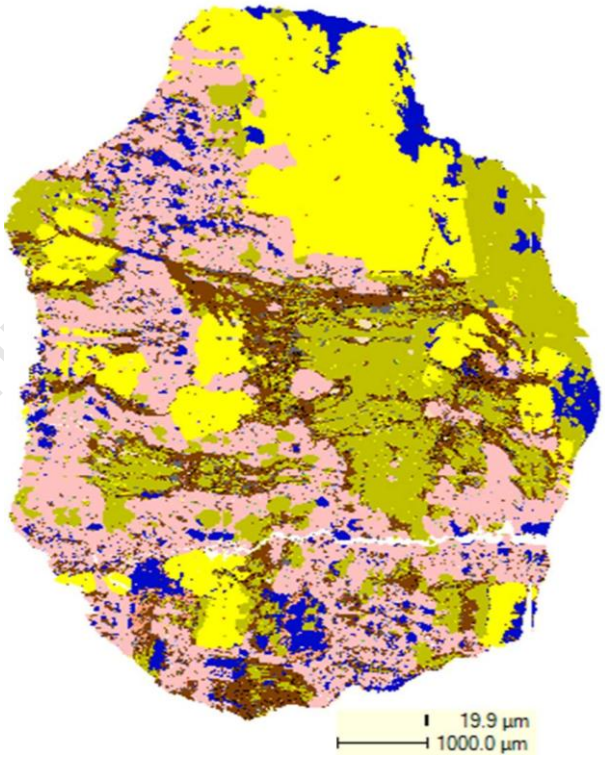

QEMSCAN image of the ore particles produced by HPGR (Note the presence of the micro-cracks in the particle prepared by HPGR.

Appendix V: Comparison of the amount of Zn, Ca and Mn in the leach liquors of the reactors.

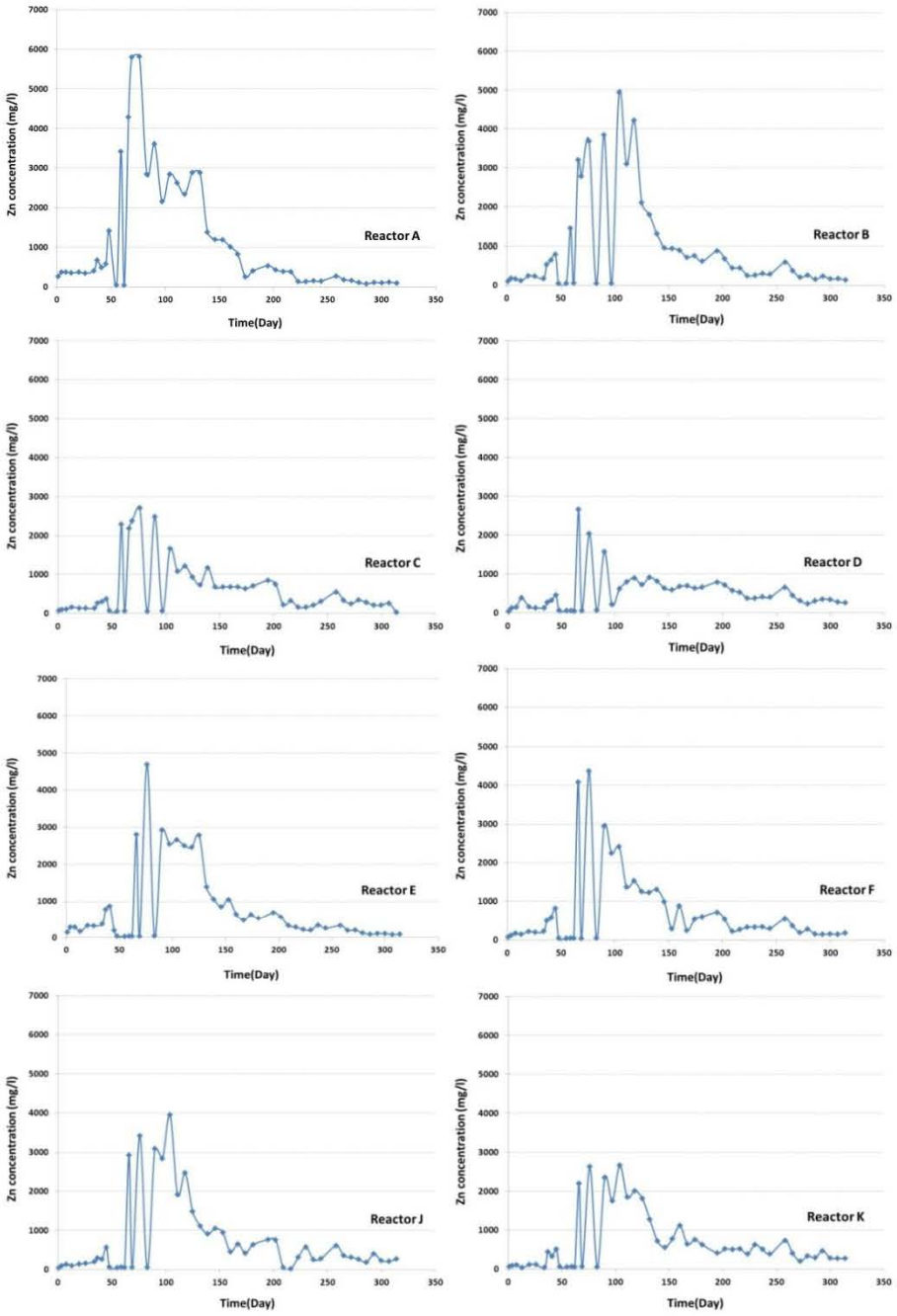

Comparison of the amount of zinc in the leach liquors of the reactors A (HPGR-95bars-Small size fraction), B (HPGR-95bars-Medium size fraction), C (HPGR-95bars-large size fraction), D (HPGR-120bars-large size fraction), E (cone crusher-Small size fraction), F (cone crusher-Medium size fraction), J (cone crusher-large size fraction) and K (HPGR-45bars-large size fraction).

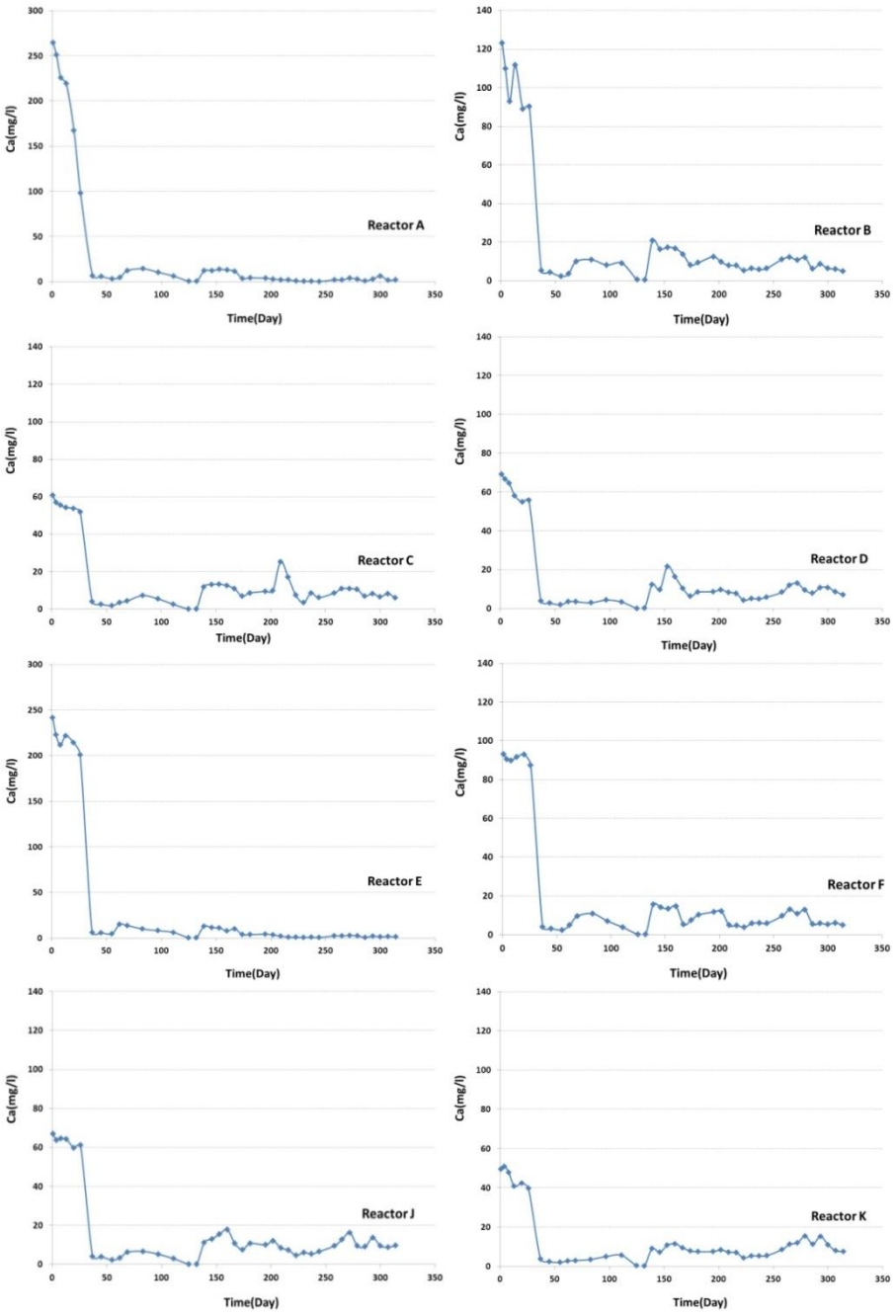

Comparison of the amount of Ca in the leach liquors of the reactors A (HPGR-95bars-Small size fraction), B (HPGR-95bars-Medium size fraction), C (HPGR-95bars-large size fraction), D (HPGR-120bars-large size fraction), E (cone crusher-Small size fraction), F (cone crusher-Medium size fraction), J (cone crusher-large size fraction) and K (HPGR-45bars-large size fraction).

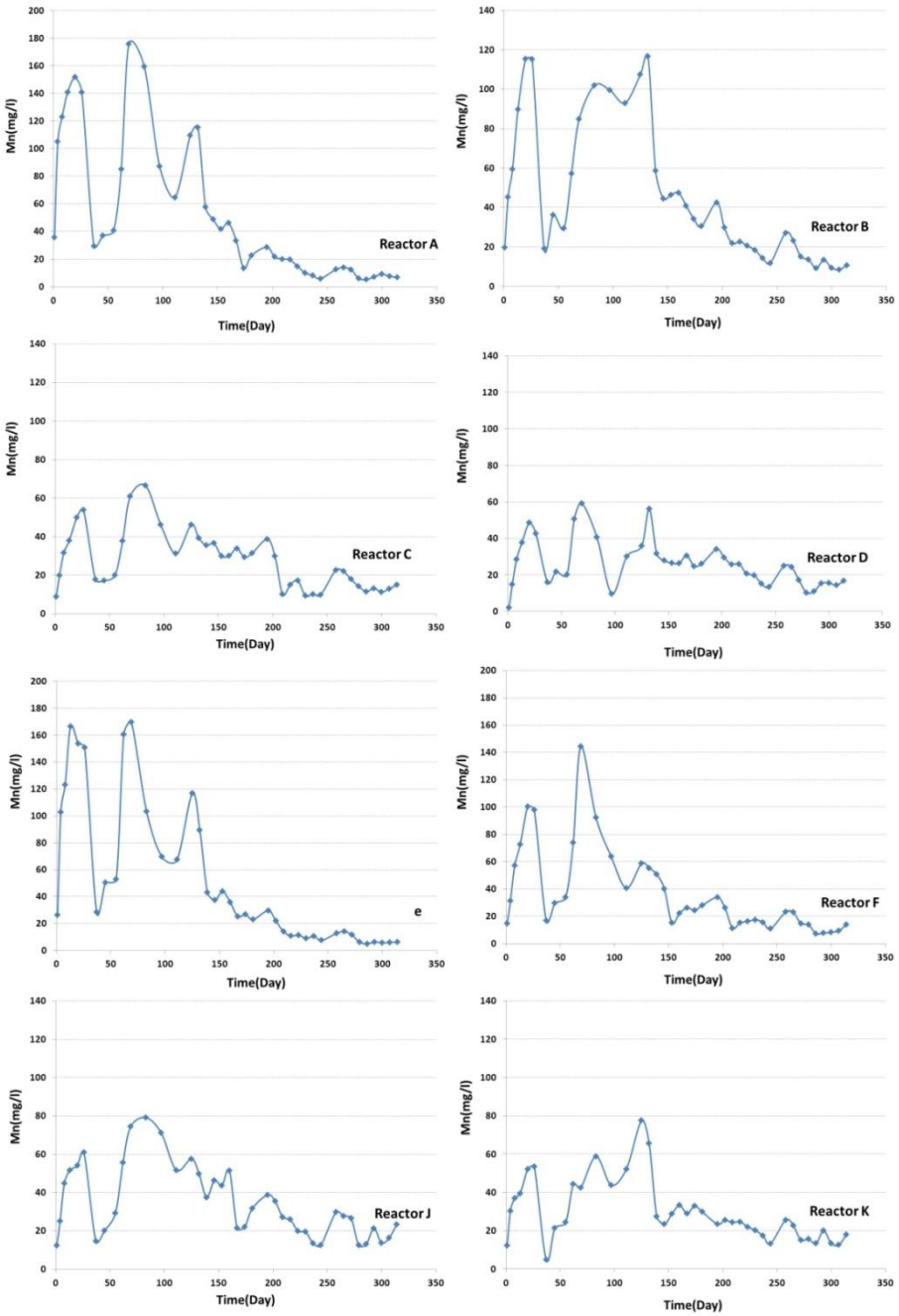

Comparison of the amount of Mn in the leach liquors of the reactors A (HPGR-95bars-Small size fraction), B (HPGR-95bars-Medium size fraction), C (HPGR-95bars-large size fraction), D (HPGR-120bars-large size fraction), E (cone crusher-Small size fraction), F (cone crusher-Medium size fraction), J (cone crusher-large size fraction) and K (HPGR-45bars-large size fraction).

Appendix VI: The defective area and attachment of the microorganism

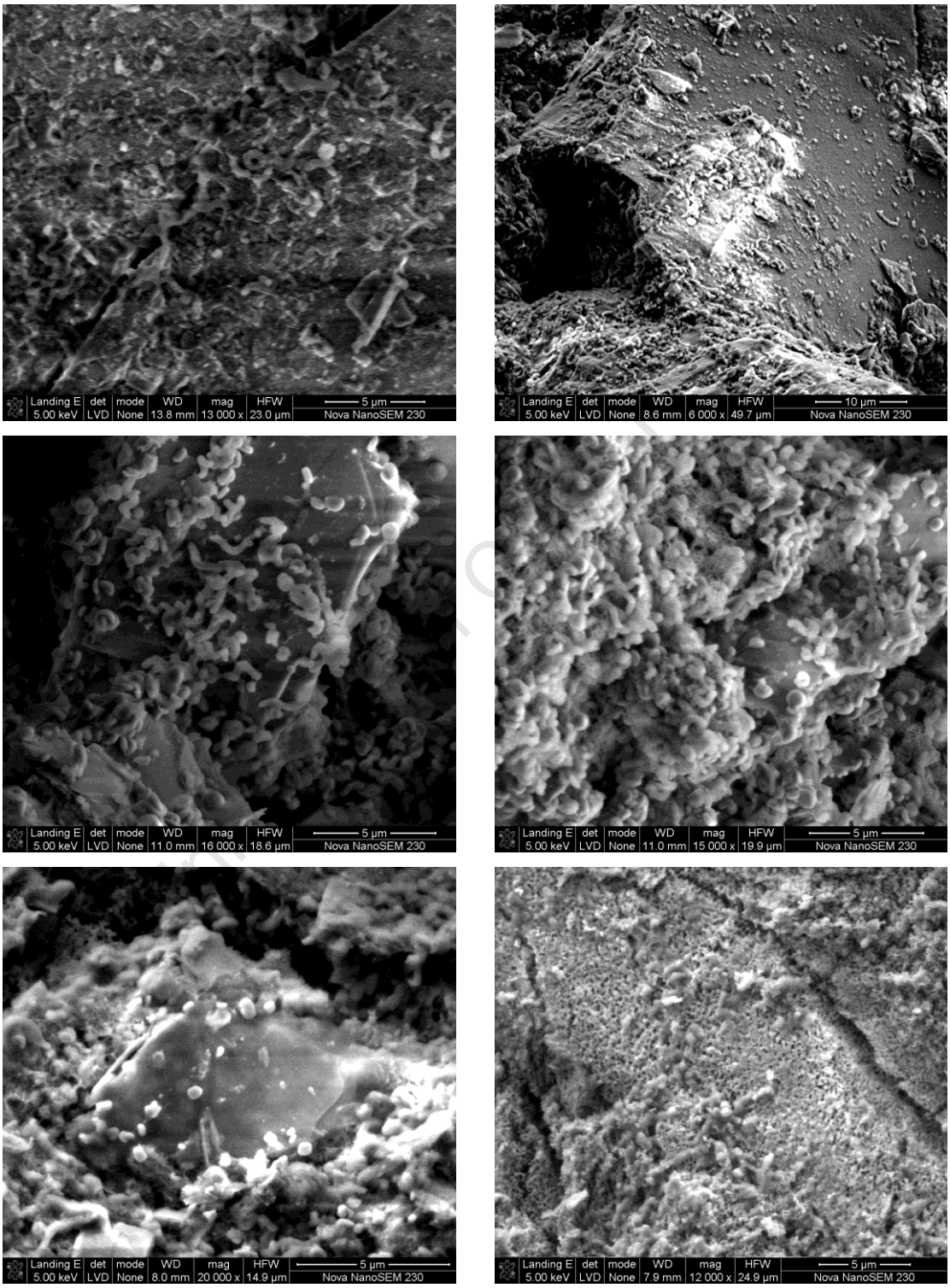

SEM microphotograph attachment of the microorganism to the defective area as a nucleation site (to be continued on the next page).

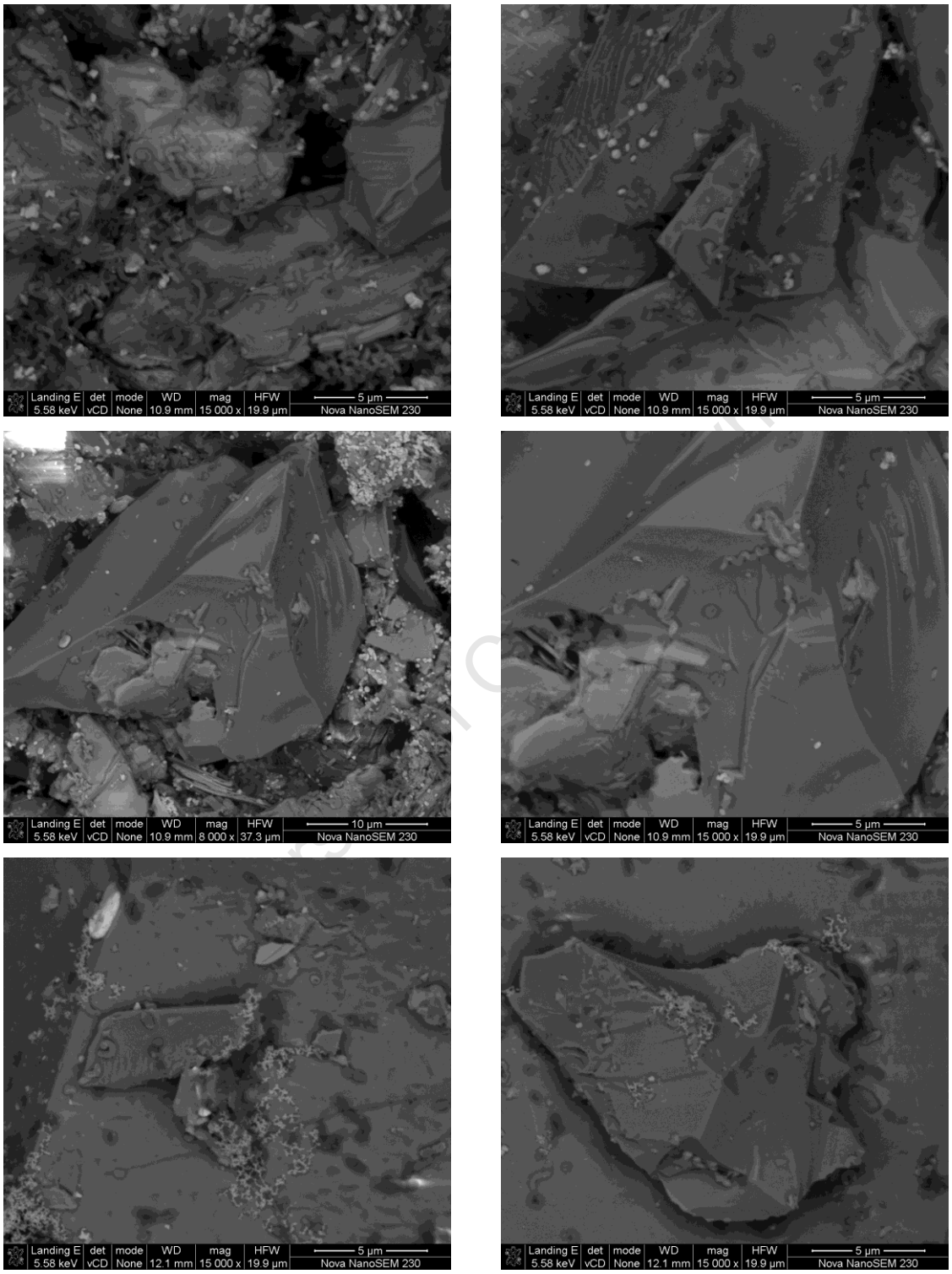

SEM microphotograph attachment of the microorganism to the defective area as a nucleation site (to be continued on the next page).

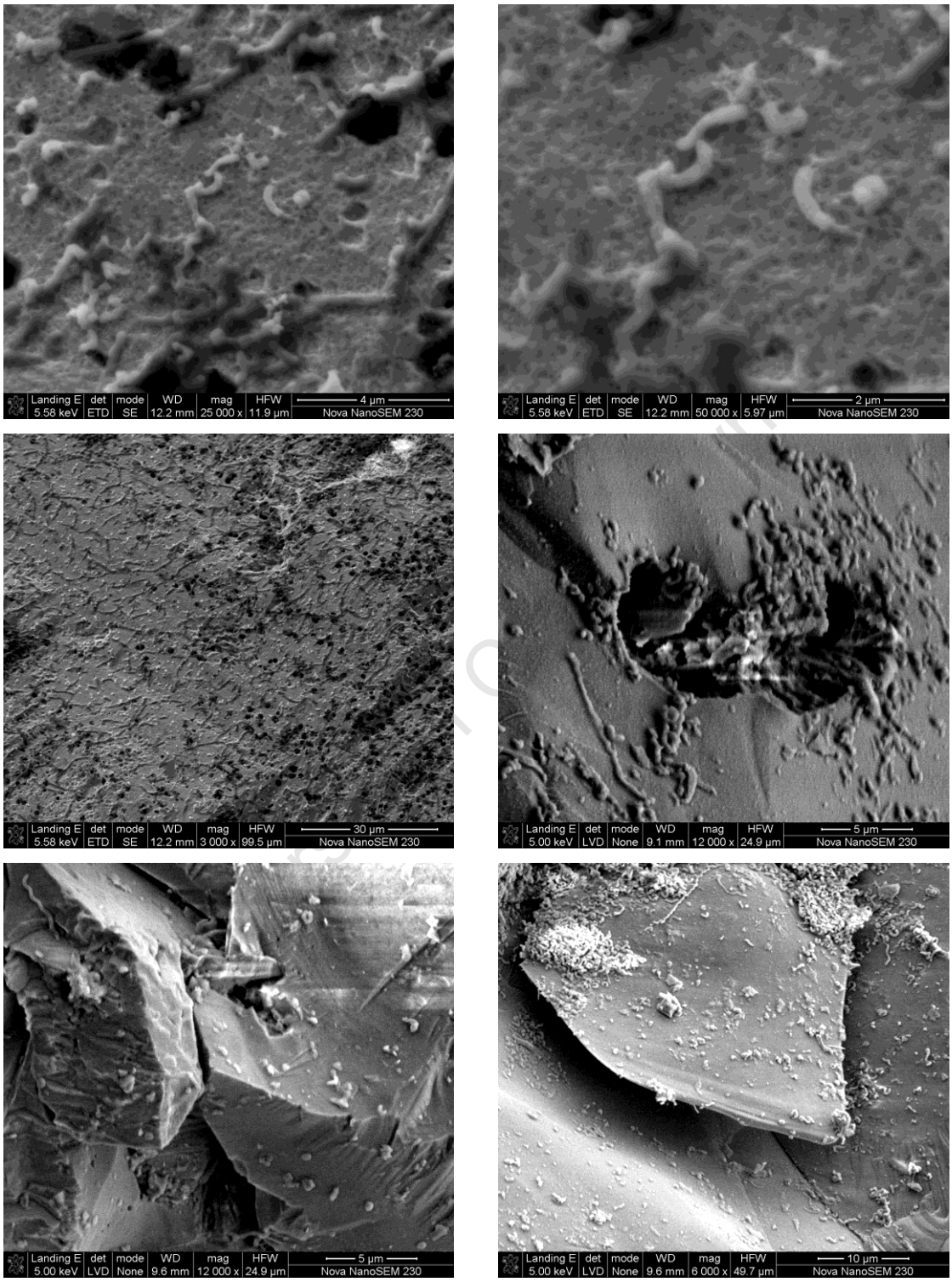

SEM microphotograph attachment of the microorganism to the defective area as a nucleation site (to be continued on the next page).

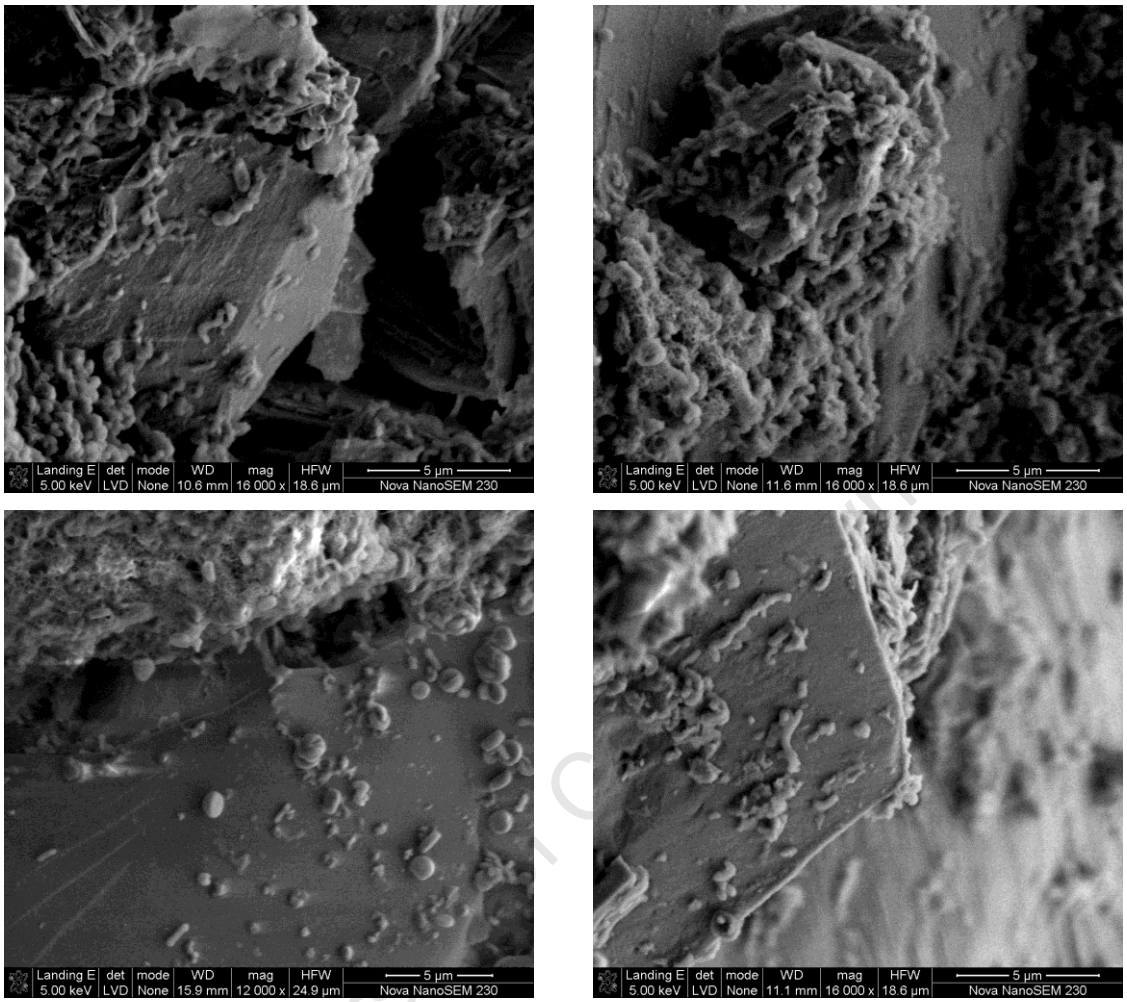

SEM microphotograph attachment of the microorganism to the defective area as a nucleation site.

Appendix VII: Leach reactors data and simulated data using the K- φ Models

Time (day)	Leach reactors data							
	A	B	C	D	E	F	J	K
0	0.07	0.04	0.03	0.02	0.05	0.03	0.02	0.02
11	0.11	0.06	0.06	0.03	0.05	0.03	0.02	0.02
17	0.16	0.12	0.08	0.06	0.10	0.10	0.06	0.06
27	0.29	0.19	0.18	0.10	0.18	0.13	0.10	0.10
41	0.36	0.23	0.23	0.15	0.22	0.17	0.12	0.13
65	0.43	0.29	0.26	0.17	0.30	0.23	0.16	0.17
79	0.49	0.39	0.30	0.19	0.36	0.27	0.19	0.23
93	0.55	0.44	0.33	0.21	0.42	0.31	0.23	0.28
107	0.62	0.49	0.37	0.25	0.46	0.36	0.26	0.31
121	0.66	0.52	0.39	0.30	0.50	0.40	0.28	0.35
135	0.72	0.55	0.42	0.33	0.52	0.42	0.31	0.37
149	0.73	0.58	0.45	0.35	0.54	0.45	0.34	0.41
163	0.75	0.60	0.48	0.38	0.56	0.46	0.35	0.43
177	0.76	0.62	0.50	0.40	0.58	0.49	0.36	0.45
191	0.76	0.64	0.51	0.42	0.59	0.51	0.38	0.48
205	0.77	0.65	0.52	0.43	0.60	0.52	0.40	0.49
219	0.78	0.66	0.53	0.45	0.62	0.54	0.41	0.51

Time (day)	Data obtained using equation: $\mathbf{X(t) = 1 - (1 + K(\varphi - 1)t)^{\frac{1}{1-\varphi}}}$							
	A	B	C	D	E	F	J	K
0	0	0	0	0	0	0	0	0
11	0.12	0.07	0.08	0.04	0.05	0.05	0.03	0.03
17	0.17	0.10	0.10	0.06	0.09	0.07	0.05	0.05
27	0.25	0.16	0.15	0.08	0.15	0.11	0.08	0.08
41	0.34	0.23	0.20	0.12	0.23	0.17	0.11	0.13
65	0.46	0.33	0.27	0.17	0.32	0.24	0.17	0.20
79	0.52	0.38	0.31	0.20	0.37	0.28	0.20	0.24
93	0.56	0.43	0.34	0.23	0.41	0.32	0.23	0.27
107	0.61	0.47	0.37	0.26	0.45	0.35	0.26	0.31
121	0.64	0.50	0.40	0.29	0.48	0.38	0.28	0.34
135	0.68	0.54	0.42	0.32	0.51	0.41	0.30	0.37
149	0.71	0.57	0.45	0.34	0.53	0.44	0.33	0.40
163	0.73	0.59	0.47	0.37	0.56	0.46	0.35	0.43
177	0.75	0.62	0.49	0.39	0.58	0.49	0.37	0.45
191	0.77	0.64	0.51	0.42	0.60	0.51	0.38	0.47
205	0.79	0.66	0.52	0.44	0.61	0.53	0.40	0.50
219	0.81	0.68	0.54	0.46	0.63	0.54	0.42	0.52

Time (day)	Leach reactors data							
	A	B	C	D	E	F	J	K
0	0.07	0.04	0.03	0.02	0.05	0.03	0.02	0.02
7	0.10	0.06	0.03	0.03	0.05	0.03	0.02	0.02
11	0.11	0.08	0.04	0.03	0.05	0.03	0.02	0.02
14	0.13	0.11	0.05	0.03	0.05	0.03	0.02	0.02
18	0.19	0.13	0.06	0.06	0.10	0.08	0.06	0.06
21	0.24	0.16	0.08	0.06	0.10	0.09	0.06	0.06
28	0.29	0.19	0.10	0.10	0.18	0.11	0.10	0.10
35	0.32	0.21	0.14	0.10	0.18	0.13	0.10	0.10
42	0.36	0.23	0.19	0.15	0.22	0.15	0.12	0.13
49	0.38	0.28	0.22	0.16	0.26	0.20	0.13	0.15
56	0.43	0.30	0.24	0.17	0.30	0.20	0.16	0.17
63	0.46	0.35	0.28	0.18	0.31	0.24	0.17	0.19
70	0.49	0.39	0.30	0.19	0.36	0.27	0.19	0.23
77	0.52	0.42	0.32	0.20	0.39	0.29	0.21	0.25
84	0.55	0.44	0.33	0.21	0.42	0.31	0.23	0.28
91	0.59	0.46	0.35	0.24	0.46	0.33	0.24	0.30
98	0.62	0.49	0.37	0.25	0.48	0.36	0.26	0.31
105	0.64	0.49	0.38	0.28	0.49	0.37	0.27	0.33
112	0.66	0.52	0.39	0.30	0.50	0.40	0.28	0.35
119	0.71	0.53	0.41	0.31	0.50	0.40	0.31	0.35
126	0.72	0.55	0.42	0.33	0.52	0.42	0.31	0.37
133	0.72	0.56	0.43	0.33	0.53	0.42	0.32	0.40
147	0.73	0.58	0.45	0.35	0.54	0.45	0.34	0.41
154	0.74	0.58	0.47	0.37	0.56	0.46	0.35	0.42
161	0.75	0.59	0.48	0.38	0.56	0.46	0.35	0.43
168	0.75	0.61	0.49	0.39	0.57	0.48	0.35	0.44
175	0.76	0.62	0.50	0.40	0.58	0.49	0.36	0.45
182	0.76	0.64	0.50	0.41	0.58	0.50	0.38	0.47
189	0.76	0.65	0.51	0.42	0.59	0.51	0.38	0.48
196	0.77	0.65	0.51	0.42	0.59	0.51	0.39	0.48
210	0.77	0.66	0.52	0.43	0.60	0.52	0.40	0.49
217	0.77	0.66	0.53	0.44	0.61	0.53	0.40	0.50
224	0.78	0.67	0.53	0.45	0.62	0.54	0.41	0.51
231	0.78	0.67	0.54	0.46	0.62	0.54	0.41	0.51
238	0.78	0.67	0.55	0.46	0.62	0.54	0.42	0.52
245	0.79	0.67	0.55	0.47	0.63	0.55	0.42	0.52
252	0.79	0.68	0.56	0.47	0.63	0.55	0.43	0.53
259	0.79	0.68	0.56	0.48	0.63	0.55	0.43	0.53
266	0.79	0.69	0.56	0.49	0.63	0.56	0.44	0.54

Time (day)	Data obtained using equation: $X(t) = \begin{cases} \alpha\left[1-\left(1+(\varphi-1)\frac{Kt}{\alpha}\right)^{\frac{1}{1-\varphi}}\right]+\beta t \\ \alpha+\beta t \end{cases}$							
	A	B	C	D	E	F	J	K
0	0.00	0.00	0	0.00	0.00	0.00	0.00	0.00
7	0.07	0.05	0.034933	0.02	0.04	0.03	0.02	0.02
11	0.11	0.08	0.05419	0.03	0.06	0.04	0.03	0.04
14	0.14	0.10	0.068303	0.04	0.08	0.06	0.04	0.05
18	0.17	0.12	0.086687	0.06	0.10	0.07	0.05	0.06
21	0.20	0.14	0.100154	0.06	0.11	0.08	0.06	0.07
28	0.26	0.18	0.130525	0.08	0.15	0.11	0.08	0.09
35	0.31	0.22	0.15946	0.10	0.19	0.14	0.10	0.11
42	0.36	0.26	0.186999	0.12	0.22	0.16	0.12	0.14
49	0.40	0.29	0.213182	0.14	0.26	0.19	0.14	0.16
56	0.44	0.32	0.23805	0.16	0.29	0.21	0.15	0.18
63	0.48	0.35	0.261644	0.18	0.32	0.24	0.17	0.20
70	0.51	0.38	0.284001	0.20	0.36	0.26	0.19	0.22
77	0.54	0.41	0.305163	0.21	0.39	0.28	0.21	0.24
84	0.57	0.43	0.325167	0.23	0.42	0.31	0.22	0.27
91	0.60	0.45	0.344051	0.25	0.44	0.33	0.24	0.29
98	0.62	0.47	0.361855	0.26	0.47	0.35	0.26	0.31
105	0.64	0.49	0.378615	0.28	0.49	0.37	0.27	0.33
112	0.66	0.51	0.394368	0.29	0.51	0.39	0.29	0.35
119	0.68	0.53	0.409151	0.30	0.52	0.41	0.30	0.37
126	0.69	0.54	0.423001	0.32	0.53	0.42	0.31	0.38
133	0.70	0.56	0.435953	0.33	0.53	0.44	0.33	0.40
147	0.73	0.58	0.459306	0.35	0.55	0.46	0.34	0.42
154	0.74	0.59	0.469776	0.37	0.55	0.46	0.35	0.43
161	0.74	0.60	0.479487	0.38	0.56	0.47	0.35	0.44
168	0.75	0.61	0.488473	0.39	0.56	0.48	0.36	0.44
175	0.76	0.62	0.496767	0.40	0.57	0.48	0.37	0.45
182	0.76	0.63	0.504402	0.41	0.58	0.49	0.37	0.46
189	0.77	0.64	0.511409	0.42	0.58	0.50	0.38	0.47
196	0.77	0.64	0.517821	0.42	0.59	0.50	0.38	0.47
210	0.78	0.65	0.528981	0.44	0.60	0.52	0.39	0.49
217	0.78	0.66	0.533791	0.45	0.61	0.52	0.40	0.50
224	0.78	0.66	0.538125	0.45	0.61	0.53	0.41	0.50
231	0.78	0.67	0.542015	0.46	0.62	0.54	0.41	0.51
238	0.79	0.67	0.545487	0.47	0.62	0.54	0.42	0.52
245	0.79	0.68	0.54857	0.47	0.63	0.55	0.42	0.53
252	0.79	0.68	0.551291	0.48	0.64	0.56	0.43	0.53
259	0.79	0.68	0.553676	0.48	0.64	0.56	0.43	0.54
266	0.79	0.68	0.555751	0.48	0.65	0.57	0.44	0.55

Appendix II: